The Henryk Niewodniczański
INSTITUTE OF NUCLEAR PHYSICS
Polish Academy of Sciences
ul. Radzikowskiego 152, 31-342 Kraków, Poland

http://www.ifj.edu.pl/publ/hab

Kraków, July 2018

Study of the Quark-Gluon Plasma with Hard Probes at the LHC

Jacek Otwinowski

Habilitation Thesis

Wydano Nakładem Instytutu Fizyki Jądrowej Im. Henryka Niewodniczańskiego
Polskiej Akademii Nauk
Kraków 2018

Recenzent: Prof. dr hab. Jan Figiel
ISBN 978-83-63542-01-6

Dla Doroty

Preface

Matter that surrounds us comes in a variety of phases that can be transformed into each other by a change of external conditions such as temperature, pressure, and composition. A good example is water that besides the liquid and gaseous phases, features a variety of solid phases [1]. Transitions from one phase to another are often accompanied by drastic changes in the physical properties of the matter, such as its electrical and thermal conductivity, elasticity, or transmittance. One may ask what happens when matter is under extreme conditions of high temperature and/or density. This question is of relevance for the early stage of the Universe as we go backwards in the cosmic evolution. It is also important in understanding of the properties of the inner core of neutron stars, the densest cosmic objects. Here the main players are no longer forces of electromagnetic origin but the strong interaction, which is responsible for the binding of protons and neutrons into nuclei and of quarks and gluons into the hadrons.

The first realistic picture of the hadronic matter at high temperature was proposed by Hagedorn in the statistical bootstrap model of hadron production [2], well before the discovery of the Quantum Chromodynamics (QCD) [3]. In this model, hadrons are considered as composite particles (resonances of lighter hadrons), which results in the exponential increase in the density of mass states, $\rho(m_{\rm h}) \propto m_{\rm h}^{-5/2} e^{m_{\rm h}/T_{\rm H}}$, where $m_{\rm h}$ is the mass of a given hadronic state and $T_{\rm H}$ is the Hagedorn temperature. This formula is well verified by summing up the measured hadronic states [4]. A fit to the data yields $T_{\rm H} \approx 170$ MeV. An immediate consequence of the model is that the logarithm of the partition function of such hadron resonance gas and, thus, all thermodynamical quantities diverge at the limiting temperature $T = T_{\rm H}$.

In 1973, Politzer [5], Gross and Wilczek [6] discovered that the QCD has properties of *asymptotic freedom*, i.e. the interaction between quarks and gluons weakens as they get closer to one another. It implies that at sufficiently high temperature and/or density, a new phase of deconfied quarks and gluons, referred to as quark-gluon plasma (QGP) [7–11], can be formed. The existence of a new phase was later confirmed in the calculations using the lattice formulation of QCD [12, 13]. Within this picture, the limiting temperature $T_{\rm H}$ is close to the critical temperature for the phase transition between hadrons and quarks and gluons. Moreover, with point-like quarks and gluons the temperature can grow beyond any limits.

These results inspired the community to explore the possibility to create and study the quark-gluon plasma by colliding heavy nuclei at high energy. In these collisions, the initial energy density and temperature should be sufficient to create the QGP for a short time. Experimental programmes started simultaneously in 1986 at the Alternating Gradient Synchrotron at the Brookhaven National Laboratory (BNL) and at the Super Proton Synchrotron (SPS) at CERN. Since 2000, the Relativistic Heavy Ion Collider (RHIC) at BNL has been colliding heavy-ions at $\sqrt{s_{\rm NN}} = 20$–200 GeV. A new era of experimental search for the QGP started in 2009, when the Large Hadron Collided (LHC) at CERN became operational. The LHC was designed to collide heavy nuclei up to that of Pb at energy of $\sqrt{s_{\rm NN}} = 5.5$ TeV, which is about 30 times larger than that at RHIC.

Author joined A Large Ion Collider Experiment (ALICE) at the LHC in 2007. ALICE is a dedicated heavy-ion detector, which was designed to exploit the unique potential of nucleus-nucleus interactions at the LHC energies. The main goal of ALICE is to study the physics of strongly interaction matter at extreme density and temperature, where the formation of the quark-gluon plasma is expected. Author has contributed to these studies using high momentum and/or high mass particles and jets (hard probes) to characterize the thermodynamic and transport properties of the QGP. Author is a key person in the ALICE Collaboration participating in measurements of transverse momentum spectra ($p_{\rm T}$) and nuclear modification factors of hard probes.

This habilitation thesis is based on the results [14–28] obtained by the author in 2010-2018. It consists of 13 chapters, list of figures, list of tables and references. An introduction to the strongly interacting matter at extreme conditions is presented in Chap 1. The experimental apparatus, including ALICE and LHC, is described in Chap. 2. Production of hard probes in high energy nuclear collisions and their interaction with the hot and dense QCD matter in theoretical models is discussed in Chap. 3. The results on the production of hard probes at RHIC are shown in Chap. 4. Properties of QCD matter produced at the LHC determined using measurements of low energy (soft) particles are discussed in Chap. 5. The following chapters contain the results obtained by the author. The $p_{\rm T}$ spectra of charged particles, charged pions, kaons and (anti)protons, D mesons, and charged jets, are presented in Chaps. 6, 7, 8, 9, respectively. The nuclear modification factors determined for charged particles, identified hadrons and jets, are discussed in Chaps. 10, 11 and 12, respectively. A summary is given in Chap. 13.

Contents

Chapter 1
Strongly Interacting Matter Under Extreme Conditions

An expected consequence of asymptotic freedom of the Quantum Chromodynamics (QCD) is that at sufficiently high temperature and/or density there is possible phase transition of strongly interacting matter from the hadron gas to a matter of deconfined quarks and gluons, the Quark-Gluon Plasma (QGP). In this chapter, an overview of theoretical and experimental studies of the QGP is presented. The main focus is on the experimental searches for the QGP using relativistic heavy-ion collisions, which is the main subject of the thesis.

1.1 Quarks and Gluons

The discovery of quarks and gluons was a gradual process that took over two decades. By the beginning of 1960s, the large number of hadrons was discovered and developing classification schemes for them became a timely question. At that point, new quantum numbers, such as isospin, baryon number and strangeness had already been introduced to group hadrons according to their decay and production properties. In 1961, a new hadron classification scheme based on SU(3) symmetry group was introduced by Gell-Mann and Ne'eman [29, 30]. This scheme allowed them to group hadrons with the same spin in multiplets. Using this approach, Gell-Mann predicted Ω^- baryon that was later discovered with appropriate properties [31]. In seeking a deeper explanation for regularities in the SU(3) classification scheme, Gell-Mann and Zweig invented in 1964 the quark model [32–34]. They postulated that the fundamental representation of the SU(3) group is a triplet of particles (*up*, *down*, *strange*) and their antiparticles. Following Gell-Mann, these particles were called *quarks*. Quarks are assigned spin-$1/2$, baryon number-$1/3$ and fractional charges ($+2/3\ e$,$-1/3\ e$,$-1/3\ e$) where e is the charge of electron. For antiquarks, the electric charge and baryon number are of opposite sign. Mesons are built from a quark-antiquark pair, while baryons are composed of three quarks. Soon later the quark model was extended by Bjorken and Glashow [35] by adding a forth flavor of quark, *charm*. This addition was proposed because it allowed for a better description of weak interaction in which quarks can change its flavor, equalized the number of known quarks with the

number of known leptons, and implied a mass formula that correctly reproduced the masses of the known mesons.

The first evidence that protons are not elementary particles came from the electron-proton deep inelastic scattering (DIS) experiments at SLAC. It has been measured [36, 37] that in a broad kinematic range the proton structure functions did not show dependence on the square of the 4-momentum (Q^2) exchanged by a virtual photon between the electron and the proton. They appeared to depend only on dimensionless variable $\omega = 2M\nu/Q^2$, where ν is the energy of virtual photon and M is the proton mass. Such scaling behavior was predicted by Bjorken [38] who showed that in the asymptotic limit ($\nu, Q^2 \to \infty$, ω fixed) the inelastic structure functions can be expressed as $\nu W_2(\nu, Q^2) \to F_2(x)$ and $W_1(\nu, Q^2) \to F_1(x)$, where $x = Q^2/2M\nu = 1/\omega$ is the Bjorken-x scaling variable. The physical significance of this scaling behavior became clear when Feynman interpreted data in terms of a model [39, 40] in which protons were composed of charged, pointlike constituents, *partons*. In this model, scaling arose naturally assuming that high-energy electron scattered elastically with quasifree parton carrying the fraction x of the total proton momentum. In his model, Feynman did not postulate any quantum numbers for the partons which could have whatever charges or spins. In the parton model, the proton structure functions for a large Q^2 have the following form

$$F_2(x) = \sum_i e_i^2 x f_i(x), \tag{1.1}$$

$$F_1(x) = \frac{1}{2x} F_2(x). \tag{1.2}$$

The proton is made of various types of partons with charges e_i, each carrying a fraction x of the proton momentum. $f_i(x)$ are the momentum distribution functions of the partons within the proton, which describe probability densities to find the parton carrying a momentum fraction x at a given Q^2. $f_i(x)$ are simply called Parton Distribution Functions (PDFs) when the spin direction of the partons is not considered. Equation (1.2) known as Callan-Gross relation [41] was obtained assuming that partons are spin-½ particles (for spin-0 particles $F_1(x) = 0$). Based on these ideas, Bjorken and Paschos formulated the first model [42] of highly inelastic electron-proton scattering in which partons were interpreted as quarks. In their model, the proton was made of three valence quarks plus cloud of quark-antiquark pairs. They have performed comparison to existing data [36] based on the sum rules, showing that this model cannot fit the data better than within $\sim 50\%$.

The next generation of electron-nucleon [43–46] and neutrino/anineutrino-nucleon [47, 48] DIS experiments allowed for precise measurements of nucleon structure functions in a broad Q^2 range. The data favored value of spin-½ for partons [43, 47], as expected for quarks. Moreover, the structure functions extracted for neutrino scatterings coincides with those for electron scatterings multiplied by the factor of about 3.6 as specified by the quark-parton model [48]. Such a good agreement provided a strong evidence that partons carry the fractional electric charge expected for quarks. These experiments have shown that there are three valence quarks in the proton (uud) and in the neutron (udd) that dominate the electron scattering at high x, plus a sea of quark-antiquark pairs ($u\bar{u}$, $d\bar{d}$, $s\bar{s}$) that is essentially the same for the two nucleons

and is largely responsible for the electron scattering at low x. Another observation was that only half of the nucleon momentum was carried by the charged partons [48], the other half being carried by neutral partons, *gluons*, as predicted by Kuti and Weisskopf [49]. Moreover, a violation of the Bjorken scaling was observed for the first time by the DIS experiments [44–46]. A slow fall-off of the structure functions as a function of Q^2 had beed anticipated in the parton model including gluons [50], in which charged quarks were surrounded by the cloud of gluons giving them a kind of structure.

One of the obvious problems of the quark-parton model was spin statistics for the baryons consisting three quarks of the same flavor and with total spin $J = {}^3/_2$, eg. the omega baryon $\Omega^- = |s\uparrow\rangle|s\uparrow\rangle|s\uparrow\rangle$. In this case, the total wave functions of quarks are fully symmetric violating the Pauli exclusion principle. This problem was resolved by introducing by Greenberg [51] a new quantum number for quarks, *color*. By analogy with the real colors, the quarks come in the primary colors (*red*, *green* and *blue*) while the antiquarks in three anti-colors (*cyan*, *magenta* and *yellow*). Thus, the three quarks that make Ω^- are distinguishable by their color. The assignment of the color is done to assert that all hadron observed in the nature are *colorless* or *white*. It means that the wave function to describe the color part of the hadron is a SU(3) singlet. The introduction of the color lead to the dramatic prediction for the e^+e^- annihilation cross section ratio, which for the leading processes involving quarks has the following form

$$R \equiv \frac{\sigma(e^+e^- \to q\bar{q} \to hadrons)}{\sigma(e^+e^- \to \mu^+\mu^-)} = 3\sum_q e_q^2. \tag{1.3}$$

Here, an extra factor of 3 arises because the cross sections for each quark color have to be added. Thus, a measurement of the total e^+e^- annihilation cross section into hadrons directly counts the number of quarks, their flavor as well as their color. The first results from the e^+e^- annihilation experiments [52, 53] confirmed that hadrons are made of colored quarks.

A complete conversion of physics community came after J/ψ discovery in the proton-Berylium at BNL [54] and e^+e^- collisions at SLAC [55], which existence could not be explained without invoking a charmed quark. Moreover, jets of hadrons were observed in high-energy electron-positron collisions [56]. A detailed analysis of the angular distributions of these jets indicated that they arose from the individual spin-½ particles, as expected for quarks. The discovery of *bottom* quark in proton-nucleus collisions ($pN \to \Upsilon + X \to \mu^+\mu^- + X$) at Fermilab [57] and a visible evidence for gluon existence seen as a additional jet (three jet events) in high-energy electron-positron collisions ($e^+e^- \to q\bar{q}g \to 3$ jets) at DESY [58–60] established a coherent picture of nucleon as composed of fractionally charged quarks and neutral gluons. This picture was finally confirmed when the heaviest top quark was discovered in proton-antiproton collisions ($p\bar{p} \to t\bar{t} + X \to WWb\bar{b} + X$) at Fermilab [61, 62].

1.2 Quantum Chromodynamics

Quantum Chromodynamics (QCD) is a quantum field theory of strong interactions between quarks and gluons, which was introduced in 1973 [3]. The QCD is a non-abelian gauge theory with the SU(3) gauge (color) symmetry. In this theory, quarks and gluons are the only fundamental particles that carry color charge [51] of strong interaction. Aside from the relativistic quantum numbers dictated by Lorenz invariance, quarks come in six flavors (up, down, strange, bottom and top). Gluons act as the exchange particles (gauge bosons) for strong force between quarks as well as participate in the strong interaction. This is unlike the photons, which mediate the electromagnetic interactions between charged particles but do not interact between each other due to the lack of electric charge. Quarks come in three color while antiquarks in three anticolor states. There are eight gluons corresponding to color-anticolor combinations excluding one that is a color singlet. The gauge invariant QCD Lagrangian is given by [4]

$$\mathscr{L} = \sum_q \overline{\psi}_{q,a} \left(i\gamma^\mu \partial_\mu \delta_{ab} - g_s \gamma^\mu t^C_{ab} A^C_\mu - m_q \delta_{ab} \right) \psi_{q,b} - \frac{1}{4} F^A_{\mu\nu} F^{A\mu\nu}, \tag{1.4}$$

where repeated indices are summed over. The $\psi_{q,a}$ are quark-field spinors for a quark of flavor q and mass m_q, with a color-index a that runs from 1 to $N_c = 3$. The quark masses are generated via the Higgs mechanism [63–65]. The quantity g_s is a strong coupling constant. The A^C_μ correspond to the gluon fields, with C running from 1 to $N_c^2 - 1 = 8$. The quark-quark and quark-gluon coupling are realized through the Dirac γ^μ and Gell-Mann t^C_ab matrices. Finally, the field tensor $F^A_{\mu\nu}$ is given by

$$F^A_{\mu\nu} = \partial_\mu A^A_\nu - \partial_\nu A^A_\mu - g_s f_{ABC} A^B_\mu A^C_\nu \quad \left[t^A, t^B \right] = i f_{ABC} t^C, \tag{1.5}$$

where f_{ABC} are the structure constants of the SU(3) group. One should note that $F^A_{\mu\nu}$ includes self-interaction between gluons, which is characteristic for the gauge theory based on a non-Abelian group. The Feynman rules of QCD involve a quark-antiquark–gluon ($q\bar{q}g$) vertex, a 3-gluon vertex (both proportional to g_s), and a 4-gluon vertex (proportional to g_s^2). The relative strength of the coupling of quarks and gluons is determined by their effective color charges (or color factors). The $C_\mathrm{F} = (N_\mathrm{c}^2 - 1)/2N_\mathrm{c} = 4/3$ is the color-factor associated with gluon emission from a quark, the $C_\mathrm{A} \equiv N_\mathrm{c} = 3$ is the color-factor associated with gluon emission from a gluon, and the $T_\mathrm{R} = 1/2$ is the color-factor for a gluon to split to a $q\bar{q}$ pair. Thus, the gluon has color charge that is larger than that for a quark by a factor $C_A/C_F = 9/4$, which has been verified experimentally with a large precision [66, 67].

In any quantum field theory the vacuum itself behaves, due to quantum fluctuations, like polarizable medium. For example, in the quantum electrodynamics (QED), an electron is surrounded by a cloud of virtual electron-positron pairs, which is polarized. Thus, the QED vacuum in the vicinity of electron becomes a polarizable medium. This effect is also known as *charge screening* because the electron *bare* charge is screened by the virtual electron-positron

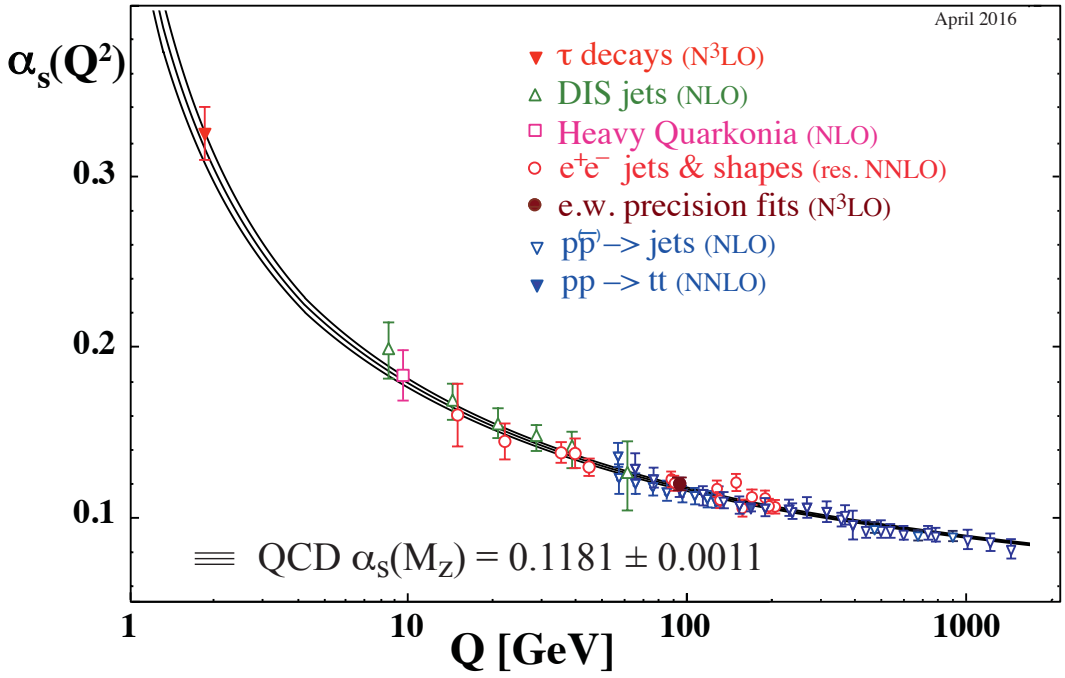

Fig. 1.1 Summary of measurements of α_s as a function of the energy scale Q [4]. The respective degree of QCD perturbation theory used in the extraction of α_s is indicated in brackets.

pairs. The key observation is that the charge screening leads to variation (running) of the QED coupling constant ($\alpha = \frac{e^2}{4\pi}$) with probing distance or momentum transfer squared (Q^2) of the process. It can be understood in a way that the cloud of virtual electron-positron pairs is more deeply penetrated with increasing Q^2 and more of the *bare* electron charge is exposed. In QED, the variation of the α with Q^2 is rather weak, $1/137 < \alpha < 1/127$ for $1(\mathrm{MeV}/c)^2 < Q^2 < 91\ (\mathrm{GeV}/c)^2$.

In QCD, the virtual quark-antiquark pairs tend to screen a color charge but the QCD vacuum also contains the gluons which participate in strong interactions. The net effect of polarization of gluon pairs is not to screen the color charge, but to augment it and change its color. This leads to an *anti-screening* of the color charge and the strong coupling becomes smaller with increasing Q^2. This behavior of QCD is known as *asymptotic freedom* and was derived in the framework of perturbation theory by Politzer [5], Gross and Wilczek [6] in 1973. At leading order, the QCD coupling constant is given by

$$\alpha_{\rm s}(Q^2) \equiv \frac{g_{\rm s}^2(Q^2)}{4\pi} = \frac{12\pi}{(33-2N_{\rm f})\ln(\mathrm{Q}^2/\Lambda^2_{\rm QCD})}, \text{ for } Q^2 \gg \Lambda^2_{\rm QCD}, \tag{1.6}$$

where $N_{\rm f}$ is the number of relevant quark flavors for momentum scale Q^2. $\Lambda_{\rm QCD}$ is the QCD scale parameter, which corresponds to the Q^2 where the non-perturbative regime of QCD begins. The value of $\Lambda_{\rm QCD}$ varies between 210 and 340 MeV/c [4] depending on number of active quarks. One should note that α_s decreases with Q^2 for $N_{\rm f} \leq 16$. The running of α_s is confirmed now by experiments to a very high precision at energy exceeding 1 TeV, as shown in Fig. 1.1 [4].

The asymptotic freedom could explain why high-energy electrons or neutrinos appeared to be hitting loosely bound quarks inside nucleons in the first deep inelastic scattering (DIS) experiments [36, 47]. The key prediction of the theory was occurrence of logarithmic in Q^2 Bjorken scaling violation of the structure functions, which arose because of the radiation of gluons needed to mediate the strong force. This prediction was confirmed with a good precision by DIS measurements with muon [68–70] and neutrino [71] beams.

The colored quarks or gluons have never been observed as isolated particles but they are confined in the colorless hadrons. This phenomenon is known as the *color confinement* or *confinement*. The current theory is that confinement is a property of strong QCD force at long-distances, however, there is no analytic proof that QCD should be confining. For example, as quark-antiquark separation grows, the gluon fields form a narrow tube (or string) between them.The energy in the tube increases with the separation distance and at some point it is more energetically favorable for a new quark-antiquark pair to spontaneously appear, than to allow the tube to extend further. This process is called hadronization, fragmentation, or string breaking, and is one of the least understood processes in particle physics.

1.3 The QCD Phase Diagram

An expected consequence of QCD asymptotic freedom is that at sufficiently high temperature T and/or baryon chemical potential $\mu_{\rm B}$[1] there is possible phase transition of strongly interacting matter from the hadron gas to a matter of deconfined quarks and gluons, the Quark-Gluon Plasma (QGP) [7–11]. However, the phase diagram of QCD matter is not well known, either experimentally or theoretically. A commonly conjectured form of the phase diagram is shown in Fig. 1.2.

At low temperature T and baryon chemical potential $\mu_{\rm B}$ the QCD coupling constant is large and quarks and gluons are confined in the colorless hadrons. Moreover, the strong interaction between quarks and gluons leads to the formation of vacuum condensates of color-singlet bosonic states. In particular, in the QCD ground state the condensate of quark-antiquark pairs

[1] The chemical potential controls the baryon density and is defined as $\mu_{\rm B} = 1/3(n_{\rm q} - n_{\bar{\rm q}})$ where $n_{\rm q}$ and $n_{\bar{\rm q}}$ denote the number densities of quarks and aniquarks, respectively. Thus, in the system with the same number of baryons and antibaryons the $\mu_{\rm B} = 0$.

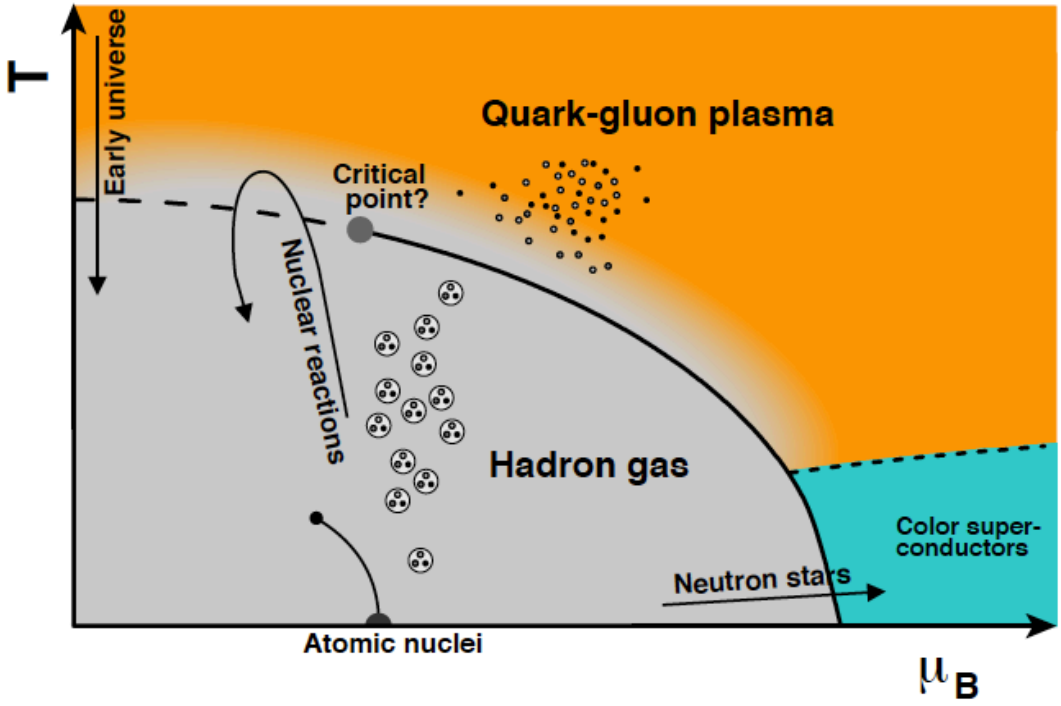

Fig. 1.2 Conjectured phase diagram of strongly interacting matter.

is formed, leading to the spontaneous breaking of a chiral symmetry of the QCD Lagrangian [72–74]. It results in the appearance of massless Goldstone bosons [75], which are identified as pions, kaons and eta mesons. The chiral symmetry is an approximate symmetry due to the *bare* mass of quarks. This is the reason why the massless Goldstone bosons acquire a finite mass. The spontaneous chiral symmetry breaking is most apparent in the nucleon mass generation, where the bare quarks are dressed by the quark-antiquark condensate, and obtain in a dynamical way a large effective mass of around 350 MeV. Thus, for u and d quarks almost 99% of their constituent mass is generated dynamically. The dynamical contribution to effective mass become less important the larger the bare mass of the quark [76]. Therefore, one can say that almost all of the mass in the visible Universe is generated dynamically through the nonperturbative structure of the QCD vacuum.

At high temperature and zero baryon chemical potential ($\mu_B = 0$) the lattice QCD[2] calculations indicate that the matter undergoes a rapid crossover [78, 79], i.e. not a true phase transition in thermodynamic sense, from a hadronic to a quark-gluon plasma at temperature T_c in the range of 145–163 MeV, with gradual and continues restoration of chiral symmetry [80–83]. The energy density in the crossover region is $\varepsilon_c = (0.18\text{–}0.5)$ GeV/fm^3, i.e. $(1.2\text{–}3.1)\varepsilon_{\text{nuclear}}$ where $\varepsilon_{\text{nuclear}}$ denotes the nuclear density. A predicted crossover has the immediate implica-

[2] The only known way to solve the QCD equations from first principles in the region of strong α_s is to discretize the QCD Lagrangian density on a discrete Euclidean space-time lattice (see [12, 13, 77] for more details).

tion for the cosmology. It would mean that the transition from the quark-gluon plasma to the hadron gas in the early Universe was smooth. Thus, one should not expect the signatures of a first-order phase transition such as generation of gravitational waves, formation of baryon inhomogeneities or primordial black holes (see Refs. [84, 85] for reviews).

Recently, the lattice QCD calculations were extended to the very large temperatures to describe the evolution of the universe from temperatures from several hundreds of GeV to the MeV scale [86, 87]. Here, for the fist time all Standard Model fermions and bosons and electroweak interactions were included in the lattice calculations. The key results of the calculations are the equation of state (EoS) and the temperature dependence of the topological susceptibility (χ) of QCD, which were used to predict the dark matter's axion mass, $50 < m_{\rm A} < 1500$ μeV, assuming that the axions are formed during the post-inflation period.

While the lattice QCD calculations are relatively precise at $\mu_{\rm B} = 0$, they cannot be used for evaluation of the phase boundary at $\mu_{\rm B} > 0$ due to the numerical difficulties[3]. However, for relatively small baryon chemical potential one can study QCD on the lattice using a Taylor series expansion in terms of chemical potentials [89, 90].The hope is to find the second order phase transition point - the QCD critical point - located at some finite value of chemical potential (Fig. 1.2). It would be a starting point of the first-order phase transition line at larger values of $\mu_{\rm B}$. The location of a possible critical point has not been determined reliably yet from the lattice QCD computations. The recent calculations [91, 92], performed up to order $(\mu_{\rm B}/T)^6$, disfavor the existence of a critical point in the QCD phase diagram for $\mu_{\rm B}/T \leq 2$ and $T/T_{\rm c}(\mu_{\rm B} = 0) > 0.9$. The same calculations show that the $T_{\rm c}$ decreases slowly with $\mu_{\rm B}$, by around 2–5% at $\mu_{\rm B} = 300$ MeV.

At low temperature and high $\mu_{\rm B}$ (high net baryon density) the various QCD-inspired models [93–99] predict the first-order phase transition from hadronic to color superconductor phase, a degenerate Fermi gas of quarks with a condensate of quark Cooper pairs near the Fermi surface, in which both the QCD color (gauge) and chiral symmetries are spontaneously broken. This breaking of color symmetry is analogous to the breaking of electromagnetic gauge invariance in superconductivity [100], and thus is called *color superconductivity*. It is important to note that quarks, unlike electrons, have color, flavor as well as spin degrees of freedom, so many different patterns of pairing are possible, which can led to many different color superconducting phases (see Refs. [101, 102] for more details).

A prime motivation for carrying out heavy-ion collisions was learning about matter in the deep interiors of neutron stars [7]. Unfortunately, such collisions cannot probe matter at the low temperature and high baryon densities (5–10 times normal matter density). Thus, deducing neutron star properties requires constructing a picture of their interiors fitting together neutron star observations with theoretical pictures of cold dense matter that are consistent with what we know about dense matter at high temperatures. An example of such approach is presented in Refs. [103, 104], where the equation of state of neutron star matter is determined in a wide density range ($\mu_{\rm B} = 1$–3 GeV) interpolating between results from low-energy chi-

[3] This is related to the numerical sign problem in evaluating the integral of a highly oscillatory partition function (see Ref. [88] for more details).

ral effective theory and high-density perturbative QCD, with constraints on the EoS coming from the observation of macroscopic properties of neutron stars. In particular, the discovery of neutron stars with masses of around two solar masses [105, 106] and measurement of tidal deformabilities of neutron stars involved in the merger [107] provide strong constraints on the properties of dense QCD matter. One should note that the measurement of tidal deformabilities has been recently possible thanks to detection of gravitational waves, which open a new chapter in astrophysical observation. In the future it will be interesting to see whether astrophysical constraints can lead to robust statements about the existence of quark matter inside cores of neutron stars.

1.4 Relativistic Heavy-Ion Collisions

Relativistic collisions of heavy ions provide the tool to study matter at extremely high temperatures and densities in the laboratory. In these collisions, the initial energy density and temperature may be sufficient to create the quark-gluon plasma for a short time. The space-time picture of a heavy ion collision proposed by Bjorken in 1983 [108] is depicted in Fig. 1.3. In the following, the different stages of the collision are illustrated.

Prior to the collision two incoming nuclei are moving at almost speed of light and are seen by the stationary observer as Lorentz-contracted discs. These nuclei, are mostly composed of gluons that carry only tiny faction of the longitudinal momenta of their parent nucleons, Bjorken $x \ll 1$. At very high energies, the density of gluons is rapidly increasing as a function of decreasing x, or increasing Q, as measured by ZEUS at HERA [109]. This might lead to the gluonic form of matter, which is dense and weakly coupled, known as the Colour Glass Condensate (CGC) [110, 111].

At time $\tau = 0$, the two nuclei hit with each other and the interactions start developing. The hard parton-parton collisions involving relatively large transferred momenta $Q \gtrsim 10$ GeV occur at very early times ($\tau \sim 1/Q$) due to the uncertainty principle. These collisions are responsible for the production of the high energetic particles (hard probes) carrying transverse energies and momenta of the order of Q. Hard processes with $Q^2 \gg \Lambda^2_{\mathrm{QCD}}$ are theoretically calculable in the framework of perturbative QCD. The production of particles in hard processes will be discussed in detail in the following sections.

In the pre-equilibrium phase, the bulk of the semi-hard ($Q \sim 1$ GeV) processes occur. Most of the hadrons seen in the detector are produced vi the hadronisation of the initial-state gluons and quarks liberated at this stage of collision. Just after being liberated, they form a relatively dense medium with an average energy density $\varepsilon \sim 14$ GeV/fm^3 [112], as estimated for central Pb–Pb collisions at the LHC. The strong interactions between these partons leads to a rapid thermalization at a time $\tau \sim 1$ fm/c. The outcome of the thermalization process is the high-temperature phase of QCD known as the quark-gluon plasma. The mechanism of the rapid thermalization has not been fully understood yet [113]. One possibility is that the rapid transi-

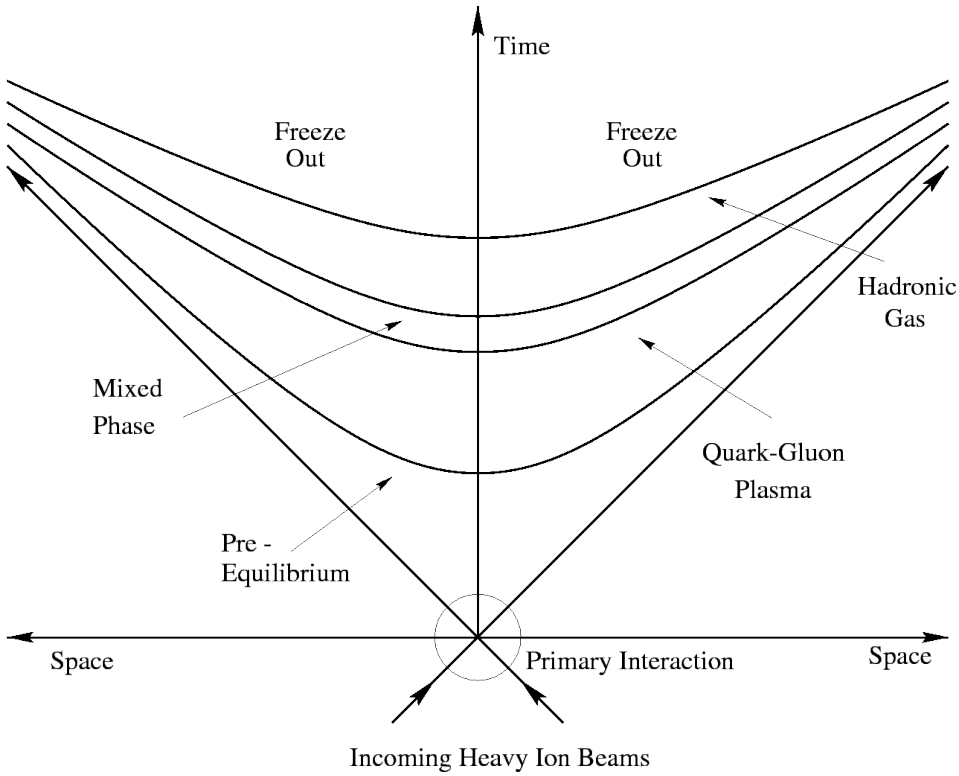

Fig. 1.3 Different stages of the relativistic heavy-ion collision [108].

tion from the CGC initial state to the thermalized QGP is due to instabilities in a intermediate phase called glasma [114].

The quark-gluon plasma keeps expanding and cooling down which implies that the temperature is space and time dependent, i.e. thermal equilibrium is reached only locally, and eventually hadronizes when the temperature falls below T_c and energy density decreases to about 1 GeV/fm^3, which happen at $\tau \sim 10$ fm/c. This phase can be successfully described by relativistic hydrodynamics assuming that the QGP expands as a liquid, as confirmed by the observation of radial and elliptic particle flow in heavy-ion collisions [115, 116]. Even below T_c the hadron gas is still very dense, with a mean free path of the hadrons much smaller than the system size, and can be described by hydrodynamics as well.

The hadron gas continues to expand and cool and eventually the rate of inelastic collisions becomes small. At this stage, the chemical freeze-out is reached and the hadron yields become fixed. From the measured yields of particles with different mass the temperature of the chemical freeze-out can be deduced using thermal models [117, 118]. The kinetic freeze-out occurs when also the elastic collisions cease and the particle momenta are fixed. This marks the transition from a liquid description to the free streaming particles. The bulk particle spectra follow a thermal (exponential) distribution in the local rest frame reflecting the freeze-out tem-

perature. The measured identified particle spectra can be well described if a blue-shift from a common radial velocity is folded into the exponential spectra leading to the so-called Blast-Wave (BW) parameterization [119, 120]. After the chemical freeze-out and kinetic freeze-out, decays of resonances and unstable particles occur. Particles that reach the detector consist of directly produced hadrons and hadrons from decays.

This enumeration of the various stages of a heavy-ion collision already illustrates the variety and complexity of the forms of matter liberated by the collision on its way to the detectors. In principle, all these forms of matter and their mutual transformations admit an unambiguous theoretical description in the QCD framework.

1.5 Experiments with Heavy Ions

The phase diagram of strongly interacting matter has been studied experimentally in nucleus-nucleus collisions at relativistic energies for more than 30 years. Experimental programmes started simultaneously in 1986 at the Alternating Gradient Synchrotron at the Brookhaven National Laboratory (BNL) and at the Super Proton Synchrotron (SPS) at CERN. At both facilities, collisions were studied initially with light atomic nuclei, up to silicon (Si) and sulphur (S), and then with heavy ions such as gold (Au) and lead (Pb), as projectile. In these fixed-target experiments the center-of-mass energy per colliding nucleon pair ($\sqrt{s_{\mathrm{NN}}}$) reached $\sqrt{s_{\mathrm{NN}}} = 4.6$ GeV and 17.2 GeV, respectively. The first evidence for the production of a new state of matter, which features many of the characteristics of theoretically predicted quark-gluon plasma, was reported from the Pb programme at the SPS (see Ref. [121] for a review). Presently, the NA61/SHINE experiment at the SPS studies the onset of deconfinement and searchers for the QCD critical point by measuring the hadron production as a function of collision energy and system [122].

New generation of of heavy-ion experiments started in 2000 at the Relativistic Heavy Ion Collider (RHIC) at BNL, where Au ions are collided at $\sqrt{s_{\mathrm{NN}}} = 20$–$200$ GeV. All four RHIC experiments (BRAHMS, PHOBOS, PHENIX and STAR) have discovered a new phase of nuclear matter that exhibits the properties of the strongly interacting, nearly perfect liquid [123–126]. This state of matter is almost opaque to traversing partons, leading to a marked reduction of their energy. This phenomenon of parton energy loss is often referred to as *jet quenching* [127]. The first evidence of jet quenching has been observed at RHIC from the suppression of high-p_{T} hadrons studying the nuclear modification factor [128, 129] and the suppression of back-to-back high-p_{T} hadron correlations [130]. Presently, the search for the QCD critical point is realized with the beam energy scan programme at RHIC [131].

A new era of experimental search for the QGP started in 2009 when the Large Hadron Collided (LHC) [132] at CERN became operational. The LHC was designed to collide heavy nuclei up to that of Pb at energy of $\sqrt{s_{\mathrm{NN}}} = 5.5$ TeV, which is about 30 times larger than that at RHIC. The ALICE [133] heavy-ion experiment, the ATLAS [134] and the CMS [135] general-purpose experiments, as well as the LHCb (since 2015) [136] have been participated

Year	Accelerator	Main Projectile	$\sqrt{s_{\rm NN}}$ (GeV)
1985	AGS (BNL)	Si	5.4
1985	SPS (CERN)	S	20
1993	AGS (BNL)	Au	4.8
since 1994	SPS (CERN)	Pb	17
since 2000	RHIC (BNL)	Au	200
since 2010	LHC (CERN)	Pb	2760
since 2015	LHC (CERN)	Pb	5020

Table 1.1 Selected heavy-ion accelerators and their center of mass energies. The designed LHC energy will reach $\sqrt{s_{\rm NN}} = 5.5$ TeV.

in the heavy-ion program at the LHC. During the first phase of the LHC running (Run-1, 2009–2013) the Pb–Pb collisions were delivered at a lower energy of $\sqrt{s_{\rm NN}} = 2.76$ TeV[4]. The first results from the LHC confirmed that a new phase of strongly interacting matter is formed in Pb–Pb collisions that behaves as a nearly perfect liquid of extremely low viscosity [116]. Presently, the second phase of the LHC running (Run-2, 2015–2018) is ongoing, where the Pb ions are collided at energy of $\sqrt{s_{\rm NN}} = 5.02$ TeV. The energy available at the LHC allows us to study the parton energy loss (or jet quenching) in the the kinematic range which vastly exceeds that available at RHIC. The jet quenching is quantitatively evident at LHC already by visual inspection of dijets for which a striking energy imbalance develops in central Pb–Pb collisions [138].

The heavy-ion accelerators discussed above are listed in Table 1.1. One should note that the leap in the available $\sqrt{s_{\rm NN}}$ in each generation was more than an order of magnitude. The consequences of this increase for the created medium at RHIC and at the LHC are further discussed in the following chapters.

[4] It was decided to limit the magnetic field in the LHC super-cooled magnets due to the faulty electric connections; these faulty connection caused the serious incident in 2009 which let to damage of about 50 magnets [137].

Chapter 2
The ALICE Experiment at the Large Hadron Collider

A Large Ion Collider Experiment (ALICE) [133, 139–141] is designed to exploit the unique potential of nucleus-nucleus interactions at the LHC energies. The main goal of ALICE is to study the physics of strongly interaction matter at extreme density and temperature, where the formation of the quark-gluon plasma is expected. The existence of the QGP and its properties are key issues in QCD for the understanding of confinement and chiral-symmetry restoration. In addition to heavy-ion collisions, the ALICE Collaboration studies collisions of protons (pp) and protons with ions (p–Pb) that primarily provide reference data for the nucleus-nucleus collisions as well as allow for the number of other QCD studies. The LHC accelerator and the ALICE experiment are briefly described in this chapter.

2.1 The Large Hadron Collider

The Large Hadron Collider (LHC) [132] is the highest-energy particle collider ever constructed, which was built by the European Organization for Nuclear Research from 1998 to 2008. The LHC is placed in a tunnel of 27 kilometers in circumference, as deep as 175 meters beneath the France-Swiss border near Geneva, Switzerland. The collider ring contains two adjacent parallel beam pipes that intersect at four points, each containing a proton (or ion) beam, which travel in opposite directions around the ring. Two beams are guided by 1624 superconducting, helium-cooled magnets, and are brought into collision at the intersection points. This design is much more compact than that at RHIC, where two completely independent rings are used, however, it does not allow to vary the field strength separately for the two beams. Therefore, for collisions of nuclei with different A/Z it results in asymmetric collisions. The LHC was designed to collide protons at $\sqrt{s} = 14$ TeV with an unprecedented luminosity of 10^{34} cm^{-2}s^{-1}, as well as heavy ions (Pb) at energy up to $\sqrt{s_{\mathrm{NN}}} = 5.5$ TeV with a peak luminosity of 10^{27} cm^{-2}s^{-1}.

The CERN accelerator complex including the LHC is shown in Fig. 2.1. Prior to being injected into the main accelerator, the particles are prepared by a series of systems that successively increase their energy. The first system is the linear particle accelerator LINAC 2

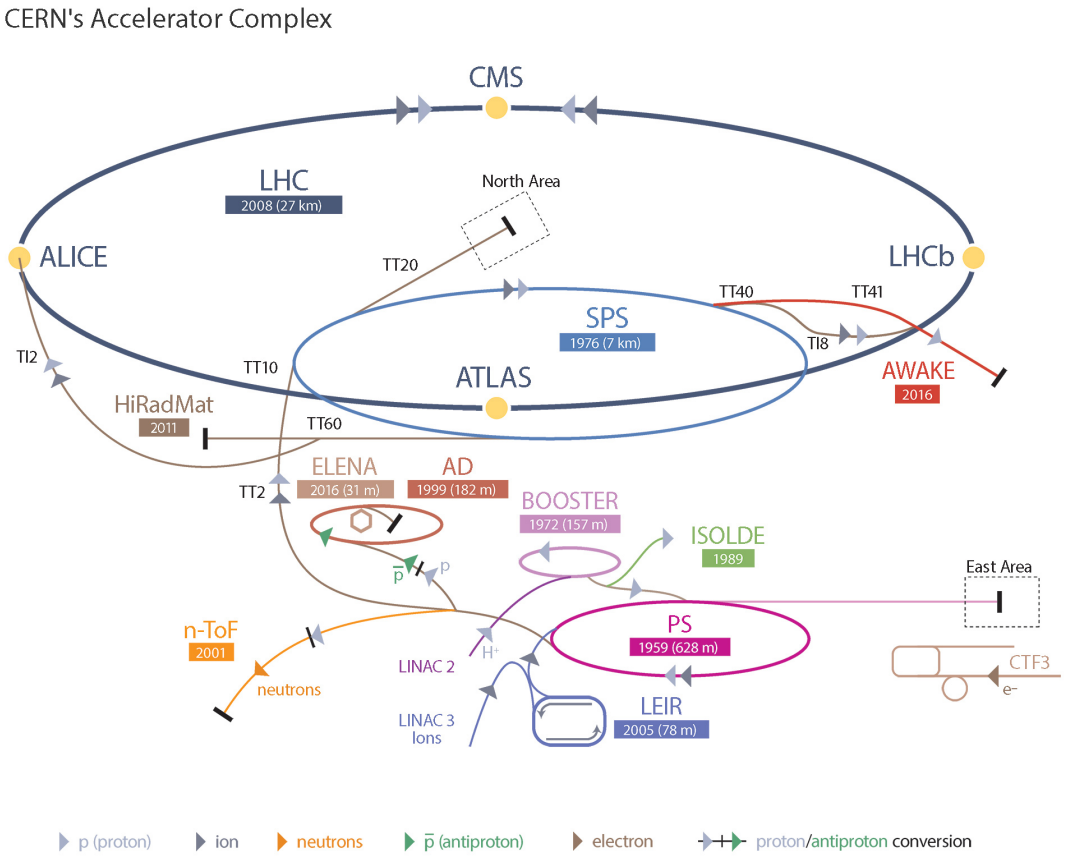

Fig. 2.1 Schematic view of the CERN accelerator complex including the LHC with the four main experiments. The nominal energy in the PS, SPS and LHC accelerators (in GeV) is given for protons. Figure is taken from Ref. [142].

generating 50 MeV protons, which feeds the Proton Synchrotron Booster (PSB). The protons are accelerated in the PSB to 1.4 GeV and injected into the Proton Synchrotron (PS), where they are accelerated to 26 GeV. Finally the Super Proton Synchrotron (SPS) is used to further increase their energy to 450 GeV before injecting into the LHC ring. In the LHC, the proton bunches are accumulated and accelerated to their peak energy, and finally circulated for 10 to 24 hours while collisions occur at the four intersection points. The maximum of 2808 bunches with around 10^{11} protons in each bunch can be stored in the LHC. The interactions between the two beams can take place every 25 ns. The ions are first accelerated by the linear accelerator LINAC 3 and then stored and accelerated in the Low-Energy Ion Ring (LEIR). Then, the ions are further accelerated by the PS and SPS before being injected into LHC ring, where they reach a colliding energy. The ions are accelerated at each step to the proton energy

scaled by Z/A. For example, the lead ions can achieve energy of $Z/A \cdot 7000 \approx 2760$ GeV per nucleon.

The LHC started operation with proton beams in September 2008, but a faulty electrical connection let to the rupture of a liquid helium enclosure, causing both magnet quench and several tons of helium gas escaping with explosive force [137]. The incident resulted in damage to over 50 superconducting magnets and delayed further operations by 14 months. The LHC restarted operation on November 20 in 2009 with proton beams at the injection energy of 450 GeV. Due to the safety reasons, in the first phase of data taking, LHC Run-1 (2009-2013), the collider was running at lower beam energies compared to nominal values. Protons were collided at energies up to $\sqrt{s_{\rm NN}} = 8$ TeV, lead ions at energy of $\sqrt{s_{\rm NN}} = 2.76$ TeV, and protons with lead ions at energy of $\sqrt{s_{\rm NN}} = 5.02$ TeV. The proton (ion) beam energies increased to $\sqrt{s_{\rm NN}} = 13(5.02)$ TeV during a second phase of data taking, LHC Run-2 (2015-2018). The ALICE experiment is located at Interaction Point 2 (IP2) and has collected data from all collision systems at the LHC.

2.2 The ALICE Apparatus

The ALICE detection system [133, 141] is schematically shown in Fig. 2.2. It consists of a central barrel and forward muon spectrometer, with overall dimensions of $16 \times 16 \times 26$ m^3 and total weight of ~ 10000 tons. The ALICE coordinate system [143] is a right-handed orthogonal Cartesian system with the origin at the LHC interaction point IP2. The anticlockwise beam direction defines the z axis, the x axis is horizontal and points approximately towards the LHC center, and the y axis is vertical and points upwards. The azimuthal angle ϕ is measured around the z axis and the polar angle θ is measured from the z axis. The ALICE is divided into A ($z > 0$) and C ($z < 0$) sides.

The central barrel includes the Inner Tracking System (ITS) [145], the Time Projection Chamber (TPC) [146, 147], the Transition Radiation Detector (TRD) [148, 149], the Time-Of-Flight (TOF) [150, 151], the Photon Spectrometer (PHOS) [152, 153], the Electromagnetic Calorimeter (EMCAL) [154, 155], the Di-Jet Calorimeter (DCAL) [156], the Charged-Particle Veto (CPV) [157, 158] the High Momentum Particle Identification Detector (HMPID) [159], which are immersed in the 0.5 T magnetic field provided by the L3 solenoid magnet. These detectors have 18-fold segmentation in azimuth, i.e. they are divided into 18 sectors, each covering 20°.

The ITS is used for the tracking and particle identification. It consists of six layers of silicon detectors: two silicon pixel detectors (SPD), two silicon drift detectors (SDD) and two Silicon Strip Detectors (SDD), with distances from the beam axis between $r = 3.9$ cm and $r = 43$ cm (see inset in Fig. 2.2), which measure track space points close to the interaction point. Each layer covers a full azimuthal angle while the pseudorapidity ($\eta \equiv -\ln\left[\tan(\theta/2)\right]$) coverage differs for the individual layers, ranging from $|\eta| < 2.0$ to $|\eta| < 0.9$, respectively. The information from the ITS layers is used for a precise tracking and primary and secondary

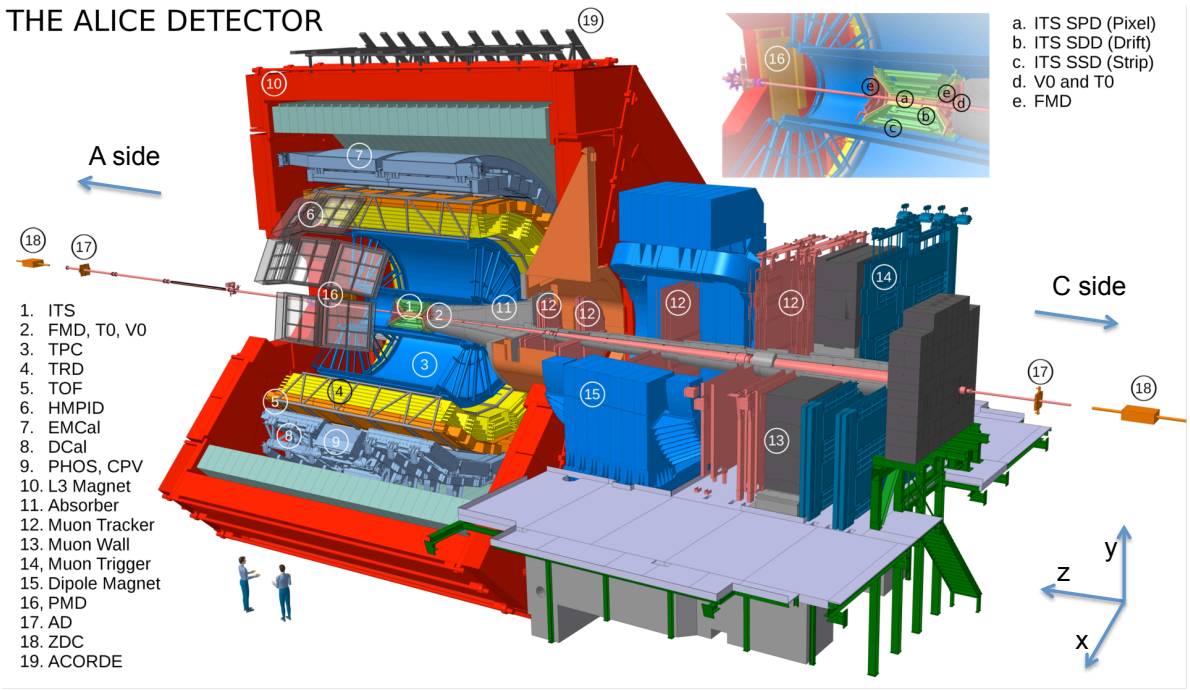

Fig. 2.2 ALICE schematic layout as of 2018. The central-barrel detectors (ITS, TPC, TRD, TOF, PHOS, EMCal, DCAL, CPV and HMPID) are embedded in a solenoid magnetic field and are used for particle detection at mid-rapidity. The cosmic-ray trigger detector ACORDE is positioned on top of the magnet. Forward detectors (PMD, FMD, V0, T0, AD and ZDC) are used for triggering, event characterization and multiplicity studies. The MUON spectrometer is placed at forward rapidities. The inset shows in detail the ALICE inner detectors surrounding the interaction region close to the beam pipe. Shown are SPD, SDD and SSD layers of the ITS, the FMD detectors placed on the A and C sides, and V0 and T0 detectors placed on the C side. Figure is based on Ref. [144].

vertices reconstruction. A low amount of the ITS material, about 1% of a radiation length X_0 per layer, allows to track particles with momenta down to $p_{\mathrm{T}} = 80$ MeV/c. The SSD and SSD layers are also used for particle identification via specific energy loss, $\mathrm{d}E/\mathrm{d}x$, for particles with momenta $p_{\mathrm{T}} < 0.7$ GeV/c. A high granularity SPD detector has also been used as a trigger detector for selection of pp as well as Pb–Pb collisions.

The TPC is a main tracking detector in the central barrel with an excellent particle identification capabilities. It is a gaseous detector surrounding the ITS, with the inner radius of 85 cm, the outer radius of 247 cm, and the longitudinal coverage $-250 < z < 250$ cm. It covers central rapidity, $|\eta| < 0.9$, and the full azimuthal angle. The TPC drift volume of 90 m^3 is filled with Ne-CO_2-N_2 gas mixture and is divided into two parts (A/C side) by the central electrode at high voltage of -100 kV. The electrons produced in ionization process on both sides of the cathode drift in the electric field (parallel to the beam axis) towards the end plates, which are covered by the Multi-wire Proportional Chambers (MWPCs) with pad readout plane. Seg-

mentation of the readout plane allows for position reconstruction in two dimensions (x, y), while the third z coordinate is determined using the drift time of electrons. The maximum number of 159 space points and $\mathrm{d}E/\mathrm{d}x$ samples can be measured along the track, allowing for the excellent tracking performance and particle identification at the highest particle densities. The achived $\mathrm{d}E/\mathrm{d}x$ resolution is better than 7% [147] and allows for identification of charged pions and kaons, as well as protons for p_{T} up to 20 GeV/c.

The TRD is located outside of the TPC at a radial distance of 2.9–3.6 m from the interaction point, covering pseudorapidity range of $|\eta| < 0.9$ and the full azimuth[1]. It consists of six layers of MWPCs filled with Xe-CO_2, with a fibre/foam radiator in front of each chamber and is used for charged-particle tracking and electron identification via transition radiation and $\mathrm{d}E/\mathrm{d}x$ for p_{T} larger than 1 GeV/c. The TRD can be also used as a trigger detector for electrons and high-p_{T} charged particles. By requiring several particles above some p_{T} threshold, a jet trigger has been implemented as well.

The TOF detector is made of Resistive Plane Chambers (RPC) and is placed at radius of 3.78 m. It covers $|\eta| < 0.9$ and the full azimuth and is used for particle identification at intermediate momentum, where the TPC $\mathrm{d}E/\mathrm{d}x$ cannot be used. In particular, the TOF $\mathrm{d}E/\mathrm{d}x$ measurement provides good pion/kaon separation up to $p_{\mathrm{T}} = 4$ GeV/c and proton/kaon separation up to $p_{\mathrm{T}} = 2.5$ GeV/c at the level of 3σ. The time resolution of TOF is better than 40 ps (RMS), which allows for a precise measurement of the time-of-flight and the velocity β of charged particles produced in the interaction. Furthermore, the TOF delivers weak-up pre-trigger signal for the TRD and has been also successfully used for triggering on cosmic rays.

The cylindrical volume outside of the TOF is shared by three electromagnetic calorimeters PHOS, EMCAL and DCAL. The PHOS is made of lead-tungstate crystals with 2×2 cm^2 cross section and covers $|\eta| < 0.12$ and $220^\circ < \phi < 320^\circ$ [2]. The EMCAL is a lead-scintillator sampling calorimeter with projective cells $\Delta\eta \times \Delta\phi \approx 0.025 \times 0.025$, which covers $|\eta| < 0.7$ and $80^\circ < \phi < 187^\circ$ [3], giving partial back-to-back calorimeter coverage with PHOS. The back-to-back calorimeter coverage was extended by adding the DCAL electromagnetic calorimeter (on the PHOS side) in 2014. The DCAL has an identical construction adopted from the EMCAL and covers $0.22 < |\eta| < 0.7$ and $80^\circ < \phi < 147^\circ$. These calorimeters are used for high-momentum photon and electron measurements. The EMCAL is also used to measure the neutral hadronic energy of jets carried by photons, i.e. π^0 and η neural mesons. The energy resolution of PHOS (EMCAL) is about 1% (2%) at 100 GeV [144]. These calorimeters have been used to trigger on high-energy photons and electrons. The EMCAL has been also successfully used to trigger on jets.

The CPV is a multi-wire proportional chamber with cathode pad readout placed on the top of one PHOS module to suppress charged-particle background of the direct photon sample

[1] The TRD installation was completed in 2014, see Ref. [144] for more details.
[2] The full PHOS azimuthal acceptance (5 modules) is quoted. As of 2017, only 3 PHOS modules are installed.
[3] The EMCAL installation was completed in 2012, see Ref. [144] for more details.

detected in PHOS. The CPV detector was installed in 2014 and its main purpose is to improve neutral-cluster identification in PHOS.

The HMPID is a ring-imagining Cherenkov detector with a liquid C_6F_{14} radiator and CsI photo-cathode, which covers $|\eta| < 0.6$ and $1^\circ < \phi < 57.6^\circ$. It is used for the charged hadron identification at intermediate p_T, providing a good kaon/proton separation up to $p_T \approx 5$ GeV/c.

The forward MUON spectrometer [160, 161] is used to measure muons and heavy-quark resonances (J/ψ, ψ', Υ, Υ', Υ'') in the pseudorapidity range $-4 < \eta < -2.5$. It consists of a dipole magnet providing a $\int Bdz = 3$ Tm field (bending tracks vertically), five tracking stations each based on two Cathode Pad Chambers, two triggering stations each equipped with two planes of Resistive Plane Chambers, and two absorbers to efficiently filter out primary hadrons and low-energy muons from pion and kaon decays. The key features of the muon spectrometer are good J/ψ acceptance down to $p_T = 0$ and high readout granularity resulting in an occupancy of 2% in central Pb–Pb collisions. The combined effect of the front absorber and of the muon filter leads to a detection threshold of $p \gtrsim 4$ GeV/c for tracks matching the trigger.

Several smaller detectors for global event characterization and triggering are located at forward angles. The plastic scintillator detector VZERO (V0) [162, 163] is used for charged particle measurements, for triggering and event centrality determination. The V0 consists of two detectors located at forward pseudorapidity on both sides of the interaction region, covering $2.8 < \eta < 5.1$ (V0A) and $-3.7 < \eta < -1.7$ (V0C), and full azimuth. Each detector is segmented into 4 rings in the radial direction and 8 sectors in azimuth. Such segmentation allows the measurement of anisotropic flow observables and the determination of an event plane.

The TZERO (T0) detector [162] delivers the time and longitudinal position of the interaction. It consists of two arrays of 12 quartz-Čerenkov counters placed close to the beam pipe, covering $4.61 < \eta < 4.92$ (T0A) and $-3.28 < \eta < -2.97$ (T0C) in pseudorapidity, and full azimuth. It also provides an accurate start signal for the TOF detector and wake-up pretrigger for the TRD. Its time resolution is about 50 ps (RMS).

The silicon Forward Multiplicity Detector (FMD) [162] is dedicated to measurement of charged particles. The FMD consists of five rings: three on the A side and two on the C side, and covers pseudorapidity $1.7 < \eta < 5.0$ and $-3.4 < \eta < -1.7$, and full azimuth. It is partially overlapping with the SPD, which allow for charged particle multiplicity measurements over a large η range.

The Zero Degree Calorimeter (ZDC) [164] consists of two quartz-tungsten neutron calorimeters ZN covering $|\eta| > 8.8$ and full azimuth, two brass-quartz proton calorimeters ZP covering $6.5 < |\eta| < 7.5$ and $|\phi| < 10^\circ$, and electromagnetic calorimeter ZEM covering $4.8 < \eta < 5.7$ and $|\phi| < 16^\circ$. The ZN and ZP are used to count spectators, while ZEM is used to resolve ambiguity between central (few spectator nucleons) and peripheral (spectator nucleons bound in nuclear fragments) collision.

In 2014, two forward hodoscopes (AD) [165] were installed at 18 m (A side) and 20 m (C side) away from the ALICE interaction point to study diffractive physics and photon induced

processes. They cover pseudorpidity ranges $4.8 < \eta < 6.3$ and $-7 < \eta < -4.9$ on the A and C sides, respectively. Each of the AD detector consists of 8 cells made of scintillation plastic of 22×22 cm^2 area and 2.5 cm thickness each, arranged around the beam pipe in two layers. With these detectors, the ALICE sensitivity to diffractive masses is close to the diffraction threshold of 1.08 GeV/c^2, which corresponds to the sum of proton and pion masses.

The preshower/gas-counter Photon Multiplicty Detector (PMD) [166, 167] is designed to measure the multiplicity and spatial distribution of photons on the A side, covering $2.3 < \eta < 3.7$ and the full azimuth. The gas counter are segmented hexagonal cells with an area of 0.22 cm^2 each.

An array of scintillators ACORDE covers $|\eta| < 1.3$ and $|\phi| < 60^\circ$ and is placed on top of the L3 magnet. It is used to trigger on cosmic rays.

2.3 Central Barrel Tracking

ALICE was designed to provide a good track reconstruction efficiency and precision for momenta up to $p_{\mathrm{T}} = 100$ GeV/c in the highest particle densities. The track finding and fitting algorithms are based on the Kalman filter [168] and are discussed in detail in Refs. [141, 169, 170]. A detailed description of the vertex reconstruction algorithms can be found in Refs. [141, 171]. The performance of the track and vertex reconstruction for the ALICE data collected in 2009–2013 is presented in detail in Ref. [144]. In this section, the tracking and vertex reconstruction procedures in ALICE are outlined.

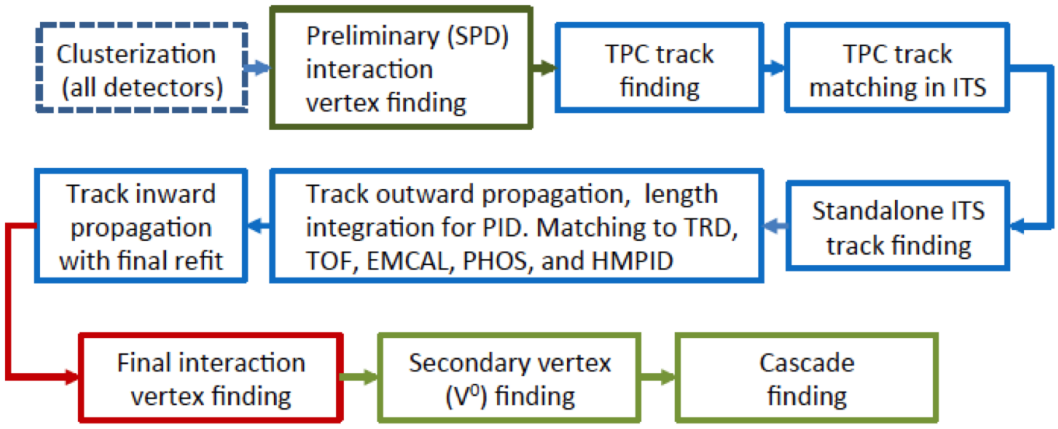

Fig. 2.3 The event reconstruction scheme in the ALICE central barrel. The reconstruction begins from the cluster finding and finish with the reconstruction of cascades. Figure is taken from Ref. [144].

The momentum resolution and the particle identification performance critically depend on the quality of the calibration. The actual position of the detectors (alignment), the maps of dead or noisy channels, and the time and the amplitude calibration parameters are used in the

reconstruction. For the drift detectors (SDD, TPC, TRD), the gain and the time response are calibrated differentially as a function of space coordinates and time. The calibration strategy and calibration sources are discussed in detail in Ref. [144].

A charged particle track in the solenoidal magnetic field of the central barrel follows a helix, which can be parametrized with the five track parameters (y, z, $\sin(\phi)$, $\tan(\theta)$, q/p_{T}) as a function of x in a local (detector sub-system) coordinate system, as explained in detail in Ref. [141]. The inverse transverse momentum, q/p_{T}, with q the charge of the particle, can be derived from the measured track curvature. The errors on the five track parameters are correlated and are given by a 5×5 covariance matrix, which is determined during the tracking.

Figure 2.3 shows an event reconstruction using information for the central barrel detectors. The reconstruction begins from the cluster finding, which is performed for all detectors. The clusters are characterized by positions, signal amplitudes, signal times, etc., and their associated errors (see Ref. [141] for more details).

In order to start track-finding procedure the preliminary vertex position has to be estimated. The preliminary vertex position is estimated with the *VertexerSPDz* and *VertexerSPD3D* algorithms [171], which are based on the track segments (or tracklets) reconstructed correlating cluster pairs in the two layers of the SPD detector. The *VertexerSPDz* algorithm is used in Pb–Pb collisions to determine z-vertex position (along beam axis) using the average location of the collision region in the transverse plane. The precision of the z-vertex position reconstruction increases with the charged particle multiplicity (N_{ch}) and is better than $\sigma_{\mathrm{z}} = 20$ μm for $N_{\mathrm{ch}} > 1000$ [172]. The vertex position in the transverse (x,y) plane is determined by the beam position, which is know with the resolution $\sigma_{\mathrm{x,y}} = 15$–$150$ μm [144], depending on the beam parameters such as β^* and emittance ε. The *VertexerSPD3D* is used in pp and p–Pb collisions to determine all three (x,y,z) vertex coordinates, with the precision better than 300 μm for the charged particle density $\mathrm{d}N_{\mathrm{ch}}/\mathrm{d}\eta > 5$.

The track finding and fitting is performed in the central barrel in three stages, following an inward-outward-inward propagation scheme [169]. The first track inward propagation starts at the outer TPC radius where the track candidates (seeds) are found using two different seeding algorithms with the primary vertex constrain and without any constrain. All seeds are extrapolated to the inner radius of the TPC with the Kalman filter taking into account multiply scattering and mean energy loss described by the Bethe-Bloch formula. Whenever possible, new clusters are associated with the track candidate and the track parameters are more refined. Since the clusters can be reused by different seeds, the same physical track can be reconstructed multiple times. In order to avoid this, a special algorithm is used to search for pairs of tracks with a fraction of common clusters exceeding a certain limit. Only tracks with at least 20 clusters (out of maximum 159 possible) and with more than 50% of the clusters expected for a given track position are accepted.

The ITS tracker prolongs the TPC tracks as close as possible to the primary vertex and the tracks are assigned additional, precisely reconstructed ITS clusters, which further improves estimation of the track parameters. After all track candidates from the TPC are assigned ITS clusters, a special ITS stand-alone tracking is applied to reconstruct tracks from remaining

ITS clusters. It tries to reconstruct all tracks that were not found in the TPC due to p_{T} cut off, dead zones between TPC sectors, and particle decays. The algorithm is able to reconstruct particle tracks with momenta down to $p_{\mathrm{T}} = 80$ GeV$/c$.

The track outward propagation starts from the vertex back to the outer layer of the ITS and then towards outer radius of the TPC. Once the outer radius of the TPC is reached, the precision of the estimated track parameters is good enough to extrapolate to the TRD, TOF, HMPID, PHOS, EMCAL and DCAL detectors, where they are identified. Finally all tracks are refitted (inward propagation with final refit) with the Kalman filter to the primary vertex, or to the innermost possible radius in the case of the secondary tracks, and their parameters and associated covariance matrices are determined.

The global tracks reconstructed in TPC and ITS are used to determine (x, y, z) coordinates of the final interaction vertex, with a higher precision than with SPD tracklets alone. The precise vertex fit is performed using global track weighting algorithm to suppress contribution from outliers (see Ref. [144] for more details). The resolution of the reconstructed vertex position in the transverse plane (σ_{xy}) is better than 100 μm for the charged particle density $\mathrm{d}N_{\mathrm{ch}}/\mathrm{d}\eta > 5$.

In the next steps, the reconstruction of secondary particles from photon conversion and particle decays, and of secondary vertices is performed. For each unlike-sign pair of preselected tracks (called V^0 candidate) the point of closest approach (PCA) between the two tracks is calculated. The V^0 candidates (e.g. $K^0_{\mathrm{s}} \to \pi^-\pi^+$) are then subjected to further cuts as described in detail in Ref. [144]. Then the search for the cascades (e.g. $\Xi^0 \to \Lambda^0\pi^-$) is performed. The reconstruction of more complex secondary vertices is performed later at the analysis stage. It will be discussed in detail for the heavy-flavor hadron decays.

The longitudinal and transverse distances of closest approach (DCA) to the primary vertex for primary particles is determined in pp, p–Pb and Pb–Pb collisions with resolution that increases with momentum from 300 μm at $p_{\mathrm{T}} = 0.15$ GeV$/c$ to 15 μm at $p_{\mathrm{T}} = 20$ GeV$/c$. One should note that this resolution includes the primary vertex resolution, which is better in the higher multiplicity Pb–Pb collisions. The transverse momentum relative resolution, $\sigma p_{\mathrm{T}}/p_{\mathrm{T}}$, is a function of momentum and is approximately 3–4% at $p_{\mathrm{T}} = 0.15$ GeV$/c$, has a minimum of 1.0% at $p_{\mathrm{T}} = 1$ GeV$/c$, and increases linearly for larger p_{T} approaching 3–10% at $p_{\mathrm{T}} = 50$ GeV/c, depending on the precision of space point calibration. The tracking efficiency is a function of p_{T} and is above 78% for $p_{\mathrm{T}} > 0.3$ GeV$/c$ for the standard track selection, independently of colliding system and collision centrality.

2.4 Trigger and Data Taking

There are three triggering levels Level-0 (L0), Level-1 (L1) and Level-2 (L2) for the data taking with ALICE. The L0 trigger decision is generated in ~ 9 μs by the Central Trigger Processor (CTP) [173] based on inputs from the trigger detectors V0, T0, EMCal, PHOS and MUON trigger chambers, and information about the LHC bunch filling scheme. The CTP evaluates trigger inputs from the trigger detectors every machine clock cycle (~ 25 ns) after

collision. The events accepted at L0 are further evaluated by the L1 trigger algorithm in the CTP, which makes decision in $\sim 6.5\ \mu$s. The L0 and L1 decisions are delivered to the detectors with a latency of about 300 ns. The L2 decision taken with latency of 100 μs, corresponding to the full drift time of electrons in the TPC, triggers the sending of the event data to the Data Acquisition (DAQ) system [173] and, in parallel, to the High Level Trigger (HLT) system [173], where event building and data compression are performed. Information about the LHC bunch filling scheme is used by CTP to suppress the beam-induced background (see Ref. [144] for more details).

Minimum-bias (MB) trigger configurations were based on combination of signals from the V0 and SPD detectors. The minimum bias $\mathrm{MB_{OR}}$ (V0A or V0C or SPD) and/or $\mathrm{MB_{AND}}$ (V0A and V0C) triggers were used for pp and p–Pb data taking. The low-luminosity Pb–Pb data in 2010 were also collected with the high-efficiency $\mathrm{MB_{OR}}$ trigger. The V0-based triggers were used for central 0–10% (CENT) and semi-central 0–50% (SEMI) Pb–Pb collisions in 2011. The thresholds were applied separately to the sums of the output charges of V0A and V0C, and then the coincidence of the two sides was required. These triggers were complemented by a requirement of signals in both ZDCs (MBZ) in order to suppress electromagnetic interactions between the lead ions. A full list of trigger settings in Run-1 is discussed in Ref. [144].

ALICE has collected data for all the collision systems and energies offered by the LHC. All data sets recorded by ALICE in Run-1 are summarized in Ref. [144]. The data sets used in analyses presented in the thesis are listed in Table 2.1. The data taking started in fall 2009 with pp collisions at $\sqrt{s} = 0.9$ TeV, collected at very low luminosity. In 2010, the pp collision energy increased to $\sqrt{s} = 7$ TeV and the luminosity was gradually increased. In this period, the pp interaction rate was low (below a few kHz) and ALICE mostly triggered on minimum-bias interactions. In this year, the LHC delivered for the first time Pb–Pb collisions at $\sqrt{s}$ = 2.76 TeV and at low luminosity, which are considered as a reference ALICE data. In the subsequent high-intensity pp, p–Pb and Pb–Pb running in 2011–2013, ALICE usually split its data-taking into minimum-bias and rare-trigger blocks, for which the interaction rate was reduced to O(10) kHz and O(100) kHz, respectively. Methods for reducing the luminosity are described in detail in Ref. [144]. For minimum bias runs, the pp and p–Pb interaction rates were on the level of 10 kHz, enough to reach 95% of the maximum detector readout rate while keeping the mean number of interactions per bunch crossing (μ) low, nominally below 0.05, in order to avoid significant same-bunch pileup. In 2015, ALICE took pp and Pb–Pb data at $\sqrt{s_{\mathrm{NN}}} = 5.02$ TeV with interaction rates 14–100 kHz and 0.4–8 kHz, respectively.

Year	System	$\sqrt{s_{\mathrm{NN}}}$ (TeV)	Running Mode
2009	pp	0.9	$\mathrm{MB_{OR}}$
2010	pp	0.9	$\mathrm{MB_{OR}}$
	pp	7.0	$\mathrm{MB_{OR}}$ + rare
	Pb–Pb	2.76	$\mathrm{MB_{OR}}$
2011	pp	2.76	$\mathrm{MB_{AND}}$ + rare
	Pb–Pb	2.76	CENT + SEMI + MBZ + rare
2012	p–Pb	5.02	$\mathrm{MB_{AND}}$ (pilot)
2013	p–Pb	5.02	$\mathrm{MB_{AND}}$ + rare
	Pb–p	5.02	rare
2015	pp	5.02	$\mathrm{MB_{AND}}$
2015	Pb–Pb	5.02	$\mathrm{MB_{AND}}$ + rare

Table 2.1 Data taking with ALICE detector for the selected data sets used in the presented analyses. Shown are collision system, colliding energy and running mode [144].

2.5 Determination of Collision Centrality

2.5.1 A–A Collisions

Since nuclei are extended objects, the volume of the interacting region depends on the impact parameter (b) of the collision, defined as the distance between the centers of the two colliding nuclei in a plane transverse to the beam axis. It is customary in the field of heavy-ion physics to introduce the concept of the centrality of the collision, which is directly related to the impact parameter and inferred by comparison of data with simulations of the collisions.

The geometrical Glauber model [174–176] has been used to determine collision centrality of nuclear collisions. This model describes the nuclear collision as a superposition of binary nucleon-nucleon interactions. The collision centrality is expressed in the number of binary nucleon-nucleon collisions N_{coll}, in the number of participating nucleons N_{part} (i.e. the number of nucleons that suffered at least one inelastic collision) and by the nuclear overlap function T_{AA}, which are calculated for a given value of the impact parameter and for a realistic initial distribution of nucleons inside the nucleus assuming that nucleons follow straight trajectories (eikonal approximation). The T_{AA} and N_{coll} are related via the effective size of the nucleon given by the inelastic nucleon-nucleon cross section σ_{NN}, $T_{\mathrm{AA}} = N_{\mathrm{coll}}/\sigma_{\mathrm{NN}}$. The average geometrical quantities $\langle N_{\mathrm{part}} \rangle$, $\langle N_{\mathrm{coll}} \rangle$ and $\langle T_{\mathrm{AA}} \rangle$ for a given centrality interval (range of the impact parameters) can be also obtained from the model.

In practice, the Monte Carlo implementation of the Glauber model [177] is used to calculate the average geometrical quantities. The advantage of the Monte Carlo approach compared to analytical calculations is that it is possible to simulate event-by-event experimentally observable quantities (e.g. the charged particle multiplicity) and to apply similar centrality cuts as in the analysis of real data.

Neither impact parameter b nor geometrical quantities, such as N_{part} nor N_{coll} can be directly measured. In experiment, the centrality determination is based on the measured average charged-particle multiplicity or energy carried by particles close to the beam axis. The collision centrality is usually expressed as the percentage of the total nuclear interaction cross section. It allows to relate the measured distributions with the geometrical overlap region of colliding nuclei and to determine the average geometrical quantities. The different centrality estimators based on information from the V0, ZDC, SPD and TPC detectors are used in ALICE [178], with the best centrality resolution achieved for the sum of amplitudes of the V0A and V0C signals (V0M).

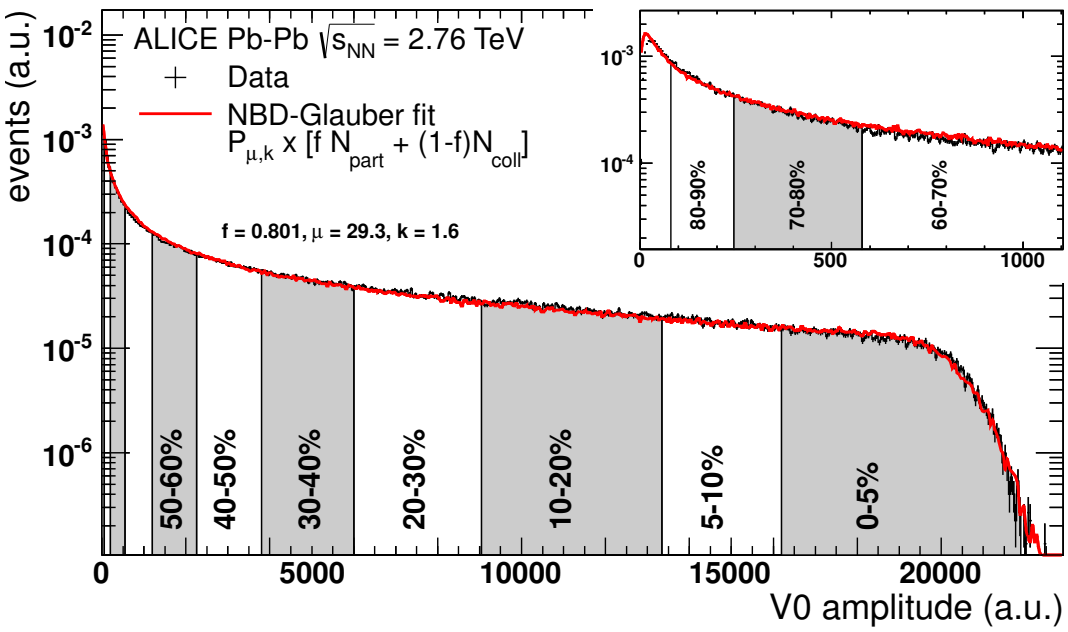

Fig. 2.4 Distribution of the V0 amplitudes (sum of the V0A and V0C signals) measured in Pb–Pb collisions at $\sqrt{s_{\mathrm{NN}}} = 2.76$ TeV with the NBD-Glauber fit. The centrality intervals obtained from the V0 amplitudes are indicated. The inset shows the most peripheral centrality intervals. Figure is taken from [144].

Figure 2.4 shows the V0M distribution fitted with the Monte Carlo Glauber model, coupled to the model of particle production according to a Negative Binomial Distribution (NBD) [178]. Only the range of 0–90% of the total cross section is used for the fit because the contamination with background events from electromagnetic (QED) processes, beam-induced background and trigger inefficiencies are negligible in this range. Centrality percentiles as indicated in Fig. 2.4 are obtained by sharp cuts on the V0M distribution, and the corresponding geometrical quantities are obtained from the NBD-Glauber fit.

2.5.2 p–A Collisions

ALICE has also addressed the p–Pb collision centrality determination [22], which is based on different event activity estimators, i.e. charged particle multiplicities measured in three different pseudorapidity regions as well as the energy measured at beam rapidity with the zero-degree calorimeters (ZDCs). In contrast to Pb–Pb collisions, in p–Pb collisions large multiplicity fluctuations together with a limited range of participating nucleons, generate a dynamical bias in centrality classes based on particle multiplicities, and centrality classification of the event (see Fig. 2.4) may select a sample of nucleon-nucleon collisions which is biased compared to a sample defined by cuts on the impact parameter b, as discussed in Ref. [22].

The centrality determination with the ZDCs is based on detection of so-called *slow* nucleons produced in the interaction: protons in the proton ZDC (ZP) and neutrons in the neutron ZDC (ZN). The multiplicity of slow nucleons is expected to be monotonically related to $N_{\rm coll}$ [179] and can therefore be used as a centrality estimator. Emitted nucleons are classified as *black* or *grey*. This terminology originates from emulsion experiments where it was related to the track grain density. Black nucleons are defined to have velocity $\beta < 0.25$ in the nucleus rest frame and are produced by nuclear evaporation processes, while grey nucleons having $0.25 < \beta < 0.7$ are mainly nucleons knocked out from the nucleus. Experiments at lower collision energies has shown that the multiplicities and momenta of emitted nucleons weakly depend on on the projectile energy in a broad momentum range from 1 GeV to 1 TeV [179], which suggest that the emission of slow nucleons is mainly dictated by nuclear geometry.

In order to relate the energy deposited in the ZDCs to the number of binary collisions ALICE developed a model for the slow nucleon emission (SNM) based on the parametrization of experimental results at lower collision energies (see Ref. [22] for more details). The main features of the measured energy distribution in the neutron calorimeter on the Pb-side are reasonably well described by the SNM coupled to the probability distribution of $N_{\rm coll}$ calculated from the Glauber Monte-Carlo, as shown in Fig. 2.5. The $\langle N_{\rm coll}\rangle$ is then calculated for centrality classes defined by deviding the energy spectrum in percentiles of the hadronic cross-section. However, the $N_{\rm coll}$ determination provided by the SNM-Glauber model is model-dependent. Therefore, ALICE proposed the hybrid method [22] to provide an unbiased centrality estimator, which is based on two main assumptions. The first is to assume that an event selection based on ZN does not introduce any bias on the soft particle (bulk) at mid-rapidity and on the high-$p_{\rm T}$ particle production. The second assumption is that the charged-particle multiplicity measured at mid-rapidity scales with the number of participants. These assumptions were verified with the data from RHIC and LHC. Three sets of $\langle N_{\rm coll}\rangle$ were calculated under following assumptions:

- $N_{\rm coll}^{\rm mult}$: the charged-particle multiplicity at mid-rapidity is proportional to $N_{\rm part}$,
- $N_{\rm coll}^{\rm high-p_T}$: the yield of charged high-$p_{\rm T}$ particles at mid-rapidity is proportional to $N_{\rm coll}$,

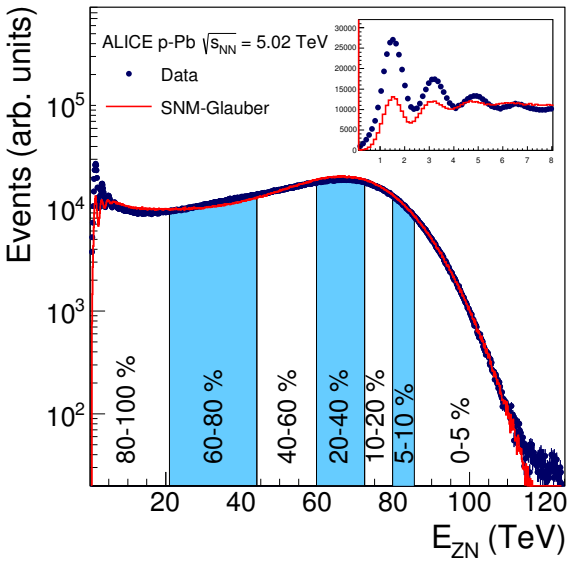

Fig. 2.5 Neutron energy spectrum measured in the Pb-remnant side ZN calorimeter. The distribution is compared with the corresponding distribution from the SNM-Glauber model (explained in the text) shown as a line. Centrality classes are indicated in the figure. The inset shows a zoom-in on the most peripheral events. Figure is taken from Ref. [22].

- $N_{\rm coll}^{\rm Pb-side}$: the target-going charged-particle multiplicity is proportional to the number of participant (wounded) target nucleons ($N_{\rm part}^{\rm target} = N_{\rm part} - 1 = N_{\rm coll}$).

Therefore, in order to obtain the average number of binary NN collisions in each centrality interval, the minimum bias value of $\langle N_{\rm part}\rangle_{\rm MB} = 7.9$ for p–Pb collisions, is scaled using the ratio of the multiplicity at mid-rapidity:

$$\langle N_{\rm part}\rangle_{\rm i}^{\rm mult} = \langle N_{\rm part}\rangle_{\rm MB} \cdot \left(\frac{\langle {\rm d}N/{\rm d}\eta\rangle_{\rm i}}{\langle {\rm d}N/{\rm d}\eta\rangle_{\rm MB}}\right)_{-1<\eta<0}, \tag{2.1}$$

$$\langle N_{\rm coll}\rangle_{\rm i}^{\rm mult} = \langle N_{\rm part}\rangle_{\rm i}^{\rm mult} - 1. \tag{2.2}$$

In a similar way the minimum bias value of $\langle N_{\rm coll}\rangle_{\rm MB} = 6.9$ is scaled using the ratio of the yield of high-$p_{\rm T}$ particles at mid-rapidity to obtain $N_{\rm coll}^{{\rm high}-p_{\rm T}}$,

$$\langle N_{\rm coll}\rangle_{\rm i}^{\rm high-p_T} = \langle N_{\rm coll}\rangle_{\rm MB} \cdot \frac{\langle S\rangle_{\rm i}}{\langle S\rangle_{\rm MB}}, \tag{2.3}$$

where S denotes the charged-particle yield for $10 < p_{\rm T} < 20$ GeV/c. Alternatively, one can use the Pb-side multiplicity to obtain $N_{\rm coll}^{\rm Pb-side}$,

$$\langle N_{\rm coll}\rangle_{\rm i}^{\rm Pb-side} = \langle N_{\rm coll}\rangle_{\rm MB} \cdot \frac{\langle S_{\rm raw}\rangle_{\rm i}}{\langle S_{\rm raw}\rangle_{\rm MB}}, \tag{2.4}$$

where S_{raw} denotes the raw signal of the innermost ring of V0A detector. The obtained $\langle N_{\mathrm{coll}} \rangle$ values in ZN-centrality classes are summarized in Ref. [22].

2.6 Detector Simulations

During data taking each of the data taking periods was split into several data samples (runs) with different trigger and/or detector settings. In order to determine corrections for detector effects, Monte-Carlo detector simulations were anchored to the corresponding data runs, taking into account dead channels maps and time dependent calibration parameters. The events were generated using several default generators and were transported through the detector with GEANT3 [180]. In this section, a short characteristic of the event generators used for the corrections of the p_{T} spectra from pp, p–Pb and Pb–Pb collisions presented in this work is given. The following generators were used for corrections:

- PYTHIA is a standard program for generation of high-energy collisions, comprising a coherent set of physics models for the evolution from a few-body hard process to a complex multihadronic final state. It is intended to describe all components of the total cross section in hadronic collisions, including elastic, diffractive and non-diffractive interactions. Currently, this generator allows for colliding hadrons (pp, pn, πp) including antiprotons and antineutrons, as well as leptons ($\mathrm{e}^+\mathrm{e}^-$ and $\mu^+\mu^-$), at energies 10 GeV $< \sqrt{s} <$ 100 TeV. The perturbative parton shower evolution in PYTHIA includes initial state radiation (ISR), final state radiation (FSR) as well as multiple parton interaction (MPI). It is now possible to use separate PDFs for the hard interaction, and for the subsequent showers and multiple interactions. Hadronisation is based on the Lund string fragmentation framework [181]. Two versions of the generator PYTHIA6 [182, 183] and newer PYTHIA8 [184, 185] have been used for corrections of p_{T} spectra of charged particles measured in pp collisions. In practice, several tunes of these generators with updated parameters using constraints imposed by measurements have been considered.
- PHOJET [186] can be considered as a Monte-Carlo implementation of the two-component Dual Parton Model (DPM) [187]. It is used to generate particles in soft and hard QCD processes in hadron-hadron, hadron-photon and photon-photon collisions from a few GeV up to the highest cosmic ray energies. The momenta of the partons entering the hard scattering processes are obtained using conventional PDFs as well and PDFs of the pomeron [188], a hypothetical particle that was introduced to explain particle production in diffractive interactions. The PHOJET includes the initial state radiation and multiple final state interactions, while hadronization is based on Lund model for the jet fragmentation [189, 190]. The PHOJET was used as alternative generator to PYTHIA for corrections of p_{T} spectra in pp collisions.
- DPMJET [191, 192] is based on the Dual Parton Model and unifies features of DTUJET [193] and PHOJET models. This generator is capable of simulating hadron-nucleus,

nucleus-nucleus, photon-hadron, photon-photon and photon-nucleus interactions from a few GeV up to the highest cosmic ray energies. The Monte Carlo realization of the Gribov-Glauber multiple scattering formalism allows the calculation of total, elastic, quasi-elastic and production cross sections for any high-energy nuclear collision. Individual hadron(photon, nucleon)-nucleon interactions are described by PHOJET including multiple hard and soft pomeron exchanges, initial and final state radiation as well as diffraction. All color neutral strings are hadronized according to the Lund model as implemented in PYTHIA. The DPMJET-III [192] has been used for corrections of p_{T} spectra in p–Pb and Pb–Pb collisions.

- HIJING [194] is a Monte-Carlo generator to study jet and multiparticle production in high energy pp, p–A and A–A collisions at energy from 5 GeV to several TeV. The model includes multiple minijet production, nuclear shadowing of parton distribution functions, and a schematic mechanism of jet interactions in dense matter. Glauber geometry for multiple collisions is used to calculate p–A and A–A collisions. The main features included in HIJING are as follows: i) soft jet production is modeled based on Lund FRITIOF [195] and DPM models, ii) multiple minijet production with initial and final state radiation is included based on PYTHIA, iii) an impact-parameter dependent PDF is introduced to study the sensitivity of observables to the gluon shadowing, iv) a model of jet quenching to study dependence of high-p_{T} particle production on energy loss of parton traversing dense QCD matter. These generator was used for corrections of p_{T} spectra in Pb–Pb collsions.

Chapter 3
Hard Probes of the Quark-Gluon Plasma

Particles produced in nuclear collisions with large transverse momentum and/or mass, $p_{\mathrm{T}}, m \gg \Lambda_{\mathrm{QCD}}$ are well suited to study the hottest and densest phases of the reaction. Such probes originate from partonic scatterings with a large momentum transfer Q and thus are directly coupled to the fundamental QCD degrees of freedom. They are produced in very short time-scales, $\tau \sim 1/Q$, what allow them to propagate through (and potentially affected by) the medium. Moreover, their cross section can be theoretically predicted using the perturbative QCD (pQCD) framework [196]. The increased energy of A–A collisions at the LHC relative to those at RHIC leads to much larger cross sections for hard processes. Energetic quarks and gluons can be observed as jets or single particles with p_{T} larger than 100 GeV/c. Similarly, high-p_{T} photons, charmonium and bottomonium states and weak bosons W and Z are copiously produced at the LHC. The details of production and propagation of these high-p_{T} probes can be used to explore the mechanism of parton energy loss and deconfinement in the medium.

3.1 Particle Production in Hard Processes

In high-energy hadron-hadron or nucleus-nucleus collisions, the production of high-p_{T} particles can be computed from the underlying parton-parton hard processes using the QCD factorization theorem [197]. The hard inelastic cross section for a production of hadron h in nuclear collision can be factorized

$$\mathrm{d}\sigma_{\mathrm{AB}\to\mathrm{h}} = f_{\mathrm{A}}^{\mathrm{a}}\left(x_1, Q^2\right) \otimes f_{\mathrm{B}}^{\mathrm{b}}\left(x_2, Q^2\right) \otimes \mathrm{d}\sigma_{\mathrm{ab}\to\mathrm{i}}\left(x_1, x_2, Q^2\right) \otimes D_{\mathrm{i}\to\mathrm{h}}\left(z, Q^2\right), \qquad (3.1)$$

where the different factors denote:

- the non-perturbative parton distribution functions $f_{\mathrm{A}}^{\mathrm{a}}\left(x_1, Q^2\right)$ and $f_{\mathrm{B}}^{\mathrm{b}}\left(x_2, Q^2\right)$ in the two colliding nuclei. They depend on the parton momentum fraction in the nucleus $x = p_{\mathrm{a,b}}/p_{\mathrm{A,B}}$ and the momentum transfer Q^2, and are determined in the lepton-nucleus deep-inelastic

scatterings and proton-nucleus or deuteron-nucleus collisions (see Refs. [198, 199] for more details),

- the perturbative partonic cross section $\sigma_{\mathrm{ab}\to\mathrm{i}}$ for the production of parton i, calculable for the $Q^2 \gg \Lambda^2_{\mathrm{QCD}}$ up to a given order of α_{s} within pQCD framework,
- the non-perturbative universal fragmentation function (FF) $D_{\mathrm{i}\to\mathrm{h}}\left(z, Q^2\right)$ of the scattered parton i into hadron h that carries fraction $z = p_{\mathrm{h}}/p_{\mathrm{i}}$ of the parton momentum. They are determined experimentally in e^+e^-, electron-proton and proton-proton collisions (see Ref. [200] for a recent review).

The QCD factorization is valid if the characteristic time and length scales of the hard parton-parton interaction ($\tau \sim 1/Q$) are short compared to those of the soft interactions between partons in the initial state (PDFs), and of the fragmentation process of hard scattered partons in the final state (FFs). The dijet production in nucleus-nucleus collision based on the QCD factorization is shown schematically in Fig. 3.1.

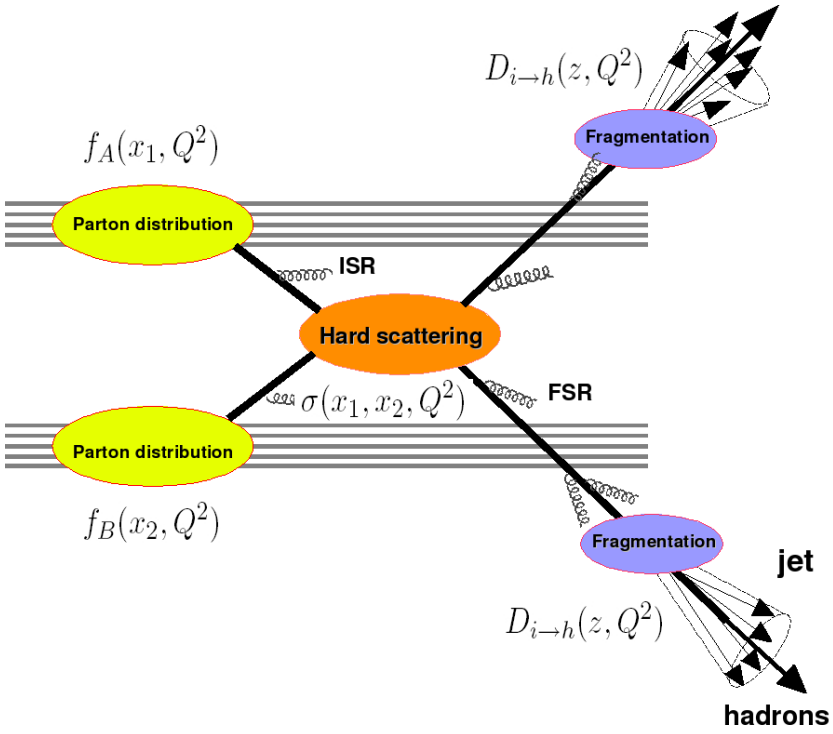

Fig. 3.1 Schematic picture of dijet production in high-energy nucleaus-nucleaus collisions based on the QCD factorization theorem. The parton distribution functions $f_{\mathrm{A}}\left(x_1, Q^2\right)$ and $f_{\mathrm{B}}\left(x_2, Q^2\right)$, partonic cross section $\sigma\left(x_1, x_2, Q^2\right)$ and fragmentation function $D_{\mathrm{i}\to\mathrm{h}}\left(z, Q^2\right)$ are shown. The IRS (FSR) represents the initial (final)-state radiation. Figure is taken from [201].

3.1.1 Nuclear Parton Distribution Functions

The parton distribution functions of a nucleon can be modified if it is bound in a nucleus. This nuclear modification was observed for the first time by the EMC collaboration in deep scattering of muons on deuterium and on heavier nuclei [202, 203]. The data show that the structure functions of the nucleon measured in nuclei are different from those measured on quasi-free nucleons in deuterium, with the ratios below unity for $x < 0.05$ (*shadowing*) and $0.25 < x < 0.7$ (*EMC effect*).

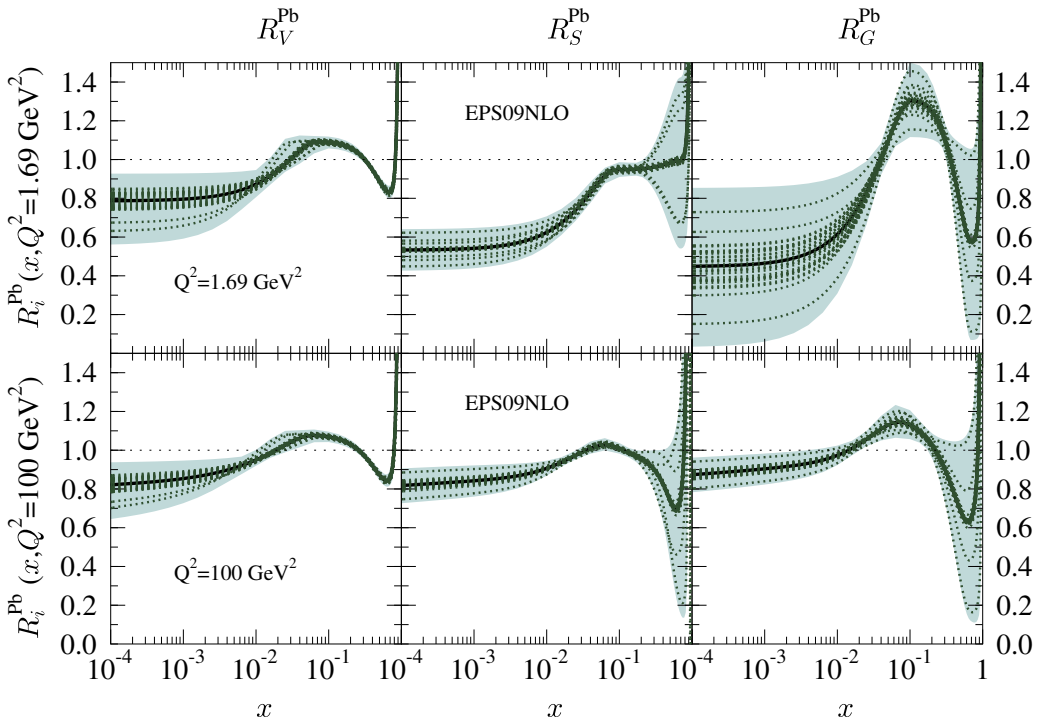

Fig. 3.2 The nuclear modifications of parton distribution functions for valence quarks R_{V}, sea quarks R_{S} and gluons R_{G} determined for lead ions at fixed momentum transfer $Q^2 = 1.69$ GeV^2 and 100 GeV^2 [198]. The thick black lines indicate the best-fit results, whereas the dotted green curves denote the error sets. The shaded bands indicate the total systematic uncertainties.

The nuclear parton distribution functions (nPDFs) are presently determined using next-to-leading order (NLO) pQCD calculations with various types of experimental input, including deep inelastic lepton-nucleus scattering, proton-nucleus and deuteron-nucleus collisions [198, 199]. Within this framework, the bound proton NLO PDFs $f_{\mathrm{i}}^{\mathrm{A}}\left(x,Q^2\right)$ are defined for each flavor i by

$$f_{\mathrm{i}}^{\mathrm{A}}\left(x,Q^2\right) \equiv R_{\mathrm{i}}^{\mathrm{A}}\left(x,Q^2\right) f_{\mathrm{i}}^{\mathrm{N}}\left(x,Q^2\right), \tag{3.2}$$

where $R_{\mathrm{i}}^{\mathrm{A}}\left(x,Q^2\right)$ denotes the nuclear modification to the free proton PDF $f_{\mathrm{i}}^{\mathrm{N}}\left(x,Q^2\right)$. The resulting nuclear modifications for lead ions for momentum transfers $Q^2 = 1.69$ GeV^2 and 100 GeV^2 are shown in Fig. 3.2 [198]. The modifications for the valence quarks R_{V}, sea quarks R_{S} and gluons R_{G} are determined in comparison to the free proton $f_{\mathrm{i}}^{\mathrm{N}}\left(x,Q^2\right)$ from the CTEQ6.1M set [204]. The shadowing effect at small x is clearly visible for all flavors while the EMC effect is seen for the valence quarks, taking into account systematic uncertainties. There is also visible enhancement for $x \sim 0.1$ (*antishadowing*) for valence quarks and gluons, as well as for $x \sim 1$ (*Fermi motion*) for all flavors. The EPS09NLO nuclear modifications have been used in the model comparisons to ALICE p–Pb data [16, 21] and will be discussed in detail the subsequent chapters. The new calculations of nuclear modifications (EPPS16) including the LHC p–Pb data has recently become available [199] and are in agreement with the previous EPS09NLO nPDFs. However, the systematic uncertainties are still significant for all components and more data is therefore required, in particular at small x, for the quantitative studies.

The shadowing may be an indication of saturation effects in the nucleus, which is also indicated by the ZEUS results from the electron-proton deep inelastic scattering [205]. The obtained PDFs show that the gluon density grows extremely rapidly at small x with increasing momentum transfer, which for increasing colliding energy $\sqrt{s}$ would cause a more rapid increase of the total cross section than allowed by the unitarity [206]. A solution to this problem is provided by the gluon saturation models, e.g. the Color-Glass Condensate (CGC) [110, 111]. In this model, the grow of the gluon density is tamed by the gluon recombination ($gg \rightarrow g$) processes, which lead to a saturation of gluon density at small x. The saturation effects become more important for heavy nuclei, since the saturation scale Q_{s} depends on the gluon density per transverse area seen by a probe traversing a nucleus. Thus, $Q_{\mathrm{s}}^2 \propto A^{1/3}$ for nucleus with A number of nucleons.

The saturation effects are relevant for small transverse momenta. However, the saturation has been also proposed as a possible explanation of the suppression of hadrons at higher p_{T} observed in the heavy-ion collisions. This is often referred to as *cold nuclear matter* (CNM) effect. It has been tested by author with the ALICE data on p–Pb collisions [16, 21] and will be discussed in the subsequent chapters.

3.1.2 Parton Fragmentation Functions

The non-perturbative fragmentation functions describe how the color-carrying quarks and gluons transform into color-neutral particles such as hadrons or photons, which is the most intriguing QCD process. For a depth overview of this field and a detailed list of available datasets and experimental results see Ref. [200]. In this section a short overview is presented.

The best studied is the integrated FF, $D_{\mathrm{i}\rightarrow\mathrm{h}}\left(z,Q^2\right)$, which describes the fragmentation of an unpolarized parton of type i into an unpolarized hadron of type h, where the hadron carries the fraction z of the parton momentum. Here, only longitudinal momentum of the hadron is

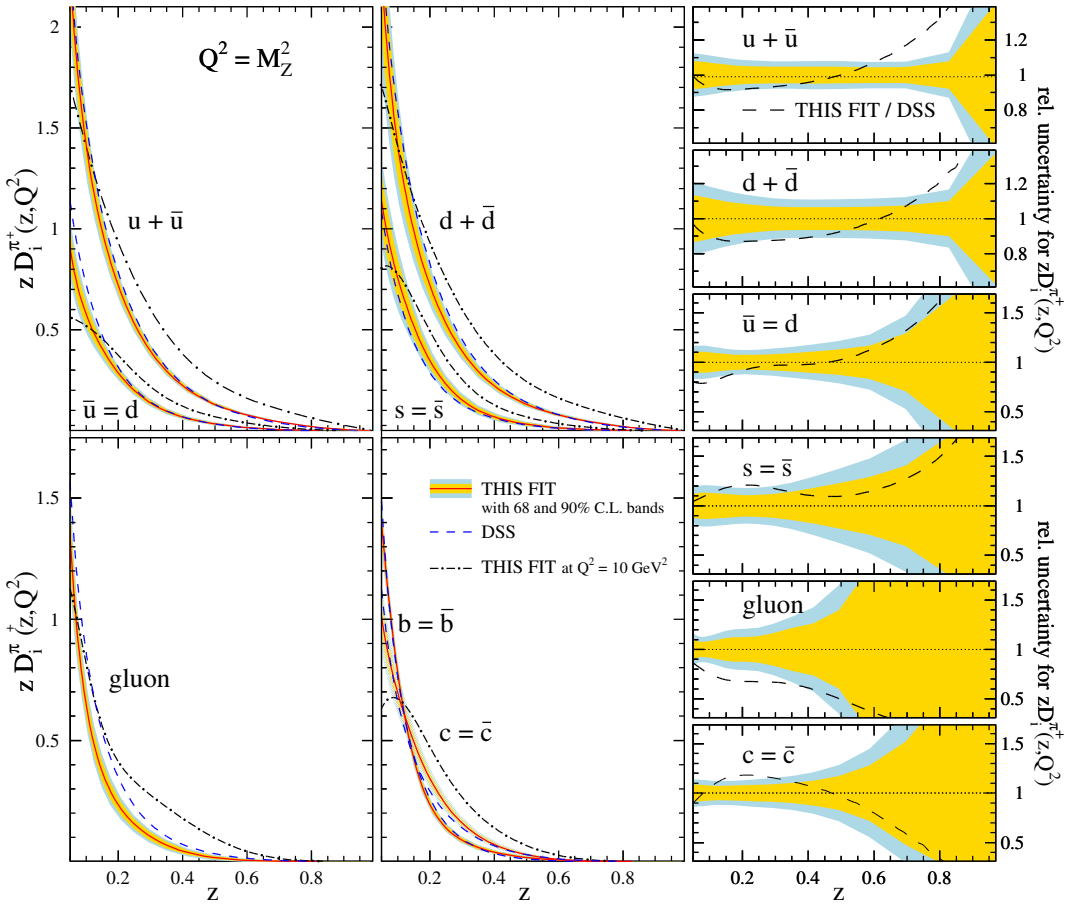

Fig. 3.3 The individual FFs for positively charged pions at $Q^2 = M_Z^2$ along with uncertainty estimates at 68% and 90% C.L. indicated by the inner and outer shaded bands, respectively [207]. The right-hand-side panels show the corresponding relative uncertainties. The calculations at $Q^2 = 10$ GeV^2 (dashed-dotted lines) are also depicted. A comparison to the previous analysis by DSS [208] (dashed lines) is also shown.

considered, i.e. the component of the momentum along the direction of motion of the parton. The transverse momentum of the hadron relative to the parton is integrated over. In addition to the integrated FF, one can consider a number of other FFs by including the spin of the parton and/or hadron, the transverse momentum of the hadron relative to the parton, higher-twist effects, and fragmentation into more than one hadron (see Ref. [200] for more details).

The FFs are determined based on the NLO and recently next-to-next-to-leading NNLO pQCD calculations [209] of input data from various processes including

- single-inclusive hadron production in electron-positron annihilation, $e^+ + e^- \to h + X$,

- semi-inclusive deep-inelastic lepton-nucleon scattering, $l + N \rightarrow l + h + X$,
- single-inclusive hadron production in proton-proton collisions, $p + p \rightarrow h + X$.

In order to make use of all measured processes, global fits are essential to extract FFs. The first simultaneous fit of $e^- e^+$ and $l + N$ and pp data to extract the integrated FFs was performed by de Florian, Sassot, and Stratmann (DSS) [208, 210, 211]. They included precise RHIC data to extract the FFs of pions and kaons as well as CDF and UA1 and UA2 data for the extraction of FFs for unidentified charged hadrons and protons. Surprisingly, the NLO pQCD calculations with the DDS FFs could not describe the ALICE high-p_{T} spectra for the neutral pions and eta mesons [212] as well as for the unidentified charged hadrons [18] (author result). The latter will be discussed in detail in the subsequent chapters.

Recently, the new DDS proton-to-pion FFs have been released [207]. The new DSS fit solves the problem with a refit including the ALICE data on neutral pions [212] and removing the PHENIX low p_{T} points, which cause the most tension, via a minimum p_{T} cut. The resulting state-of-art FFs for parton-to-pion fragmentation are shown in Fig. 3.3. For comparison, the results of previous DDS fit [208] (dashed lines) are also shown.

A new development is the measurement of hadrons in jets at the LHC which allows a direct access to the z dependence of FFs in pp, p–Pb and Pb–Pb collisions. The first results have been reported by ATLAS [213–216] and CMS [217, 218]. Recently, ALICE has released preliminary results on the strange-particle production in jets in p–Pb and Pb–Pb collisions [219], which should provide an important input for the determination of FFs. Moreover, the comparison of FFs in pp, p–Pb and Pb–Pb are expected to improve our understanding of possible modifications of parton showers due to interactions with the quark-gluon plasma, referred to as *jet quenching* [127].

3.2 Parton Energy Loss Mechanisms

The total energy loss of a parton traversing QCD medium is a sum of collisional and radiative terms $\Delta E = \Delta E_{\mathrm{coll}} + \Delta E_{\mathrm{rad}}$ (Fig. 3.4). Their relative contribution to the total energy loss depends on the properties of the medium. The main differences between the QED and QCD energy loss is that the QCD coupling α_s changes more rapidly with momentum transfer Q than α_{em}, and that the effective strength of the coupling of quarks and gluons depends on their color factors. In general, the QCD energy loss is a function of the parton energy E, mass M and color factor C_{R}, the medium temperature T, the QCD coupling α_{s}, and the distance L which parton travels in the medium, $\Delta E(E, M, C_{\mathrm{R}}, \alpha_{\mathrm{s}}, T, L)$. Presently, models of jet quenching with a hydrodynamical medium expansion are used to calculate parton energy loss (see e.g. Ref. [220–222]), where the parton-parton interaction cross section depends on the local medium properties. In this section, a few quantitative features of the energy loss mechanisms with examples of model implementation are presented. For a depth review of the field see Refs. [201, 220–224].

Fig. 3.4 Diagrams for collisional (left) and radiative (right) energy loss of a quark with incident energy E traversing the quark-gluon plasma. Figure is taken from Ref. [201].

3.2.1 Collisional Energy Loss

High energy quarks and gluons propagating through the quark-gluon plasma lose energy via elastic scatterings with the thermal partons of the medium (Fig. 3.4, left). It was originally calculated by Bjorken [127] in analogy to ionization energy loss of charged particles in ordinary matter. More detailed calculations of the collisional energy loss were performed by various authors [223, 225–227]. The obtained collisional energy loss per unit distance, $\mathrm{d}E_{\mathrm{coll}}/\mathrm{d}x$, for a high energetic parton ($E \gg M \gg T$) is given by [223]:

- light quark or gluon

$$-\left.\frac{\mathrm{d}E_{\mathrm{coll}}}{\mathrm{d}x}\right|_{q,g} \approx \pi C_{\mathrm{R}} \alpha_{\mathrm{s}}\left(m_{\mathrm{D}}^2\right) \alpha_{\mathrm{s}}(ET)\, T^2 \left(1+\frac{n_{\mathrm{f}}}{6}\right) \ln\left(\frac{ET}{m_{\mathrm{D}}^2}\right), \tag{3.3}$$

- heavy quark

$$-\left.\frac{\mathrm{d}E_{\mathrm{coll}}}{\mathrm{d}x}\right|_{Q} \approx -\left.\frac{\mathrm{d}E_{\mathrm{coll}}}{\mathrm{d}x}\right|_{q,g} - \frac{2}{9}\pi C_{\mathrm{R}} \alpha_{\mathrm{s}}\left(M^2\right) \alpha_{\mathrm{s}}(ET)\, T^2 \ln\left(\frac{ET}{M^2}\right), \tag{3.4}$$

where n_{f} is the number of thermally equilibrated quark flavors, $C_{\mathrm{R}} = C_{\mathrm{F}} = 4/3 (C_{\mathrm{R}} = N_{\mathrm{c}} = 3)$ is color factor for quark(gluon). The m_{D} is the Debye screening mass in the QGP, where $m_{\mathrm{D}}^2 = 4\pi\alpha_{\mathrm{s}} T^2 (1 + n_{\mathrm{f}}/6)$. It characterizes the typical momentum exchange with the plasma and gives an order of thermal masses of the plasma constituents. One can note that the amount of collisional energy loss is linearly proportional to the medium thickness and depends only logarithmically on the initial parton energy.

3.2.2 Radiative Energy Loss

The dominant mechanism of energy loss of a high energetic parton in a QCD medium is via medium-induced multiple gluon radiation [223, 228–234], which is illustrated in Fig. 3.4

(right). The underlying process is that a parton traversing the medium acquire momentum (or virtuality) due to interaction with the medium. The amount of acquired momentum is determined by the *transport coefficient* $\hat{q}$, which defines the scattering properties of the medium,

$$\hat{q} \equiv \frac{m_{\mathrm{D}}^2}{\lambda} = m_{\mathrm{D}}^2 \rho \sigma, \tag{3.5}$$

where λ is the mean free path, ρ is medium density and σ is the integrated cross section.

The radiative energy loss depends on the thickness of the medium. In practice, the two extreme cases for thin ($L \ll \lambda$, Bethe-Heitler regime) and thick ($L \gg \lambda$, Landau-Pomeranchuk-Migdal regime) media are considered. The difference between them is such that for the thick media the interference effects need to be taken into account. For a high energetic light parton of energy ω, the radiative energy loss is given by [223]:

- Bethe-Heitler (BH) regime ($L \ll \lambda$)

$$\Delta E_{\mathrm{rad}}^{\mathrm{BH}} \approx \alpha_{\mathrm{s}} \hat{q} L^2 \ln\left(\frac{E}{m_{\mathrm{D}}^2 L}\right), \tag{3.6}$$

- Landau-Pomeranchuk-Migdal (LPM) regime ($L \gg \lambda$)

$$\Delta E_{\mathrm{rad}}^{\mathrm{LMP}} \approx \begin{cases} \alpha_{\mathrm{s}} \hat{q} L^2 & (\omega < \omega_{\mathrm{c}}), \\ \alpha_{\mathrm{s}} \hat{q} L^2 \ln\left(E/\hat{q}L^2\right) & (\omega > \omega_{\mathrm{c}}), \end{cases} \tag{3.7}$$

where for a thick medium ($L \gg \lambda$) the energy loss is further differentiated into the regimes of soft ($\omega < \omega_{\mathrm{c}}$) and hard ($\omega > \omega_{\mathrm{c}}$) gluon radiation, with respect to the characteristic radiated gluon energy $\omega_{\mathrm{c}} = \hat{q}L^2/2$.

Gluon radiation off a heavy-quark can differ from the case of a massless parton. Due to kinematics constraints, the radiation is suppressed at angles θ smaller than the ratio of the quark mass M to its energy E, $\theta < M/E$. The distribution of gluons emitted by heavy-quark differs from the gluon spectrum of light partons $\mathrm{d}P_{\mathrm{q}}$ by the factor [235]

$$\mathrm{d}P_{\mathrm{Q}} = \mathrm{d}P_{\mathrm{q}} \left(1 + \frac{\theta_0^2}{\theta^2}\right)^{-2}, \quad \theta_0 \equiv \frac{M}{E}. \tag{3.8}$$

This effect is known as the *dead cone* [235, 236] and results in a reduction of the total gluon radiation emitted by heavy quarks. The total amount of reduction depends on a non-trivial way on the various scales (E, M, L) of the problem and is presented in detail in [223]. Thus, the radiative energy loss in the QGP is expected to be largest for gluons and then follows the mass ordering of the quarks ($q = u$, d, s), charm (c) and bottom (b):

$$\Delta E_{\mathrm{rad}}^{\mathrm{g}} > \Delta E_{\mathrm{rad}}^{q} > \Delta E_{\mathrm{rad}}^{\mathrm{c}} > \Delta E_{\mathrm{rad}}^{\mathrm{b}} \tag{3.9}$$

It has been addressed by the author and is discussed in detail in the subsequent chapters.

3.2.3 Energy Loss in Strongly Coupled Plasma

Previously, the energy loss calculations in an ideal quark-gluon plasma have been discussed. However, the nuclear matter produced in the heavy ion collisions at RHIC or LHC shows the properties of strongly coupled, almost perfect liquid [116, 123–126], which is often referred to as a strongly coupled quark-gluon plasma (sQGP). Recently, it has been shown that the parton energy loss in the sQGP can be calculated in an alternative way [237–244] based on the Anti-de-Sitter/Conformal-Field-Theory (AdS / CFT) correspondence between weakly-coupled gravity and strongly-coupled gauge theories [245, 246]. In these models, what acts on the gluon cloud is a longitudinal drag force of order $F \sim T^2$, and thus the virtuality scale of the hard parton after propagating distance L in the plasma is $Q^2 \sim (F \cdot L)^2 \sim T^4 L^2$. The resulting radiative energy loss is given parametrically by [224]

$$\Delta E_{\mathrm{rad}}^{\mathrm{AdS/CFT}} \approx T^4 L^3. \tag{3.10}$$

It can be noted that the radiated energy has different dependence on the path length as well as on the temperature as compared to the results obtained with the pQCD-based models for the ideal QGP. Using the AdS/CFT-based approach it has been shown [240] that production of charm and beauty hadrons is strongly suppressed at high-p_{T} and suppression is much stronger compared to that obtained using pQCD-based model [247] for the ideal QGP. It can provide an alternative explanation for the similarity of the nuclear modification factor of light- and heavy-flavor hadrons measured at RHIC as well as at the LHC. Recently, the first calculation of the light-flavor jet energy loss in the sQGP has been reported [243]. Using a novel light-flavor jet definition in the AdS/CFT theory the jet nuclear modification factors were found to be in agreement with the LHC measurements [248–250].

3.3 Modeling of Parton Energy Loss

In this section the pQCD-based models for the parton energy loss calculation will be briefly described. For a review of the currently available models see Refs. [220–222]. The energy-loss formulas (Eqs. 3.6 and 3.7) refer to idealistic situation of a static and uniform QGP plasma with the equation-of-state of ideal gas. However, the situation is much more complex for a realistic plasma produced in heavy-ion collisions:

- the initial conditions (medium size and energy density) are not well known and fluctuate event-by-event,
- the medium expands with a large velocity ($\sim 0.7c$) and its properties given by Debye mass and transport coefficient are position and time dependent,
- the flavor and initial energy of the probing parton are not well known.

3.3.1 Models of Radiative Energy Loss

There are four main classes of models which have been developed to address radiative parton energy loss in a realistic plasma:

- path-integral formalism: BDMPS [231, 251], LCPI [230, 252] and ASW [253–256],
- opacity expansion approach: GLV [257], DGLV [258, 259] and WHDG [247],
- higher-twist (HT): HT-BW [260, 261] and HT-M [262, 263],
- finite temperature field theory approach by Arnold, Moore, and Yaffe (AMY) [264–267].

These models are based on the pQCD factorization (Eq. 3.1), where the entire effect of energy loss is encoded in the medium-modified parton fragmentation function, assuming that the final hadronization of the parton occur in the vacuum.

In the models based on the path-integral formalism, a hard parton loses energy in a multiple soft scatterings on colored scattering centers and splits into outgoing parton and gluon. In this case the medium modified fragmentation function can be factorized into a quenching weights, $P_{\rm E}(\varepsilon,\hat{q})$, which encode the probability that the propagating parton loses a fraction of energy $\varepsilon = \Delta E/E$ due to multiple (n) gluon emissions, and vacuum fragmentation function

$$D^{med}_{\rm i\to h}\left(z,Q^2\right) = P_{\rm E}(\varepsilon,\hat{q}) \otimes D^{vac}_{\rm i\to h}\left(\frac{z}{1-\varepsilon},Q^2\right). \tag{3.11}$$

The transport coefficient $\hat{q}$ is determined from the fit to the data. The longitudinal expansion of the plasma can be taken into account by rescaling the transport coefficient [254]

$$\langle\hat{q}\rangle = \frac{2}{L^2}\int_{\tau_0}^{\tau_0+L} {\rm d}\tau\cdot(\tau-\tau_0)\cdot\hat{q}(\tau_0)\left(\frac{\tau_0}{\tau}\right)^{\alpha}, \tag{3.12}$$

with $\alpha \leq 1$. The α characterizes the time-dependence of the plasma density, $\rho(\tau) \propto \tau^{-\alpha}$. For a purely longitudinal (Bjorken) expansion $\alpha = 1$, and is often assumed in phenomenological applications. For a probe propagating in the transverse plane, this will reduce the medium density such that one power of the length dependence is cancelled for a radiative energy loss, as compared to that in the static plasma (Eq. 3.7).

The opacity expansion is equivalent to the path integral approach but the gluon emission spectrum is calculated starting from the single-hard radiation, which is then expanded to account for gluon emission from multiple scatterings via recursive diagrammatic procedure [257]. It employs diagrams that are ordered in opacity $L/\lambda_{\rm g}$, where $\lambda_{\rm g}$ is the mean free path of the radiated gluon. The incident parton looses an energy fraction with probability given by a Poisson distribution [268], which is then used to model medium-modified FF in a similar way as shown in Eg. 3.11. The main parameter of the model is the density of scattering centers in the medium, or the gluon density ${\rm d}N_g/{\rm d}y$, which is obtained from the fit to the experimental data. In the GLV model, the parton energy loss has been obtained for the (1+1)D Bjorken expanding medium in the limit of large parton energy ($2E/m_{\rm D}^2 L \gg 1$) [269],

$$\frac{\Delta E}{E} \approx \frac{9C_{\mathrm{R}}\pi\alpha_{\mathrm{s}}^3}{4}\frac{1}{A_\perp}\frac{dN_{\mathrm{g}}}{dy}\frac{L}{E}\ln\frac{2E}{m_{\mathrm{D}}^2 L}, \tag{3.13}$$

where $A_\perp$ is a transverse area. It can be noted that the power of the path-length dependence is reduced from quadratic for the static plasma (Eq. 3.7) to a linear one. The Eq. 3.13 can be further simplified by relating the characteristic plasma parameters to the number of participating nucleons: $\mathrm{d}N_g/\mathrm{d}y \propto N_{\mathrm{part}}$, $L \propto N_{\mathrm{part}}^{1/3}$ and $A_\perp \propto N_{\mathrm{part}}^{2/3}$. Thus, the fractional energy loss scales approximately as $\Delta E/E \propto N_{\mathrm{part}}^{2/3}$ for a parton of fixed energy.

The higher-twist approach has been originally applied to calculate medium corrections to the total cross section in deep inelastic electron-nucleus scattering due to multiple scattering from partons confined in the nucleons [270, 271]. These corrections are enhanced by the medium length L and suppressed by the power of the hard scale Q^2. In this approach, the medium modified fragmentation function is expressed by

$$D_{i\to h}^{med}\left(z,Q^2\right) = D_{\mathrm{i}\to\mathrm{h}}^{vac}\left(z,Q^2\right) + \Delta D_{\mathrm{i}\to\mathrm{h}}^{med}\left(z,Q^2\right), \tag{3.14}$$

where medium effects due to modified splitting functions in the parton shower [260] are encoded in the additive contribution $\Delta D_{i\to h}^{med}\left(z,Q^2\right)$. From the fit to the data the average energy loss suffered by the parton can be extracted.

The AMY approach describes parton energy loss in a hot QGP with temperature $T \gg g_{\mathrm{s}}T$. This approach properly treats a coherence effect, known as the Landau-Pomeranchuk-Migdal effect [272], which controls the strength of gluon radiation (up to $\mathscr{O}(g_{\mathrm{s}}T)$ corrections) in the thermal medium. A hard parton traversing the QGP undergoes a series of soft scatterings with other constituents of the medium inducing the collinear radiation. The evolution of the hard parton distribution (P) in the medium is given by [266],

$$\frac{\mathrm{d}P_{\mathrm{a}}(p)}{\mathrm{d}t} = \int \mathrm{d}k \sum_{\mathrm{b,c}} \left[P_{\mathrm{b}}(p+k)\frac{\mathrm{d}\Gamma_{\mathrm{ac}}^{\mathrm{b}}(p+k,p)}{\mathrm{d}k\mathrm{d}t} - P_{\mathrm{a}}(p)\frac{\mathrm{d}\Gamma_{\mathrm{bc}}^{\mathrm{a}}(p,k)}{\mathrm{d}k\mathrm{d}t}\right], \tag{3.15}$$

where $\Gamma_{\mathrm{ac}}^{\mathrm{b}}(\Gamma_{\mathrm{bc}}^{\mathrm{a}})$ denote the transition rates b $\to$ ac(a $\to$ bc) for different partons. The resulting medium modified FFs are obtained as the convolution of the vacuum FFs with the hard parton distributions [267],

$$D_{\mathrm{a}\to\mathrm{h}}^{med}\left(z,Q^2\right) = \int \mathrm{d}p_{\mathrm{f}}\frac{z^{'}}{z}\sum_a P_{\mathrm{a}}(p_{\mathrm{f}},p_{\mathrm{i}})D_{\mathrm{a}\to\mathrm{h}}^{\mathrm{vac}}\left(z^{'},Q^2\right), \tag{3.16}$$

where $z = p_{\mathrm{h}}/p_{\mathrm{i}}$ and $z^{'} = p_{\mathrm{h}}/p_{\mathrm{f}}$, with momenta of the hard partons p_{i} and p_{f} immediately after hard scattering and prior to exit the medium. The model of the medium is contained in the space-time profile chosen for the initial temperature T. The model is convoluted with a longitudinally expanding QGP to obtain quantitative results on the jet quenching.

3.3.2 Jet Quenching Monte-Carlo Models

The Monte-Carlo models of jet quenching allow study in-medium modifications of parton showers on event-by-event basis. Such models can be used to address more detailed experimental observables based on particle distributions within jets. Moreover, the sensitivity of these observables to the jet quenching can be tested with the full simulations of the experimental setup with a realistic detector response.

The parton showers, govern by the DGLAP [273–275] evolution of the fragmentation functions, are the basic ingredients of the event generators such as PYTHIA [276] and HERWIG [277], which are often used for comparison with the real data in pp collisions. Thus, medium effects can be included by modifying splitting functions. JEWEL [278] and YAJEM [279] Monte-Carlo models based on the PYTHIA fragmentation are commonly used to simulate parton shower evolution in the presence of a dense medium. The JEWEL model modifies the PYTHIA parton shower via elastic scatterings and medium induced radiation in a medium with fully microscopic dynamics. YAJEM increases the virtuality of the traversing partons according to the medium transport coefficient $\hat{q}$ which measures the virtuality gain per unit path length, and this medium-induced virtuality leads to increased radiation. The energy loss is calculated in a dynamically expanding medium.

3.4 Jet Quenching and Nuclear Modification Factor

Parton-energy loss prior to hadronization (jet quenching) [127] is expected to affect hard probe observables. It is schematically illustrated in Figure 3.5 for dijet production in high-energy proton-proton and heavy-ion collisions. The hard parton interaction with the medium created in heavy-ion collision can affect jet energy as well as fragmentation function and results in various observable consequences compared to the same measurements in proton-proton or proton-nucleus collisions. It can lead to

- suppression of the production of high-p_{T} hadrons,
- dependence of the hadron p_{T} spectra on the collision geometry (centrality and orientation with respect to reaction plane),
- modification of the hadron ratios at high p_{T},
- attenuation and p_{T}-broadening of jets,
- softening and distortion of the jet multiplicity distributions.

The modification of high-p_{T} particle or jet production is quantified with the nuclear modification factor R_{AA}, defined as the ratio of the particle (jet) p_{T} spectrum in A–A collisions to that in pp collisions scaled by the average number of binary nucleon–nucleon collisions $\langle N_{\mathrm{coll}} \rangle$ for a given centrality class of A–A collisions,

$$R_{\mathrm{AA}} = \frac{\mathrm{d}N_{\mathrm{AA}}/\mathrm{d}p_{\mathrm{T}}}{\langle N_{\mathrm{coll}} \rangle \mathrm{d}N_{\mathrm{pp}}/\mathrm{d}p_{\mathrm{T}}} = \frac{\mathrm{d}N_{\mathrm{AA}}/\mathrm{d}p_{\mathrm{T}}}{\langle T_{\mathrm{AA}} \rangle \mathrm{d}\sigma_{\mathrm{pp}}/\mathrm{d}p_{\mathrm{T}}}, \tag{3.17}$$

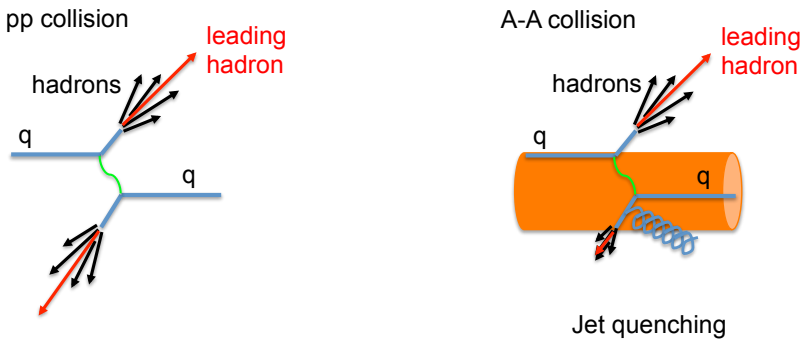

Fig. 3.5 Schematic view of dijet production in high-energy proton-proton (left) and heavy-ion (right) collisions. Jet quenching in a medium can affect jet energy and fragmentation function.

where N_{AA} and N_{pp} are the charged-particle yields in A–A and pp collisions and σ_{pp} is the production cross section in pp collisions, respectively. The average nuclear overlap function, $\langle T_{\mathrm{AA}} \rangle = \langle N_{\mathrm{coll}} \rangle / \sigma_{\mathrm{inel}}^{\mathrm{NN}}$, where $\sigma_{\mathrm{inel}}^{\mathrm{NN}}$ is the total inelastic nucleon-nucleon cross section, depends on the collision centrality and is determined using Monte-Carlo Glauber model as discussed in Sec. 2.5.

It is also common to quantifiy nuclear modification in central with respect to peripheral A–A collisions by using

$$R_{\mathrm{CP}} = \frac{\frac{\mathrm{d}N_{\mathrm{AA}}/\mathrm{d}p_{\mathrm{T}}}{\langle N_{\mathrm{coll}} \rangle}(\mathrm{central})}{\frac{\mathrm{d}N_{\mathrm{AA}}/\mathrm{d}p_{\mathrm{T}}}{\langle N_{\mathrm{coll}} \rangle}(\mathrm{peripheral})}. \tag{3.18}$$

The measurements of nuclear modification factors for charged particles, identified light- and heavy-flavor hadrons and jets have been addressed by author and are discussed in the subsequent chapters.

Chapter 4
Discovery of Jet Quenching at RHIC

The first measurement of hadron production in central Au–Au collisions at $\sqrt{s_{\rm NN}} = 130$ GeV at RHIC showed a suppression of hadron spectra for $p_{\rm T}$ up to 6 GeV/c as compared to the scaled expectation from pp collisions [128, 129]. However, the reference $p_{\rm T}$ spectra in pp collisions used for the $R_{\rm AA}$ determination were not available at the same $\sqrt{s_{\rm NN}}$ and they were derived based on the interpolation procedure leading to the large systematic uncertainties. The observation of jet quenching was confirmed later with a set of crucial measurements at the maximum RHIC energy of $\sqrt{s_{\rm NN}} = 200$ GeV including charged hadrons [130, 280–284], neutral pions [285–287], eta mesons [288] and direct photons [289]. A short overview of the RHIC measurements released before the LHC era is presented in this chapter.

4.1 Dihadron Azimuthal Correlations

The measurements of high-$p_{\rm T}$ two-hadron angular correlations provide the most direct evidence for production of jets in high-energy nuclear collisions and allow for the study of the jet quenching phenomenon. The STAR collaboration has measured two-particle azimuthal correlations for the high-$p_{\rm T}$ charged particles in pp, d–Au and Au–Au collisions at $\sqrt{s_{\rm NN}} = 200$ GeV [130, 282]. The two-particle azimuthal correlations are defined as

$$D(\Delta\phi) \equiv \frac{1}{N_{\rm trigger}} \frac{1}{\varepsilon} \frac{{\rm d}N}{{\rm d}(\Delta\phi)}, \tag{4.1}$$

where $N_{\rm trigger}$ is the number of trigger particles within $4 < p_{\rm T}({\rm trig}) < 6$ GeV/c. Each distribution results from the correlation of each trigger particle with all associated particles having $2 < p_{\rm T} < p_{\rm T}({\rm trig})$ GeV/c in the same event. The ε is the efficiency for finding the associated particle. The analysis is performed for particles within $|\eta| < 0.7$, which translates to the relative pseudorapidity range $|\eta| < 1.4$.

The comparison of the opposite-sign and same-sign two-particle correlation strength indicates that the hard scattering and fragmentation is the predominant source of charged hadrons with $p_{\rm T} > 4$ GeV/c in pp, p–Pb and Au–Au collisions. The opposite-sign correlation domi-

nates over same-sign, which is related to the dynamical charge correlations between hadrons from the leading and next-to-leading jets that originate from the $q\bar{q}$ pairs. The most striking feature is an increasing suppression of back-to-back relative to small-angle correlations with increasing centrality of Au–Au collisions. The back-to-back correlation strength decreases with increasing N_{part} and is consistent with zero for the most central collisions [130]. These observations appear consistent with a large energy loss in a system that is opaque to the propagation of high momentum partons or their fragmentation products.

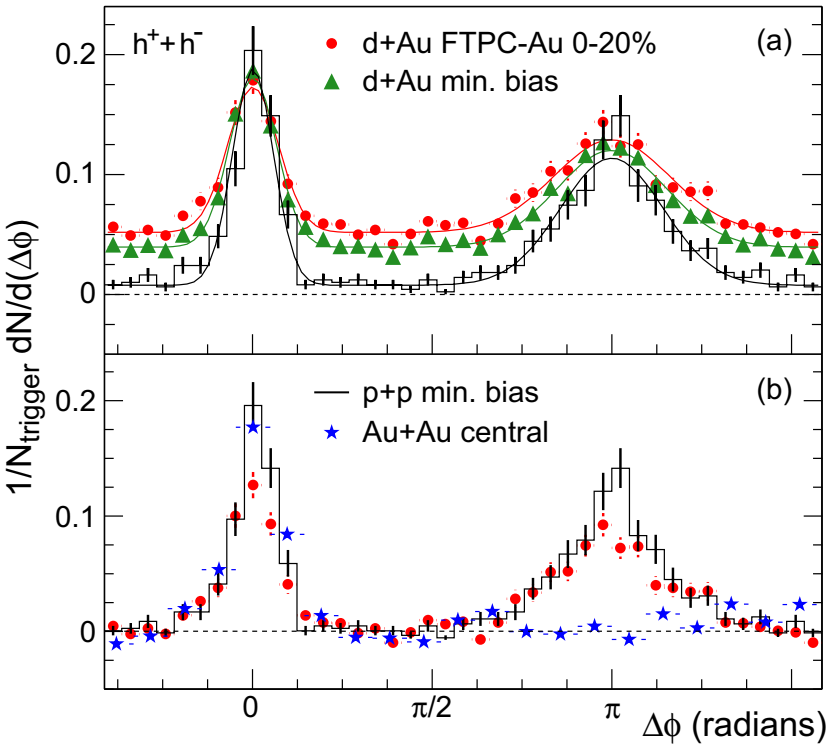

Fig. 4.1 Top: Efficiency corrected two-particle azimuthal distributions for minimum-bias and central p–Au collisions [282], and for pp collisions [130] at $\sqrt{s_{\mathrm{NN}}} = 200$ GeV. The curves represent fits to the distributions with the function defined by the sum of Gaussian peaks and a constant (see Ref. [282] for details). Bottom: Comparison of pedestal-subtracted two-particle azimuthal distributions for central p–Au collisions to those for pp and central Au–Au collisions [130]. Figure is taken from Ref. [282].

Figure 4.1 shows the two-particle azimuthal distribution measured in minimum-bias and central d–Au collisions [282], and in pp and central Au–Au collisions [130]. While the near side ($\Delta\phi \sim 0$) peak is similar for all thee collision systems, the back-to-back ($\Delta\phi \sim \pi$) peak in central Au–Au (Fig. 4.1, bottom) shows a dramatic suppression relative to pp and d–Au collisions. This contrast between Au–Au and d–Au collisions indicates that a strong suppression is related with the final state effects in dense medium produced in central Au–Au collisions.

4.2 Nuclear Modification Factors

The parton energy loss has been quantified at RHIC with nuclear modification factors measured for charged hadrons [280–284, 290, 291], neutral pions [285–287] and eta mesons [288], as well as direct photons [289] in Au–Au and d–Au collisions at $\sqrt{s_{\mathrm{NN}}} = 200$ GeV. In the absence of nuclear effects such as shadowing or Cronin effect [292], hard process should scale with the number of binary nucleon-nucleon collisions, and nuclear modification factor $R_{\mathrm{AB}} = 1$ (see Sec. 3.4).

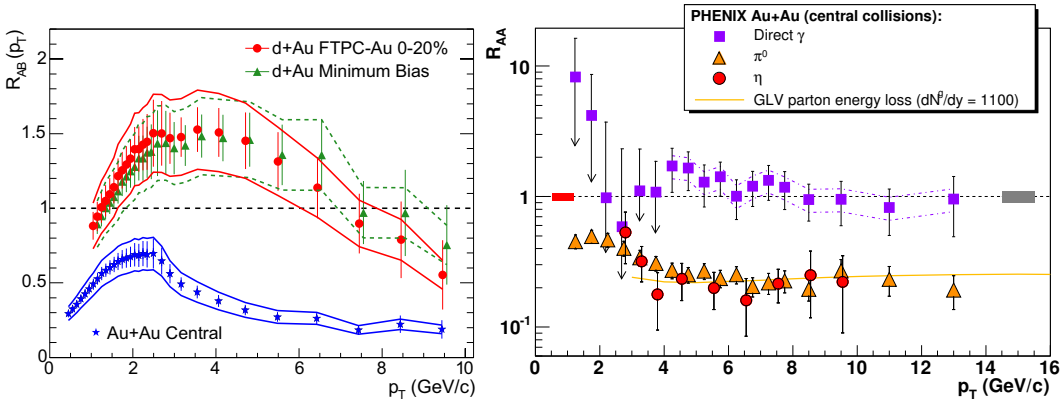

Fig. 4.2 Left: $R_{\mathrm{AB}}(p_{\mathrm{T}})$ of charged hadrons measured in central (0–5%) Au–Au and in central (0–20%) [281] and minimum-bias p–Pb collisions at $\sqrt{s_{\mathrm{NN}}} = 200$ GeV [282]. Figure is taken from Ref. [282]. Right: R_{AA} measured for π^0 [286] and η mesons [288] and direct photons [289] in central Au–Au collisions at $\sqrt{s_{\mathrm{NN}}} = 200$ GeV, with centrality classes 0–10%, 0–20% and 0–10%, respectively. The boxes represent the normalization uncertainty related to the $\langle T_{\mathrm{AA}} \rangle$ (left) and pp cross section (right) determination. The solid yellow curve is a GLV parton energy loss prediction [293]. Figure is taken from Ref. [294].

Figure 4.2 (left) shows nuclear modification factors of charged particles in minimum-bias and central d–Au collisions, and in central Au–Au collisions at $\sqrt{s_{\mathrm{NN}}} = 200$ GeV [282]. The R_{AB} measured in p–Pb collisions shows enhancement up to ~ 1.5 for transverse momenta $2 < p_{\mathrm{T}} < 6$ GeV and decreases for larger p_{T} to ~ 0.8 at $p_{\mathrm{T}} = 9.5$ GeV/c, independently of collision centrality. On the other hand, the R_{AB} in central Au–Au collisions exhibits a large suppression of hadron spectra up to factor of 5 at high p_{T}. A similar suppression is observed for the high-p_{T} π^0 and η mesons (Fig. 4.2, right) measured in central Au–Au collisions [286, 288]. The observed suppression is independent of light-quark neutral meson mass and is almost constant for $p_{\mathrm{T}} > 5$ GeV/c. The R_{AA} of π^0 has been later measured up to 20 GeV/c [287] showing the same, constant suppression. Moreover, the direct-photon R_{AA} [289] scales with the number of binary nucleon-nucleon collisions, as shown in Fig. 4.2 (right), providing a strong confirmation that the observed large suppression of high p_{T} hadron production in

central Au–Au collisions is dominantly a final-state effect due to parton energy loss in the medium, rather than an initial-state effect.

The nuclear modification factors have been also measured in the limited p_{T} range for $\pi^{\pm}$, $K^{\pm}$, p and $\bar{p}$ [295], as shown in Fig. 4.3 (left). As expected, the suppression of high-p_{T} charged pions is identical to that for π^0. For kaons there is a similar trend as for pions over a more limited p_{T} range, while for protons and antiprotons there is an enhancement at $p_{\mathrm{T}} = 2$–4 GeV/c, which is related to the Cronin effect and a strong radial flow developing in heavy-ion collisions.

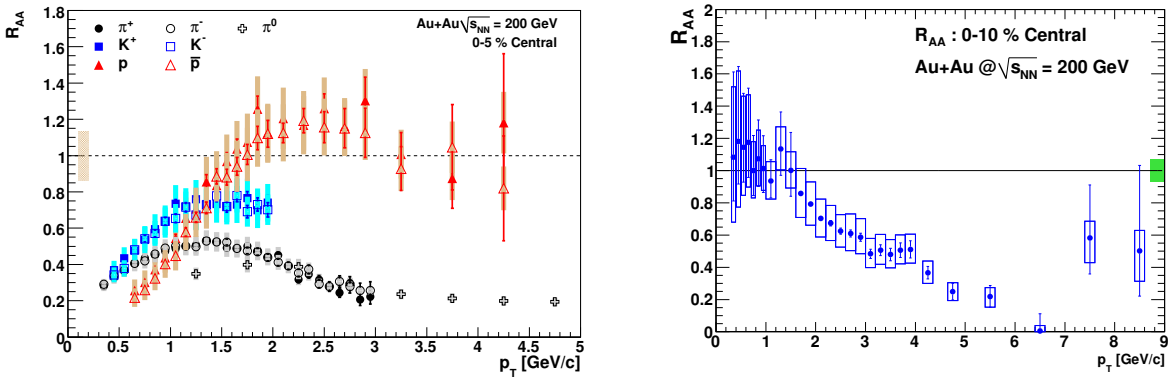

Fig. 4.3 Left: R_{AA} of $\pi^{\pm}$, π^0, $K^{\pm}$, p and $\bar{\mathrm{p}}$ in central (0–5%) Au–Au collisions at $\sqrt{s_{\mathrm{NN}}} = 200$ GeV [295]. The data for identified charged hadrons in Au–Au collisions are taken from Ref. [296]. The R_{AA} of π^0 is taken from Ref. [287]. Right: Open heavy-flavor electron R_{AA} in central (0–10%) Au–Au collisions at $\sqrt{s_{\mathrm{NN}}} = 200$ GeV [297]. Both figures: The p_{T} dependent systematic uncertainties are shown as boxes around data points. The boxes at unity denote the normalization uncertainties.

The substantial modification of the p_{T} spectra of electrons from semileptonic weak decays of heavy-flavor mesons in Au–Au collisions as compared with pp collisions were observed by the PHENIX experiment [297–300]. Figure 4.3 (right) shows the nuclear modification factor of heavy-flavor electrons measured in central (0–5%) collisions [297]. Surprisingly, the same suppression is observed for open-heavy flavor electrons and for light-flavor π^0 and η mesons at high p_{T}, which indicates that the *dead cone* effect (see Sec. 3.2.2 for details) is small at RHIC energies. However, it is not a direct measurements of heavy-quark production (as with open charm or beauty mesons, e.g. $D \to \pi K$ or $B \to J/\psi K$) and quantitative comparison with the suppression of the light mesons requires an understanding of the decay kinematics of open charm and bottom mesons.

At RHIC, it has been also verified that the fragmentation of hard partons to π^0 or η mesons is not affected by the medium by studying the η/π^0 ratio as a function of p_{T} in pp, d–Au and Au–Au collisions [288]. This is in agreement with the picture that hard scattered parent partons first lose energy in the QGP and then fragment in vacuum into leading hadrons following the same fragmentation function as in elementary collisions. Thus, the radiative energy loss

approaches (see Sec. 3.3.1 for details) that the medium modification can be factorized into energy loss probability and vacuum fragmentation function at rescaled energy seems to be valid at RHIC energies.

The RHIC results reviewed in this chapter were the main motivation for author to address the nuclear modification factor measurements at the LHC. The enhanced production cross sections of hard probes at the LHC and advanced particle identification techniques used in ALICE allow for the precise measurements of light and heavy-flavor hadron spectra in substantially extended p_{T} range as compared to that at RHIC. The obtained results will be discussed in the subsequent chapters.

Chapter 5
Soft Particle Production and Medium Properties at the LHC

Measurements of low-energy particles with transverse momenta below a few GeV/c (vast majority of produced hadrons), referred to as soft particles or *bulk*, is crucial to understand properties of hot and dense QCD matter produced in heavy-ion collisions. For example, the multiplicity distributions of soft particles can be used to to determine the initial energy density reached during collision, the identified particle p_{T} spectra give information about conditions at and shortly after hadronization, while correlations between particles measure size and lifetime of the system as well as characterize the transport properties of the medium via collective flow phenomena. These measurements provide constraints on the medium properties that are used in the parton energy loss models [221, 222]. In this chapter a short review of soft particle production at the LHC will be presented.

5.1 Charged Particle Multiplicity

The most basic quantity studied with soft particles is the charged-particle multiplicity per unit of pseudorapidity, $\mathrm{d}N_{\mathrm{ch}}/\mathrm{d}\eta$. The averaged values of $\langle \mathrm{d}N_{\mathrm{ch}}/\mathrm{d}\eta \rangle \approx 1600(1950)$ have been measured at $|\eta| < 0.5$ in central (0-5%) Pb–Pb collisions at $\sqrt{s_{\mathrm{NN}}} = 2.76(5.02)$ TeV at the LHC [301–303]. From the measured multiplicity, one can derive a rough estimate of the energy density with the help of a formula first proposed by Bjorken [108] that relates the energy density to the transverse energy,

$$\varepsilon \geq \frac{\mathrm{d}E_{\mathrm{T}}/\mathrm{d}\eta}{\tau_0 \pi R^2} = \frac{3}{2}\,(E_T/N)\,\frac{\mathrm{d}N_{\mathrm{ch}}/\mathrm{d}\eta}{\tau_0 \pi R^2}, \tag{5.1}$$

where τ_0 is the thermalization time (see Sec. 1.4), R is the nuclear radius, and E_{T}/N is the transverse energy per emitted particle. Assuming that $\tau_0 \approx 1$ fm/c and $E_{\mathrm{T}}/N \approx 1$ GeV, the initial energy density is about 14 GeV/fm^3 in central Pb–Pb collisions at $\sqrt{s_{\mathrm{NN}}} = 2.76$ TeV [112], which is about factor of three higher than at the highest energy at RHIC [123–126], and is much larger as compared to the critical value from the lattice QCD calculations,

$\varepsilon_c = 0.18$–0.5 GeV/fm^3 [83]. Thus, one can expect that the quark-gluon plasma is produced in heavy-ion collisions at the LHC.

Figure 5.1 (left) shows the average charged-particle density per participant pair, $\langle \mathrm{d}N_{\mathrm{ch}}/\mathrm{d}\eta \rangle / \left(\langle N_{\mathrm{part}} \rangle / 2 \right)$, measured as a function of $\sqrt{s_{\mathrm{NN}}}$ in inelastic pp [304–307] and p$\bar{\mathrm{p}}$ [308] collisions, in non-single diffractive (NSD) p–Pb [309] and d–Au [291] collisions, and in central Pb–Pb [302, 303, 310–312] and Au–Au [313–317] collisions. The $\sqrt{s_{\mathrm{NN}}}$-dependence of $\langle \mathrm{d}N_{\mathrm{ch}}/\mathrm{d}\eta \rangle / \left(\langle N_{\mathrm{part}} \rangle / 2 \right)$ can be fitted with a power law of the form $a \cdot s^b$. It gives an exponent of $b = 0.155 \pm 0.004$ for A–A, which gives much stronger dependence than that for the smaller systems where a value of $b = 0.103 \pm 0.002$ is obtained. Thus, particle production is no longer compatible with a logarithmic dependence with $\sqrt{s_{\mathrm{NN}}}$, which was valid for the data up to the highest RHIC energy. Moreover, the same values of $\langle \mathrm{d}N_{\mathrm{ch}}/\mathrm{d}\eta \rangle / \left(\langle N_{\mathrm{part}} \rangle / 2 \right)$ measured for p–Pb and d–Au and pp indicate that the strong rise with $\sqrt{s_{\mathrm{NN}}}$ observed for A–A is not related to the particle production in multiple collisions of participating nucleons.

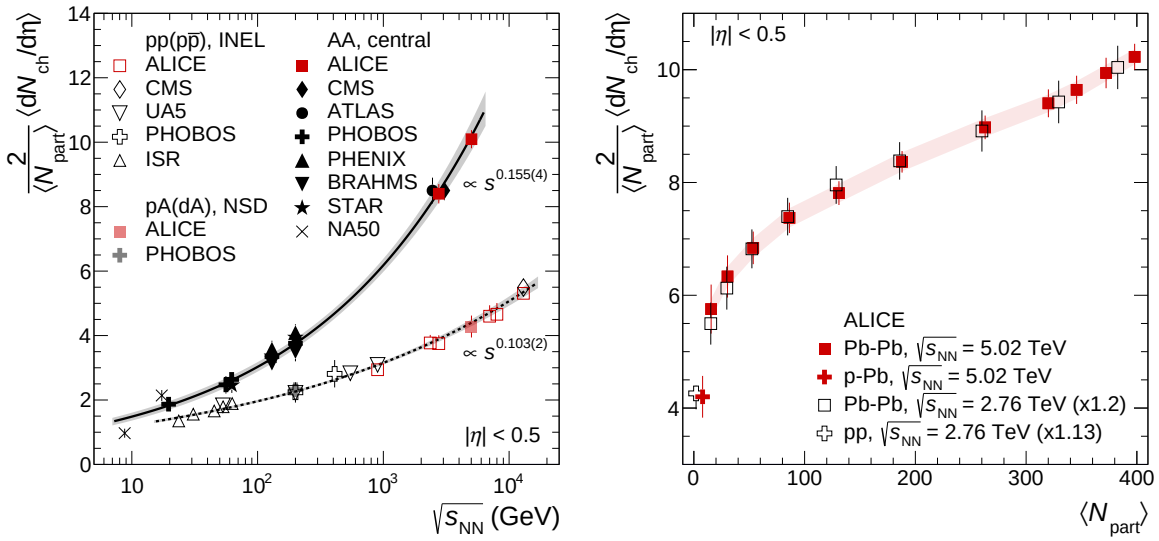

Fig. 5.1 Left: Values of $\langle \mathrm{d}N_{\mathrm{ch}}/\mathrm{d}\eta \rangle / \left(\langle N_{\mathrm{part}} \rangle / 2 \right)$ in central Pb–Pb [302, 303, 310–312] and Au–Au collisions [313–317] are shown as a function of $\sqrt{s_{\mathrm{NN}}}$, together with measurements in INEL pp [304–307] and p$\bar{\mathrm{p}}$ [308] collisions, and in non-single diffractive (NSD) p–Pb [309] and d–Au [291] collisions. Lines indicate fits with a power-law dependence on $\sqrt{s_{\mathrm{NN}}}$. The shaded bands show the uncertainties on the extracted power-law dependencies. The central Pb–Pb measurements from CMS and ATLAS at $\sqrt{s_{\mathrm{NN}}} = 2.76$ TeV were shifted horizontally for better visibility. Right: Dependence of $\langle \mathrm{d}N_{\mathrm{ch}}/\mathrm{d}\eta \rangle / \left(\langle N_{\mathrm{part}} \rangle / 2 \right)$ on the average number of participants $\langle N_{\mathrm{part}} \rangle$ measured by ALICE in pp [307], p–Pb [309] and Pb–Pb [302, 303] collisions. The Pb–Pb and pp data from lower energy are scaled up by 1.2 and 1.13, respectively. The error bars for Pb–Pb data at $\sqrt{s_{\mathrm{NN}}} = 5$ TeV indicate the point-to-point centrality-dependent uncertainties while the shaded band shows the correlated contributions. The error bars for the rest of the systems denote the total uncertainty. Figures are taken from Ref. [303].

Figure 5.1 (right) compares the centrality dependence of particle production in pp [307], p–Pb [309] and Pb–Pb [302, 303] collisions measured by ALICE. The Pb–Pb and pp data from lower energy are scaled up by 1.2 and 1.13, which were obtained using the power-law dependence with $\sqrt{s_{\rm NN}}$. The $\langle {\rm d}N_{\rm ch}/{\rm d}\eta \rangle / \left(\langle N_{\rm part} \rangle /2 \right)$ increases with Pb–Pb collision centrality by a factor of ~ 1.8, independently of collision energy. The similar increase is also observed at RHIC energies [317, 318]. It is surprising that this increase of particle production with collision centrality is almost constant up to TeV energies. One should expect that hard processes, which scale with the number of binary collisions, should contribute significantly to particle production at the LHC and lead to a steeper centrality dependence. Therefore, there needs be a mechanism which limit the growth of multiplicity, e.g. gluon saturation or shadowing, in order to describe the centrality and energy evolution of the particle production, as discussed in detail in Ref. [303].

5.2 Identified Particle Spectra

Even at the LHC energies, the vast majority of all hadrons ($> 95\%$) has momenta below 2 GeV/c. These hadrons are produced in non-perturbative processes which cannot be calculated using perturbative QCD framework. In elementary e^+e^- or pp collisions, the particle $p_{\rm T}$ spectra are described by the QCD-inspired models, e.g. PYTHIA [276], EPOS [319], etc., with a large amount of parameters. In heavy-ion collisions, the particle yields and spectra are consistent with the statistical-thermal [117, 320–322] and hydrodynamical [319, 323–325] models.

Figure 5.2 shows $p_{\rm T}$ spectra [120] for pions, kaons and protons measured by ALICE in central 0–5% (left) and peripheral 70–80% (right) Pb–Pb collisions at $\sqrt{s_{\rm NN}} = 2.76$ TeV in comparison with measurements in Au–Au collisions at $\sqrt{s_{\rm NN}} = 200$ GeV [296, 316] and hydrodynamical model calculations. A dramatic change in spectral shapes from RHIC to LHC energies is observed, with the protons in particular showing a flatter distribution. A flattening of the spectra, more pronounced at low $p_{\rm T}$ and for heavier particles, is expected in the hydrodynamical models as a consequence of the blue-shift induced by the collective expansion (radial flow). The radial flow is stronger with increasing collision centrality and energy. A comparison between two energies based on results from the the Blast-Wave model [119] fits to the spectra shows that the radial flow in central collisions at the LHC is about 10% stronger than at RHIC [120].

The hydrodynamical models give fairly good description of the $p_{\rm T}$ spectra in central Pb–Pb collisions (Fig. 5.2, left). In peripheral collisions (Fig. 5.2, right), these models (EPOS is missing) give a poor description of the data, indicating the limit of applicability of hydrodynamics.

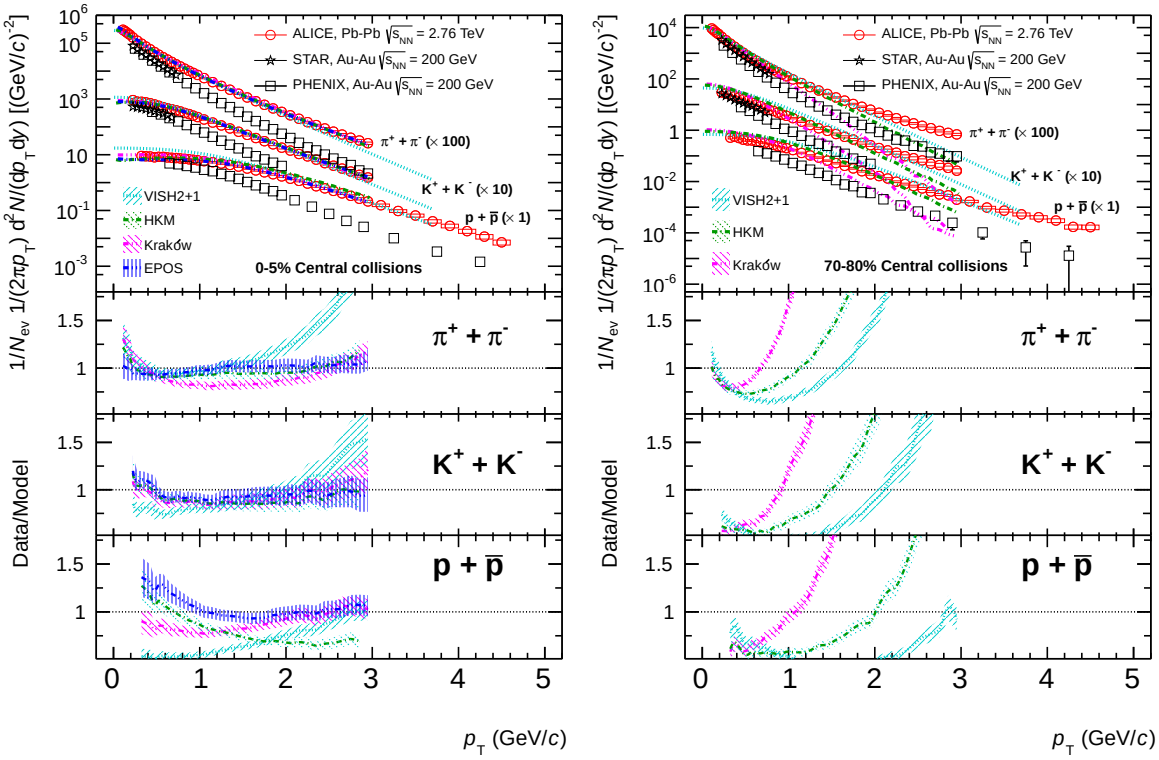

Fig. 5.2 Transverse momentum spectra for pions, kaons and protons measured by ALICE in central 0–5% (left) and peripheral 70–80% (right) Pb–Pb collisions at $\sqrt{s_{\mathrm{NN}}} = 2.76$ TeV. The spectra are compared with measurements at lower collision energy at RHIC [296, 316] and with hydrodynamical model calculations [319, 323–325]. Figures are taken from Ref. [120].

5.3 Identical Particle Correlations

The freeze-out volume, i.e. the size of the matter when strong interactions cease, and the total lifetime of the created system, i.e. the time between collision and freeze-out, can be measured by identical particle interferometry or *femtoscopy*, also referred to as Hanbury-Brown-Twiss (HBT) correlations (see Ref. [326] for a review). For identical bosons (fermions), quantum statistics leads to an enhancement (depletion) for particles emitted nearby in phase space. This enhancement modifies the two-particle correlation function, measured in energy and momentum variables, and can be related via a Fourier transformation to the space and time distribution of the emitting source, namely the space-time hypersurface of last rescattering.

These correlations do not measure the size of the entire source. Instead, they address the dimensions of the region of homogeneity, i.e. the size and shape of the phase space cloud of outgoing particles whose velocities have a specific magnitude and direction. If the collective expansion of the produced matter is strong, as is the case in central collisions, then the region of homogeneity is significantly smaller than the entire source volume.

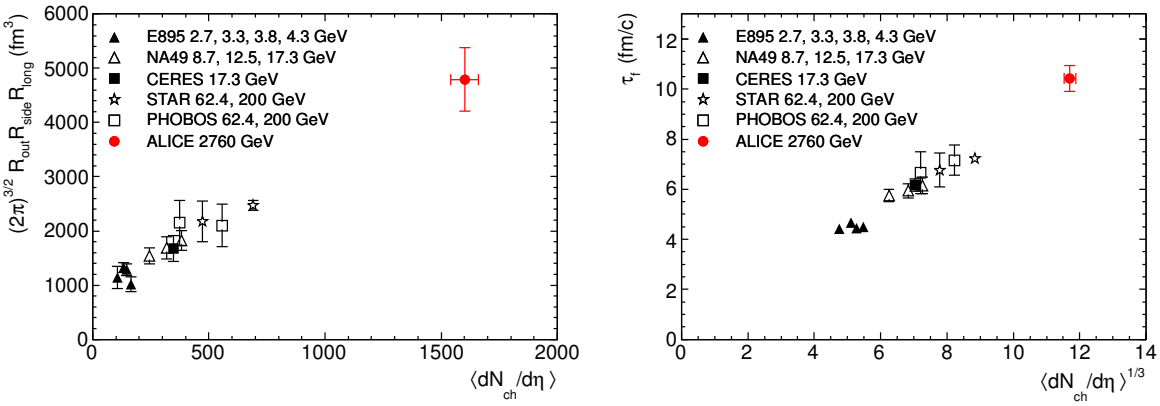

Fig. 5.3 Left: Local freeze-out volume (left) and the system lifetime (decoupling time) τ_f (right) measured by identical pion interferometry with ALICE at the LHC [327] in comparison to central Au–Au and Pb–Pb collisions at lower energies [316, 328–335]. Both figures are taken from Ref. [116].

Figure 5.3 shows results from two-pion correlations measurements for the central heavy-ion collisions from very low up to LHC energies as a function of $\mathrm{d}N_{\mathrm{ch}}/\mathrm{d}\eta$. The total freeze-out volume (Fig. 5.3, left) is a product of geometrical factor and the radii measured in three orthogonal directions (R_{long}, R_{side}, R_{out}). This volume shows a linear increase with the charged-particle pseudorapidity density and is two times larger at the LHC than at RHIC, reaching approximately 5000 fm^3. The system lifetime τ_f (Fig. 5.3, right) is estimated from the pair-momentum dependence of R_{long} [327] and increases by 30% as compared to RHIC, to approximately 10 fm/c. The evolution from RHIC to the LHC of the individual radius parameters (R_{long}, R_{side}, R_{out}), as well as their pair momentum dependence is in agreement with hydrodynamical models [327, 336].

5.4 Azimuthal Flow

The nuclear overlap zone in collisions with nonzero impact parameter is not azimuthally symmetric, as schematically shown in Fig. 5.4 (left). It has an almond shape whose deformation changes with centrality. In non-central collision, the pressure gradient between the center of the overlap zone and its periphery varies with azimuth and is strongest in the direction of the reaction plane angle, ψ_{RP}, which coincides with the direction of the minor axis of the almond. The developing collective flow is proportional to the pressure gradient and therefore strongest toward the reaction plane (Fig. 5.4, right), leading to an anisotropic distribution of particles, as suggested for the first time by Ollitrault [337].

The flow pattern is quantified by Fourier expansion of particle transverse momentum spectra measured in azimuthal angle ϕ [338],

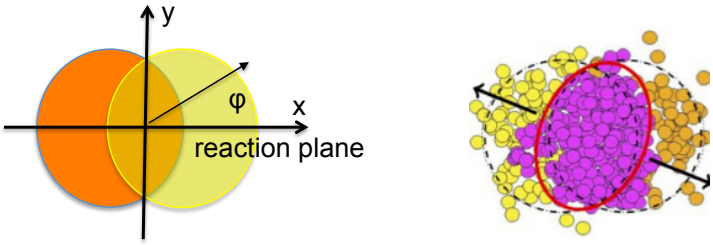

Fig. 5.4 Left: Schematic view of non-central heavy-ion collision. The angle ϕ is measured with respect to the reaction plane. Right: The heavy-ion collision from an event generator. The asymmetry in momentum of particles emitted in and out of the reaction plane is due to the different pressure gradients between the center of the overlap zone and its periphery.

$$E\frac{\mathrm{d}^3N}{\mathrm{d}^3p} = \frac{1}{2\pi p_\mathrm{T}}\frac{\mathrm{d}^2N}{\mathrm{d}p_\mathrm{T}\mathrm{d}y}\left(1+2\sum_{n=1}^{\infty} v_\mathrm{n}\cos\left[n\left(\phi-\psi_\mathrm{n}\right)\right]\right), \tag{5.2}$$

where v_n is the Fourier coefficient, which can be determined as a function of p_T, $v_\mathrm{n}\left(p_\mathrm{T}\right) = \langle\cos\left[n\left(\phi-\psi_\mathrm{n}\right)\right]\rangle$, where average is calculated over particles produced in a given p_T interval and over events in a given centrality class. The order of Fourier harmonics is denoted by n, ϕ is the azimuthal particle angle, and ψ_n is the angle of the spatial plane of symmetry of harmonic n. There are several methods to determine the ψ_n on event-by-event basis, by use of ϕ asymmetry generated by the flow itself or v_n coefficients (see Refs. [144, 339] for details).

The v_1 is known as a directed flow, which is most prominent close to beam rapidity and can be used to investigate of the initial conditions in heavy-ion collisions with spectator nucleons (see Ref. [340] for more details). In the past, the most attention was paid to the elliptic flow (v_2), which is directly related to the almond shape of the overlap zone in non-central collisions (see Fig. 5.4), where the symmetry axis angle $\psi_2 \approx \psi_\mathrm{RP}$. However, it has been realized [341] that the event-by-event fluctuations in distribution of nucleons in colliding nuclei can lead to irregular shapes of the reaction zone and the corresponding initial pressure gradients. The irregular pressure gradients show no symmetry with respect to the reaction plane and therefore induce higher harmonic flow patterns. Fluctuations can also tilt the symmetry angle of v_2, $\psi_2 \neq \psi_\mathrm{RP}$ (see Fig. 5.4, right), which leads to event-by-event fluctuations of the elliptic flow direction and magnitude.

The elliptic flow magnitude increases continuously with $\sqrt{s_\mathrm{NN}}$ from SPS/RHIC to LHC energies [345]. At the highest RHIC energy, v_2 reaches the value [123–126] compatible with that predicted by the hydrodynamics for a perfect fluid, i.e. fluid without internal friction and vanishing shear viscosity η, usually quoted as the ratio of shear viscosity to entropy density η/s. Based on the AdS/CFT correspondence it has been argued that the η/s has a lower bound of $\eta/s \geq 1/4\pi$ [346] for a large class of strongly interacting quantum field theories at finite temperature and zero chemical potential. The value of η/s has been extracted from flow measurements at RHIC by comparing the $v_2\left(p_\mathrm{T}\right)$ with results from viscous hydrodynamic calculations and by fitting the centrality dependence of the average p_T-integrated elliptic flow.

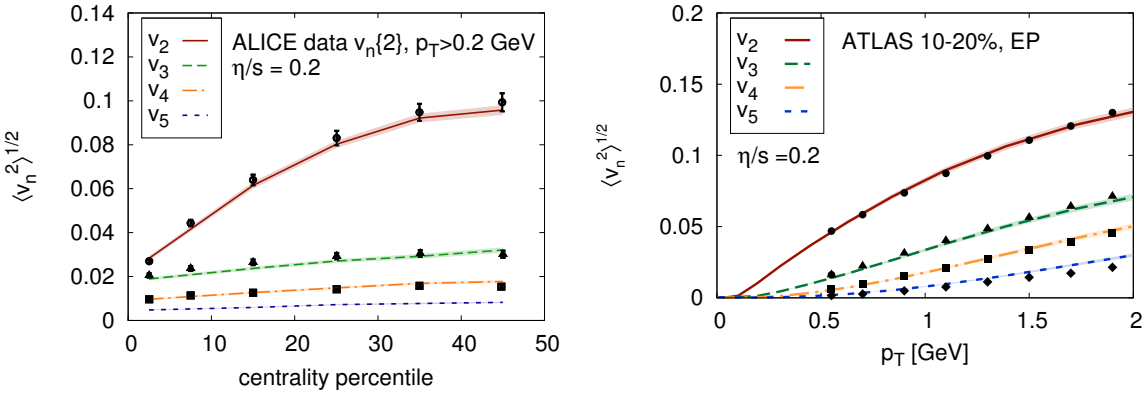

Fig. 5.5 The p_{T}-integrated flow coefficients v_n for $n \in \{2,3,4\}$ as a function of centrality measured by ALICE [342] (left) and $v_n(p_{\mathrm{T}})$ for $n \in \{2,3,4,5\}$ as a function of p_{T} measured by ATLAS [343] (right) in Pb–Pb collisions at $\sqrt{s_{\mathrm{NN}}} = 2.76$ TeV, in comparison to event-by-event anisotropic flow calculations (shaded bands) [344]. The ratio $\eta/s = 0.2$ was used in the calculations. Both figures are taken from [344].

The early calculations yield $\eta/s < (2.5-5)/4\pi$ [347–350], close to the lower bound value. This observation has lead to discovery of new form of matter - (almost) perfect liquid - produced in heavy-ion collisions at RHIC.

At the LHC, the measured $v_2(p_{\mathrm{T}})$ is very similar to that at RHIC, while the p_{T}-integrated elliptic flow is larger by around 30% than at RHIC [342, 345, 353–355], as a consequence of stronger radial flow. Figure 5.5 shows the p_{T}-integrated and p_{T}-differential flow coefficients v_n for charged particles measured in Pb–Pb collisions at $\sqrt{s_{\mathrm{NN}}} = 2.76$ TeV [342, 343]. The elliptic flow depends strongly on centrality and p_{T}, and dominates over higher harmonic flow coefficients in non-central Pb–Pb collisions. For the most central collisions, the elliptic and triangular flow (v_3) show similar values, which point to the large event-by-event fluctuations of the initial spacial geometry that generate v_3 [353]. The data are compared to event-by-event (3+1)D viscous hydrodynamical calculations (MUSIC) [344] with initial conditions simulated using IP-Glasma model [356]. The results of calculations with $\eta/s = 0.2$, which is similar to that at RHIC, are in good agreement with data for all flow coefficients. Thus, it can be concluded that the matter created at the LHC behaves like the (almost) perfect liquid.

The flow coefficients $v_{\mathrm{n}}\,(\mathrm{n} \in \{2,3,4,5\})$ have been also measured for identified light-flavor hadrons in Pb–Pb collisions at the LHC [351, 357]. Figure 5.6 shows the p_{T}-differential v_2 for pions, kaons and protons measured by ALICE in Pb–Pb collisions at $\sqrt{s_{\mathrm{NN}}} = 2.76$ TeV in four centrality intervals [351]. For $p_{\mathrm{T}} < 2$ GeV/c, a clear mass ordering is seen, which is related with a depletion in the particle spectrum at low p_{T} values due to the radial flow. This depletion increases with increasing particle mass and transverse velocity. Therefore, the heavier particles have smaller v_2 values compared to lighter particles at a given p_{T}. The similar mass ordering is also seen at low p_{T} for higher flow harmonics ($\mathrm{n} > 2$) [351]. Furthermore, the v_2 shows crossing for particles with different mass, which depending on the collision central-

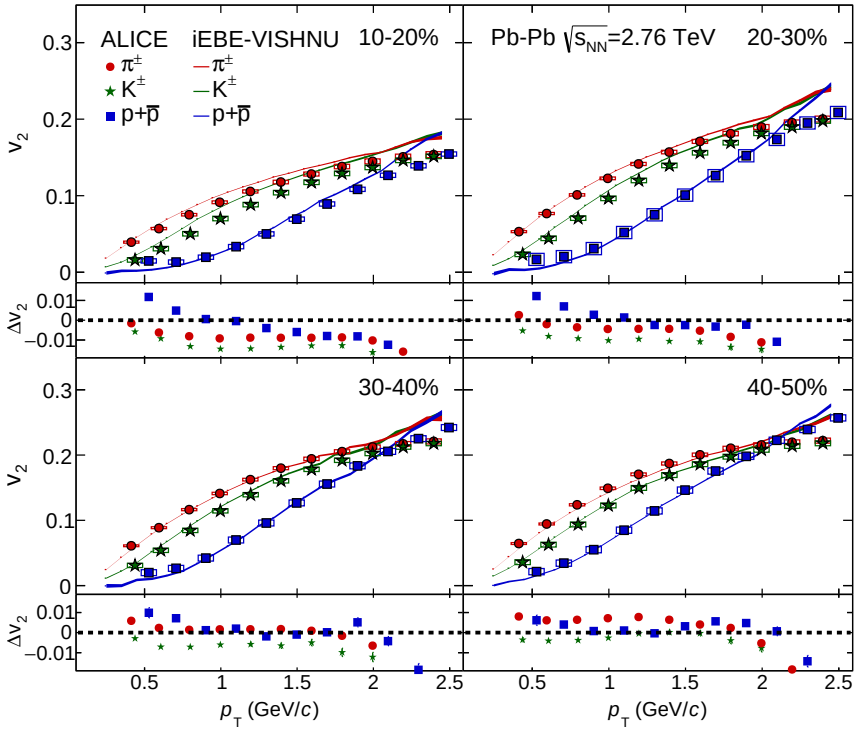

Fig. 5.6 The p_{T}-differential v_2 for pions, kaons and protons measured for four centrality intervals in Pb–Pb collisions at $\sqrt{s_{\mathrm{NN}}} = 2.76$ TeV [351]. The measurements are compared with model calculations (iEBE-VISHNU) [352], which are shown as lines in top panels. The differences between data and model v_2 are shown in the bottom panels.

.

ity and order of the flow harmonic, takes place at different p_{T} values. The crossing point for central collisions occurs at higher p_{T} values of v_n since the common velocity field, which exhibits a significant centrality dependence, affects heavy particles more. The data are compared with calculations based on iEBE-VISHNU, an event-by-event version of the VISHNU hybrid model [352], which couples $(2+1)$D viscous hydrodynamics to a hadron cascade UrQMD model [358], while initial fluctuating conditions are simulated with AMPT model [359]. This model gives the best fit to the data (Fig. 5.6, lower panels) for the following parameters: thermalization time $\tau = 0.4$ fm/c, transition temperature $T_c = 165$ MeV, and the ratio $\eta/s = 0.08$. It can reproduce data within 10–15% for $p_{\mathrm{T}} < 2$ GeV/c. The similar agreement is achieved for the higher harmonics.

The p_{T} range for $v_{\mathrm{n}}\,(\mathrm{n} \in \{2,3\})$ measurement for light-flavor hadrons in non-central Pb–Pb collisions was recently extended up to $p_{\mathrm{T}} = 20$ GeV/c [360]. The observed magnitude of the (anti-)proton elliptic and triangular flow is larger than that of pions in the range of 3–10 GeV/c. This behavior is qualitatively consistent with a picture where particle production in this inter-

mediate p_{T} region includes interaction of jet fragments with bulk matter, as discussed in e.g. Ref. [319]. For $p_{\mathrm{T}} > 10$ GeV/c, where particle production is dominated by fragmentation of hard partons, the v_2 is different than zero and is similar for hadron species, while the higher harmonics are consistent with zero. This behavior of v_2 is well reproduced by the parton energy loss calculations based on the WDHG model [361], where azimuthal anisotropy in particle momentum distribution is caused by the path-length dependence of parton energy loss (see also Ref. [362]).

The non-zero elliptic flow has been also measured by ALICE for heavy-flavor D [363, 364] and J/ψ [365, 366] mesons in non-central Pb–Pb collisions at $\sqrt{s_{\mathrm{NN}}} = 2.76$ and 5.02 TeV. The v_2 of D mesons measured in the p_{T} range of 2–16(2–20) GeV/c at $\sqrt{s_{\mathrm{NN}}} = 2.76(5.02)$ TeV is comparable with that of light-flavor hadrons. For $p_{\mathrm{T}} < 6$ GeV/c, this result indicates that the interactions with the medium constituents transfer to charm quarks information on the azimuthal anisotropy of the system, suggesting that low momentum charm quarks take part in the collective motion of the system. A positive v_2 observed for $p_{\mathrm{T}} > 6$ GeV/c can be related to the path-length dependence of the partonic energy loss. The positive J/ψ elliptic is observed in non-central Pb–Pb collisions in the intermediate p_{T} range of 1–6 (2–8) GeV/c at $\sqrt{s_{\mathrm{NN}}} = 2.76(5.02)$ TeV, indicating that they inherit their flow from thermalized charm quarks.

Chapter 6
Measurement of p_{T} Spectra of Charged Particles in pp, p–Pb and Pb–Pb Collisions

ALICE has measured transverse momentum spectra of charged particles in pp collisions at $\sqrt{s} = 0.9$, 2.76, 5.02, 7 and 13 TeV [14, 18, 25, 28], p–Pb collisions at $\sqrt{s_{\mathrm{NN}}} = 5.02$ TeV [16, 21, 22, 28] and Pb–Pb collisions at $\sqrt{s_{\mathrm{NN}}} = 2.76$ and 5.02 TeV [15, 17, 28]. All quoted results have been obtained by author. Most of the reported data sets were recorded by ALICE during the first LHC data taking period in 2009–2013, while the pp data at $\sqrt{s} = 5.02$ and 13 TeV and Pb–Pb data at $\sqrt{s_{\mathrm{NN}}} =$ 5.02 TeV were recorded in 2015. While analyzing pp and Pb–Pb data at the highest collision energy the pp and Pb–Pb data at $\sqrt{s} = 2.76$ TeV and p–Pb data at $\sqrt{s_{\mathrm{NN}}} = 5.02$ TeV were also reanalyzed [28]. The reanalysis was warranted by significant improvements in track selection and efficiency corrections, which benefit from the experience accumulated in the past years as well as better knowledge of the particle production at the LHC energies. In this chapter, the technical aspects of charged-particle analysis and resulting p_{T} spectra used for the determination of nuclear modification factors are presented.

6.1 Spectra Analysis

The goal of the analysis was to determine the p_{T} spectra of primary charged particles. A primary charged particle is defined in ALICE [367] to be a charged particle with a mean proper lifetime τ larger than 1 cm/c, which is either produced directly in the interaction or from decays of particles with τ smaller than 1 cm/c, excluding particles produced in interactions with the detector material. According to the definition, the sample of primary charged particles includes e^-, μ^-, π^-, K^+, p, Σ^-, Σ^+, Ξ^-, Ω^- and heavy-flavor hadrons, and their antiparticles. However, the primary charged particle spectrum is dominated by pions, kaons and protons, which account for more than 95%, as estimated using ALICE measurements of identified hadrons [28]. The analysis is based on tracking information from the ITS and TPC detectors, located in the central barrel of the experiment. The kinematic ranges selected for particle measurement in pp, p–Pb and Pb–Pb collisions (Tab. 6.1) are determined by the event and track selection criteria, available statistics, as well as rapidity shift ($\Delta y = 0.465$) in p–Pb collisions.

The event and track selection criteria are identical for all data sets and are optimized for the best track quality and minimal contamination from secondary particles.

System	$\sqrt{s_{\mathrm{NN}}}$ (TeV)	year	p_{T} range (GeV/c)	psudorapidity range
pp	0.9	2010	0.15–20	$\lvert\eta\rvert < 0.8$
pp	2.76	2011	0.15–32	$\lvert\eta\rvert < 0.8$
pp	5.02	2015	0.15–50	$\lvert\eta\rvert < 0.8$
pp	7	2010	0.15–50	$\lvert\eta\rvert < 0.8$
p–Pb	5.02	2012, 2013	0.15–50	$-0.3 < \eta_{\mathrm{cms}} < 1.3$
Pb–Pb	2.76	2010	0.15–50	$\lvert\eta\rvert < 0.8$
Pb–Pb	5.02	2015	0.15–50	$\lvert\eta\rvert < 0.8$

Table 6.1 Data sets and kinematic ranges used in the analysis of nuclear modification factors.

The data are presented as p_{T}-differential cross sections for inelastic (INEL) pp collisions originating from single-diffractive (SD), double-diffractive (DD) and non-diffractive (ND) processes, and as invariant p_{T} yields for non-single diffractive (NSD) p–Pb collisions and centrality-selected INEL Pb–Pb collisions. Corrections for detector effects were determined using MC simulations as well as data driven methods.

6.1.1 Trigger and Event Selection

The minimum-bias (MB) interaction trigger was based on signals from the forward scintillator arrays (V0A and V0C) and the two innermost layers of the ITS, the Silicon Pixel Detector (SPD), in coincidence with two beam bunches crossing in the ALICE interaction region. The pp collisions at $\sqrt{s} = 2.76$ TeV were selected requiring a signal in either one of the V0A or the V0C detectors or in the SPD ($\mathrm{MB_{OR}}$). The Pb–Pb collisions at $\sqrt{s_{\mathrm{NN}}} = 2.76$ TeV were selected based on different combinations of hits in the SPD and either V0A or V0C detector (see Ref. [144] for more details). For measurements of pp, p–Pb and Pb–Pb collisions at $\sqrt{s_{\mathrm{NN}}} = 5.02$ TeV the trigger required a signal in both V0A and V0C detectors ($\mathrm{MB_{AND}}$).

In addition, the offline event selection was applied to reject beam-induced background in all collision systems. The background events were efficiently rejected by exploiting the timing signals in the two V0 detectors. In Pb-Pb collisions background was also rejected exploiting the correlation between the arrival times measured in each neutron Zero Degree Calorimeter (ZDC), positioned on both sides of the interaction point at 114.0 m for pp and Pb–Pb data at $\sqrt{s_{\mathrm{NN}}} = 2.76$ TeV and at 112.5 m for the rest data sets. The contamination from electromagnetic interactions in Pb–Pb collisions was strongly suppressed using signals from the ZDCs (see Ref. [144] for more details).

The primary event vertex was determined with tracks from the central barrel. For the analysis of pp collisions, if no vertex was found using tracks, the vertex reconstruction was per-

formed using SPD tracklets (track segments reconstructed based on the information from the two innermost layers of the ITS). To ensure a uniform acceptance and reconstruction efficiency witin $|\eta| < 0.8$, only events with a reconstructed vertex within $|z_{\rm v}| < 10$ cm from the center of the detector along the beam direction were used in the analysis.

6.1.2 Track Selection

A set of cuts based on the number of space points and the quality of the momentum fit in the TPC and ITS was applied to the reconstructed tracks [17, 28]. The tracks candidates in the TPC were required to cross at least 120 pad rows (out of 159), and χ^2 per point of the momentum fit smaller than 4. Such tracks were extrapolated to the ITS and used for further analysis if at least 2 matching hits (out of maximum 6) in the ITS, including at list one in the SPD are found. The χ^2 per reconstructed hit in the ITS was required to be smaller than 36.

The primary track selection is based on the distance of closest approach in the transverse plane $|d_{\rm xy}| < A + B \cdot p_{\rm T}^{C}$, with $A = 0.0182$ cm, $B = 0.035$ cm $\cdot$ GeV$/c$, C = -1.0 and $p_{\rm T}$ in units of GeV$/c$, and along the beam axis $|d_{\rm z}| < 2$ cm. In order to improve the purity of primary track reconstruction at high $p_{\rm T}$ we developed a procedure [17] where we compare track parameters from the combined ITS and TPC track reconstruction algorithm to that derived only from the TPC and constrained by the interaction vertex point. The distance computed between these two tracks reconstructed for the same track candidate,

$$\chi^2_{\rm TPC-ITS} = (\mathbf{v}_{\rm TPC} - \mathbf{v}_{\rm TPC-ITS})^{\mathbf{T}} \cdot (\mathbf{C}_{\rm TPC} + \mathbf{C}_{\rm TPC-ITS})^{-\mathbf{1}} \cdot (\mathbf{v}_{\rm TPC} - \mathbf{v}_{\rm TPC-ITS}), \qquad (6.1)$$

where $\mathbf{v}_{\rm TPC}$, $\mathbf{v}_{\rm TPC-ITS}$ and $\mathbf{C}_{\rm TPC}$, $\mathbf{C}_{\rm TPC-ITS}$ represent the measured track parameter vectors and their covariance matrices, respectively. The $\chi^2_{\rm TPC-ITS}$ was required to be smaller than 36. This cut in fact removes high-$p_{\rm T}$ fake tracks, which originate from spurious matches of low $p_{\rm T}$ particles in the TPC to hits in the ITS, and would result in an incorrect momentum assignment. A full list of cuts is presented in Refs. [17, 368].

The track selection criteria were improved in the recent analysis of charged-particle $p_{\rm T}$ spectra [28]. In addition to mentioned cuts, the track length (L) measured on the TPC readout plane (projection) was required to be $L > A - B \cdot p_{\rm T}^{C}$, with $A = 130$ cm, $B = 1.0$ cm $\cdot$ GeV$/c$, $C = -1.5$ and $p_{\rm T}$ in units of GeV$/c$. Moreover, additional requirements for the number of the TPC pad-rows and clusters assigned to the track were applied (see Ref. [28] for more details).

6.1.3 Corrections

The data are presented as differential cross sections for inelastic pp collisions

$$\frac{{\rm d}^2\sigma_{\rm ch}}{{\rm d}\eta\,{\rm d}p_{\rm T}} = \sigma^{\rm pp}_{\rm MB} \cdot \frac{1}{N^{\rm MB}_{\rm ev}} \frac{{\rm d}^2 N_{\rm ch}}{{\rm d}\eta\,{\rm d}p_{\rm T}} \equiv \sigma^{\rm pp}_{\rm MB} \cdot \frac{N^{\rm rec}_{\rm ch}(\Delta\eta, \Delta p_{\rm T}) \cdot C(\Delta\eta, \Delta p_{\rm T})}{N^{\rm rec}_{\rm ev} \cdot \Delta\eta \Delta p_{\rm T}} \cdot \varepsilon_{\rm VZ}, \qquad (6.2)$$

and transverse momentum spectra for non-single diffractive (NSD) p–Pb and centrality-selected INEL Pb–Pb collisions

$$\frac{1}{N_{\mathrm{ev}}}\frac{\mathrm{d}^2N_{\mathrm{ch}}}{\mathrm{d}\eta\,\mathrm{d}p_{\mathrm{T}}} \equiv \frac{N_{\mathrm{ch}}^{\mathrm{rec}}(\Delta\eta,\Delta p_{\mathrm{T}})\cdot C(\Delta\eta,\Delta p_{\mathrm{T}})}{N_{\mathrm{ev}}^{\mathrm{rec}}\cdot\Delta\eta\,\Delta p_{\mathrm{T}}}\cdot\varepsilon_{\mathrm{MB}}\cdot\varepsilon_{\mathrm{VZ}}, \tag{6.3}$$

which are obtained by correcting the charged particle yields $N_{\mathrm{ch}}^{\mathrm{rec}}$ reconstructed in the $(\Delta\eta,\Delta p_{\mathrm{T}})$ intervals for all detector effects that either influence the event reconstruction, and thus are relevant only for the overall normalization (event-level corrections), or influence the track reconstruction and are relevant for both the spectral shape and normalization (track-level corrections). The $\varepsilon_{\mathrm{MB}}$ and $\varepsilon_{\mathrm{VZ}}$ denote the MB trigger and event vertex reconstruction efficiencies, and and $C(\Delta\eta,\Delta p_{\mathrm{T}})$ are track-level correction factors, determined for the $(\Delta\eta,\Delta p_{\mathrm{T}})$ intervals. Note that the presented yields or cross sections correspond to the average values in the p_{T} intervals (bins) and are plotted versus p_{T} at the bin center. There are no addition corrections on the spectra related to the finite bin width in p_{T}. Details of the correction procedure are described in the following sections.

6.1.3.1 Event-Level Corrections

In Eq. 6.2 the minimum-bias cross section $\sigma_{\mathrm{MB}}^{\mathrm{pp}}$ for triggered pp collisions was determined using van-der-Meer scans. It depends on the trigger settings and amounts to $47.8^{2.5}_{-3.0}$ mb at $\sqrt{s}=0.9$ TeV, 55.4 ± 1.0 mb at $\sqrt{s}=2.76$ TeV and 62.2 ± 2.2 mb at $\sqrt{s}=7$ TeV for the $\mathrm{MB_{OR}}$ [369], and 51.2 ± 1.2 mb at $\sqrt{s}=5.02$ TeV for the $\mathrm{MB_{AND}}$ [370]. The differential charged-particle yields $\mathrm{d}^2N/\mathrm{d}\eta\mathrm{d}p_{\mathrm{T}}$ were calculated for the MB event class $\left(N_{\mathrm{ev}}^{\mathrm{MB}}\right)$ by normalizing to the number of reconstructed events $N_{\mathrm{ev}}^{\mathrm{rec}}$, which have a reconstructed event vertex within $|z_{\mathrm{v}}|<10$ cm from of the center of the detector and correcting for the event vertex reconstruction efficiency $\varepsilon_{\mathrm{VZ}}$. The $\varepsilon_{\mathrm{VZ}}$ depends on the trigger settings, on the event generator used for corrections and on the collision energy, and amounts to 83%, 85% and 88% for INEL pp events at $\sqrt{s}=0.9$, 2.76 and 7 TeV, respectively. It was determined [369] based on GEANT3 detector simulations with PYTHIA6 (Perugia 0 tune) event generator [183, 371]. The $\varepsilon_{\mathrm{VZ}}$ in the recent analysis of charged-particle p_{T} spectra amounts to 88.3%(97.7%) at $\sqrt{s}$ = 2.76(5.02) TeV [28], as estimated using simulations with PYTHIA8 (Monash 2013 tune) event generator [184, 372].

For NSD p–Pb collisions, the efficiency of the trigger and event vertex reconstruction ($\varepsilon_{\mathrm{MB}}\cdot\varepsilon_{\mathrm{VZ}}$, as in Eq. 6.3) is about 99.2% [16], which was estimated using a combination of event generators including: i) DPMJET for NSD p–Pb interactions [192], ii) PHOJET tuned to pp data at $\sqrt{s}=2.76$ and 7 TeV [186] together with a Glauber model [373] for the contribution from SD interactions, and iii) STARLIGHT [374] used together with PYTHIA or PHOJET for the proton excitation in the electromagnetic field of the $^{208}_{82}$Pb nucleus. The DPMJET generator, which is based on the Gribov-Glauber approach and treats soft and hard scattering processes in an unified way, includes incoherent SD collisions of the projectile proton with target nucleons that are concentrated mainly on the surface of the nucleus. The SD collisions

were removed by requiring that at least one of the binary nucleon-nucleon interaction is NSD. The relative weight of the events in the cocktail is given by the cross sections of the corresponding processes, which are taken to be 2.0 b(0.1 b) for NSD(SD) collisions estimated from the Glauber model, and 0.1–0.2 b for EM interactions obtained from STARLIGHT calculations. The contributions from SD and EM interactions were found to be negligible for a given trigger settings.

For Pb–Pb collisions, the trigger and event vertex reconstruction is fully efficient for the centrality intervals within 0–80% range considered in this work, as estimated using Monte Carlo simulations with GEANT3 and HIJING [194] event generator.

6.1.3.2 Track-Level Corrections

The differential charged-particle yields $\mathrm{d}^2N_{\mathrm{ch}}/\mathrm{d}\eta\mathrm{d}p_{\mathrm{T}}$ (Eq. 6.2 and 6.3) are obtained from the reconstructed yields of tracks $N_{\mathrm{ch}}^{\mathrm{rec}}(\Delta\eta,\Delta p_{\mathrm{T}})$ corrected using correction factors $C(\Delta\eta,\Delta p_{\mathrm{T}})$, which are products of acceptance, efficiency, contamination and p_{T} resolution. The numerical values of primary charged-particle reconstruction efficiency, contamination with secondary particles and p_{T} resolution correction for selected systems are listed in Table 6.2.

System	$\sqrt{s_{\mathrm{NN}}}$ (TeV)	event class	p_{T} range (GeV/c)	efficiency	contamination	$\frac{\sigma(p_{\mathrm{T}})}{p_{\mathrm{T}}}$ correction
pp	0.9	INEL	0.15–20	40–73%	0.6–7%	$< 2.0\%$
pp	2.76	INEL	0.15–32	36–68%	0.6–7%	$< 4.0\%$
pp	5.02	INEL	0.15–50	33–77%	0.7–9%	$< 5\%$
pp	7	INEL	0.15–50	40–73%	0.6–7%	$< 6.5\%$
p–Pb	5.02	NSD	0.15–50	41–80%	0.4–7%	$< 1.5\%$
Pb–Pb	2.76	0–5%	0.15–50	37–69%	0.7–13.4%	$< 4.0\%$
Pb–Pb	2.76	70–80%	0.15–50	38–71%	0.7–7%	$< 8.0\%$
Pb–Pb	5.02	0–5%	0.15–50	31–75%	0.7–20%	$< 3.0\%$
Pb–Pb	5.02	70–80%	0.15–50	32–77%	0.7–10%	$< 4.0\%$

Table 6.2 The numerical values of primary charged-particle reconstruction efficiency, contamination with secondary particles and p_{T} resolution correction for pp collisions at $\sqrt{s} = 0.9$, 2.76 and 7 TeV [18] and $\sqrt{s}$ = 5.02 TeV [28], p–Pb collisions at $\sqrt{s_{\mathrm{NN}}} = 5.02$ TeV [21], and Pb–Pb collisions at $\sqrt{s_{\mathrm{NN}}} = 2.76$ TeV [17] and $\sqrt{s_{\mathrm{NN}}} = 5.02$ TeV [28].

6.1.3.3 Tracking Efficiency

The efficiency and purity of the primary charged particle reconstruction as well as acceptance correction for the p–Pb data are calculated using Monte Carlo event generators with GEANT3 detector modeling combined with data-driven corrections. In the early analyses of charged-particle p_{T} spectra the corrections for detector efficiency were determined based exclusively

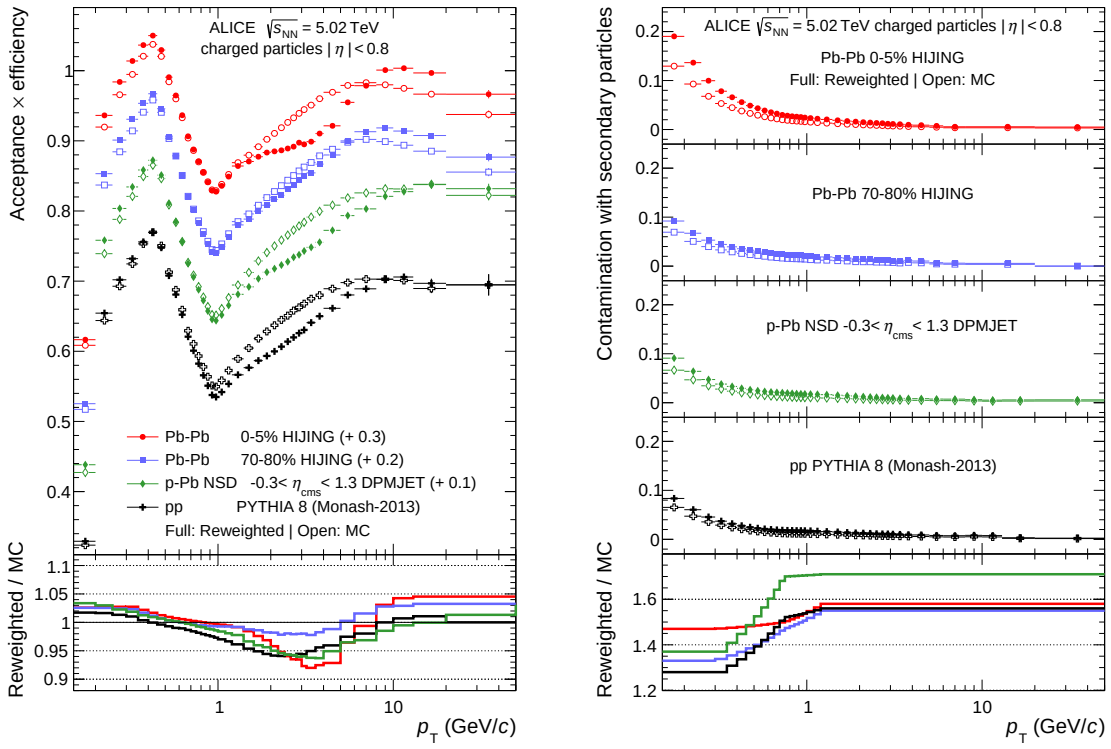

Fig. 6.1 Left: Combined tracking efficiency and acceptance as a function of p_T for different collision systems determined based on Monte-Carlo detector simulations with selected event generators and a reweighting method. For better visibility, the curves for p–Pb and Pb–Pb are offset by the indicated values. The effect of the reweighting on the efficiency corrections is shown in the bottom panel. The systematic uncertainties of the reweighting ($< 2.4\%$) are not shown. Right: Contamination from secondary particles estimated from Monte Carlo simulations and from the distance of closest approach (d_{xy}) fits in data. The effect of the reweighting of secondary particles is shown in the bottom panel. The systematic uncertainties on the scaling factors ($< 20\%$) are not shown. Both figures are taken from Ref. [28].

on detectors simulations with selected event generators. In the recent analysis [28], the detector efficiencies obtained from simulations for different collisions systems were reweighted using measured identified-particle fractions, which are different as compared to those in the event generators. The resulting reweighted efficiencies differ by 2–7% with respect to simulated values, with the largest modifications in the intermediate p_T and for the central Pb–Pb collisions, as shown in Fig. 6.1 (left). The reweighting procedure is discussed in detail in Ref. [28]. The obtained tracking efficiency depends on p_T, collision system and centrality, and ranges between 31% and 77% for the considered data sets and track selection criteria.

6.1.3.4 Secondary Particle Contamination

The contribution from secondary particles, i.e. products of weak decays of kaons, Λ hyperons and muons, and particles arising from interactions in the detector material, was estimated using the distance of closest approach (d_{xy}) distributions of particles in data and Monte Carlo simulations. Exploiting the differences, especially in the tails, of the d_{xy} distributions between primary and secondary particles, the measured distributions were fitted by a linear combination of d_{xy} distributions (templates) for primary and secondary particles obtained from the Monte Carlo simulations in different p_{T} bins, as described in detail in Ref. [120]. The contamination from secondary particles from simulations were rescaled up with the scaling factors to match those in the data (up to factor of 1.7 for p–Pb collisions), as shown in the bottom panel of Fig. 6.1 (right) [28]. The contamination is a function of p_{T} and collision system (Fig. 6.1, right), and amounts to $\sim 8\%(20\%)$ in pp(Pb–Pb) collisions at $p_{\mathrm{T}} = 0.15$ GeV$/c$ and decreases below 1% for $p_{\mathrm{T}} > 5$ GeV$/c$.

6.1.3.5 Acceptance Correction in p–Pb

The two-in-one magnet design of the LHC imposes the same magnetic rigidity of the beams in the two rings. The configuration for p–Pb collisions with protons at 4 TeV energy colliding with $^{208}_{82}$Pb ions at 82×4 TeV results in a shift in the rapidity of the nucleon–nucleon center-of-mass system by $\Delta y_{\mathrm{NN}} = 0.465$ in the direction of the proton beam. Therefore, the detector coverage $|\eta_{\mathrm{lab}}| < 0.8$ corresponds to roughly $-0.3 < \eta_{\mathrm{cms}} < 1.3$. For massless or high p_{T} particles $\eta_{\mathrm{cms}} = \eta_{\mathrm{lab}} + \Delta y_{\mathrm{NN}}$, but the differential yield of non-massless particles at low p_{T} suffers from a distortion, which is estimated and corrected for based on the HIJING event generator weighted by the measured relative particle abundances [27, 375].

The proper transformation of the η_{lab} under the boost along z-direction with Δy_{NN} is given by the formula

$$\sinh(\eta_{\mathrm{cms}}) = \sinh(\eta_{\mathrm{lab}} - \Delta y_{\mathrm{NN}}) - \left(\sqrt{\frac{m^2}{p_{\mathrm{T}}^2} + \cosh^2(\eta_{\mathrm{lab}})} - \cosh(\eta_{\mathrm{lab}}) \right) \sinh(\Delta y_{\mathrm{NN}}), \quad (6.4)$$

where the first term corresponds to the shift and the second term is an additional correction, which can become arbitrary large depending on a particle mass to momentum ratio m/p_{T}. The boost moves particles in/out of the η-acceptance, leading to increase or decrease of the measured yield. The corrections were derived using the pseudorapidity distribution measured for inclusive charged particles in the present data sample [309].

The η-acceptance corrections are calculated as a function of m/p_{T} using the ratio of the $\mathrm{d}N/\mathrm{d}\eta_{\mathrm{cms}}$ to the $\mathrm{d}N/\mathrm{d}\eta_{\mathrm{lab}}$ (Eq. 6.4) integrated in the corresponding pseudorapidity intervals,

$$C_{\mathrm{acc}}\,(m/p_{\mathrm{T}}) = \frac{\int_{\eta_1}^{\eta_2} \mathrm{d}N/\mathrm{d}\eta_{\mathrm{cms}}\,(m/p_{\mathrm{T}})\,\mathrm{d}\eta}{\int_{\eta_1+\Delta y_{\mathrm{NN}}}^{\eta_2+\Delta y_{\mathrm{NN}}} \mathrm{d}N/d\eta_{\mathrm{lab}}\,(m/p_{\mathrm{T}})\,\mathrm{d}\eta}. \quad (6.5)$$

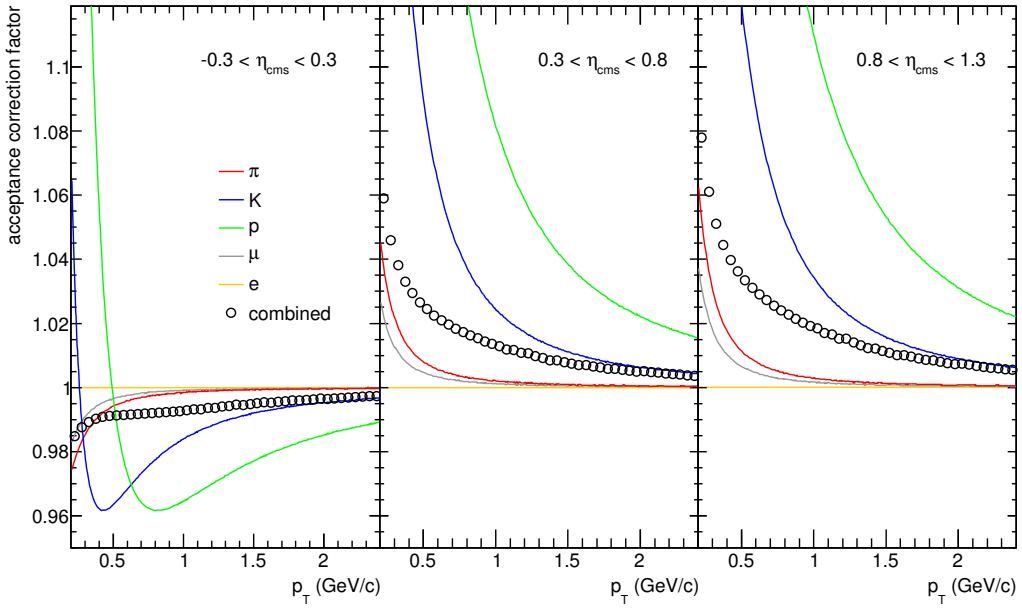

Fig. 6.2 Acceptance correction factors for pion, kaons, protons, electrons and muons as a function of p_{T} and the overall correction factors applied for the three analyzed pseudorapidity intervals in p–Pb collisions at $\sqrt{s_{\mathrm{NN}}} = 5.02$ TeV. Figure is taken from Ref. [368].

The overall η corrections for charged particle p_{T} spectra as a function of p_{T} is obtained as an weighted average over the single particle contributions

$$C_{\mathrm{acc}}\left(p_{\mathrm{T}}\right) = \sum_{i=\pi,K,p} \frac{n_{\mathrm{i}}}{n_{\pi}+n_{K}+n_{p}} C_{\mathrm{acc}}\left(m_{\mathrm{i}}/p_{\mathrm{T}}\right). \tag{6.6}$$

The obtained correction factors are shown in Fig. 6.2 for pion, kaons, protons, electrons and muons as a function of p_{T} as well as the overall correction factors applied for the three analyzed pseudorapidity intervals in p–Pb collisions. The overall correction factors depends on p_{T} and pseudorapidity interval reaching up to 8% at the lowest p_{T}.

6.1.3.6 Momentum Resolution

The transverse momentum of charged particles is reconstructed from the track curvature measured in the ITS and TPC detectors. The modification of the spectra arising from the finite momentum resolution is estimated from the error obtained from the corresponding covariance matrix element of the Kalman fit. Figure 6.3 shows relative p_{T} resolution as a function of p_{T} for pp, p–Pb and Pb–Pb. For low transverse momenta ($p_{\mathrm{T}} < 1$ GeV/c), the resolution is dominated by the multiple scattering and shows no difference between collision systems. The best resolution $\sigma(p_{\mathrm{T}})/p_{\mathrm{T}} \approx 1\%$ is obtained at $p_{\mathrm{T}} = 1$ GeV/c for all collisions systems. For

larger transverse momenta the resolution is deteriorated by the space point resolution used in the tracking and reaches 10% for pp and Pb–Pb, and 3% for p–Pb for the largest p_{T}. For pp and Pb–Pb data sets at $\sqrt{s_{\mathrm{NN}}} = 5.02$ TeV the resolution got improved and is similar to that for p–Pb [28]. The different p_{T} resolution depending on the data set is due to different quality of space point position calibration, which influences on the tracking performance. The p_{T} resolution was verified by studying the widths of the invariant mass distributions of K^0_{s} reconstructed from their decays to two charged pions. It was also verified that the resolution does not depend on Pb–Pb collision centrality.

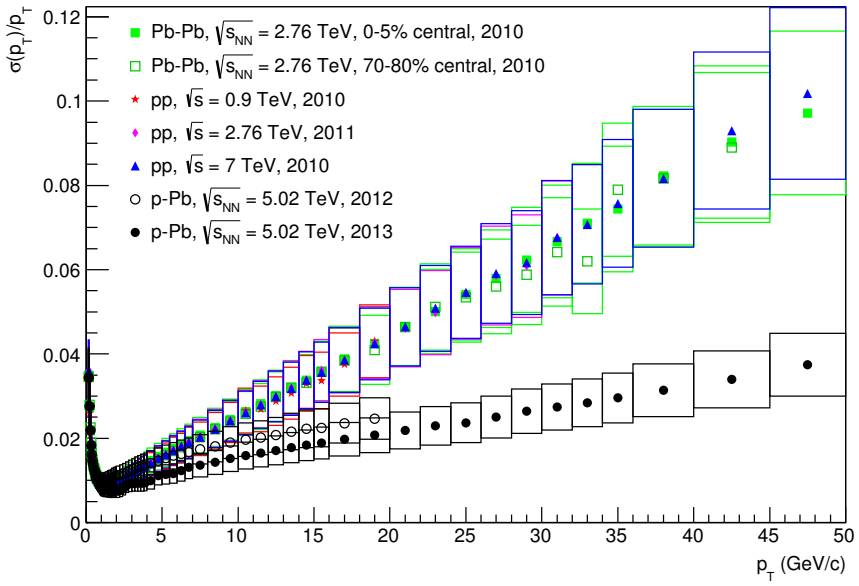

Fig. 6.3 Relative p_{T} resolution obtained from the measured track covariance matrix in pp, p–Pb and Pb–Pb collisions. The boxes around data points denote assigned systematic uncertainties. Figure is taken from Ref. [368].

To account for the finite p_{T} resolution, correction factors to the spectra for $p_{\mathrm{T}} > 10$ GeV/c were determined using an unfolding procedure [18, 28]. For the lower momenta corrections are negligible. The p_{T} dependent correction factors are applied (bin-by-bin) to the measured p_{T} spectra. They depend on the collision energy and collision system as well as on collision centrality, due the change of the spectral shape. For $\sqrt{s_{\mathrm{NN}}} = 5.02$ TeV, the correction factors reach 5%, 1.5% and 3%(4%) at $p_{\mathrm{T}} = 50$ GeV/c for pp, p–Pb and 0-5%(70–80%) central Pb–Pb collisions, respectively. For $\sqrt{s_{\mathrm{NN}}} = 2.76$ TeV, they amount to 4% for pp and 4%(8%) for 0-5%(70–80%) central Pb–Pb collisions at the highest p_{T}.

6.1.3.7 Event Selection Bias

The event selection (trigger and vertex) introduces a small p_T-dependence in the correction on the p_T spectra in pp collisions. This is due to the fact that the low-multiplicity pp events, which are also characterized by a softer spectrum, are mostly rejected by the trigger and vertex selection criteria. The effect on the p_T spectra was calculated from simulations with the PYTHIA8 (Monash 2013 tune) and the PYTHIA6 (Perugia2011 tune) event generators and was estimated to be around 0.4–0.6%(2.2–2.6%) for $p_T < 1$ GeV/c at $\sqrt{s} = 2.76(5.02)$ TeV [28]. The spectra are corrected by the average bias of these two generators, resulting in 0.5%(2.4%) corrections to the spectra.

6.1.4 Systematic Uncertainties

The systematic uncertainties were estimated for pp [18, 28], p–Pb [16, 21] and Pb–Pb [17, 28] collisions using similar procedure. This procedure applied in the most recent analysis of charged-particle p_T spectra [28] is listed below.

- The effect of the selection of events based on the vertex position is studied by comparing the fully corrected p_T spectra obtained with alternative vertex selections: $|z_v| < 5$ cm and $|z_v| < 20$ cm.
- The systematic uncertainties related to the track selection criteria were studied by varying the track quality cuts. In particular, we varied the upper limits of the track fit quality parameters in the ITS (χ^2_{ITS}/N_{hits}) and the TPC ($\chi^2_{TPC}/N_{clusters}$) in the ranges of 25–49 and 3–5, respectively. The systematic uncertainties related to high-p_T fake tracks [17] were estimated by modifying the upper limits of the track matching criteria given by the $\chi^2_{TPC-ITS}$ in the range of 25–49. The resulting uncertainty dominates at high p_T for all collision systems.
- The systematic uncertainty on the secondary-particle contamination includes contributions from the template fits to the measured d_{xy} distributions. We varied the fit model using templates with two (primaries, secondaries) or three (primaries, secondaries from material, secondaries from weak decays of K^0_s and Λ) components, as well as the fit ranges. The maximum difference between the data and the 2 component-template fit is summed in quadrature with the difference between results obtained from the 2 and the 3 component-template fits and result is assigned as the systematic uncertainty on the contamination. This contribution dominates for the lowest p_T, independently of the collision system.
- The systematic uncertainty on the primary particle composition consists of several contributions, including the extrapolation of the spectra to low p_T, the approximation of the relative particle abundances at high p_T, the efficiency parameterization at high p_T, the uncertainties of the measured particle spectra and the MC assumptions on the $\Sigma^{\pm}/\Lambda$ spectra ratios. For the extrapolation to low p_T, we studied different parameterizations (Bylinkin and Rostovtsev [376], modified Hagedorn [377], Blast-Wave [119]) and fit ranges. We varied

the p_{T} thresholds for the approximation of the relative particle abundances as well as the efficiency parameterization at high p_{T}. The measured particle spectra were varied within systematic uncertainties (one particle species at a time), and the resulting differences to the nominal spectra were added in quadrature to the systematic uncertainties. We also assigned an additional uncertainty related to the different spectral shape of $\Sigma^{\pm}$ and Λ from the MC generators.

- To account for the imperfect description of the experimental setup in simulations, we compared the track matching between the TPC and the ITS information in data and Monte Carlo after scaling of the fraction of secondary particles obtained from the fits to the d_{xy} distributions. After rescaling the fraction of secondary particles, the agreement between data and Monte Carlo is within 4%. This value is assigned as an additional systematic uncertainty.
- The systematic uncertainty on the p_{T} resolution was estimated using the azimuthal angle dependence of the $1/p_{\mathrm{T}}$ spectra for positively and negatively charged particles. The relative shift of the spectra for oppositely charged particles along $1/p_{\mathrm{T}}$ determines the size of uncertainty for a given angle. We used the RMS of the $1/p_{\mathrm{T}}$ shift distribution for the full azimuth as additional smearing of the p_{T} resolution. To take into account the decrease in the p_{T} resolution with increasing interaction rate, we have studied the systematic uncertainty for the pp and Pb–Pb data sets at $\sqrt{s_{\mathrm{NN}}} = 5.02$ TeV, obtained from the difference of the spectra at high and low interaction rate. The uncertainty is negligible for pp collisions, and is about 1% for Pb–Pb collisions.
- For the correction due to the trigger and vertex selection, calculated as the average bias of two generators, half of the value is assigned as systematic uncertainty.
- The systematic uncertainty for the acceptance correction on the p–Pb data was estimated by varying the relative particle abundances within their measured uncertainties and by changing the fit function for the low-p_{T} extrapolation. The uncertainty is sizable only at low p_{T} where it reaches 0.2%.
- The material budget in the simulation was varied by $\pm$4.5% [144], resulting in the systematic uncertainty in the range of 0.1–0.9%.
- The normalization uncertainty on the spectra in pp collisions was propagated from the cross section measurements.
- The systematic uncertainties related to centrality selection were estimated by a comparison of the p_{T} spectra when the limits of the centrality classes are shifted due to an uncertainty of $\pm$ 0.5% in the fraction of the hadronic cross section used in the analysis and by a comparison of results obtained using the SPD detector to estimate centrality as opposed to the V0A and V0C.

The relative systematic uncertainties on the p_{T} spectra obtained in the most recent analysis of charged particles are summarized in Table 6.3 [28]. For the evaluation of the total systematic uncertainty all contributions are considered to be uncorrelated and they are summed in quadrature. The improved reconstruction and track selection in the reanalysis of pp and Pb–Pb data at $\sqrt{s_{\mathrm{NN}}} = 2.76$ TeV and p–Pb data at $\sqrt{s_{\mathrm{NN}}} = 5.02$ TeV [28] lead to significantly

Source of Uncertainty	pp		p–Pb	Pb–Pb	
	2.76 TeV	5.02 TeV	5.02 TeV	2.76 TeV	5.02 TeV
Event selection	0.9%	0.5%	0.1%	1.5%	0.14%
Track selection	0.4–3.8%	0.6–3.5%	0.6–3.8%	1.0–2.0%	0.6–4.9%
Secondary particles	0.5–5.1%	0.0–2.8%	0.0–2.1%	0.0–4.0%	0.0–4.5%
Particle composition	0.1–1.6%	0.2–2.4%	0.4–2.2%	0.0–2.0%	0.2–2.0%
Matching efficiency	1.0–4.0%	0.0–1.1%	0.3–3.2%	0.2–2.0%	0.2–1.2%
Trigger and vertex selection	0.0–0.5%	0.0–1.2%	–	–	–
p_{T} resolution	0.0–0.2%	0.0–1.4%	0.0–0.7%	0.0–2.7%	0.0–0.4%
Interaction rate	–	0.0%	–	–	1.0%
Material budget	0.1–0.9%	0.1–0.9%	0.1–0.9%	0.1–0.9%	0.1–0.9%
Acceptance	–	–	0.0–0.2%	–	–
Combined Uncertainty	3.9–6.8%	1.5–4.4%	1.7–4.5%	2.6–4.6%	1.4–5.2%
Normalization	1.9%	2.3%	3.1%	–	–
Centrality	–	–	–	0.1–3.6%	0.1–3.5%

Table 6.3 Contributions to the relative systematic uncertainty for p_{T} spectra in pp, p–Pb, and Pb–Pb collisions [28]. The ranges correspond to the maximal variation within the measured p_{T} range of 0.15–50 GeV/c, as well as Pb–Pb centrality intervals. The p_{T}-dependent contributions are assumed to be independent and are summed in quadrature, resulting in the combined uncertainty.

reduced systematic uncertainties by a factor of about 2 as compared to previously published results [16–18, 21].

6.2 p_{T} Spectra in pp Collisions at $\sqrt{s} = 0.9$, 2.76 and 7 TeV

The transverse momentum spectra measured by ALICE in pp collisions at $\sqrt{s} = 0.9$, 2.76 and 7 TeV [18] are presented in this section. The measurement was performed in the pseudorapidity range $|\eta| < 0.8$ for particles with $p_{\mathrm{T}} > 0.15$ GeV/c. The measured spectra were used to construct reference pp spectra for comparison with Pb–Pb spectra at $\sqrt{s_{\mathrm{NN}}} = 2.76$ TeV [17] and p–Pb spectrum at $\sqrt{s_{\mathrm{NN}}} = 5.02$ TeV [16, 21].

In total 6.8×10^6, 65×10^6 and 150×10^6 pp events at $\sqrt{s} = 0.9$, 2.76 and 7 TeV, which fulfill the $\mathrm{MB_{OR}}$ trigger and offline selection criteria, were selected for analysis. The differential cross section for inelastic pp collisions as a function of p_{T} is shown in Fig. 6.4 for the three measured collision energies. The spectral shape shows a clear evolution at high p_{T} with collision energy from 0.9 to 7 TeV. The total p_{T}-dependent systematic uncertainties, showed in the bottom panel of Fig. 6.4, demonstrate the accuracy of the measurements for all energies over the full p_{T} range. The corresponding normalization uncertainties amount to $+5.1/-4.0\%$, $\pm 1.9\%$ and $\pm 3.6\%$.

The p_{T} spectra are compared to NLO pQCD calculations [378] for $p_{\mathrm{T}} > 3$ GeV/c which are based on collinear factorization and use the CTEQ6.6M PDFs [379] and the DSS FFs

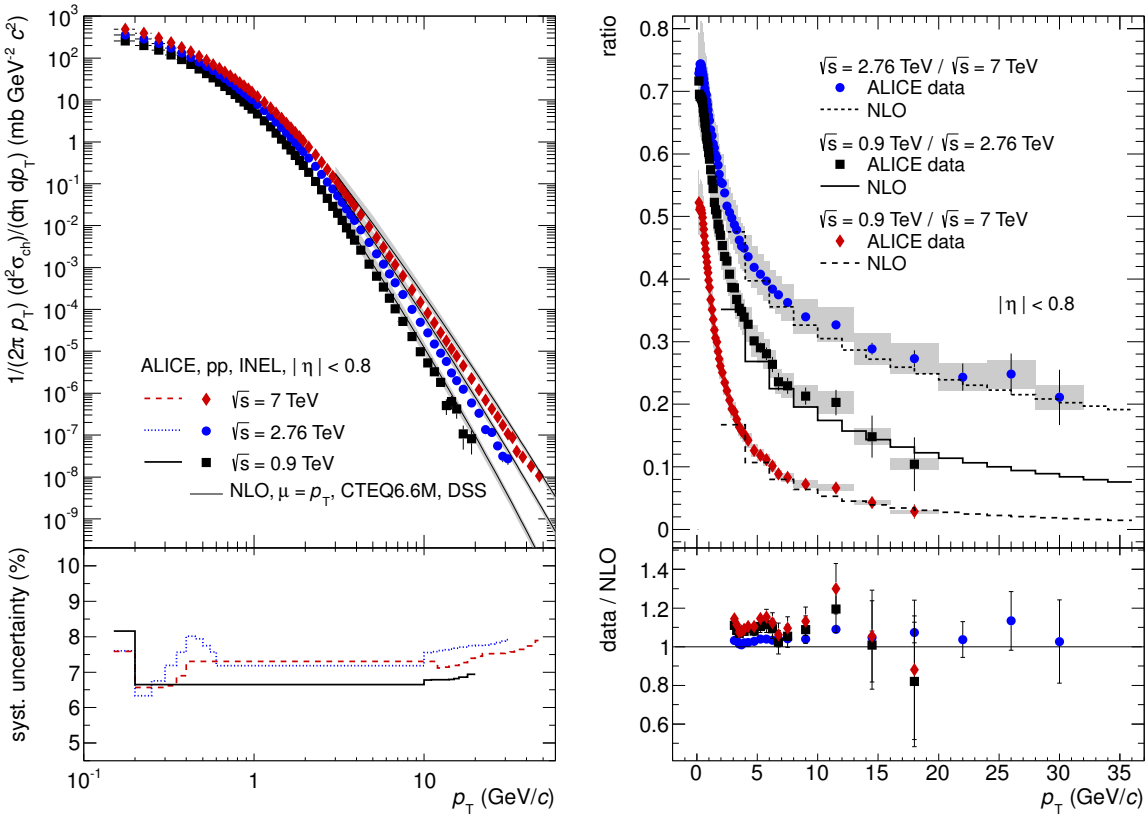

Fig. 6.4 Left: Differential cross section of charged particles in inelastic pp collisions at $\sqrt{s} = 0.9$, 2.76 and 7 TeV as a function of p_{T} compared to a NLO-pQCD calculation at the same energy [378]. Only statistical uncertainties are shown. The relative p_{T} dependent systematic uncertainties on the spectra are shown in the bottom panel. Right: Ratio of differential cross sections of charged particles in INEL pp collisions at different collision energies as a function of p_{T}. Grey boxes denote p_{T} dependent systematic uncertainties. Normalization uncertainties are not shown. The histograms show the same ratio determined from NLO calculations. In the bottom panel, the ratio of data and NLO derived from upper panel is shown. A variation of the scale of the NLO gives a systematic uncertainty on the double ratio of 0.5–23.6% (0.9 TeV / 2.76 TeV), 1.0–37.8% (0.9 TeV / 7 TeV) and 2.4–12.3% (2.76 TeV / 7 TeV). Both figures are taken from Ref. [18].

[380, 381], with the factorization, renormalization and fragmentation scales $\mu_{\mathrm{f}} = \mu_{\mathrm{r}} = \mu_{\mathrm{f}'} = \mu = p_{\mathrm{T}}$. The calculations show similar evolution of the high-p_{T} dependence with $\sqrt{s}$ but overpredict data by a factor of about two (see discussion in Sec. 3.1.2). Similar observations have been reported for measurements of neutral mesons by ALICE [212] and charged hadrons by CMS [382].

The grey bands show the theoretical uncertainty on the NLO calculations corresponding to $\mu = 2p_{\mathrm{T}}$ and $\mu = p_{\mathrm{T}}/2$. The scale uncertainties decrease with collision energy and p_{T}

to 20–30% at $\sqrt{s_{\mathrm{NN}}}$ = 7 TeV. The systematic uncertainties of the PDFs and FFs determined from the fits to the data are much smaller compared to the scale uncertainties and are not shown. Better agreement between data and calculations is observed for $\mu = 2p_{\mathrm{T}}$ indicating that the involved partonic energy scale of the jet is larger than p_{T} of the measured particle. The poor description of the data with NLO-pQCD has been attributed to the gluon-to-hadron fragmentation function, as discussed in Sec. 3.1.2.

Though the differential p_{T} cross section at a given $\sqrt{s}$ is not well described by the NLO pQCD calculations, the relative dependence on p_{T} of the cross sections measured at two different collision energies is described much better. Figure 6.4 (right) shows the ratio of differential cross sections of charged particles in INEL pp collisions at different collision energies as a function of p_{T}. For comparison, the same ratios are shown for NLO pQCD calculations. The total p_{T}-dependent systematic uncertainties on the ratios (show as grey boxes) were evaluated taking into account correlated contributions and amount to 8.1–9.8%, 7.8–9.8% and 7.9–9.9% for 0.9 TeV / 2.76 TeV, 0.9 TeV / 7 TeV and 2.76 TeV / 7 TeV, respectively. The corresponding normalization uncertainties amount to $+5\%/-4.4\%$, $+6.2\%/-5.4\%$ and $\pm 4.1\%$, which were obtained assuming that the contributions from the individual spectra are uncorrelated. The variation of the renormalisation, factorization and fragmentation scale in the NLO pQCD calculations ($\mu = p_{\mathrm{T}}/2 - 2p_{\mathrm{T}}$) results in systematic uncertainty on the double ratio of 0.5–23.6% for 0.9 TeV / 2.76 TeV, 1.0–37.8% for 0.9 TeV / 7 TeV and 2.4–12.3% for 2.76 TeV / 7 TeV. For all three ratios the good agreement between data and NLO calculations is found, as shown in the lower panel of Fig. 6.4 (right). This observation was used for construction of reference pp spectra to determine nuclear modification factors.

6.3 Reference pp Spectra

The comparison of the particle production in p–Pb and Pb–Pb to pp in terms of the nuclear modification factors requires reference spectrum in pp at the same collision energy. For the first measurement of nuclear modification factors R_{AA} in ALICE [15] no measurement of pp at the same collision energy was available, and pp-reference spectrum was obtained using power-law interpolation between the invariant yields measured at $\sqrt{s} = 0.9$ and 7 TeV. To account for the uncertainty of the method the alternative pp references were determined for $p_{\mathrm{T}} > 6.5$ GeV/c [15], resulting in the large systematic uncertainties on the R_{AA} from -15% to $+50\%$ for $6.5 < p_{\mathrm{T}} < 20$ GeV/c. In the following publication of R_{AA} [17] and R_{pPb} [16, 21] the pp references were constructed based on the p_{T} differential cross sections measured in pp collisions at $\sqrt{s} = 0.9$, 2.76 and 7 TeV [18]. The details of the pp-reference construction at $\sqrt{s} = 2.76$ TeV and 5.02 TeV [18] are briefly described in the following sections.

6.3.1 Reference pp Spectrum at $\sqrt{s} = 2.76$ TeV

The statistics in measurement of pp reference at $\sqrt{s} = 2.76$ TeV spectra allows to reach $p_{\mathrm{T}} = 32$ GeV/c, as shown in Fig. 6.4 [18]. In order to measure the R_{AA} up to $p_{\mathrm{T}} = 50$ GeV/c, the extrapolation procedure was applied. The p_{T} spectrum was parametrized for $p_{\mathrm{T}} > 5$ GeV/c (Fig. 6.5) by so-called modified Hagedorn function [377],

$$\frac{1}{2\pi p_{\mathrm{T}}} \frac{\mathrm{d}^2\sigma_{ch}^{pp}}{\mathrm{d}\eta\,\mathrm{d}p_{\mathrm{T}}} = A \frac{p_{\mathrm{T}}}{m_{\mathrm{T}}} \left(1 + \frac{p_{\mathrm{T}}}{p_{\mathrm{T},0}}\right), \tag{6.7}$$

where $m_{\mathrm{T}} = \sqrt{p_{\mathrm{T}}^2 + m_0^2}$ denotes the transverse mass with pion mass m_0 assumed for all particle tracks. For $p_{\mathrm{T}} > 32$ GeV/c, the obtained parametrization was used for extrapolation. The resulting pp reference at $\sqrt{s} = 2.76$ TeV includes data points for $0.15 < p_{\mathrm{T}} < 5$ GeV/c, parametrization for $5 < p_{\mathrm{T}} < 32$ GeV/c, and extrapolation for $32 < p_{\mathrm{T}} < 50$ GeV/c. The bottom panel of Fig. 6.5 shows the quality of the parametrization and p_{T}-dependent systematic uncertainties on the p_{T} spectrum and pp reference. The systematic uncertainties on the pp reference include variation of the lower boundary of the fit range ($3 < p_{\mathrm{T}} < 32$ GeV/c, $7 < p_{\mathrm{T}} < 32$ GeV/c) of the modified Hagedorn function. The statistical and systematic uncertainties from the spectrum are propagated to the parametrization and extrapolation. Statistical uncertainties in the extrapolated part of the reference are obtained from the covariance matrix of the parametrization. The systematic uncertainties on the spectrum are propagated to the reference by application of the full extrapolation procedure using the measured data points shifted up and down by the total systematic uncertainty. The total p_{T}-dependent systematic uncertainties on the pp reference span from 6.4% to 19% (Fig. 6.5, bottom panel) in the measured p_{T} range.

Figure 6.6 shows the comparison of the constructed pp reference at $\sqrt{s} = 2.76$ TeV with the alternative references [18]. All references agree within systematic uncertainties for $p_{\mathrm{T}} > 20$ GeV/c. The pp reference generated with PYTHIA8 agrees with the new pp reference for $p_{\mathrm{T}} > 15$ GeV/c. Below $p_{\mathrm{T}} = 20$ GeV/c, the PYTHIA8 spectrum shape is similar to the measured reference. The pp reference obtained by CMS [383] agrees the best for $p_{\mathrm{T}} < 6$ GeV/c. The overall normalization systematic uncertainties $\pm 1.5\%(\pm 6\%)$ for ALICE (CMS) are not included in the comparison. The pp reference determined using NLO scaling of the p_{T} spectrum measured in pp collisions at $\sqrt{s} = 7$ TeV, as shown in Fig. 6.4 (right),

$$\left.\frac{\mathrm{d}^2\sigma}{\mathrm{d}\eta\,\mathrm{d}p_{\mathrm{T}}}\right|_{2.76\text{ TeV}} = \left.\frac{\mathrm{d}^2\sigma}{\mathrm{d}\eta\,\mathrm{d}p_{\mathrm{T}}}\right|_{7\text{ TeV}} \cdot \frac{\left.\frac{\mathrm{d}^2\sigma}{\mathrm{d}\eta\,\mathrm{d}p_{\mathrm{T}}}\right|_{\text{NLO, 2.76 TeV}}}{\left.\frac{\mathrm{d}^2\sigma}{\mathrm{d}\eta\,\mathrm{d}p_{\mathrm{T}}}\right|_{\text{NLO, 7 TeV}}}, \tag{6.8}$$

is in agreement with the new reference in the p_{T} range 3–50 GeV/c (lower limit is determined by the NLO calculations). The pp reference determined based on interpolation between 0.9 and 7 TeV spectra [15] disagrees with the constructed reference for $p_{\mathrm{T}} > 6$ GeV/c.

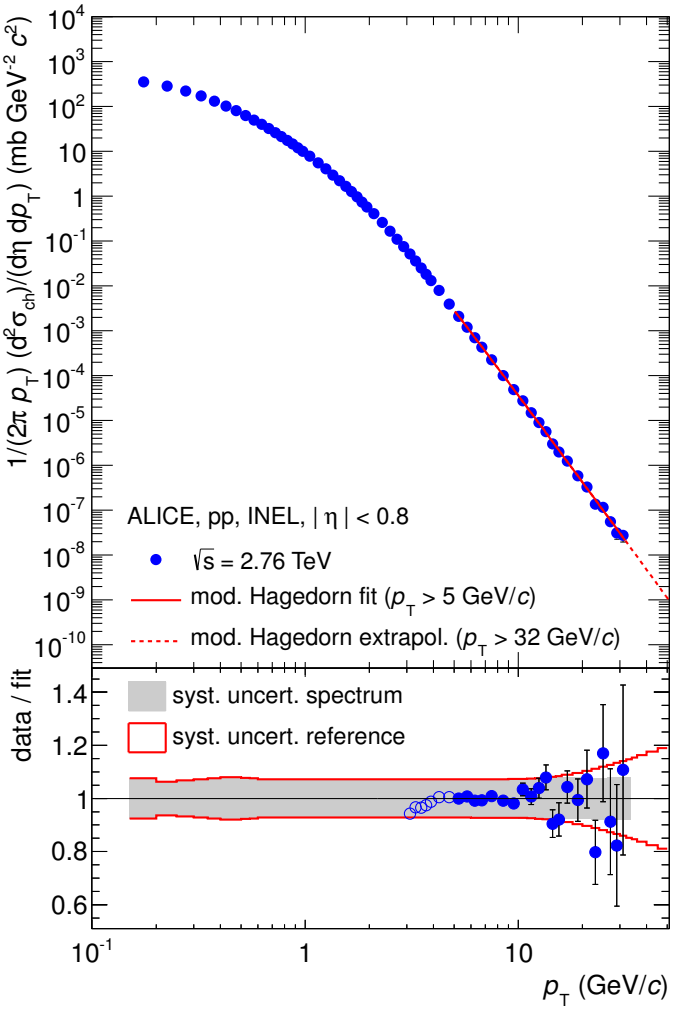

Fig. 6.5 Differential cross section of charged particles in INEL pp collisions at $\sqrt{s} = 2.76$ TeV as a function of p_{T} [18], together with the parametrization for $p_{\mathrm{T}} > 5$ GeV/c and the extrapolation for $p_{\mathrm{T}} > 32$ GeV/c with modified Hagedorn function [377]. In the bottom panel, the data to fit ratio is shown (solid circles).The open circles show comparison to the parametrization extrapolated towards lower p_{T}. The systematic uncertainties on the data points and on the pp reference spectrum are denoted with a gray band and solid red lines, respectively. The overall normalization systematic uncertainties $\pm 1.9\%$ is not shown.

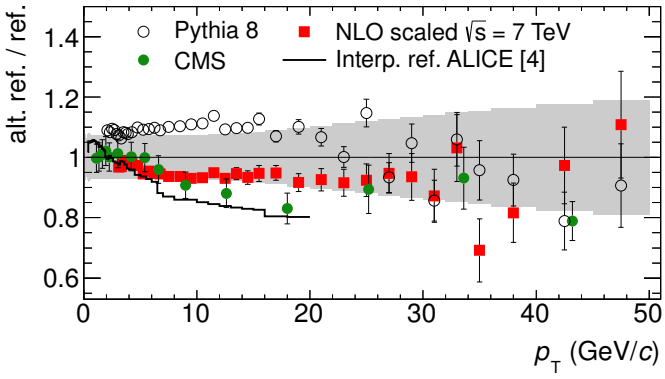

Fig. 6.6 Ratio of alternative references to the constructed pp reference at $\sqrt{s} = 2.76$ TeV [18]. The grey band indicates the total p_T dependent systematic uncertainty. The overall normalization systematic uncertainties $\pm 1.9\%$ ($\pm 6\%$) for ALICE (CMS [383]) are not shown.

6.3.2 Reference pp Spectrum at $\sqrt{s} = 5.02$ TeV

In order to measure the nuclear modification factors in p–Pb collisions at $\sqrt{s_{\rm NN}} = 5.02$ TeV [16, 21] the pp reference at the same energy was needed. However, no measurements in pp collisions at this energy was available at that time. Therefore, the pp reference was constructed using differential cross sections measured in pp collisions at $\sqrt{s} = 2.76$ and 7 TeV collisions [18]. Three methods were combined to obtain the pp reference at $\sqrt{s_{\rm NN}}$ = 5.02 TeV, which are listed below.

- For low transverse momenta, $0.15 < p_{\rm T} < 5$ GeV/c, the interpolation between cross sections measured at $\sqrt{s} = 2.76$ TeV and 7 TeV for a given $p_{\rm T}$ was performed, assuming power-law dependence of the cross section on the $\sqrt{s}$. Here, the maximum systematic uncertainty from the underlying spectra has been assigned for the pp reference.
- For $5 < p_{\rm T} < 50$ GeV/c, the differential cross section at $\sqrt{s} = 7$ TeV was scaled to $\sqrt{s} = 5.02$ TeV using the NLO-pQCD calculations (Eq. 6.8). Systematic uncertainties on the pp reference include systematic uncertainties from the pp spectra, difference to the interpolated pp reference, and maximum difference to the scaled references determined for the alternative scales, $\mu = p_{\rm T}/2$ and $\mu = 2p_{\rm T}$.
- For $20 < p_{\rm T} < 50$, the NLO-scaled $p_{\rm T}$ spectrum was parametrized with the power-law function to be used as reference. The statistical and systematic uncertainties from the spectrum were propagated to the parametrization using the same procedure as described in Sec. **??**. Here, the lower boundary of the fit for the systematic uncertainty determination were varied between 15–25 GeV/c.

Such procedure was applied for pp reference determined in $|\eta_{\rm cms}| < 0.3$ [16]. Here, the parametrization at high $p_{\rm T}$ was used starting already from 5 GeV/c. For the $R_{\rm pPb}$ measure-

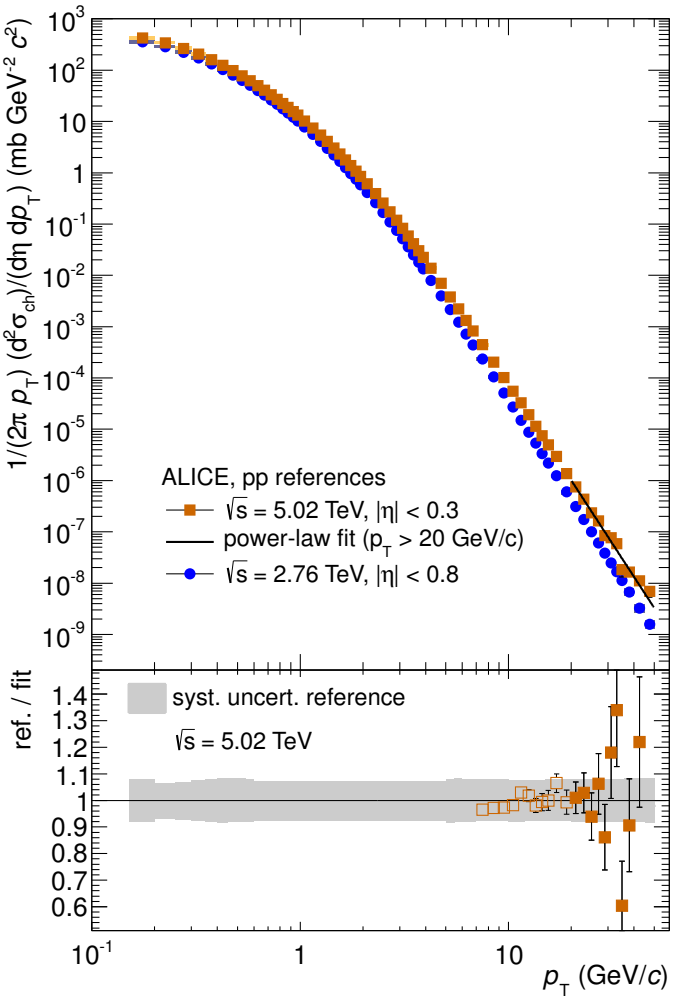

Fig. 6.7 Top: Constructed pp references for $\sqrt{s}$ = 2.76 and $\sqrt{s}$ = 5.02 TeV [18]. Bottom: Comparison of NLO-scaled reference at $\sqrt{s}$ = 5.02 TeV to parametrization. The parametrization is used for $p_{\mathrm{T}} > 20$ GeV/c. The open squares show comparison to the parametrization extrapolated towards lower p_{T}. The grey band indicates the total p_{T}-dependent systematic uncertainties. The normalization uncertainty ($\pm 3.6\%$) is not shown.

ments with 2013 p–Pb data [21] the pp reference was determined in $|\eta_{\mathrm{cms}}| < 0.8$ using interpolation for $p_{\mathrm{T}} < 5$ GeV/c and NLO-scaled spectrum for higher p_{T}.

The total p_{T}-dependent systematic uncertainty on the pp references measured in the $|\eta_{\mathrm{cms}}| < 0.3$ and $|\eta_{\mathrm{cms}}| < 0.8$, ranges between 7.7–8.2% and 6.8–8.2%, respectively. The normalization uncertainty on the pp reference ($\pm 3.6\%$) is propagated from the p_{T} spectrum measured at $\sqrt{s} = 7$ TeV. The constructed pp reference at $\sqrt{s} = 5.02$ TeV for the $|\eta_{\mathrm{cms}}| < 0.3$ is shown in Fig. 6.7 together with the pp reference at $\sqrt{s} = 2.76$ TeV [18] discussed above. The

p_{T} spectrum at $\sqrt{s} = 5.02$ TeV is shown with power-law parametrization for $p_{\mathrm{T}} > 20$ GeV/c. In the bottom panel, a comparison of the NLO-scaled reference and the parametrization is shown.

6.4 p_{T} Spectra in p–Pb Collisions at $\sqrt{s_{\mathrm{NN}}} = 5.02$ TeV

The p_{T} spectra of charged particles in p–Pb collisions at $\sqrt{s_{\mathrm{NN}}} = 5.02$ TeV at the LHC has been presented for the first time by ALICE [16]. These data were recorded during a short LHC p–Pb run in September 2012, in preparation for the main run scheduled at the beginning of 2013. The number of p–Pb events used for the analysis amounts to 1.7×10^6. The p_{T} spectra were measured in three pseudorapidity intervals $|\eta_{\mathrm{cms}}| < 0.3$, $0.3 < \eta_{\mathrm{cms}} < 0.8$ and $0.8 < \eta_{\mathrm{cms}} < 1.3$, for p_{T} in the range 0.5–20 GeV/c. In this analysis, the p_{T} threshold was set to 0.5 GeV/c to reduce systematic uncertainties related to rapidity shift (see Sec. 6.1.3.5 for details), which are sizable only at low p_{T}. For $p_{\mathrm{T}} = 0.5$ GeV/c they reach 0.6% for $|\eta_{\mathrm{cms}}| < 0.3$, 4.3% for $0.3 < \eta_{\mathrm{cms}} < 0.8$ and 5.1% for $0.8 < \eta_{\mathrm{cms}} < 1.3$. The total systematic uncertainties exhibit a weak p_{T} and η_{cms} dependence and range between 5.2% and 5.5% for $|\eta_{\mathrm{cms}}| < 0.3$, and between 5.6% and 7.1% for $0.8 < \eta_{\mathrm{cms}} < 1.3$. The normalization uncertainty amounts to 3.1% [309].

The p_{T} spectra measured in non-single diffractive p–Pb collisions at $\sqrt{s_{\mathrm{NN}}} = 5.02$ TeV for the three pseudorapidity intervals are shown in Fig. 6.8 (left) [16] together with the constructed pp references spectrum, scaled by the nuclear overlap function $\langle T_{\mathrm{pPb}} \rangle = \langle N_{\mathrm{coll}} \rangle / \sigma_{\mathrm{NN}} = 0.0983 \pm 0.0035$ mb^{-1}, with $\langle N_{\mathrm{coll}} \rangle = 6.9 \pm 0.7$ and $\sigma_{\mathrm{NN}} = 70 \pm 5$ mb. $\langle N_{\mathrm{coll}} \rangle$ was calculated for the minimum-bias p–Pb collisions (no centrality selection) with the Glauber model (see Ref. [309] for details). The measured p_{T} spectra show a weak pseudorapidity dependence, as demonstrated in the bottom panel of the figure. At high p_{T}, the p_{T} distributions in p–Pb collisions are similar to that in pp collisions.

The high statistics of p–Pb collisions at $\sqrt{s_{\mathrm{NN}}} = 5.02$ TeV was collected by ALICE in 2013. The p_{T} spectra based on the 60 times larger data sample (106×10^6) than in previous analysis [16] has been reported in Ref. [21]. These data allow for a significant extension of the transverse momentum range up to 50 GeV/c, as shown in Fig. 6.8 (right).

The p_{T} spectra are presented in three pseudorapidity intervals (note the opposite η_{cms} sign convention in Ref. [309][1]) for $0.15 < p_{\mathrm{T}} < 50$ GeV/c. For comparison, the pp reference determined in the broad pseudorapidity range $|\eta_{\mathrm{cms}}| < 0.8$, scaled by the $\langle T_{\mathrm{pPb}} \rangle = 0.0983 \pm 0.0035$ mb^{-1} [309], is also shown. The total p_{T}-dependent systematic uncertainties are function of η_{cms} and range between 3.4% and 6.7% in the measured p_{T} range, while the normalization uncertainty amounts to 3.1%.

[1] The sign convention was changed such that in the p–Pb collisions the proton beam goes towards negative η. It is a common LHC convention.

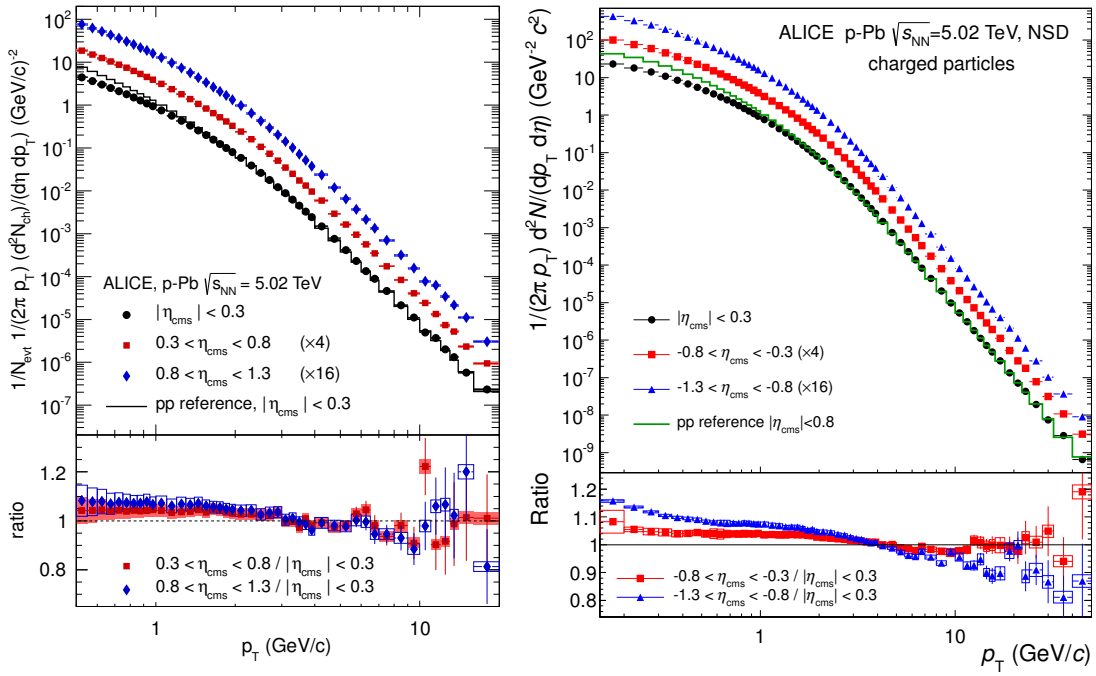

Fig. 6.8 Transverse momentum distributions of charged particles in NSD p–Pb collisions for different pseudorapidity ranges measured by ALICE in 2012 [16] (left) and in 2013 [21] (right). For better visibility, the spectra are scaled by the indicated factors. The histogram represents the reference spectrum in pp collisions scaled by the nuclear overlap function $\langle T_{\mathrm{pPb}} \rangle = 0.0983 \pm 0.0035$ mb^{-1} determined for the minimum-bias (no centrality selection) p–Pb collisions. The lower panels show the ratios of the spectra at backward pseudorapidities to that at $|\eta_{\mathrm{cms}}| < 0.3$. The boxes represent the p_{T}-dependent systematic uncertainites. The normalization uncertainty of the spectra ($\pm 3.1\%$) is not shown. Note the different sign convention for positive/negative pseudorapidity for the two measurements.

The ratios of the spectra for backward pseudorapidity ranges ($-0.8 < \eta_{\mathrm{cms}} < -0.3$ and $-1.3 < \eta_{\mathrm{cms}} < -0.8$) to that at $-0.3 < \eta_{\mathrm{cms}} < -0.3$ are shown in bottom panels of Figure 6.8. The shape of the p_{T} spectra changes when going from central to backward (Pb-side) pseudorapidity. It confirmed the previous observations for data collected in the 2012 pilot-run [16] with better significance and extended p_{T} range.

ALICE has also measured p–Pb spectra of charged particles as a function of collision centrality [22], as shown in Fig. 6.9. The measurement was performed for seven centrality classes in the central pseudorapidity $|\eta| < 0.3$ and $0.15 < p_{\mathrm{T}} < 30$ GeV/c, with $\sim 106 \times 10^6$ events. The centrality selection (see Sec. 2.5.2 for details) was based on information from the neutron ZDC (ZN) located on the Pb-remnant side (A-side in the ALICE coordinate system). The systematic p_{T}-dependent systematic uncertainties are independent of collision centrality and range between 3.4% and 5.8%, as shown in the bottom panel. The normalization uncertainty

is around 3.1% as for minimum-bias measurements. It is visible that the spectral shape at high p_{T} is independent of collision centrality and can be described by the power-law.

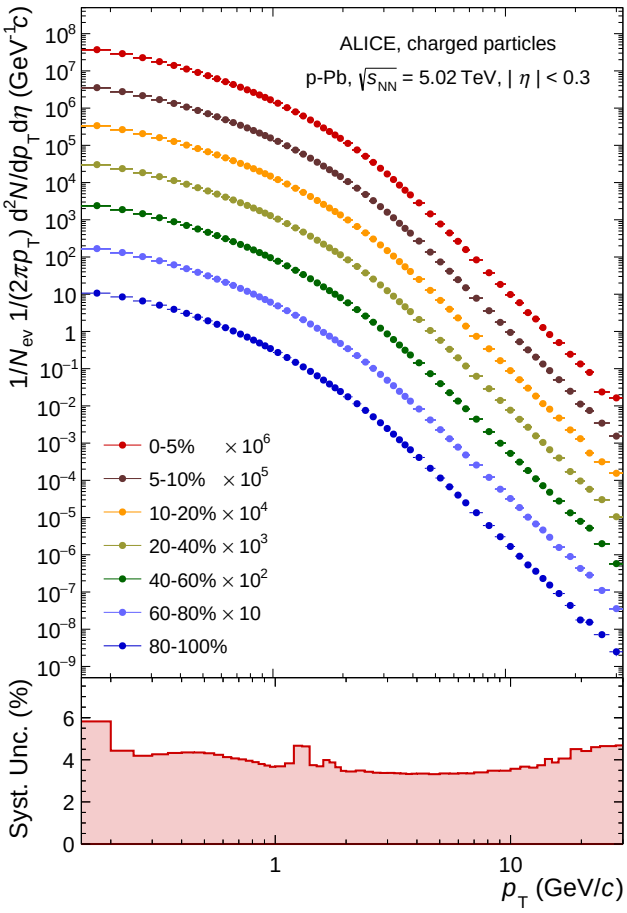

Fig. 6.9 The p_{T} spectra of charged primary particles measured in p–Pb collisions at $\sqrt{s_{\mathrm{NN}}} = 5.02$ TeV as a function of collision centrality [22]. For better visibility, spectra are scaled by indicated factors. The p_{T}-dependent systematic uncertainties, independent of collision centrality, are shown in the bottom panel. The normalization uncertainty of the spectra ($\pm 3.1\%$) is not shown.

6.5 p_{T} Spectra in Pb–Pb Collisions at $\sqrt{s_{\mathrm{NN}}} = 2.76$ TeV

The p_{T} spectra of charged particles in Pb–Pb collisions at $\sqrt{s_{\mathrm{NN}}} = 2.76$ TeV at the LHC has been reported for the first time by ALICE in Ref. [15]. This analysis was based on the 2.3×10^6 events collected in 2010, which passed the minimum-bias trigger and offline selection criteria (see Sec 6.1.1 for details). The spectra were determined for central 0–5% and peripheral 70–80% Pb–Pb collisions in the central pseudorapidity $|\eta| < 0.8$ and $0.3 < p_{\mathrm{T}} < 20$ GeV/c (Fig. 6.10, left), with the p_{T}-dependent systematic uncertainties in the range 5–7% and 8–10%, respectively.

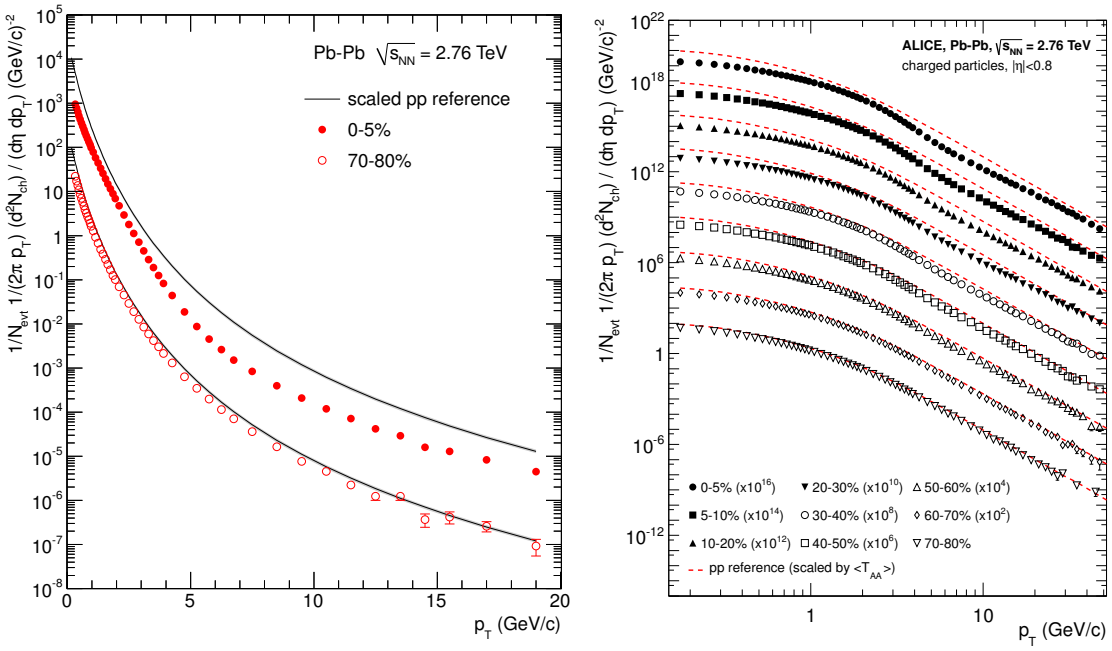

Fig. 6.10 The invariant yields of charged particles measured in Pb–Pb collisions at $\sqrt{s_{\mathrm{NN}}} = 2.76$ TeV for two (left panel) [15] and nine (right panel) [17] centrality intervals. The solid/dashed lines show the pp reference spectra [15, 18] scaled by the nuclear overlap function determined for each centrality interval and by the Pb–Pb spectra scaling factors (right panel). In the left panel, the error bars indicate statistical uncertainties, while the systematic uncertainties are smaller than the symbols. The systematic uncertainties of the pp reference spectra are contained within the thickness of the lines and statistical uncertainties are not shown. In the right panel, the p_{T}-dependent systematic and statistical uncertainties for Pb–Pb are added in quadrature. The uncertainties on the pp reference spectra are not shown.

This measurement was later extended by ALICE [17] by adding more Pb–Pb data samples ($\sim 1.6 \times 10^7$ events). The p_{T} spectra were determined in nine centrality intervals and in the kinematic range $|\eta| < 0.8$ and $0.15 < p_{\mathrm{T}} < 50$ GeV/c (Fig. 6.10, right). The total systematic uncertainties on the corrected p_{T} spectra depend on p_{T} and event centrality and amount to

collision system	$\sqrt{s_{\mathrm{NN}}} = 2.76$ TeV	$\sqrt{s_{\mathrm{NN}}} = 5.02$ TeV
pp	52×10^6	109×10^6
p–Pb	-	107×10^6
Pb–Pb (0–80%)	13×10^6	20×10^6

Table 6.4 Number of events used in the analysis for various systems and energies. The analysis of Pb–Pb events was performed for the 0–80% centrality range.

8.2–13.5% (10.3–13.4%) in the most central (peripheral) collisions. For better visibility, the p_{T} spectra in Pb–Pb are scaled by factors indicated in the figure. The pp-reference spectra scaled by the nuclear overlap functions and by the Pb–Pb spectra scaling factors are also shown for comparison. At low p_{T}, Pb–Pb spectra differ from the pp reference which is in agreement with the previously observed scaling behavior of the charged particle production as a function of centrality [301, 302, 384] (see also Sec. 5.1 for discussion). The shape of the Pb–Pb p_{T} spectra changes with collisions centrality with marked depletion at high p_{T} around 5 GeV/c, indicating a strong suppression of charged-particle production.

6.6 p_{T} Spectra in pp and Pb–Pb Collisions at $\sqrt{s_{\mathrm{NN}}} = 5.02$ TeV

The measurement of p_{T} spectra of primary charged particles in pp and Pb–Pb collisions at $\sqrt{s_{\mathrm{NN}}} = 5.02$ TeV and p_{T} spectra obtained from the reanalysis of pp and Pb–Pb data at $\sqrt{s}$ = 2.76 TeV and p–Pb data at $\sqrt{s_{\mathrm{NN}}} = 5.02$ TeV [28] are presented in this section. The number of events satisfying the trigger and offline selection criteria for various collision systems and energies are listed in Table 6.4. The measurement was performed in the kinematic range $|\eta| < 0.8$ and $0.15 < p_{\mathrm{T}} < 50$ GeV/c. All contributions to the systematic uncertainties on the p_{T} spectra obtained in this analysis are listed in Table 6.3.

Figure 6.11 shows the fully corrected p_{T} spectra of primary charged particles measured in pp and Pb–Pb collisions at $\sqrt{s_{\mathrm{NN}}} = 2.76$ TeV (left) and in pp, p–Pb and Pb–Pb collisions at $\sqrt{s_{\mathrm{NN}}} = 5.02$ (right). The Pb–Pb spectra are presented in nine centrality classes. For pp collisions, the p_{T}-differential cross sections are divided by the corresponding inelastic nucleon-nucleon cross section at $\sqrt{s} = 2.76$ (61.8 mb) and 5.02 TeV (67.6 mb) [385], respectively. The relative systematic uncertainties for the various datasets are shown in the bottom panels. Substantial improvements in track selection and efficiency corrections have been achieved as compared to previous analyses [16–18, 21]. However the uncertainties on the pp spectra at $\sqrt{s_{\mathrm{NN}}} = 2.76$ TeV are still larger than those for the other data sets due to larger number of inactive channels in the SPD [144], which affects the primary track reconstruction. In Pb–Pb collisions, the shape of the p_{T} spectrum varies strongly with collision centrality. For peripheral collisions, the spectral shape is similar to that measured in pp and p–Pb collisions. With increasing collision centrality, a marked depletion of the Pb–Pb spectra develops for $p_{\mathrm{T}} > 5$ GeV/c.

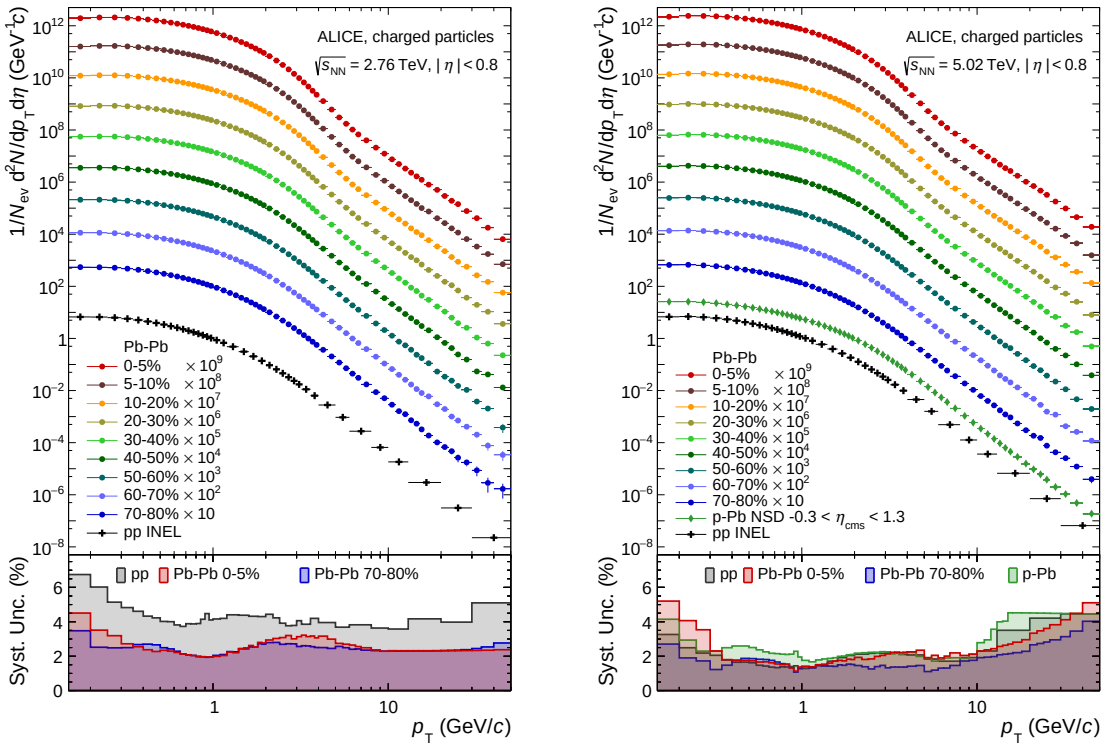

Fig. 6.11 Transverse momentum distributions of primary charged particles measured in $|\eta| < 0.8$ and in nine centrality intervals in Pb–Pb collisions at $\sqrt{s_{\mathrm{NN}}} = 2.76$ (left) and 5.02 TeV (right) [28]. For better visibility, the spectra are scaled by the indicated factors. The spectra in pp collisions, obtained scaling the cross section by $\sigma_{\mathrm{inel}}^{\mathrm{NN}}$, and in NSD p–Pb collisions at $\sqrt{s_{\mathrm{NN}}} = 5.02$ TeV are also shown. The relative p_{T}-dependent systematic uncertainties are shown in the bottom panels for various datasets (they do not contain the normalization uncertainties).

Figure 6.12 shows the ratios of p_{T} spectra measured at $\sqrt{s_{\mathrm{NN}}} = 5.02$ TeV and $\sqrt{s_{\mathrm{NN}}} = 2.76$ TeV in Pb–Pb and pp collisions. The ratios for Pb–Pb collisions are determined in nine centrality classes ranging from 0–5% (top-left) to the 70–80% (bottom-right). As indicated by the ratios, the p_{T} spectra measured at higher collision energy are significantly harder for both Pb–Pb and pp collision systems. One can see that there is a similar energy dependence of the ratio for peripheral (70–80%) Pb–Pb and in pp collisions, while towards central Pb–Pb collisions a gradual reduction of the ratio is apparent.

The reanalysis of the p_{T} spectra in pp and Pb–Pb collisions at $\sqrt{s} = 2.76$ TeV and p–Pb collisions at $\sqrt{s_{\mathrm{NN}}} = 5.02$ TeV using improved track selection and efficiency correction procedure leads to the p_{T} spectra which differs as compared to those obtained in previous analyses. The differences depends on collision system, collision centrality and momentum, and reach

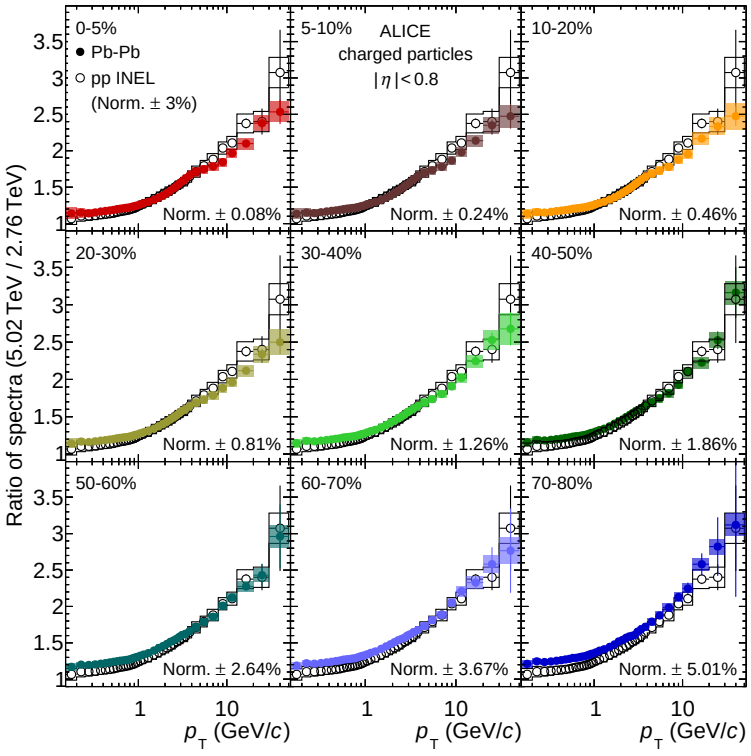

Fig. 6.12 Ratio of transverse momentum spectra at $\sqrt{s_{\mathrm{NN}}}$ = 5.02 and $\sqrt{s_{\mathrm{NN}}}$ = 2.76 TeV for Pb–Pb collisions, for nine centrality classes, and for pp collisions (repeated in each panel) [28]. The relative normalization uncertainties due to the centrality determination are indicated for each centrality class. For the pp spectrum, the relative normalization uncertainty is ±3%.

up to 10% for pp, 7% for p–Pb and 15% for the most central (0–5%) Pb–Pb collisions in the intermediate p_{T} range 2–3 GeV$/c$. The largest contribution to the differences arises from the efficiency reweighting procedure, as shown in Fig. 6.1.

Chapter 7
Measurement of p_{T} Spectra of $\pi^{\pm}$, $\mathrm{K}^{\pm}$ and p($\bar{\mathrm{p}}$) in pp, p–Pb and Pb–Pb Collisions

ALICE has an excellent particle identification capabilities for most of hadrons with momenta up to p_{T} = 20 GeV/c [144]. Author has contributed to the measurements of high-p_{T} spectra of charged pions, kaons and (anti)protons in pp, p–Pb and Pb–Pb collisions [23, 24, 27]. The analysis details and resulting p_{T} spectra are presented in this chapter. The obtained results are based on the data collected by ALICE in 2010–2013.

The measurement of charged pions, kaons and (anti)protons ($\pi^{\pm}$, $\mathrm{K}^{\pm}$, p, $\bar{\mathrm{p}}$) spectra has been performed with the ALICE central barrel. The identification of $\pi^{\pm}$, $\mathrm{K}^{\pm}$ and p($\bar{\mathrm{p}}$) was based on the information from different particle identification (PID) detectors, as listed in Table 7.1 [24]. From the lowest to the highest p_{T}, the results were obtained using the specific energy loss (dE/dx) in the ITS and TPC detectors, the time-of-flight measured by the TOF, the Cherenkov angle measured by the HMPID, and the TPC dE/dx in the relativistic rise region.

system	ITS+TPC+TOF	HMPID	TPC dE/dx rel. rise
$\pi^{\pm}$	0.1–3.0	1.5–4.0	2.0–20.0
$\mathrm{K}^{\pm}$	0.2–3.0	1.5–4.0	3.0–20.0
p($\bar{\mathrm{p}}$)	0.3–4.6	1.5–6.0	3.0–20.0

Table 7.1 The p_{T} ranges used in the particle identification with the ALICE central barrel detectors [24].

The identification of $\pi^{\pm}$, $\mathrm{K}^{\pm}$ and p($\bar{\mathrm{p}}$) at low and intermediate momenta ($p_{\mathrm{T}} < 6.0$ GeV/c) is discussed in detail in Refs. [23, 27, 120, 144, 375, 386]. In this chapter, the focus is on the hadron identification at high p_{T} based on the TPC dE/dx in the relativistic rise region of the Bethe-Bloch (BB) curve.

7.1 Spectra Analysis at High p_{T}

For the charged pion, kaon and (anti)proton spectra analysis at high p_{T} [23, 24, 27], the event and track selection follows closely that of the inclusive charged particle analysis [17]. The same spectrum normalization is adopted so that the systematic uncertainties related to event and track selection are common, allowing a precise comparison between the nuclear modification factors for inclusive and identified charged hadrons. The charged particle identification at high p_{T} is based on the TPC $\mathrm{d}E/\mathrm{d}x$ in the relativistic rise regime of the Bethe-Bloch curve, where the $\langle \mathrm{d}E/\mathrm{d}x \rangle$ separation between particles with different masses is nearly constant, as shown in Fig. 7.1 [144]. It requires a precise knowledge of $\langle \mathrm{d}E/\mathrm{d}x \rangle$ and $\mathrm{d}E/\mathrm{d}x$ resolution (σ) for each particle species. The separation can be quantified by the separation power between two particle species (i,j) expressed in the number of standard deviations, where the absolute $\langle \mathrm{d}E/\mathrm{d}x \rangle$ difference is normalized to the arithmetic average of the resolutions,

$$S_{\sigma} = \frac{\langle \mathrm{d}E/\mathrm{d}x \rangle_{\mathrm{i}} - \langle \mathrm{d}E/\mathrm{d}x \rangle_{\mathrm{j}}}{0.5 \cdot (\sigma_i + \sigma_j)}. \tag{7.1}$$

The separation power between π–p, π–K and K–p determined as a function of momentum in 0–5% central Pb–Pb collisions is around $S_{\sigma} = 3$, 2 and 1 for $p > 5$ GeV/c, respectively, and is nearly constant at large momenta [24]. The S_{σ} increases with decreasing collision centrality by up to 30% in 60–80% peripheral Pb–Pb collisions. In pp and p–Pb collisions, the increase is $\sim 40\%$ (see Refs. [24, 27] for more details).

The analysis of the $\mathrm{d}E/\mathrm{d}x$ spectra is aimed at extracting the relative yields of $\pi^{\pm}$, $\mathrm{K}^{\pm}$ and p($\bar{\mathrm{p}}$), referred to as the particle fractions f_{id}, as a function of p_{T} and rapidity y. The invariant yields of identified hadrons are then obtained using the inclusive p_{T} spectra of charged particles, $\mathrm{d}^2N/\mathrm{d}p_{\mathrm{T}}\mathrm{d}\eta$ (see Chap. 6 for details), with the following formula

$$\frac{\mathrm{d}^2N_{\mathrm{id}}}{\mathrm{d}p_{\mathrm{T}}\mathrm{d}y} = \mathrm{J}_{\mathrm{id}} \cdot \frac{\varepsilon_{\mathrm{ch}}}{\varepsilon_{\mathrm{id}}} \cdot f_{\mathrm{id}} \cdot \frac{\mathrm{d}^2N}{\mathrm{d}p_{\mathrm{T}}\mathrm{d}\eta}, \tag{7.2}$$

where J_{id} is Jacobian correction (η to y) for a given hadron, and $\varepsilon_{\mathrm{ch}}$ and $\varepsilon_{\mathrm{id}}$ are reconstruction efficiencies for charged particles and for a given hadron, respectively. The determination of f_{id}, J_{id} and $\varepsilon_{\mathrm{ch}}/\varepsilon_{\mathrm{id}}$ is discussed in the following sections.

7.1.1 Particle Fractions at High p_{T}

Figure 7.2 shows of the $\mathrm{d}E/\mathrm{d}x$ obtained for Pb–Pb collisions at $\sqrt{s_{\mathrm{NN}}} = 2.76$ TeV in six centrality intervals, for particles with $8 < p < 9$ GeV/c and $|\eta| < 0.2$ [27]. The $\mathrm{d}E/\mathrm{d}x$ is normalized to the average energy loss $\langle \mathrm{d}E/\mathrm{d}x_{\mathrm{MIP}} \rangle$ of the minimum ionization particles with $0.4 < p < 0.55$ and $40 < \mathrm{d}E/\mathrm{d}x < 60$. The pion, kaon, and proton yields are extracted by fitting a sum of four Gaussian functions (including electrons) to the $\mathrm{d}E/\mathrm{d}x$ spectra. The muons

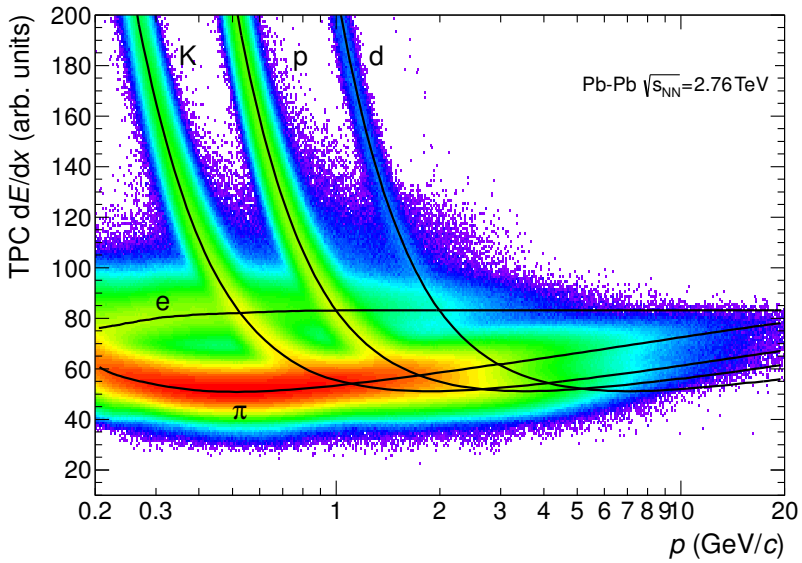

Fig. 7.1 Specific energy loss ($\mathrm{d}E/\mathrm{d}x$) in the TPC vs. particle momentum in Pb–Pb collisions at $\sqrt{s_{\mathrm{NN}}} = 2.76$ TeV [144]. The lines show the parameterizations of the expected mean energy loss $\langle \mathrm{d}E/\mathrm{d}x \rangle$.

from heavy-flavor decays are subtracted from the pions yields based on the measured electron yields while contribution from deuterons and tritons is negligible ($\ll 1\%$) in the considered momentum range.

In order to reduce number of degrees of freedom in the fit from 12 to 4, the parametrization of the Bethe-Bloch ($\langle \mathrm{d}E/\mathrm{d}x \rangle$) and $\mathrm{d}E/\mathrm{d}x$ resolution (σ) are extracted as a function of $\beta\gamma$ using identified particles. For each momentum interval, the extracted $\langle \mathrm{d}E/\mathrm{d}x \rangle$ and σ are used to fix the position and width of each Gaussian. The Bethe-Bloch curve is parameterized as follows [24]:

$$\left\langle \frac{\mathrm{d}E}{\mathrm{d}x} \right\rangle = a \cdot \left[\frac{1+(\beta\gamma)^2}{(\beta\gamma)^2} \right]^e + \frac{b}{c} \cdot \log \left[\frac{1+(\beta\gamma)^c}{1+\exp\left[c \cdot (a-d)/b\right] \cdot (1+\beta\gamma)^c} \right], \tag{7.3}$$

where a, b, c, d, and e are free parameters. The parameter d denotes the $\langle \mathrm{d}E/\mathrm{d}x \rangle$ in the Fermi-Plateau regime for $\beta\gamma > 1000$. The relative $\mathrm{d}E/\mathrm{d}x$ resolution, $\sigma/\langle \mathrm{d}E/\mathrm{d}x \rangle$, as a function of $\langle \mathrm{d}E/\mathrm{d}x \rangle$ is parametrized with the second order polynomial,

$$\sigma/\langle \mathrm{d}E/\mathrm{d}x \rangle = a_0 + a_1 \cdot \langle \mathrm{d}E/\mathrm{d}x \rangle + a_2 \cdot \langle \mathrm{d}E/\mathrm{d}x \rangle^2, \tag{7.4}$$

which was found to describe data well.

Due deterioration of the TPC $\mathrm{d}E/\mathrm{d}x$ performance with increasing multiplicity [144], the curves differ significantly and have to be extracted separately for pp, p–Pb and each Pb-Pb centrality class. The parameters a, b, d and e were determined using samples of identified particles: secondary pions ($30 < \beta\gamma < 60$) and protons ($3 < \beta\gamma < 7$) from K^0_{s} and Λ weak decays,

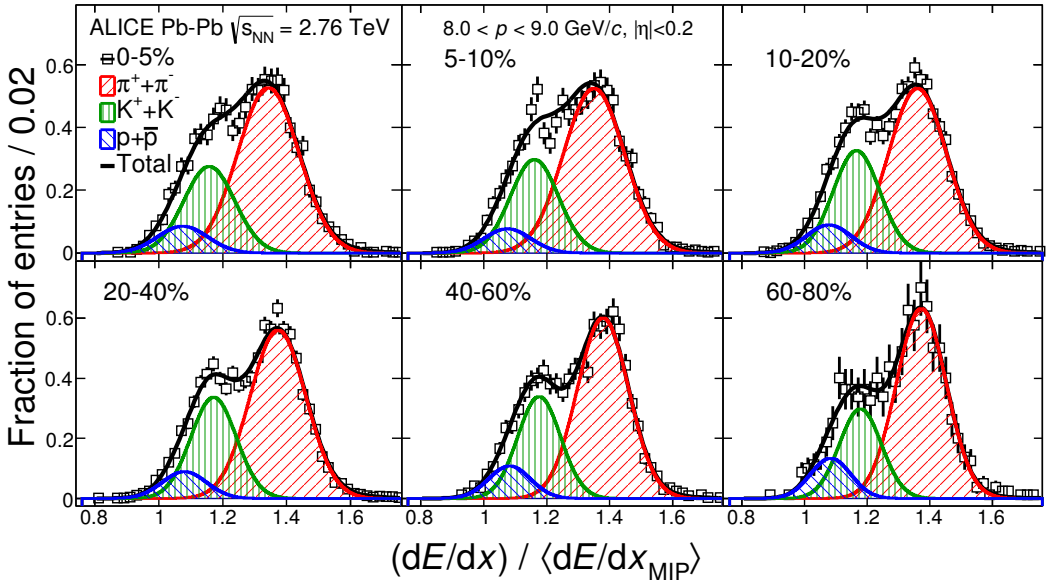

Fig. 7.2 TPC $\mathrm{d}E/\mathrm{d}x/\langle \mathrm{d}E/\mathrm{d}x_{\mathrm{MIP}}\rangle$ distributions measured in Pb–Pb collisions at $\sqrt{s_{\mathrm{NN}}} = 2.76$ TeV in six centrality intervals, for particles with $8 < p < 9$ GeV/c and $|\eta| < 0.2$ [24]. The spectra are normalized to the integrated yields. The signals are fitted to a sum of four Gaussian functions for pions (rightmost Gaussian), kaons, protons (leftmost Gaussian), and electrons that have a small contribution ($< 1\%$) and are not visible.

and electrons from photon conversions, fixing the Bethe-Bloch for $\beta\gamma > 1000$. In addition, the data samples with TOF enhanced ($\beta_{\mathrm{TOF}} > 1$) primary pions were used to further constrain the BB curve. The same information is used to determine the relative $\mathrm{d}E/\mathrm{d}x$ resolution as a function of $\langle \mathrm{d}E/\mathrm{d}x\rangle$, which amount to 5.5–7.5% for MIPs and improves with increasing $\langle \mathrm{d}E/\mathrm{d}x\rangle$ in the relativistic rise region to about 4.5–5.5%, for the discussed data samples. The BB and resolution curves were determined for kaons and protons in the full p interval while for pions for $p < 7$ GeV/c. For $p > 7$ GeV/c, pion $\langle \mathrm{d}E/\mathrm{d}x\rangle$ is restricted by the relativistic rise until $\langle \mathrm{d}E/\mathrm{d}x\rangle$ reaches plateau. It limits the transverse momentum reach to $p_{\mathrm{T}} \approx 20$ GeV/c in this analysis. The parameterizations of the Bethe-Bloch and resolution curves for pp, p–Pb and Pb–Pb can be found in Ref. [24, 27].

The particle fractions, i.e. the contribution of charged pions, kaons and (anti)protons to the yields of inclusive charged particles, obtained as a function of transverse momentum, are plotted in Fig. 7.3 as a function of Pb–Pb collision centrality for the four η intervals [24]. The extracted fractions as a function of p_{T} were obtained bin-by-bin using weighting procedure

$$f_{\mathrm{id}}\left(\langle p_{\mathrm{T}}\rangle_{\mathrm{i}}\right) = \sum_{\mathrm{j}} f'_{\mathrm{id}}\left(\langle p_{\mathrm{T}}\rangle_{\mathrm{j}}\right) \mathrm{R}\left(\langle p_{\mathrm{T}}\rangle_{\mathrm{i}}, \langle p_{\mathrm{T}}\rangle_{\mathrm{j}}\right), \tag{7.5}$$

where $f_{\mathrm{id}}\left(f'_{\mathrm{id}}\right)$ is given in bins of $p_{\mathrm{T}}(p)$ and R is a response matrix containing information about the correlation between p and p_{T}. It was found that all four pseudorapidity intervals are

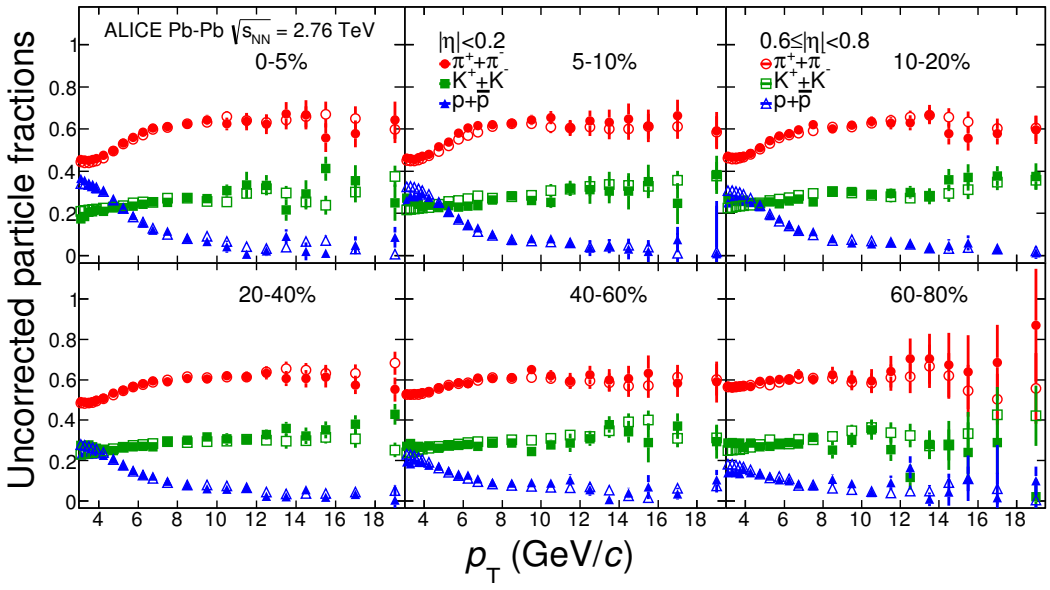

Fig. 7.3 Uncorrected particle fractions as a function of p_T for $|\eta| < 0.2$ (full markers) and $0.6 \leq |\eta| < 0.8$ (empty markers) in Pb–Pb collisions at $\sqrt{s_{NN}} = 2.76$ TeV [24].

consistent and the final fractions used to obtain the spectra (see Eq. 7.2) are computed as the weighted average of the four pseudorapidity intervals.

7.1.2 Corrections

The particle fractions measured in Pb–Pb, p–Pb and pp collisions are corrected for relative efficiency ($\varepsilon_{ch}/\varepsilon_{id}$) differences using simulations with the following event generators: HIJING for Pb–Pb, DPMJET for p–Pb, and PYTHIA and PHOJET for pp collisions (see Sec. 2.6 for the generator description). The relative efficiency correction, $\varepsilon_{ch}/\varepsilon_{id}$, was found to be consistent within $\pm 3\%$ for all collision systems and Pb–Pb centrality classes [24, 27]. Therefore, average correction was used and a systematic uncertainty of 3% was assigned. The relative efficiency correction factors are shown in Fig 7.4 for peripheral and central Pb–Pb collisions [24]. The corrections are below unity because the inclusive charged particle spectra contain weakly decaying baryons such as Σ, Ξ, and Ω for which the reconstruction efficiency is close to zero in the measured p_T range. Moreover, the pion and proton relative fractions were corrected for the feed-down from weak decays based on the analysis of distance of closest approach distributions in data and Monte-Carlo detector simulations [120] (see also Sec. 6.1.3.4 for details). The Jacobian correction from psudorapidity to rapidity spectra is also shown. As expected, the largest correction is observed at low p_T and reaches up to 4% for protons and

1% for kaons at p_{T} = 3 GeV/c. For pions this correction is negligible in the measured p_{T} range.

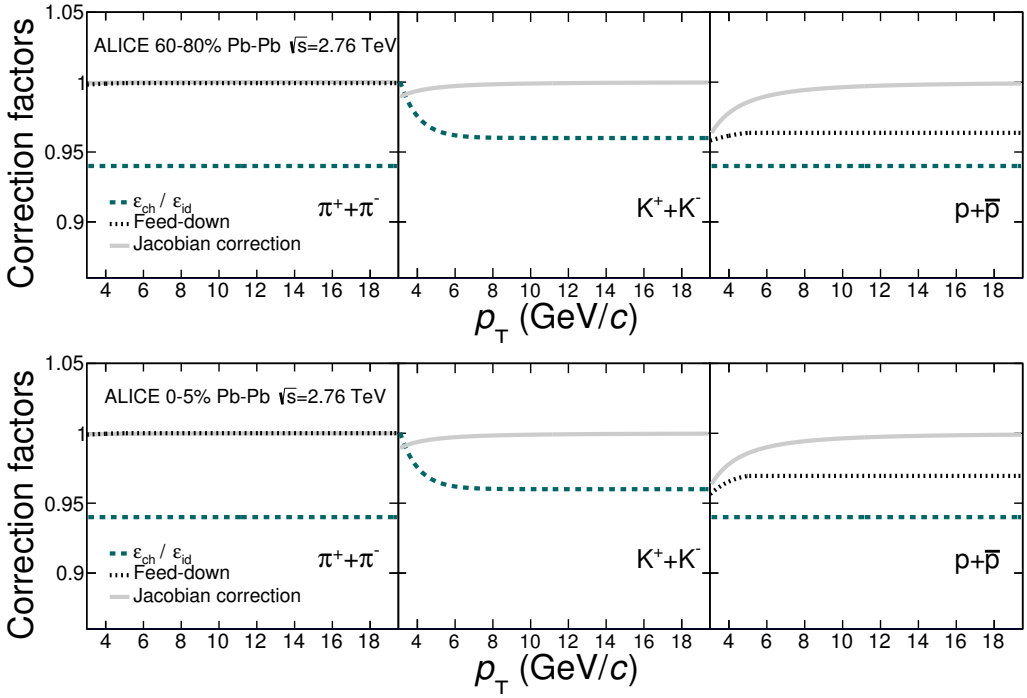

Fig. 7.4 Correction factors as a function of p_{T} applied to the fractions of pions (left panels), kaons (middle panels) and protons (right panels) for peripheral (top) and central (bottom) Pb–Pb collisions [24]. The relative efficiency ($\varepsilon_{\mathrm{ch}}/\varepsilon_{\mathrm{id}}$) correction, feed-down and Jacobian corrections are shown. The corrections to pion fractions due to the muon contamination is small ($< 1\%$) and is not shown.

7.1.3 Systematic Uncertainties

The contributions to the systematic uncertainties on the invariant yields of pions, kaons and protons for pp and Pb–Pb (0–5% and 60–80% centrlity) collisions at $\sqrt{s_{\mathrm{NN}}} = 2.76$ TeV are shown in Table 7.2 [24]. The systematic uncertainties are reported for the two representative p_{T} values. A complete set of numerical values for the data sets discussed in this work can be found in Refs. [23, 24, 27]. The same procedure was used to determine systematic uncertainties for all collisions systems. It is listed below for pp and Pb–Pb spectra analysis.

- The uncertainties related to track and event selection criteria were taken from inclusive charged particle spectra (see Sec. 6.1.4 for details).

- Half of the correction for the feed-down from week decays (see Fig. 7.4) was assigned as a systematic uncertainty.
- Half of the correction for high-p_{T} muons arising from heavy-flavor hadron semileptonic decays was assigned as a systematic uncertainty.
- The efficiency ratios $\varepsilon_{\mathrm{ch}}/\varepsilon_{\mathrm{id}}$ was found to be nearly independent of p_{T} (a small dependence is only observed for kaons), similar for all systems and model independent within 3%, which was assigned as systematic uncertainty on the efficiency correction.
- The systematic uncertainty on the fractions is mainly due to the uncertainties in the parameterization of the Bethe-Bloch and resolution curves used to constrain the fits. The deviation of the fitted curves from the actual measured means and widths of the $\mathrm{d}E/\mathrm{d}x$ spectra obtained from the analysis of the external pion, proton, and electron samples were histogrammed for several $\mathrm{d}E/\mathrm{d}x/\langle \mathrm{d}E/\mathrm{d}x_{\mathrm{MIP}} \rangle$ intervals. In a given $\mathrm{d}E/\mathrm{d}x/\langle \mathrm{d}E/\mathrm{d}x_{\mathrm{MIP}} \rangle$ interval, the standard deviation of the distributions were taken as the systematic uncertainty associated with extraction of means and widths. In addition, the statistical uncertainties on the extracted BB parametrizations in peripheral Pb–Pb conditions were found to be comparable to the systematic uncertainties and taken into account in the variations. The total systematic uncertainty is assigned as the quadratic sum of both contributions. The propagation of the uncertainties to the particle fractions is done by refitting the $\mathrm{d}E/\mathrm{d}x$ spectra, while randomly varying the constrained parameters $\langle \mathrm{d}E/\mathrm{d}x \rangle$ and σ within their uncertainties, assuming Gaussian distributions centered at the nominal values.

7.2 p_{T} Spectra in pp and Pb–Pb Collisions at $\sqrt{s_{\mathrm{NN}}} = 2.76$ TeV

The measurement of high-p_{T} spectra of charged pions, kaons and (anit)protons in pp and Pb–Pb collisions at the LHC was presented for the first time by ALICE [23]. The spectra were obtained with 40×10^6 pp and 11×10^6 Pb–Pb minimum-bias events collected in 2010 and 2011. The Pb–Pb spectra were determined in the central (0–5%) and peripheral (60–80%) collisions. The analysis was later extended including all Pb–Pb centrality classes [24].

Figure 7.5 shows invariant yields for pions, kaons and protons measured in pseudorapidity $|\eta| < 0.8$, in pp and Pb–Pb collisions at $\sqrt{s_{\mathrm{NN}}} = 2.76$ TeV [24]. The Pb–Pb spectra are presented in six centrality classes. For $p_{\mathrm{T}} < 3$ GeV/c, a hardening of the spectra is observed going from peripheral to central events. This effect is mass dependent and is characteristic of hydrodynamic flow, as discussed in Ref. [120] (see also Sec. 5.2). At high p_{T}, a reduction of the particle yield with increasing centrality is observed.

The proton-to-pion and kaon-to-pion ratios as a function of p_{T} for pp and Pb–Pb collisions are shown in Fig. 7.6. The proton-to-pion ratio in Pb–Pb (Fig. 7.6, top) shows a characteristic maximum at $p_{\mathrm{T}} \approx 3$ GeV/c, which decreases with decreasing centrality towards value observed in pp collisions. The observed maxima are approximately 20% above the peak values measured by PHENIX [387] and STAR [388], when p/π^+ and $\bar{\mathrm{p}}/\pi^-$ ratios are averaged and

Pb–Pb at $\sqrt{s_{\mathrm{NN}}} = 2.76$ TeV (0–5%)						
	$\pi^+ + \pi^-$		$\mathrm{K}^+ + \mathrm{K}^-$		p + $\bar{\mathrm{p}}$	
p_{T} GeV/c	2.0	10	3.0	10	3.0	10
Uncertainty						
Event and track selection	8.4%	8.2%	8.2%	8.1%	8.2%	8.1%
Feed-down correction	$< 0.1\%$	$< 0.1\%$	–	–	2.1%	1.5%
Correction for muons	0.1%	1.7%	–	–	–	–
Efficiency correction	3.0%	3.0%	3.0%	3.0%	3.0%	3.0%
Bethe-Bloch and σ param.	1.5%	2.2%	18%	8.4%	9.8%	17%
Pb–Pb at $\sqrt{s_{\mathrm{NN}}} = 2.76$ TeV (60–80%)						
Uncertainty						
Event and track selection	10%	9.7%	9.8%	9.7%	9.8%	9.7%
Feed-down correction	$< 0.1\%$	$< 0.1\%$	–	–	2.0%	1.8%
Correction for muons	0.3%	0.8%	–	–	–	–
Efficiency correction	3.0%	3.0%	3.0%	3.0%	3.0%	3.0%
Bethe-Bloch and σ param.	1.4%	2.4%	16%	7.1%	20%	29%
pp at $\sqrt{s}$ = 2.76 TeV						
Uncertainty						
Event and track selection	7.4%	7.6%	7.4%	7.6%	7.4%	7.6%
Feed-down correction	$< 0.1\%$	$< 0.1\%$	–	–	2.0%	1.8%
Correction for muons	0.4%	0.6%	–	–	–	–
Efficiency correction	3.0%	3.0%	3.0%	3.0%	3.0%	3.0%
Bethe-Bloch and σ param.	1.1%	1.7%	16%	5.7%	24%	17%

Table 7.2 Summary of the systematic uncertainties for the charged pion, kaon, and (anti)proton spectra determined for central (top) and peripheral (middle) Pb–Pb collisions, and for pp (bottom) collisions [24]. Contributions from the event and track selection are taken from the inclusive charged particle analysis for pp [18] and Pb–Pb [17] collisions.

data are corrected for feed-down. The kaon-to-pion ratio also exhibits a small maximum in central Pb-Pb collisions (Fig. 7.6, bottom) around p_{T} = 3 GeV/c, which has not been observed at RHIC.

For p_{T} larger than 10 GeV/c, both particle ratios behave like those in pp, suggesting that fragmentation function at high p_{T} is not modified in Pb–Pb collisions. It has been checked that the integrated kaon-to-pion(proton-to-pion) ratios for $p_{\mathrm{T}} > 10$ GeV/c as a function of centrality, are consistent within systematic uncertainties of 10%(20%).

7.3 p_{T} Spectra in p–Pb collisions at $\sqrt{s_{\mathrm{NN}}} = 5.02$ TeV

The transverse momentum spectra of charged pions, kaons and (anti)protons measured in $-0.5 < y < 0$ in p–Pb collisions at $\sqrt{s_{\mathrm{NN}}} = 5.02$ TeV are shown in Fig. 7.7 [27]. The p–

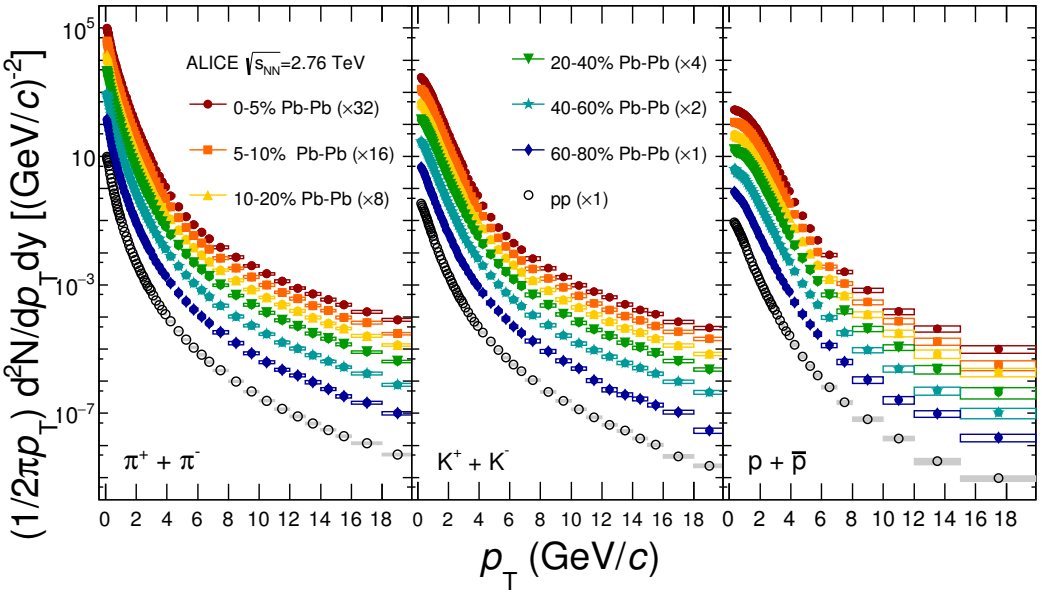

Fig. 7.5 Transverse momentum spectra of charged pions (left panel), kaons (middle panel), and (anti)protons (right panel) measured in $|\eta| < 0.8$), in Pb–Pb and pp collisions at $\sqrt{s_{\mathrm{NN}}} = 2.76$ TeV [24]. The systematic uncertainties are plotted as boxes around data points. The spectra were scaled by the indicated factors for clarity.

Pb spectra are presented for NSD events and for different V0A multiplicity classes from the highest (0–5%) to the lowest (80–100%) multiplicities. For p_{T} below 2–3 GeV$/c$, the spectra become harder as the multiplicity increases and the change is most pronounced for protons (like in Pb–Pb collisions), also reported in Ref. [375]. In Pb–Pb collisions, this effect is commonly attributed to the radial flow. For larger momenta, the spectra follow a power-law shape as expected from perturbative QCD.

Figure 7.8 shows the kaon-to-pion and the proton-to-pion ratios as a function of p_{T} for different V0A multiplicity classes measured at mid-rapidity $-0.5 < y < 0$ in p–Pb collisions at $\sqrt{s_{\mathrm{NN}}} = 5.02$ TeV [27]. The ratios in p–Pb collisions are compared to those measured in INEL pp collisions at $\sqrt{s} = 2.76$ [23] and 7 TeV (low-p_{T} spectra from Ref. [389]). Within systematic and statistical uncertainties, the p_{T}-differential kaon-to-pion ratios (Fig. 7.8, bottom) do not show any multiplicity dependence, and results are similar to those for INEL pp collisions at both energies. In contrast, the p_{T}-differential proton-to-pion ratios show a clear multiplicity evolution at low and intermediate momenta ($p_{\mathrm{T}} < 10$ GeV$/c$), which is qualitatively similar to the centrality evolution observed in Pb–Pb collisions [23, 24], as shown in Fig. 7.6.

It has been checked that for the central (0–5%) p–Pb and peripheral (60–80%) Pb–Pb events having similar charged particle multiplicity ($\mathrm{d}N_{\mathrm{ch}}/\mathrm{d}\eta \sim 50$), the kaon-to-pion ratios are in agreement within systematic uncertainties for all systems including pp at $\sqrt{s} = 7$ TeV. On

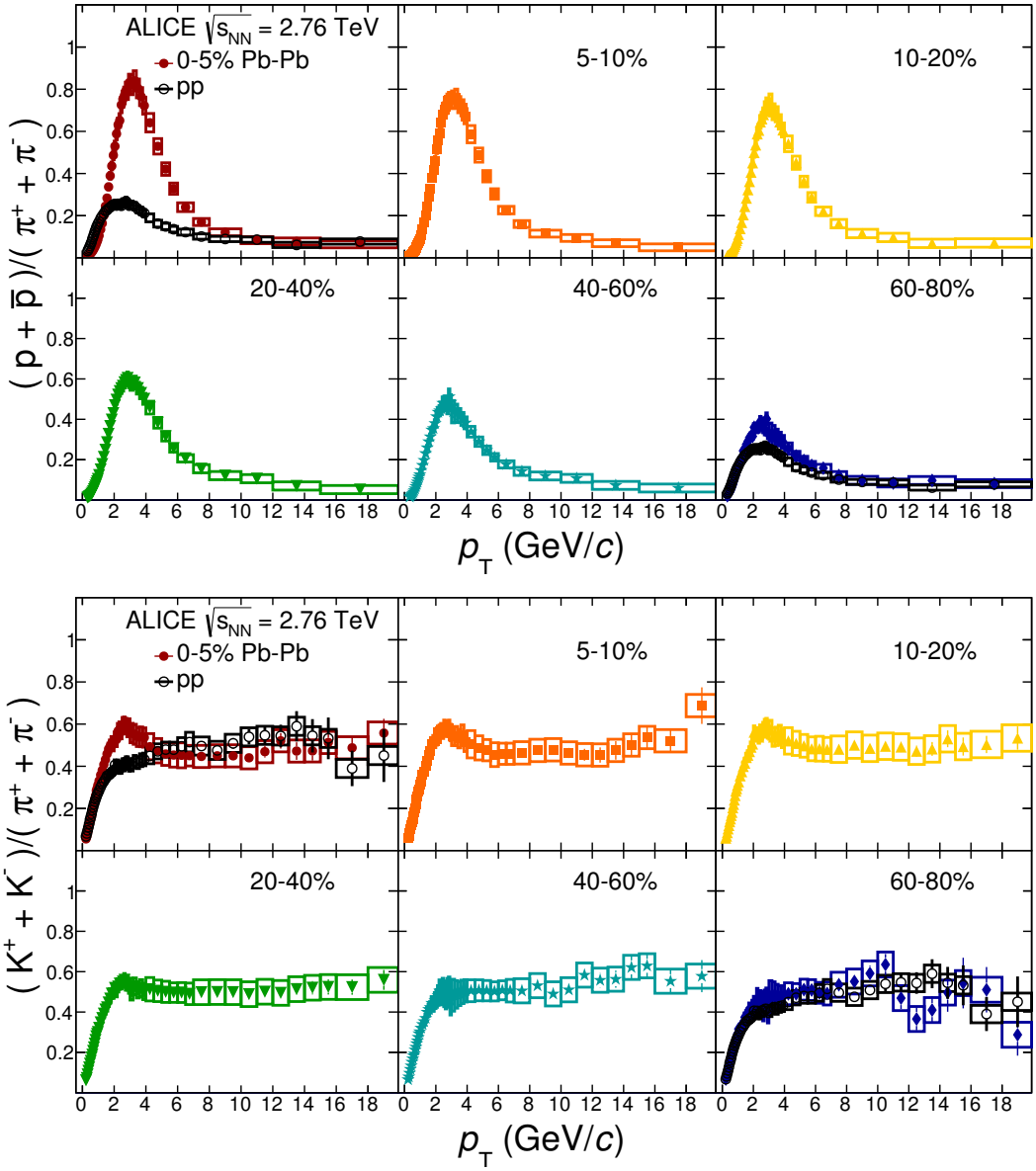

Fig. 7.6 (Anti)proton-to-pion (top) and kaon-to-pion (bottom) ratios as a function of transverse momentum (solid markers) for six Pb–Pb centrality classes [24]. The pp results (open markers) are overlaid with the most central and the most peripheral centrality class. Boxes around data points denote systematic uncertainties.

the other hand, the proton-to-pion ratios exhibit similar flow-like features for the p-Pb and Pb–Pb systems, with the ratios below the pp 7 TeV baseline for $p_{\mathrm{T}} < 1$ GeV/c and above for $p_{\mathrm{T}} > 1.5$ GeV/c. Quantitative differences are observed between p–Pb and Pb–Pb results,

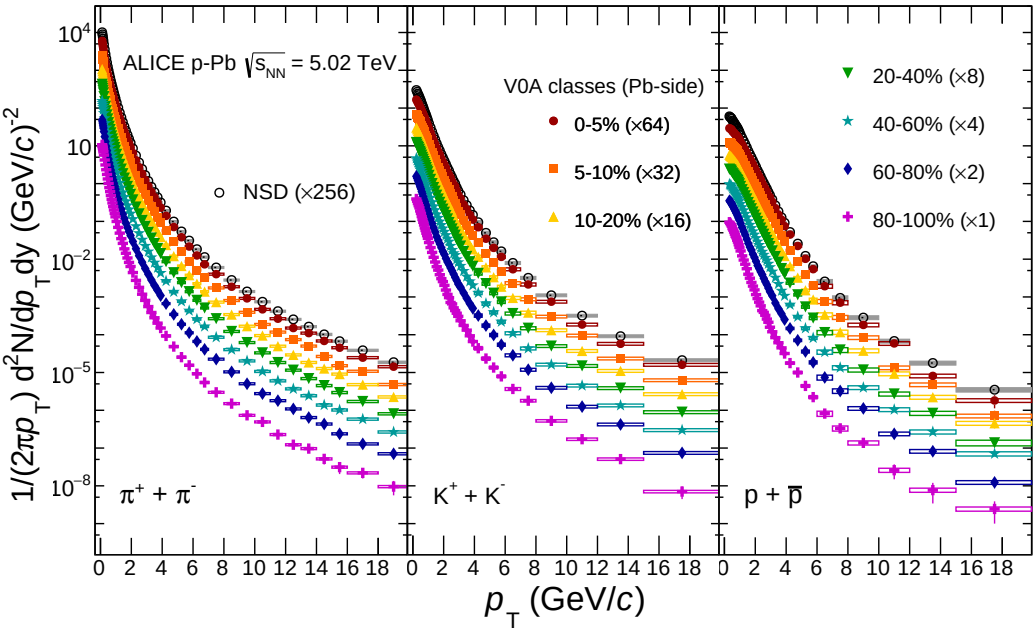

Fig. 7.7 Transverse momentum spectra of charged pions (left panel), kaons (middle panel) and protons (right panel) measured at mid-rapidity ($-0.5 < y < 0$) in p–Pb collisions at $\sqrt{s_{\rm NN}} = 5.02$ TeV [27] for NSD events (open markers) and for different V0A multiplicity classes (full markers). Boxes around data points denote systematic uncertainties. The spectra are scaled by the indicated factors for better visibility.

but they can be attributed to the differences in the initial state overlap geometry and the beam energy.

The particle ratios at high momenta ($p_{\rm T} > 10$ GeV$/c$) measured in multiplicity dependent p–Pb collisions are similar to that in INEL pp collisions. Taking into account that the same ratios were also found in centrality selected Pb–Pb collisions (see Fig. 7.6) one can conclude that they are system-size independent.

7.4 Reference pp Spectrum at $\sqrt{s} = 5.02$ TeV

In order to quantify any particle species dependence of the nuclear effects in p–Pb collisions, comparison to the reference $p_{\rm T}$ spectra in pp collisions is needed. In the absence of pp data at $\sqrt{s} = 5.02$ TeV, the pp reference spectra were obtained [27] using charged pion, kaon and (anti)proton $p_{\rm T}$ spectra measured at $\sqrt{s} = 2.76$ and 7 TeV [23, 27]. The pp reference spectra were build by interpolating between $p_{\rm T}$ spectra at these two energies to the energy of the p–Pb collisions in each $p_{\rm T}$ bin, assuming power-law dependence as a function of $\sqrt{s}$. The method was cross-checked using spectra at $\sqrt{s} = 5.02$ TeV generated by PYTHIA8, and the

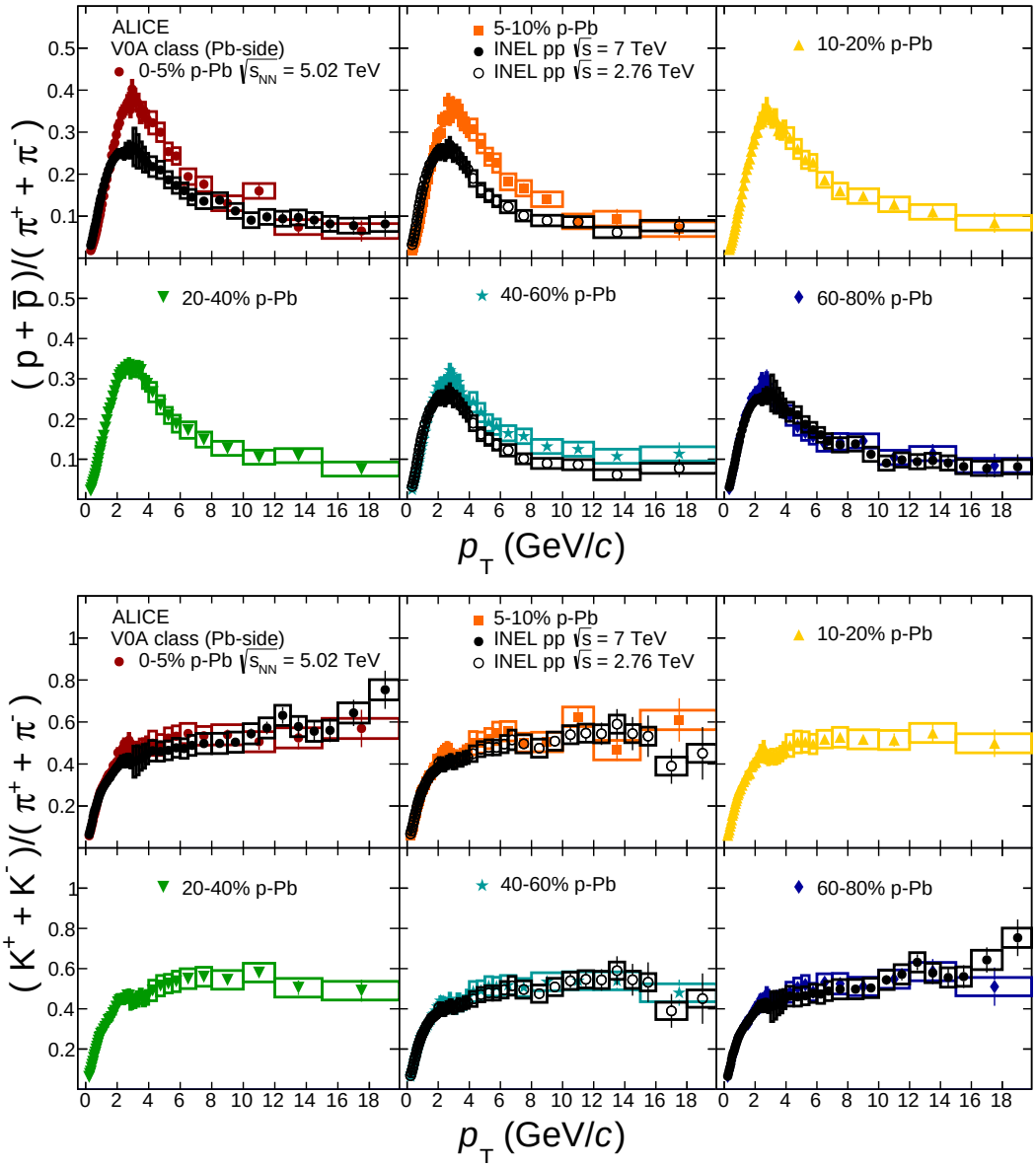

Fig. 7.8 (Anti)proton-to-pion (top) and kaon-to-pion ratios as a function of p_{T}, measured at mid-rapidity ($-0.5 < y < 0$) in p–Pb collisions at $\sqrt{s_{\mathrm{NN}}} = 5.02$ TeV [27] for for the different V0A multiplicity classes. The comparison to the ratios in INEL pp collisions at $\sqrt{s} = 2.76$ [23] and 7 TeV (low-p_{T} spectra [389]) for selected multiplicity classes is also shown. Boxes around data points denote systematic uncertainties. The spectra are scaled by the indicated factors for better visibility.

differences between interpolated and simulated spectra ware found negligible. The maximum relative uncertainty of the spectra at $\sqrt{s} = 2.76$ and 7 TeV were assigned as systematic uncer-

tainty to the reference. The total systematic uncertainties are below 8.6%, 10% and 18% for pion, kaon and proton spectra, respectively.

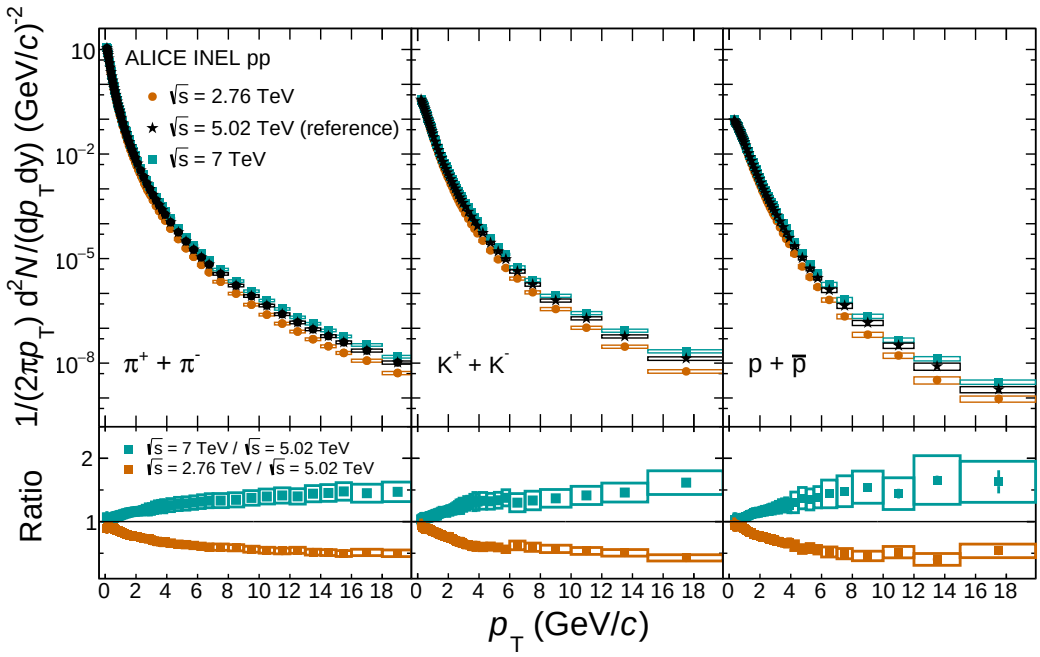

Fig. 7.9 Top: Transverse momentum spectra of charged pions (left), kaons (middle), and (anti)protons (right) measured in INEL pp collisions at $\sqrt{s} = 2.76$ and 7 TeV [23, 27]. The pp reference spectra at $\sqrt{s}$ = 5.02 TeV [27] constructed from the measured spectra at $\sqrt{s} = 2.76$ and 7 TeV are also shown. Boxes represent the systematic uncertainties. Bottom: The ratios of the measured spectra to the interpolated spectra are shown. Only uncertainties related to interpolation are shown.

The resulting p_{T} spectra are shown in Fig. 7.9 [27], where the interpolated p_{T} spectra at $\sqrt{s} = 5.02$ TeV (pp references) are compared to those measured in INEL pp collisions at $\sqrt{s} = 2.76$ TeV and 7 TeV.

Chapter 8
Measurement of p_{T} Spectra of D^0 ($\bar{\mathrm{D}}^0$), $\mathrm{D}^{\pm}$, $\mathrm{D}^{*\pm}$ mesons in Pb–Pb Collisions

ALICE collaboration has measured transverse momentum spectra of prompt charmed mesons D^0, D^+, D^{*+}, and their antiparticles, in pp collisions at $\sqrt{s} = 2.76$ TeV [390] and 7 TeV [391], in p–Pb collisions at $\sqrt{s_{\mathrm{NN}}} = 5.02$ TeV [392, 393] and Pb–Pb collisions at $\sqrt{s_{\mathrm{NN}}} = 2.76$ and 5.02 TeV [28, 394–396]. Author has contributed to the first D-meson measurement in Pb–Pb collisions [394], with data collected in 2010. This measurement was later extended by including higher statistics data from 2011 Pb–Pb run [395, 396]. The analysis details and p_{T} spectra of D^0, D^+, D^{*+}, and their antiparticles, measured in Pb–Pb collisions are presented in this chapter.

8.1 Spectra Analysis

The $\mathrm{D}^0(\bar{\mathrm{D}}^0)$, $\mathrm{D}^{\pm}$, $\mathrm{D}^{*\pm}$ mesons were reconstructed in the central rapidity region via their hadronic decay channels: $\mathrm{D}^0 \to \mathrm{K}^-\pi^+$ (weak decay with branching ratio BR $= 3.88 \pm 0.05\%$, mean proper decay length $c\tau = 123\ \mu m$), $\mathrm{D}^+ \to \mathrm{K}^-\pi^+\pi^+$ (weak decay, BR $= 9.13 \pm 0.19\%$, $c\tau = 312\ \mu m$), and $\mathrm{D}^{*+} \to \mathrm{D}^0\pi^+$ (strong decay, BR $= 67.7 \pm 0.5\%$) followed by $\mathrm{D}^0 \to \mathrm{K}^-\pi^+$ [397]. The yields of D mesons were extracted from an invariant mass analysis of their reconstructed decay products.

The D^0 and D^+ candidates were built from pairs and triplets of tracks with proper charge sign reconstructed using the ITS and TPC detectors, requiring $|\eta| < 0.8$, $p_{\mathrm{T}} > 0.4$ GeV/c, at least 70 associated space points (out of a maximum 159) and fit quality $\chi^2/\mathrm{ndf} < 2$ in the TPC, and at least two hits (out of 6) in the ITS, out of which at least one in either of the two SPD layers.

The D^{*+} candidates were obtained by combining the D^0 and low momentum charged particle, taking into account that the momentum of the pion from the D^{*+} decay is typically low, because of the small mass difference between the D^{*+} and D^0 mesons, $\Delta m = m_{\mathrm{D}^{*+}} - m_{\mathrm{D}^0} \approx 145.4$ MeV/c^2 [397]. The D^0-meson decay products were required $p_{\mathrm{T}} > 0.1$ GeV/c and at least three hits in the ITS, out of which at least one in the SPD. The transverse momentum of

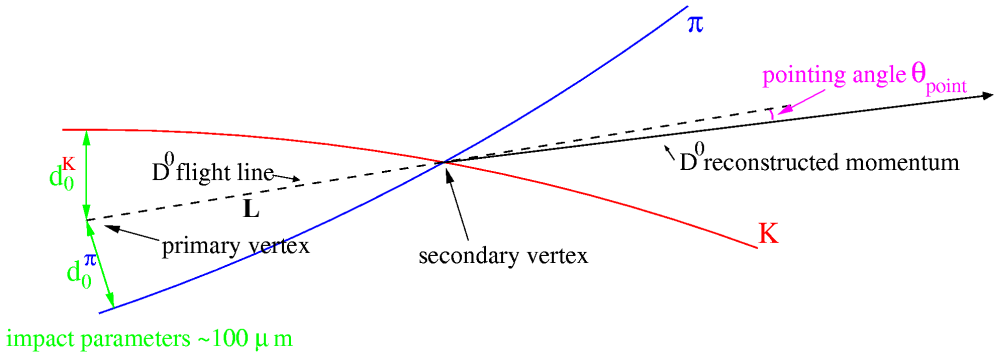

Fig. 8.1 The decay topology of D^0 mesons. The D^0 selection is based on the displacement of decay products from the primary interaction vertex via their impact parameters (d_0), the separation between primary and secondary vertices (L), and the pointing angle of the reconstructed D^0 momentum to the primary vertex (θ_{point}).

the soft pions produced in the D^{*+} decays typically ranges from 0.1 to 1.5 GeV/c, depending on the D^{*+} p_T.

The selection of the D^0 and D^+ was based on their displaced secondary vertex topologies, while D^{*+} was selected exploiting the secondary vertex topology of the produced D^0 [391, 394]. The latter was realized by using separation between primary and secondary vertices (L) and good pointing of the reconstructed D^0 to the primary vertex, as shown in Fig. 8.1. The pointing condition required a small value of the pointing angle (θ_{point}) measured between reconstructed momentum of the D^0 candidate and its flight line defined by the position of the primary and secondary vertices. In Pb–Pb collisions, two additional cuts on the projections of the pointing angle ($\theta^{\text{xy}}_{\text{point}}$) and of the decay length (L^{xy}) in the transverse plane were applied to further reduce combinatorial background. The cut values depend on D meson p_T and collision centrality, and are generally tighten in Pb–Pb compared to pp or p–Pb. They were optimized [391, 394] to have the best significance of the reconstructed D-meson signal and the highest reconstruction efficiency.

The PID selection relies on the pion and kaon identification using the specific energy loss ($\mathrm{d}E/\mathrm{d}x$) in the TPC and time-of-flight measurement in the TOF [394]. The $\pm 3\sigma$ cuts around the expected $\langle \mathrm{d}E/\mathrm{d}x \rangle$ and time-of-flight were used, leading to a strong reduction of combinatorial background by a factor of about 3 in the low-p_T region, while preserving most of the signal $\approx 95\%$. For D^{*+}, a tighter TPC $\mathrm{d}E/\mathrm{d}x$ cut of 2σ was applied for the D^0 decay products in central Pb–Pb collisions. These requirements were dependent on the track momentum. Tracks with no associated signal in the TOF detector were identified using only the TPC information. Tracks with contradictory responses from the TPC and TOF detectors were considered as unidentified and included in the analysis as compatible with both a pion and a kaon.

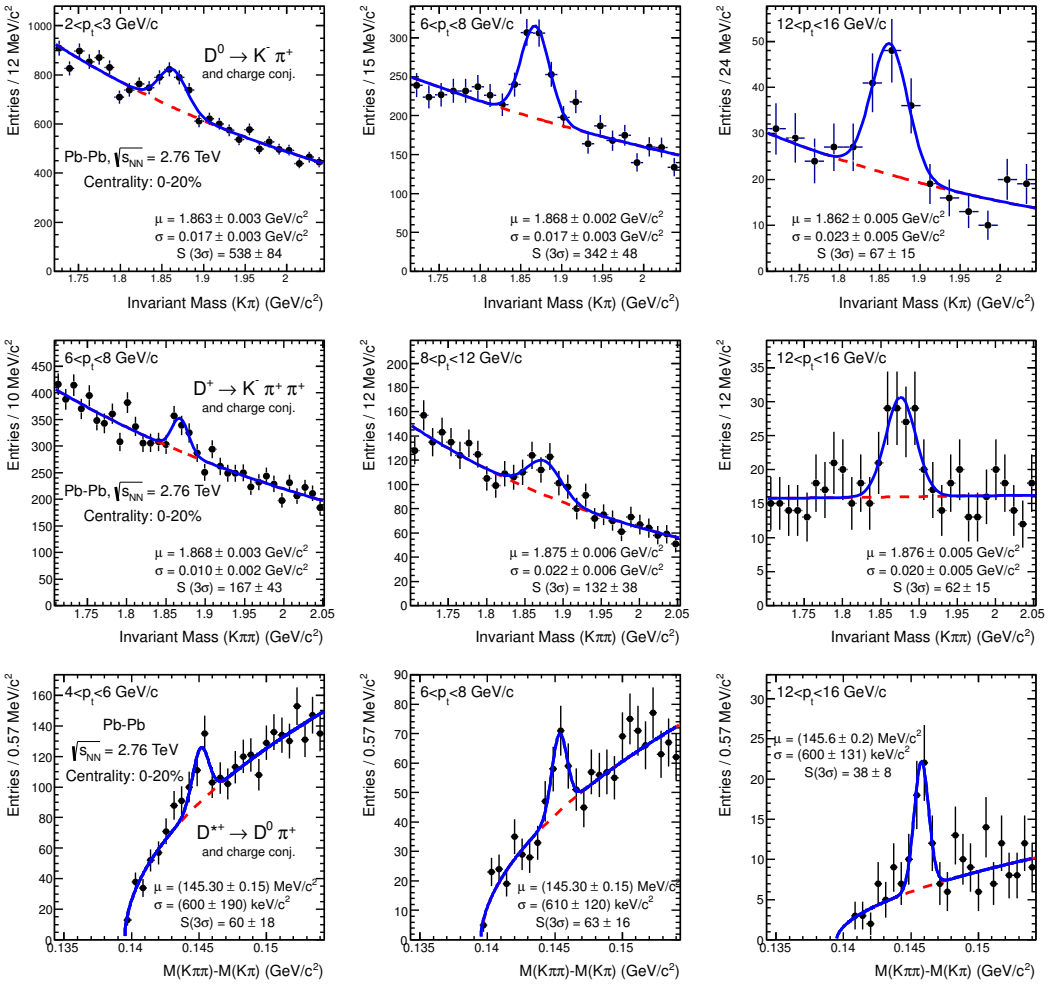

Fig. 8.2 Invariant mass distributions for D^0 (upper panels), D^+ (central panels), and D^{*+} (lower panels) candidates and their charge conjugates in selected p_{T} intervals for 0–20% central Pb-Pb collisions [394]. The curves show the fit functions described in the text. The values of mean (μ) and width (σ) of the signal peak are reported in the plots together with the raw signal yield. Only statistical uncertainties on the yields are shown.

With the track selection described above, the acceptance in rapidity for D mesons drops steeply to zero for $|y| > 0.5$ at low p_{T} and for $|y| > 0.8$ above $p_{\mathrm{T}} = 5$ GeV/c. Therefore, a p_{T} dependent fiducial acceptance cut was applied $|y| < y_{\mathrm{fid}}(p_{\mathrm{T}})$, with y_{fid} increasing from 0.5 to 0.8 in $0 < p_{\mathrm{T}} < 5$ GeV/c according to a second order polynomial function, and taking a constant value $y_{\mathrm{fid}} = 0.8$ for $p_{\mathrm{T}} > 5$ GeV/c.

The raw D-meson yields were obtained from fits to the candidate invariant mass distributions, $M(\mathrm{K}\pi)$ for D^0, $M(\mathrm{K}\pi\pi)$ for D^+, and the mass difference $\Delta M = M(\mathrm{K}\pi\pi) - M(\mathrm{K}\pi)$ for D^{*+}. Figure 8.2 shows the D^0 and D^+ invariant-mass and D^{*+} mass difference distribu-

tions for the 0-20% central Pb–Pb collisions at $\sqrt{s_{\mathrm{NN}}} = 2.76$ TeV [394]. The invariant mass distributions of D^0 and D^+ candidates were fitted with a function composed of a Gaussian function for the signal and exponential term for the background. The ΔM distribution of D^{*+} candidates was fitted with a Gaussian function for the signal and a threshold function multiplied by an exponential for the background, $a \cdot \sqrt{\Delta M - m_{\pi}} \cdot e^{b(\Delta M - m_{\pi})}$ [398], with a and b fit parameters.

8.1.1 Corrections

The production yields of prompt D mesons in Pb–Pb collisions were calculated using the following formula [394]:

$$\left.\frac{\mathrm{d}N^{\mathrm{D}}}{\mathrm{d}p_{\mathrm{T}}}\right|_{|y|<0.5} = \frac{1}{N_{\mathrm{evt}}} \frac{1}{\Delta y \Delta p_{\mathrm{T}}} \frac{f_{\mathrm{prompt}}\,(p_{\mathrm{T}}) \cdot \frac{1}{2} \cdot N_{\mathrm{raw}}^{\mathrm{D}+\bar{\mathrm{D}}}\,(p_{\mathrm{T}})\Big|_{|y|<y_{\mathrm{fid}}}}{(Acc \times \varepsilon)_{\mathrm{prompt}}\,(p_{\mathrm{T}}) \cdot \mathrm{BR}}, \tag{8.1}$$

where prompt refers to mesons not coming from weak decays of B mesons. The $N_{\mathrm{raw}}^{\mathrm{D}+\bar{\mathrm{D}}}$ are the inclusive raw yields for particles and their antiparticles, obtained from the invariant mass analysis. They were divided by the factor of two to get charge-averaged yields. The yields were corrected for the B meson feed-down contribution, with f_{prompt} denoting the prompt fraction of raw yields. The acceptance-times-efficiency $(Acc \times \varepsilon)$ denotes the product of acceptance and efficiency of prompt D mesons, where ε accounts for vertex and track reconstruction, track selection and D-meson candidate selection with the secondary vertex and particle identification cuts. The $\Delta y = 2y_{\mathrm{fid}}$ and Δp_{T} are the rapidity and transverse momentum intervals, BR is the branching ratio and N_{evt} is the number of analyzed events.

The rapidity acceptance correction $\Delta y = 2y_{\mathrm{fid}}$ assumes that the D meson yields are uniformly distributed in the measured rapidity intervals. This assumption was validated to the 1% level with PYTHIA6 (Perugia0 tune) [371] pp simulations.

The acceptance-times-efficiency $(Acc \times \varepsilon)$ corrections were obtained using GEANT3 detector simulations with combination of HIJING and PYTHIA event generators. The underlying Pb–Pb collisions at $\sqrt{s_{\mathrm{NN}}} = 2.76$ TeV were generated using HIJING, while the prompt and feed-down D mesons were added using pp events from PYTHIA6 (Perugia-0 tune) [371] with enhanced $c\bar{c}$ and $b\bar{b}$ production. The resulting $Acc \times \varepsilon$ determined for D^0, D^+ and D^{*+} mesons in $|y| < y_{\mathrm{fid}}(p_{\mathrm{T}})$ as a function of p_{T} in 0–20% central Pb–Pb collisions at $\sqrt{s_{\mathrm{NN}}} = 2.76$ TeV, is shown in Fig 8.3 [394]. The efficiencies were determined for prompt D mesons with and without PID requirement, and for feed-down D mesons, and range from 0.1% at low p_{T} to 10–20% at high p_{T}. The efficiency for feed-down D mesons is larger than for prompt D mesons by a factor of 1.5 because their production vertices are more separated from the primary vertex and are more efficiently selected by the analysis cuts. The relative difference between efficiency of prompt D mesons with and without PID requirement is below 5%, illustrating high efficiency of PID selection.

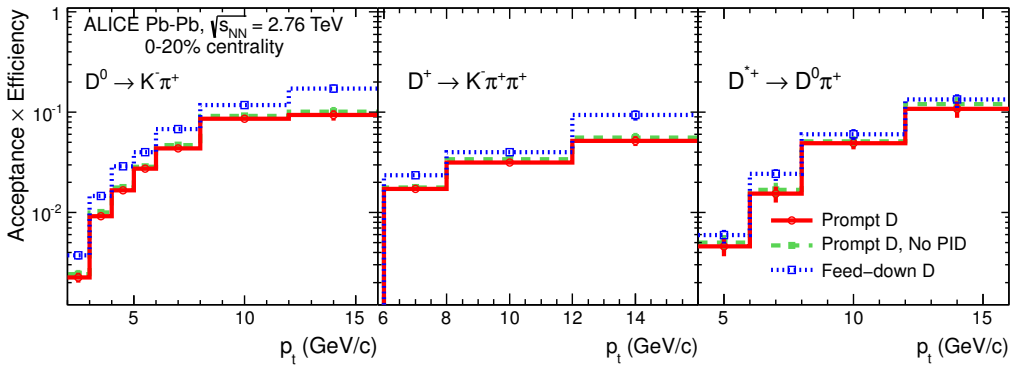

Fig. 8.3 Product of acceptance and efficiency as a function of p_{T} for D^0 (left panel) D^+ (middle panel) and D^{*+} (right panel) in 0–20% central Pb–Pb collisions at $\sqrt{s_{\mathrm{NN}}} = 2.76$ TeV [394]. The efficiency for prompt D mesons with and without PID requirement, and for D mesons arising from feed-down (B meson decays) are shown.

The fraction of prompt D mesons, f_{prompt}, was determined using the beauty production cross sections from the fixed-order next-to-leading-log resummation (FONLL) calculations [399, 400], the $\mathrm{B} \to \mathrm{D} + \mathrm{X}$ (feed-down) decay kinematics from the EvtGen package [401], and Monte Carlo efficiencies for the feed-down D mesons [394]:

$$f_{\mathrm{promt}} = 1 - \left(\frac{N_{\mathrm{raw}}^{\mathrm{D}+\bar{\mathrm{D}}\ \mathrm{feed-down}}}{N_{\mathrm{raw}}^{\mathrm{D}+\bar{\mathrm{D}}}} \right) \tag{8.2}$$

where number of feed-down D mesons ($N_{\mathrm{raw}}^{\mathrm{D}+\bar{\mathrm{D}}\ \mathrm{feed-down}}$) was calculated in Pb–Pb collisions as

$$\begin{aligned} N_{\mathrm{raw}}^{\mathrm{D}+\bar{\mathrm{D}}\ \mathrm{feed-down}} =& 2 \cdot \langle T_{\mathrm{AA}} \rangle \cdot \left(\frac{\mathrm{d}^2\sigma}{\mathrm{d}p_{\mathrm{T}}} \right)^{\mathrm{FONLL}}_{\mathrm{feed-down},\ |\eta|<0.5} \\ & \cdot R_{\mathrm{AA}}^{\mathrm{feed-down}} \cdot (Acc \times \varepsilon)_{\mathrm{feed-down}} \cdot \Delta y \Delta p_{\mathrm{T}} \cdot \mathrm{BR} \cdot N_{\mathrm{evt}}, \end{aligned} \tag{8.3}$$

where $(Acc \times \varepsilon)_{\mathrm{feed-down}}$ is the acceptance-times-efficiency for feed-down D mesons. The nuclear modification factor of the feed-down D mesons ($R_{\mathrm{AA}}^{\mathrm{feed-down}}$), is related to modification of beauty production in Pb–Pb collisions, which is currently unknown. It was assumed that the nuclear modification factors of prompt and feed-down D mesons are equal, $R_{\mathrm{AA}}^{\mathrm{feed-down}} = R_{\mathrm{AA}}^{\mathrm{prompt}}$. This hypothesis was varied in the range $1/3 < R_{\mathrm{AA}}^{\mathrm{feed-down}} / R_{\mathrm{AA}}^{\mathrm{prompt}} < 3$ to determined systematic uncertainties, which was justified by the model predictions for charm and beauty R_{AA} [247, 402] and measurements of non-prompt J/ψ (from B meson decays) R_{AA} by CMS collaboration [403]. The value of f_{promt} depends on the D meson species, the transverse momentum interval, the applied cuts, the parameters used in the FONLL B meson prediction, and the hypothesis on the $R_{\mathrm{AA}}^{\mathrm{feed-down}}$, and range from about 0.95 at low p_{T} (< 3 GeV/c) to 0.85 for larger p_{T} [394].

	Particle	D^0		D^+		D^{*+}	
0–20% centrality	p_{T} interval (GeV/c)	2–3	12–16	6–8	12–16	4–6	12–16
	Yield extraction	8%	10%	20%	10%	20%	10%
	Tracking efficiency	10%	10%	15%	15%	15%	15%
	Cut efficiency	13%	10%	15%	15%	10%	10%
	PID efficiency	$^{+15}_{-5}$%	5%	5%	5%	$^{+15}_{-5}$%	5%
	MC p_{T} shape	4%	3%	1%	5%	3%	3%
	FONLL feed-down corr.	$^{+2}_{-14}$%	$^{+6}_{-8}$%	$^{+3}_{-7}$%	$^{+7}_{-9}$%	$^{+2}_{-5}$%	$^{+2}_{-7}$%
	$R_{\mathrm{AA}}^{\mathrm{feed-down}}/R_{\mathrm{AA}}^{\mathrm{prompt}}$	$^{+4}_{-10}$%	$^{+14}_{-27}$%	$^{+7}_{-16}$%	$^{+15}_{-28}$%	$^{+4}_{-9}$%	$^{+5}_{-12}$%
	BR	1.3%		2.1%		1.5%	
	Centrality limits	< 0.1%					
40–80% centrality	p_{T} interval (GeV/c)	2–3	12–16	3–4	8–12	2–4	12–16
	Yield extraction	5%	5%	15%	15%	15%	8%
	Tracking efficiency	10%	10%	15%	15%	15%	15%
	Cut efficiency	13%	10%	10%	10%	10%	10%
	PID efficiency	$^{+10}_{-5}$%	5%	5%	5%	$^{+10}_{-5}$%	5%
	MC p_{T} shape	1%	3%	1%	3%	5%	4%
	FONLL feed-down corr.	$^{+3}_{-16}$%	$^{+4}_{-5}$%	$^{+3}_{-11}$%	$^{+4}_{-9}$%	$^{+1}_{-8}$%	$^{+1}_{-4}$%
	$R_{\mathrm{AA}}^{\mathrm{feed-down}}/R_{\mathrm{AA}}^{\mathrm{prompt}}$	$^{+5}_{-12}$%	$^{+11}_{-22}$%	$^{+6}_{-14}$%	$^{+9}_{-20}$%	$^{+2}_{-6}$%	$^{+3}_{-8}$%
	BR	1.3%		2.1%		1.5%	
	Centrality limits	3%					

Table 8.1 Summary of relative systematic uncertainties on the prompt D meson production yields in 0–20% and 40–80% central Pb–Pb collisions at $\sqrt{s_{\mathrm{NN}}} = 2.76$ TeV [394], listed for the lowest and highest p_{T} bins and for the three mesons.

8.1.2 Systematic Uncertainties

The evaluation of systematic uncertainties on the prompt D meson yields in Pb–Pb collisions is described in detail in Refs. [394–396]. In this section the main contributions to the uncertainties are briefly outlined. Generally, the systematic uncertainties depend on p_{T} and collision centrality intervals. They include contributions related to yield extraction, tracking efficiency, selection cut efficiency, PID efficiency, MC p_{T} shape, feed-down corrections, branching ratio BR, $R_{\mathrm{AA}}^{\mathrm{feed-down}}/R_{\mathrm{AA}}^{\mathrm{prompt}}$ determination, and centrality limits for Pb–Pb collisions. The numerical values determined for 0–20% and 40–80% central Pb–Pb collisions at $\sqrt{s_{\mathrm{NN}}} = 2.76$ TeV are listed in Tab. 8.1 [394]. The main contributions are listed below.

- The systematic uncertainty on the yield extraction from the invariant mass spectra in a given p_{T} interval was determined by repeating the fit in different mass range; by using different fit functions for the background. The parabola instead of an exponential fit was considered for D^0 and D^+, and a power law multiplied by an exponential or a threshold function for D^{*-}. Moreover, another method based on counting the signal in the invariant mass distribution after subtraction of the background estimated from a fit to the side bands, was also used. This method does not assume any particular shape for the invariant-mass distribution of the signal. The uncertainty was determined as the maximum difference of these results and it was found in the range 5–20%, depending on meson species, p_{T} interval and collisions centrality.
- The systematic uncertainty on the tracking efficiency includes the effects arising from the efficiency of track finding in the TPC, from the track propagation efficiency from the TPC to the ITS, and from the track quality selection. These contributions were determined by comparing the data and simulation and by varying the track selection criteria. The overall uncertainty amounts to 5% for single tracks independently of collisions centrality, which results in a 10% uncertainty for D^0 mesons (two-track final state) and 15% for D^+ and D^{*+} mesons (three-track final state).
- The residual difference in the reconstructed track properties between data and simulation might influence on D meson selection. The systematic uncertainty related to this effect was evaluated by comparing results obtained with modified selection cuts. The estimated systematic uncertainties vary in the range from 10% to 15% depending on D meson species and p_{T}, as well as collision centrality. It was verified that part of this uncertainty arises from the detector misalignment not fully described in the simulation.
- The uncertainty related to PID was determined by comparing corrected signals obtained with and without PID cuts. The resulting uncertainty ranges from $\left(^{+\ 15}_{-\ 5}\%\right)$ at low p_{T} to 5% at high p_{T}, and it is independent of meson species and collision centrality at high p_{T}.
- The difference between the real and simulated shape of the D meson p_{T} distribution might influence on the D meson reconstruction. The uncertainty arising from this effect was estimated using the two alternative p_{T} distributions from PYTHIA and FONLL, with and without nuclear modification observed in the data. It resulted in systematic uncertainty up to 5%, depending on meson species and collision centrality.
- The uncertainty on the D meson feed-down corrections, i.e. the calculation of the f_{prompt}, was estimated by varying the p_{T}-differential feed-down D-meson cross section (see Eq. 8.3) from the FONLL calculation within the theoretical uncertainties and by applying alternative method to compute f_{promt}, based on the ratio of charm and beauty FONLL cross sections, instead of the absolute beauty cross section (see Ref. [394] for more details). The resulting uncertainties range between $\left(^{+\ 3}_{-\ 16}\%\right)$ at low p_{T} and $\left(^{+\ 7}_{-\ 9}\%\right)$ at high p_{T}, depending of meson species and p_{T}.

- The uncertainty from the variation of the feed-down D-meson R_{AA} hypothesis, $1/3 < R_{\mathrm{AA}}^{\mathrm{feed-down}}/R_{\mathrm{AA}}^{\mathrm{prompt}} < 3$, ranges from $\left(^{+\ 7}_{-\ 16}\%\right)$ at low p_{T} to $\left(^{+\ 15}_{-\ 28}\%\right)$ at high p_{T}, depending of meson species and p_{T}.
- The uncertainties on the branching ratios were taken from Ref. [404].
- The contribution due to the 1.1% uncertainty on the fraction of the hadronic cross section (i.e. for the 40–80% class, 40.4–80.9% and 39.6–79.1%) used in the Glauber fit to determine the centrality classes [178] (see also Sec. 2.5) amounts to $< 0.1\%$ and 3% in 0–20% and 40–80% central collisions, respectively. In addition, the uncertainty on $\langle T_{\mathrm{AA}} \rangle$ amounts to 3.9%(4.9%) for the 0–20%(40–80%) centrality class.

8.2 p_{T} Spectra in Pb–Pb Collisions at $\sqrt{s_{\mathrm{NN}}} = 2.76$ TeV

Figure 8.4 shows the invariant yields of prompt D^0 (left panel), D^+ (middle panel), and D^{*+} mesons, and their antiparticles, measured at mid-rapidity ($|y| < 0.5$) in 0–20% and 40–80% central Pb–Pb collisions at $\sqrt{s_{\mathrm{NN}}} = 2.76$ TeV [394]. The measurement is based on the 13×10^6 Pb–Pb collisions in the centrality range (0–80%), which passed the trigger and event selection criteria. The spectra from Pb–Pb collisions, defined as the feed-down corrected production yields per event are compared to the reference spectra from pp collisions, which were obtained by applying a $\sqrt{s}$-scaling [405] of the p_{T} spectra of D mesons measured at $\sqrt{s}$ = 7 TeV [391]. For comparison, the pp reference is scaled by the average nuclear overlap function $\langle T_{\mathrm{AA}} \rangle$ determined in the corresponding centrality interval. A clear suppression of D-meson production is observed in Pb–Pb collisions as compared to the scaled pp reference, which is stronger in central than in peripheral collisions.

This measurement has been later extended by including high statistics Pb–Pb data collected by ALICE in 2011 [395, 396]. For central collisions, the number of events used in the analysis was larger by a factor of about 10 as compared to that used for the previously discussed results. This allowed for extending the measurement of p_{T} spectra to lower and higher p_{T}, from 2–16 GeV/c to 1–36 GeV/c, and for performing the study in a narrower centrality intervals. The resulting p_{T} spectra of prompt D^0 , D^+, and D^{*+} mesons, measured in 0–10% (left) and 30–50% (right) central Pb–Pb collisions, are shown in Fig. 8.5 [396].

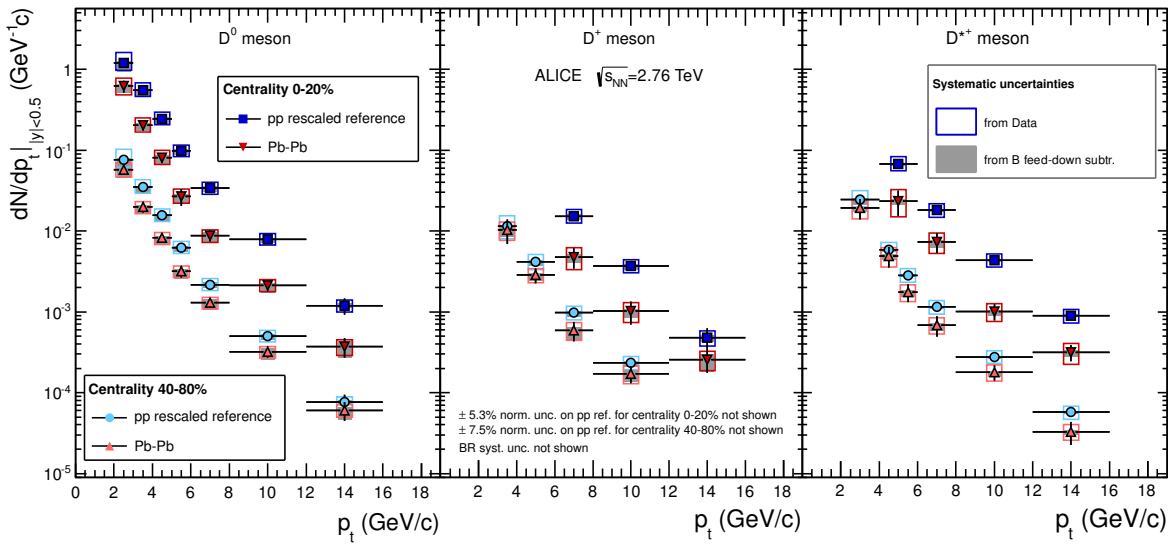

Fig. 8.4 Invariant yields of D^0 (left panel), D^+ (middle panel) and D^{*+} (right panel) mesons measured at mid-rapidity, $|y| < 0.5$, in 0–20% and 40–80% central Pb–Pb collisions at $\sqrt{s} = 2.76$ TeV [394]. The reference pp spectra scaled by $\langle T_{\mathrm{AA}} \rangle$ are also shown. The systematic uncertainties from data analysis (empty boxes) and from feed-down subtraction (full boxes) are depicted. Horizontal error bars reflect bin widths, with symbols placed at the centre of the bin.

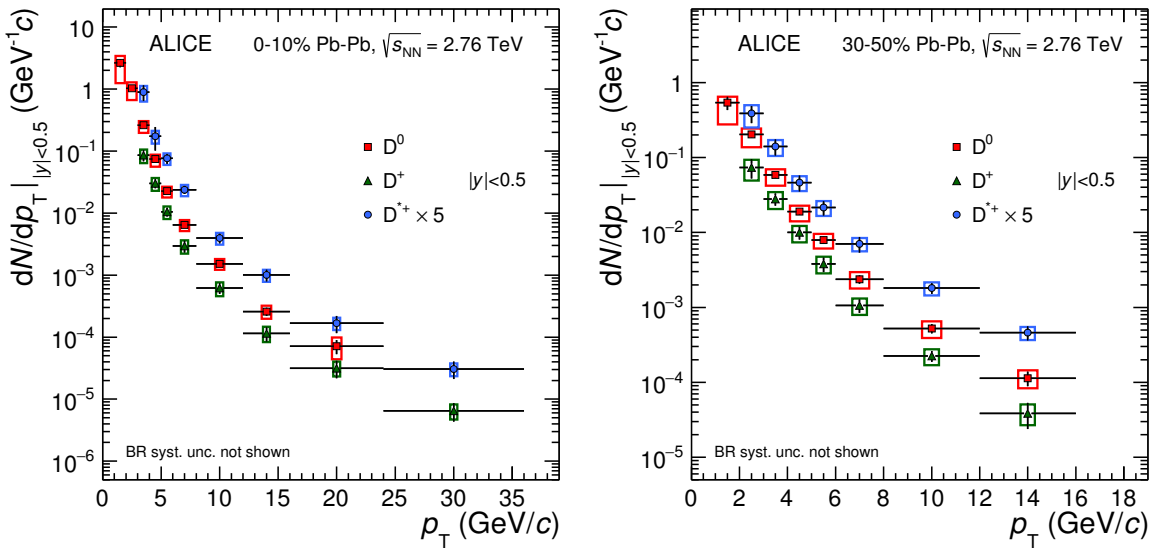

Fig. 8.5 Transverse momentum distributions of prompt D^0, D^+ and D^{*+} mesons measured at mid-rapidity ($|y| < 0.5$) in 0–10% (left) and 30–50% (right) central Pb–Pb collisions at $\sqrt{s} = 2.76$ TeV [396]. The systematic uncertainties from data analysis (empty boxes) and from feed-down subtraction (full boxes) are depicted. Horizontal error bars reflect bin widths, with symbols placed at the centre of the bin. The D^{*+} spectra are scaled by indicated factor for better visibility.

Chapter 9
Measurement of p_{T} Spectra of Charged Jets in p–Pb $\sqrt{s_{\mathrm{NN}}} = 2.76$ TeV and Pb–Pb Collisions

ALICE central barrel has a tracking system that covers the full azimuth while electromagnetic calorimeters are only installed for a smaller acceptance (roughly 10% of the tracking coverage). Therefore, two types of reconstructed jets, *charged jets* reconstructed only from charged particles and *full jets* combining charged particles and photons, are distinguished in the jet analyses. The charged jet p_{T} spectra have been measured by ALICE in pp collisions at $\sqrt{s} = 7$ TeV [406], p–Pb collisions at $\sqrt{s_{\mathrm{NN}}} = 5.02$ TeV [26] and Pb–Pb collisions at $\sqrt{s_{\mathrm{NN}}} = 2.76$ TeV [19], while the p_{T} spectra of full jets have been measured in pp [19] and in Pb–Pb collisions [248] at $\sqrt{s_{\mathrm{NN}}} = 2.76$ TeV . Author has contributed to the measurements of p_{T} spectra of charged jets in p–Pb [26] and Pb–Pb [19] collisions, which are presented in this chapter.

9.1 Jet Definition

Jet is a narrow cone of hadrons and other particles produced by the hadronization of a quark or gluon, as schematically shown in Fig. 9.1. In order to make a quantitative comparison of measurements and perturbative QCD calculations, a jet is defined by the algorithm used for recombination of jet constituents into a single four momentum vector, or in theoretical calculations, by the space (angular) cuts in the integration of partonic cross section beyond leading order. Jets in ALICE are reconstructed using sequential recombination algorithms k_{T} [407] and anti-k_{T} [408], which are insensitive to the divergences in QCD beyond leading order. These algorithms guarantee that the reconstructed jet properties do not change if one parton is replaced by two in the same direction that share the energy (*collinear safety*) and if a very soft gluon is added to the event (*infrared safety*).

The algorithms start from the list of clusters (e.g. particles, partons, or calorimeter cells) and calculate

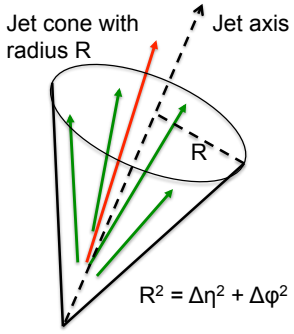

Fig. 9.1 Schematic picture of jet as a collimated spray of particles emitted in the direction of of the originally produced parton. The arrows denote the momentum vectors of the produced particles.

$$d_{\mathrm{i}} = p_{\mathrm{T,i}}^{2m} \tag{9.1}$$

$$d_{\mathrm{ij}} = \min\left(p_{\mathrm{T,i}}^{2m}, p_{\mathrm{T,j}}^{2m}\right) \cdot \frac{R_{\mathrm{ij}}^2}{D^2} \tag{9.2}$$

for each cluster i and all pair combinations ij. The distance measure d_{i} and d_{ij} use $m = 1$ for anti-k_{T} and $m = -1$ for k_T algorithm. $R_{\mathrm{ij}}^2 = \left(\eta_{\mathrm{i}} - \eta_{\mathrm{j}}\right)^2 + \left(\phi_{\mathrm{i}} - \phi_{\mathrm{j}}\right)^2$ is the squared distance in (η, ϕ), which is weighted with the distance parameter D, the free parameter of the algorithm [409]. Two clusters ij are merged if all d_{i} and d_{ij} have minimum and new cluster is added to the list. In the case the minimum is found for the single cluster i, it is marked as jet and removed from the list. This procedure is repeated until all initial clusters from the list are associated with a jet. The different exponent m used for the algorithms determines the order how particles are cluster in jets. The anti-k_{T} algorithm starts from the high-p_{T}, while k_{T} from the low-p_{T} particles. The main difference between algorithms is that the k_{T} exhibits large areas and a rather irregular jet shapes, while anti-k_{t} prefers a circular area $A \approx \pi R^2$ with radius $R = D$ for high-p_{T} jets. In ALICE, the signal jets are reconstructed based on the anti-k_{T} algorithm, while k_{T} algorithm is used to determine the underlying event background [410].

9.2 Spectra Analysis

The Pb–Pb and p–Pb data used for the analysis of p_{T} spectra were recorded by ALICE in 2010 and 2013, respectively. Similar approach for jet reconstruction is used for all collisions systems [144]. However, the most challenging is jet reconstruction in Pb–Pb due to an underlying event background [411]. Jet measurements in heavy-ion collisions employ various approaches to correct for background energy that is not associated with the jet production, and to suppress the combinatorial (false) jets induced by fluctuations of the background (e.g. via energy or momentum thresholds for particles that are used in the jet finding process). Every approach represents a compromise between potential fragmentation biases in the jet

reconstruction and a better separation of the jet signal from the background. The details of the charged jet analysis, including event and track selection criteria and jet reconstruction, are briefly discussed in this section.

9.2.1 Event and track selection

The analysis of Pb–Pb and p–Pb spectra was based on the minimum-bias events, which were selected with $\mathrm{MB_{OR}}$ and $\mathrm{MB_{AND}}$ triggers (see Sec. 2.4 for details). In addition, an offline selection was applied to remove beam-induced background events and electromagnetic interactions. To ensure a high tracking efficiency for all considered events, the primary vertex was required to be within 10 cm from the center the detector along the beam axis. For Pb–Pb selection, the vertex in the transverse plane was also required to be within 1 cm.

The track selection is based on the information from the ITS and TPC central barrel detectors, for charged particles with $0.15 < p_{\mathrm{T}} < 100$ GeV/c and $|\eta| < 0.9$. The reconstructed tracks were required to have at least 3 hits in the ITS (out of maximum 6) used in the fit to ensure adequate track momentum resolution for jet reconstruction. For tracks without any hit in the SPD, the primary vertex location was used in addition to the TPC and ITS hits for the momentum determination of the track. This reduced the azimuthal dependence of the track reconstruction efficiency due to the non-uniform SPD response, without creating track collections with different momentum resolution. Moreover, the reconstructed tracks were also required a minimum number of 70 TPC space-points (out of maximum 159), a χ^2 of the TPC track fit less than 4, and a $\chi^2_{\mathrm{TPC-ITS}}$ (Eq. 6.1) less than 36.

The relative momentum resolution, $\sigma(p_{\mathrm{T}})/p_{\mathrm{T}}$, was estimated on the track-by-track basis using covariance matrix of the track fit. For the tracks with at least 3 ITS space points the $\sigma(p_{\mathrm{T}})/p_{\mathrm{T}}$ has minimum of $\sim 1\%$ at 1 GeV/c independently of collision system, and increases to about 10% (4%) at 50 GeV/c for Pb–Pb (p–Pb) collisions. For the tracks with less than 3 ITS points (6% of track sample) the resolution at high p_{T} is worst by a factor of 2. In the considered jet sample, only 20% of jets with $p_{\mathrm{T,jet}} > 100$ GeV/c were found to contain track with p_{T} above 50 GeV/c. The track p_{T} resolution was verified by cosmic muon events and the width of the invariant mass distributions of K^0_{s}, Λ and $\bar{\Lambda}$ [17]. It was found that the resolution does not vary significantly with the collision centrality.

Tracking efficiency was estimated based on simulations using GEANT3 and HIJING event generator. In 0–10% central collisions, it is about 60% at 0.15 GeV/c, 90% at 1.5 GeV/c, and then decreases to $\sim 86\%$ for $p_{\mathrm{T}} \geq 2.5$ GeV/c. In peripheral events the track finding efficiency is $\sim 2\%$ larger than in central collisions due to the lower track multiplicity [19]. For p–Pb collisions, the efficiency is $\sim 70\%$ at $p_{\mathrm{T}} = 0.15$ GeV$/c$ and increases to $\sim 85\%$ for $p_{\mathrm{T}} \geq 1$ GeV$/c$ [26].

9.2.2 Jet Reconstruction and Background Subtraction

Jets were reconstructed with aniti-k_{T} algorithm from the FastJet package [412], with resolution parameters $R = 0.2$, 0.3 and 0.4, where the transverse momentum of a jet, $p^{\mathrm{rec}}_{\mathrm{T,ch\ jet}}$, is calculated with the boost-invariant p_{T} recombination scheme. Only jets fully contained in the acceptance, i.e. jets with the jet-axis separated from edge of the track acceptance in η by at least R, $|\eta_{\mathrm{jet}}| < \eta - R$, are considered in the analysis.

The area, A, for each jet is determined using the active area method as implemented in FastJet [413]. It is realized by adding *ghost particles* with very small momentum ($\sim 10^{-100}$ GeV/c) to the event, and the number of ghost particles in a jet measures the area. Ghost particles are uniformly generated over the tracking acceptance ($0 < \phi < 2\pi$, $|\eta| < 0.9$) with density of 200 ghost particles per unit area.

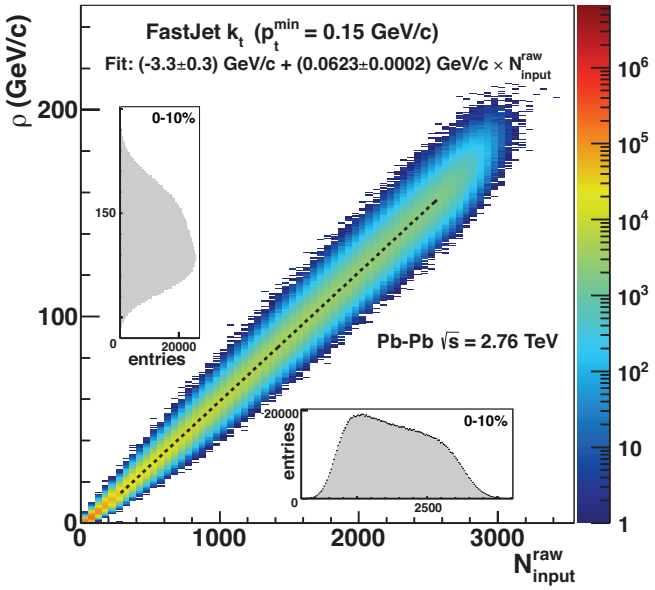

Fig. 9.2 The median of charged-particle background p_{T} density, $\rho_{\mathrm{ch}} = \mathrm{median}\{p^{i}_{\mathrm{T,ch\ jet}}/A^{i}\}$, as a function of the reconstructed (raw) track multiplicity used for the jet finding in $|\eta| < 0.9$ [411]. The dotted line is a linear fit to the centroids in each multiplicity bin. The insets show the projected distributions of ρ_{ch} and raw multiplicity for the 0–10% central events.

In Pb–Pb events, the large background consisting of particles from soft scattering processes as well as fragments from other jets, is subtracted using the procedure proposed in Refs. [410, 414]. The background is measured on an event-by-event basis by clustering all particles using k_{T} algorithm and determining the median of the transverse momentum density, $\rho_{\mathrm{ch}} = \mathrm{median}\{p^{\mathrm{i}}_{\mathrm{T,ch\ jet}}/A^{\mathrm{i}}\}$, of all clusters i in the event, excluding the leading and sub-leading clusters to limit the impact of the hard jet signal on the background estimate. The ρ_{ch} as a function of the reconstructed (raw) track multiplicity used for the jet finding in $|\eta| < 0.9$ [411],

is shown in Fig. 9.2. It reaches up to ~ 200 GeV/c for the most central collisions, for input tracks with momenta $p_{\mathrm{T}} > 0.15$ GeV/c. For the 0–10% central Pb–Pb collisions, the average p_{T}-density $\langle \rho_{\mathrm{ch}} \rangle = 138 \pm 0.02$ GeV/c, with a spread $\sigma(\rho_{\mathrm{ch}}) = 18.51 \pm 0.01$ GeV/c [411].

The signal anti-k_{T} jets in Pb–Pb events are then corrected for the average background contribution using the median ρ_{ch} [19],

$$p_{\mathrm{T,ch\ jet}} = p^{\mathrm{rec}}_{\mathrm{T,ch\ jet}} - \rho_{\mathrm{ch}} \cdot A, \tag{9.3}$$

where $p_{\mathrm{T,ch\ jet}}$ is a background subtracted jet p_{T}, $p^{\mathrm{rec}}_{\mathrm{T,ch\ jet}}$ is uncorrected jet p_{T} and A is the area of the anti-k_{T} signal jet. In order to obtain a reliable background estimate for the more sparse environment of p–Pb events a modified version of the Pb–Pb algorithm was employed [26]. It contains additional factor C to account for the phase-space regions without particles, which would otherwise not contribute to the overall area estimate. The background density for each event is then given by $\rho_{\mathrm{ch}} = \mathrm{median}\{p^{\mathrm{i}}_{\mathrm{T,ch\ jet}}/A^{\mathrm{i}}\} \cdot C$, where C is defined as

$$C = \frac{\sum_{\mathrm{j}} A^{\mathrm{j}}_{k_{\mathrm{T}}}}{A_{\mathrm{acc}}}, \tag{9.4}$$

where $\sum_{\mathrm{j}} A^{\mathrm{j}}_{k_{\mathrm{T}}}$ is the area of all k_{T} jets containing tracks, and A_{acc} is the full acceptance area ($2 \times \Delta\eta \times 2\pi$) in which charged particles are considered for the jet finding. The mean background density and its variance for all events is $\langle \rho_{\mathrm{ch}} \rangle = 1.02 \pm 0.0$ GeV/c, with a spread $\sigma(\rho_{\mathrm{ch}}) = 0.91 \pm 0.01$ GeV/c [26]. For events containing a high-p_{T} jets with $p^{\mathrm{rec}}_{\mathrm{T,\ ch.\ jet}} > 20$ GeV/c, it increases to $\langle \rho_{\mathrm{ch}} \rangle = 2.2 \pm 0.01$ GeV/c and $\sigma(\rho_{\mathrm{ch}}) = 1.47 \pm 0.09$ GeV/c [26], as expected due to larger underlying event activity (see Ref. [415] for more details). The inclusive jet distribution is then corrected via unfolding to account for background fluctuations and detector effects. Due to the presence of collective effects such as elliptic and triangular flow in heavy-ion collisions the background density differs from region-to-region. The jets with the high p_{T} leading track requirement are preferentially found in the regions of high background density (in reaction plane). Therefore, the correction for the larger background for these jets was also included in the response matrix.

9.2.3 Background Fluctuations

Jet which originate from a hard scattering contain a large amount of uncorrelated, mostly soft, background particles. The background subtraction procedure described in Sec. 9.2.2 removes the background energy on average, but the background has large region-to-region fluctuations in the event due to statistical fluctuations of the particle number and momentum as well as collective phenomena like elliptic flow. Low energy jets, for example with a momentum below 5 GeV/c, are also subject to background fluctuations, as discussed in detail in Ref. [411].

The effect of the background fluctuations was accounted for on a statistical basis in the unfolding of the measured jet p_{T} distributions. The fluctuations were quantified by placing randomly cones (RC) with the jet resolution parameter R within the acceptance of the measured

jets, $|\eta_{\mathrm{RC}}| < 0.5$ and $0 < \phi < 2\pi$. The transverse momenta for all tracks (charged particles), $p^{\mathrm{i}}_{\mathrm{T,ch}}$, falling into this cone were summed, and the difference

$$\delta p_{\mathrm{T}}^{\mathrm{ch}} = \sum_{\mathrm{i}}^{\mathrm{RC}} p^{\mathrm{i}}_{\mathrm{T,ch}} - \rho_{\mathrm{ch}} \cdot A, \tag{9.5}$$

was calculated. The $\delta p_{\mathrm{T}}^{\mathrm{ch}}$ represents the statistical (region-to-region) fluctuations of the background. An alternative method to quantify the background fluctuations was also used in which high p_{T} probes were embedded into the Pb–Pb events [411]. The events with the embedded probes were clustered with the anti-k_{T} algorithm and the background fluctuations were calculated as

$$\delta p_{\mathrm{T}}^{\mathrm{ch}} = p^{\mathrm{rec}}_{\mathrm{T,ch\ jet}} - \rho_{\mathrm{ch}} \cdot A - p_{\mathrm{T}}^{\mathrm{probe}}, \tag{9.6}$$

with respect to the transverse momentum $p_{\mathrm{T}}^{\mathrm{probe}}$ of the embedded probe.

Figure 9.3 shows the probability distribution of background fluctuations $\delta p_{\mathrm{T}}^{\mathrm{ch}}$ for the 0–10% central collisions (left) and the standard deviation of the background fluctuations $\sigma(\delta p_{\mathrm{T}}^{\mathrm{ch}})$ as a function of collision centrality (right), for the two jet resolution parameters used in the analysis [19]. The fluctuations of the background depend strongly on the jet resolution parameter and centrality. One can note that the $\delta p_{\mathrm{T}}^{\mathrm{ch}}$ distributions are asymmetric (Fig. 9.3, left) and fluctuations towards larger jet p_{T} are more probable than to lower p_{T}. It is due to the steeply falling p_{T}-spectrum that favors low-p_{T} jets with upward fluctuations over high-p_{T} jets with downward fluctuations at a given p_{T}. The $\sigma(\delta p_{\mathrm{T}}^{\mathrm{ch}})$ reaches $\sim 4.47(7.15)$ GeV/c for resolution parameter $R = 0.2(0.3)$ in the 0–10% central collisions and decreases to $\sim 1.02(1.61)$ GeV/c in the 50–80% central collisions (Fig. 9.3, right), respectively. The statistical uncertainties are less than 0.004 GeV/c due to the large sample of random cones. The upper edge of the shaded boxes indicates the $\sigma(\delta p_{\mathrm{T}}^{\mathrm{ch}})$ obtained with high-p_{T} probe embedding, where single tracks with $20 < p_{\mathrm{T}}^{\mathrm{probe}} < 110$ GeV/c were embedded in the heavy-ion events. For p–Pb collisions, the same method based on the random cones was applied to determine the background fluctuations (see Ref. [26] for more details).

9.2.4 Detector Effects on Jet Reconstruction

The jet response in the ALICE detector for Pb–Pb and p–Pb collisions has been evaluated [19, 26] using simulations with the PYTHIA6 (Perugia0 [416] and Perugia-2011 [417] tunes) event generator and GEANT3 for the detector response. It is determined on a jet-by-jet basis by comparing jets before (particle level jets) and after detector simulations (detector level jets), which are geometrically matched. The particle level jets are clustered from primary charged particles [367] produced by the event generator.

The detector effects that influence the jet energy scale and resolution are the charged particle tracking efficiency and the transverse momentum resolution, with the tracking efficiency being

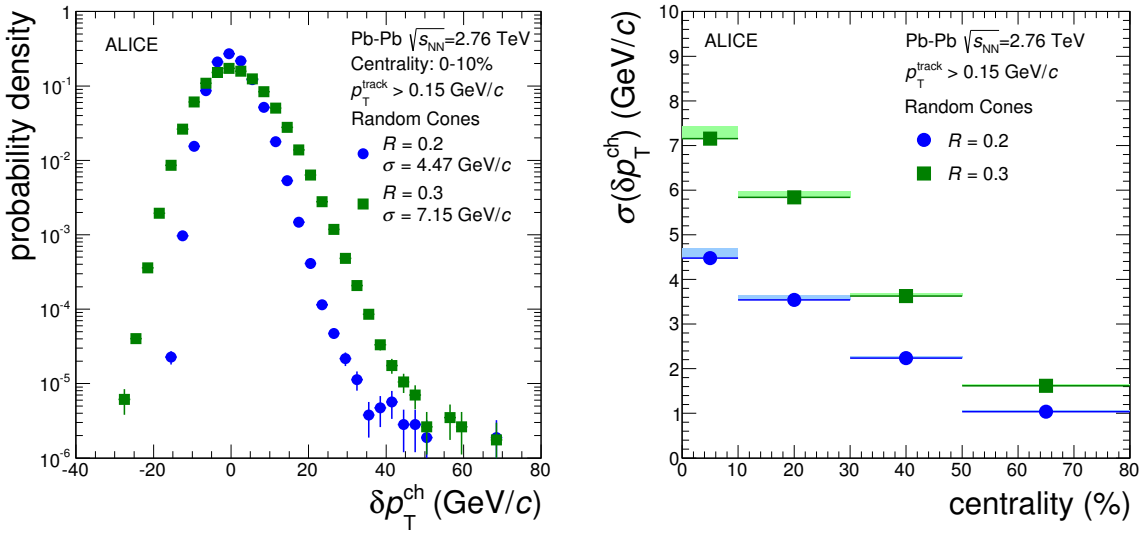

Fig. 9.3 Left: The jet background $\delta p_{\mathrm{T}}^{ch}$ distribution for jets with resolution parameter $R = 0.2$ and $R = 0.3$ determined with random cones in the 0–10% central collisions, for tracks with $p_{\mathrm{T}} > 0.15$ GeV/c. Right: The standard deviation of the background fluctuations $\sigma(\delta p_{\mathrm{T}}^{ch})$ as a function of collision centrality for $R = 0.2$ and $R = 0.3$. The shaded bands indicate systematic uncertainties estimated as difference between the width of the $\delta p_{\mathrm{T}}^{ch}$ from random cones and alternative method based on high p_{T} probe embedding. Both figures are taken from Ref. [19].

the dominant contributor. The finite p_{T} resolution of reconstructed tracks has a small effect on the jet energy resolution because the majority of the jet constituents have moderate p_{T}, where the tracking resolution is good. In addition, since the transverse momentum of the jet is the sum of the transverse momentum of independently measured tracks, the relative momentum resolution is in general better than that of individual tracks.

Fig. 9.4 (left) shows the mean of the relative difference between the transverse momenta of detector and particle level jets, $\left\langle \left(p_{\mathrm{T,ch\ jet}}^{\mathrm{det}} - p_{\mathrm{T,ch\ jet}}^{\mathrm{part}} \right) / p_{\mathrm{T,ch\ jet}}^{\mathrm{part}} \right\rangle$, as a function of the jet momentum at particle level, for the 0–10% central Pb–Pb collisions [19]. For inclusive jets the reconstructed jet momentum is 14–19% lower than the generated momentum, with a weak p_{T} dependence. The mean of the jet response is also shown for leading track biased jets, i.e. for the jets with the leading track momentum $p_{\mathrm{T}}^{\text{leading track}} > 5$ and 10 GeV/c. Those jets whose leading track is not reconstructed in the detector are rejected from the sample. This results in an improved jet energy resolution at low jet p_{T}.

The jet-finding efficiency (Fig. 9.4, right) is obtained by taking the ratio between the spectra of the particle level jets which have a detector level partner, and all particle level jets. For the leading track biased jets, the numerator consists of jets fulfilling the high p_{T} track requirement on detector level and the denominator are all particle level jets with a high p_{T} generated particle. The jet-finding efficiency for the inclusive (unbiased) jets is around unity for high p_{T}

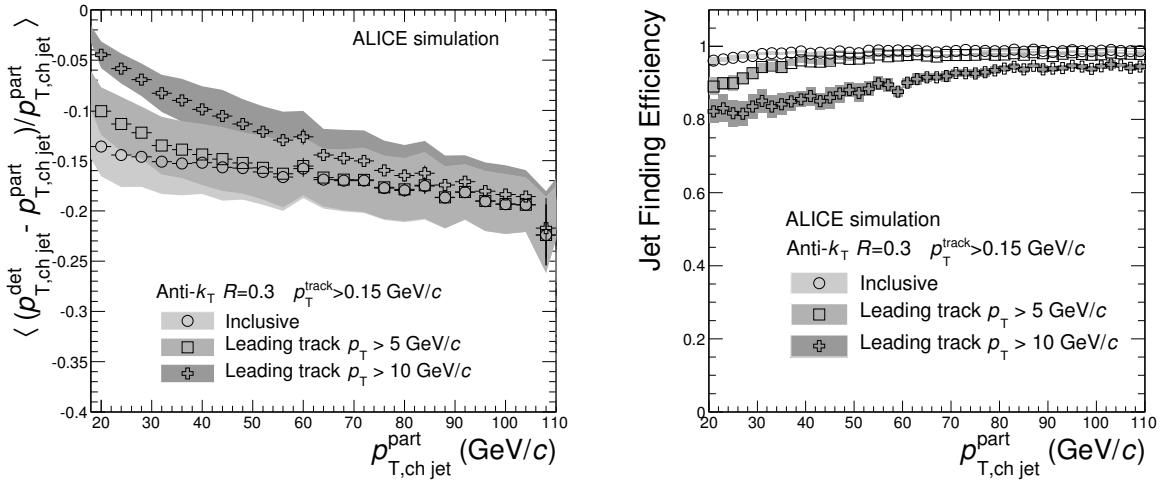

Fig. 9.4 Left: Mean of the relative difference between the detector and particle level jet p_{T} as a function of the particle level jet p_{T} for jets with resolution parameter $R = 0.3$, determined for the 0–10% central Pb–Pb collisions with the full ALICE detector simulations [19]. Systematic uncertainty originates from the uncertainty on the tracking efficiency. Right: Jet-finding efficiency for inclusive (unbiased) and leading track biased jets with resolution parameter $R = 0.3$ based on the ALICE detector simulation for the 0–10% central Pb–Pb collisions. Both figures are taken from Ref. [19].

jets. and reduces to $\sim 95\%$ for $p_{\mathrm{T}} < 20$ GeV/c due to migration of the jet axis outside the η acceptance. For leading track biased jets, the jet-finding efficiency is reduced by $\sim 5\%$ and $\sim 20\%$ for $p_{\mathrm{T}}^{\text{leading track}} > 5$ and 10 GeV/c, respectively, which is consistent with the charged particle tracking efficiency. In general, the jet-finding efficiency depends on the resolution parameter and is smaller at low p_{T} for jets with $R = 0.2$ than for jets with $R = 0.3$. It is almost independent of collision centrality and collision system.

9.2.5 Unfolding Procedure

Both background fluctuations and detector effects lead to smearing of the measured jet momentum in heavy ion collisions. These effects can be corrected for using an unfolding procedure [418–420]. The relation between the measured spectrum $\mathbf{M}_{\mathrm{m}}$ and the true jet spectrum $\mathbf{T}_{\mathrm{t}}$ is given by

$$\mathbf{M}_{\mathrm{m}} = \mathbf{R}_{\mathrm{m,t}}^{\mathrm{tot}} \cdot \mathbf{T}_{\mathrm{t}} = \mathbf{R}_{\mathrm{m,d}}^{\mathrm{bkg}} \cdot \mathbf{R}_{\mathrm{d,t}}^{\mathrm{det}} \cdot \mathbf{T}_{\mathrm{t}}, \tag{9.7}$$

where $\mathbf{R}_{\mathrm{d,t}}^{\mathrm{det}}$ is the response matrix for detector effects including efficiency, $\mathbf{R}_{\mathrm{m,d}}^{\mathrm{bkg}}$ is the response matrix for background fluctuations, and $\mathbf{R}_{\mathrm{m,t}}^{\mathrm{tot}} = \mathbf{R}_{\mathrm{m,d}}^{\mathrm{bkg}} \cdot \mathbf{R}_{\mathrm{d,t}}^{\mathrm{det}}$ it the total response matrix

including detector effects and background fluctuations.The indices m, d, and t indicate the bin number.

Figure 9.5 shows the width of the combine response $\sigma(p^{\text{det}}_{\text{T,ch jet}})/p^{\text{part}}_{\text{T,ch jet}}$ as a function of $p^{\text{part}}_{\text{T,ch jet}}$ obtained for the two jet resolution parameters for the 0–10% central Pb–Pb collisions. The width was determined by the Gaussian fit to the $(p^{\text{det}}_{\text{T,ch jet}} - p^{\text{part}}_{\text{T,ch jet}})/p^{\text{part}}_{\text{T,ch jet}}$ distributions. It can be observed that the dominant correction at low momenta originates from the background fluctuations, while at high p_{T} the detector effects dominate. Moreover, the contribution from background fluctuations significantly increases for the jets with the larger resolution parameter.

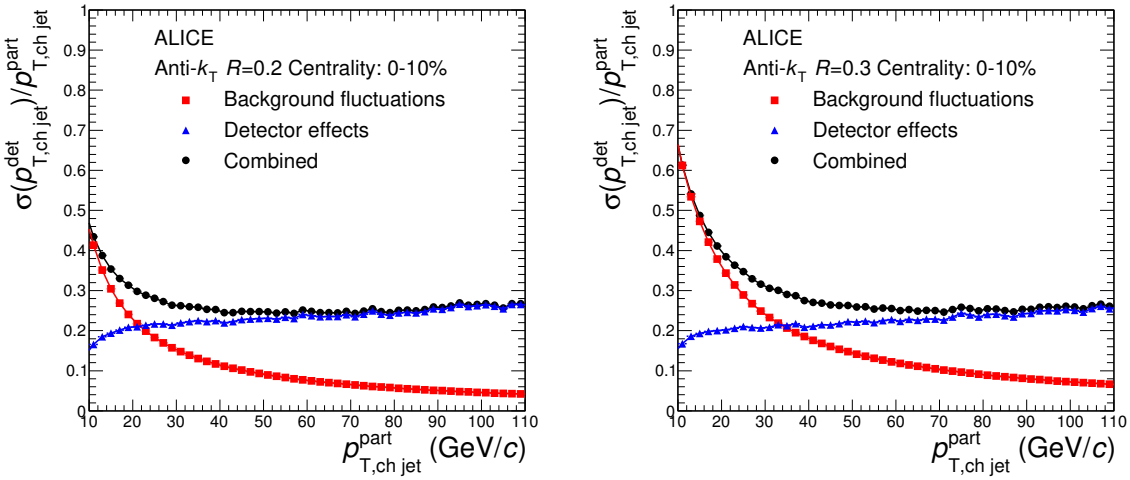

Fig. 9.5 Combined jet response for charged jets for the two resolution parameters $R = 0.2$ (left) and $R = 0.3$ (right), including background fluctuations and detector effects for the 0–10% central Pb–Pb collisions. Both figures are taken from Ref. [19].

The true jet spectrum was obtained by inverting the response matrix based on three algorithms including the χ^2 method with log-log regularization [19], the Singular Value Decomposition (SVN) method as implemented in RooUnfold [421], and the Bayesian method [419, 422]. It was found in a closure test with a thermal background model that the Bayesian method does not converge properly for this case, while the other two methods give similar results. The covariance matrix $\text{cov}(x,y)$ for the unfolded result is calculated by propagating the measurement errors in the unfolding and/or using Monte Carlo variations of the input spectra. The statistical uncertainties on the unfolded data points are the square root of the diagonal elements of the covariance matrix of the unfolded spectrum. For more details see Ref. [19]. The same unfolding procedure was applied for p–Pb collisions [26].

9.2.6 Systematic Uncertainties

The systematic uncertainties on the jet p_{T} spectra were evaluated by varying a number of key parameters in the correction procedure and by using different unfolding methods. The different contributions to the resulting systematic uncertainties for charged jet measurement in Pb–Pb collisions are outlined in this section (see Ref. [19] for more details). The same contributions were considered in analysis of p–Pb data and are discussed in detail in Ref. [26].

The contributions to systematic uncertainties on the p_{T} spectra of charged jets with a leading track momenta $p_{\mathrm{T}} > 5$ GeV/c for Pb–Pb collisions are listed in Tab. 9.1. The were determined using the following procedure:

- The uncertainties from the regularization and the unfolding procedure were evaluated by changing the regularization strength in the χ^2 approach, by comparing the results from unfolding methods, and by varying the input distribution (prior) to the unfolding algorithm. However, the Bayesian method was only included for the cases when combinatorial jets were suppressed requiring jets with a leading track with $p_{\mathrm{T}} > 5$ GeV/c or $p_{\mathrm{T}} > 10$ GeV/c. Without this selection, the Bayesian method was found to be unreliable due to large deviations at the low jet p_{T} with respect to the other unfolding methods. The prior was varied using several distributions, including the measured jet p_{T} spectrum, the pQCD inspired p_{T} spectrum or uniform p_{T} distribution. The choice of prior has a negligible effect on the final unfolded spectrum.
- The effect of combinatorial jets in the sample is evaluated by changing the minimum p_{T} of the unfolded jet spectrum and of the measured spectrum where the unfolding is applied. The minimum p_{T} of unfolded spectrum was shifted from $p_{\mathrm{T,ch\ jet}} = 0$ to $p_{\mathrm{T,ch\ jet}} = 5$ GeV/c and $p_{\mathrm{T,ch\ jet}} = 10$ GeV/c. The minimum p_{T} of the measured jet spectrum was varied by ± 10 GeV/c.
- The uncertainties on the jet background include the background fluctuations (δp_{T}) and corrections for collective flow effects. The δp_{T} uncertainty was obtained by comparing the δp_{T} response from the single-track embedding and the response from the random cones. The uncertainty due to flow effects was calculated by changing the background density, ρ_{ch} (Eq. 9.3), to the lowest and highest values found in the different azimuthal regions corresponding to perpendicular and near-side regions, respectively.
- The detector response has two main components: tracking efficiency and momentum resolution of which the tracking efficiency is the dominant uncertainty. They were estimated by using detector simulations with PYTHIA6 and HIJING event generators and by varying the track selection criteria.
- The relative uncertainty on the fraction of hadronic cross-section used in the Glauber fit to determine the centrality classes ($\sim 1\%$) was propagated to the jet spectrum by varying the limits of the centrality intervals by $\pm 1\%$.

The total systematic uncertainties were separated into two classes for the anti-correlated (shape) and correlated uncertainties over the entire p_{T} range. The shape uncertainties include

Centrality class	Resolution parameter	$R = 0.2$		$R = 0.3$	
	p_{T}-interval (GeV/c)	30–40	70–80	30–40	70–80
0–10%	Regularisation	$^{+3.4}_{-0.0}$	$^{+2.3}_{-0.3}$	$^{+9.9}_{-0.0}$	$^{+2.6}_{-6.7}$
	Unfolding method	$^{+0.0}_{-3.5}$	$^{+0.0}_{-1.1}$	$^{+0.0}_{-7.3}$	$^{+7.6}_{-0.0}$
	Minimum p_{T} unfolded	$^{+9.6}_{-0.0}$	$^{+0.3}_{-0.0}$	$^{+0.0}_{-5.9}$	$^{+0.0}_{-1.8}$
	Minimum p_{T} measured	$^{+1.7}_{-4.8}$	$^{+0.2}_{-0.3}$	$^{+0.0}_{-13}$	$^{+0.0}_{-2.1}$
	Prior	< 0.1			
	δp_{T}	$^{+0.0}_{-4.9}$	$^{+0.0}_{-2.1}$	$^{+0.0}_{-27}$	$^{+0.0}_{-4.6}$
	Detector effects	± 2.7	± 5.5	± 4.6	± 5.2
	Flow bias	$^{+0.9}_{-5.8}$	$^{+0.4}_{-4.1}$	$^{+7.3}_{-5.9}$	$^{+4.8}_{-4.1}$
	Centrality determination	0.8			
	Total shape uncertainty	$^{+10}_{-7.6}$	$^{+2.4}_{-2.4}$	$^{+9.9}_{-31}$	$^{+7.6}_{-8.6}$
	Total correlated uncertainty	$^{+2.9}_{-6.4}$	$^{+5.6}_{-6.9}$	$^{+8.6}_{-7.5}$	$^{+7.1}_{-6.6}$
50–80%	Regularisation	$^{+0.0}_{-5.5}$	$^{+13}_{-4.1}$	$^{+0.1}_{-5.1}$	$^{+17}_{-2.2}$
	Unfolding method	$^{+2.1}_{-0.0}$	$^{+0.0}_{-20}$	$^{+2.3}_{-0.0}$	$^{+0.0}_{-20}$
	Minimum p_{T} unfolded	$^{+0.3}_{-0.0}$	$^{+0.1}_{-0.0}$	$^{+1.0}_{-0.0}$	$^{+0.6}_{-0.0}$
	Minimum p_{T} measured	$^{+9.3}_{-0.0}$	$^{+0.7}_{-0.4}$	$^{+7.5}_{-0.0}$	$^{+1.0}_{-0.0}$
	Prior	< 0.1			
	δp_{T}	$^{+8.2}_{-0.0}$	$^{+2.4}_{-0.0}$	$^{+3.0}_{-0.0}$	$^{+2.2}_{-0.0}$
	Detector effects	± 3.3	± 6.2	± 3.3	± 3.1
	Flow bias	$^{+1.9}_{-1.9}$	$^{+0.3}_{-0.3}$	$^{+0.4}_{-7.2}$	$^{+0.3}_{-4.0}$
	Centrality determination	1.9			
	Total shape uncertainty	$^{+13}_{-5.5}$	$^{+13}_{-20}$	$^{+8.5}_{-5.1}$	$^{+17}_{-20}$
	Total correlated uncertainty	$^{+4.2}_{-4.2}$	$^{+6.5}_{-6.5}$	$^{+3.8}_{-8.2}$	$^{+3.6}_{-5.4}$

Table 9.1 Overview of systematic uncertainties for jet spectra with a leading track with $p_{\mathrm{T}} > 5$ GeV/c [19]. Relative uncertainties are given in percentiles for two p_{T}-intervals and two different centrality intervals.

the contributions from the unfolding and background fluctuations, while the contributions to the correlated uncertainties include the detector response, collective flow in the background, and the effect of combinatorial jets. For both cases, the corresponding contributions are added in quadrature.

9.3 p_{T} Spectra in Pb–Pb Collisions at $\sqrt{s_{\mathrm{NN}}} = 2.76$ TeV

Figure 9.6 shows charged jet p_{T} spectra measured at mid-rapidity ($|\eta_{\mathrm{jet}}| < 0.5$) with resolution parameters $R = 0.2$ (left panels) and $R = 0.3$ (right panels) for the 0–10%, 10–30%, 30–50% and 50–80% central Pb–Pb collisions at $\sqrt{s_{\mathrm{NN}}} = 2.76$ TeV [19]. The presented spectra are based on the 12.8×10^6 minimum-bias Pb–Pb collisions in the centrality range 0–80%, collected by ALICE in 2010. The jets reconstructed from charged constituents with $p_{\mathrm{T}} > 0.15$ GeV/c and $|\eta| < 0.9$, were corrected for detector effects and background fluctuations, and for the jet finding efficiency as described in the previous sections. The upper panels show the inclusive jet spectra, while the middle and lower panels show the jet spectra with a leading track momenta $p_{\mathrm{T}} > 5$ GeV/c and $p_{\mathrm{T}} > 10$ GeV/c.

The jet yield is given per event and normalized by the average number of nucleon-nucleon collisions N_{coll} corresponding to the given centrality interval. The jet yield evolves with centrality and for central collisions smaller number of jets are observed per N_{coll} than in peripheral collisions. The p_{T} range of measured jets depends on the jet selection criteria and available statistics. The momentum range is extended towards lower p_{T} for jets with a leading track selection, for which the background from combinatorial jets is reduced and unfolding procedure is more stable.

The ratio of p_{T} spectra of charged jets with $R = 0.2$ and $R = 0.3$ measured in the 0–10% and 50–80% central Pb–Pb collisions are compared to that from PYTHIA6 pp simulations in Fig. 9.7 [19]. All ratios agree within uncertainties showing that the transverse jet shape in central and semi-peripheral Pb–Pb collisions are consistent with jet shapes in vacuum. No sign of a modified jet structure is observed between $R = 0.2$ and $R = 0.3$. In addition, it is shown that the effect of selecting jets with a leading hadron with $p_{\mathrm{T}} > 5$ GeV/c or $p_{\mathrm{T}} > 10$ GeV/c is similar in Pb–Pb collisions and in PYTHIA pp events, indicating that the longitudinal momentum distribution of high p_{T} (leading) tracks in jets reconstructed in Pb–Pb collisions remains unmodified. This observation is in qualitative agreement with measurements of jet fragmentation properties by CMS [217, 423] and ATLAS [214].

9.4 p_{T} Spectra in p–Pb Collisions at $\sqrt{s_{\mathrm{NN}}} = 5.02$ TeV

Figure 9.8 shows the p_{T}-differential production cross section for charged jets measured in minimum-bias p–Pb collisions at $\sqrt{s_{\mathrm{NN}}} = 5.02$ TeV for resolution parameters $R = 0.2$ (left) and $R = 0.4$ (right) [26]. The p–Pb data were taken with the ALICE detector in 2013. In total, about 96×10^6 events were used for the analysis. The p_{T}-differential cross sections were obtained using the interaction p–Pb cross section, $\sigma_{\mathrm{V0}} = 2.09 \pm 0.07$ b, from the van der Meer scan [424].

The spectra are found to be in agreement with the scaled NLO pQCD calculations from POWEG [425, 426] combined with PYTHIA8, with PDF of proton (CTEQ6.6 [379]) corrected for the medium effects (EPS09 [198]), as shown in the lower panels. One can see that

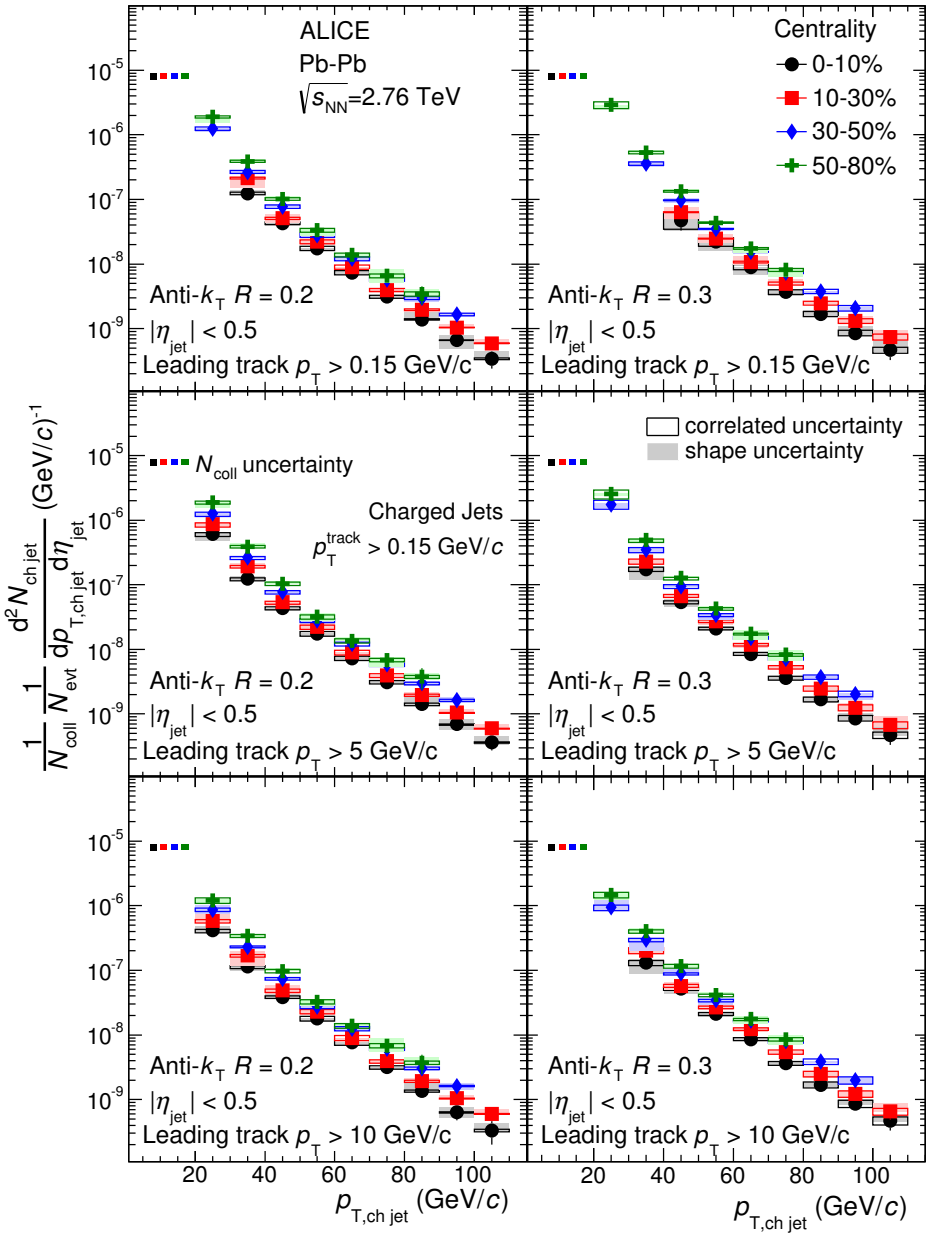

Fig. 9.6 Transverse momentum spectra of charged jets with resolution parameters $R = 0.2$ (left panels) and $R = 0.3$ (right panels) corrected for background fluctuations and detector effects [19]. The spectra are shown for three set of jets with different leading track selections: unbiased (top panels), $p_{\mathrm{T}}^{\text{leading track}} > 5$ GeV/c (middle panels), and $p_{\mathrm{T}}^{\text{leading track}} > 10$ GeV/c (lower panels). The spectra are scaled by corresponding $1/N_{\mathrm{coll}}$ for comparison. The boxes around data points denote correlated (open symbols) and uncorrelated (filled symbols) systematic uncertainties. The uncertainty bands for $p_{\mathrm{T,ch\ jets}} < 20$ GeV/c indicate normalization uncertainty related to the N_{coll} scaling.

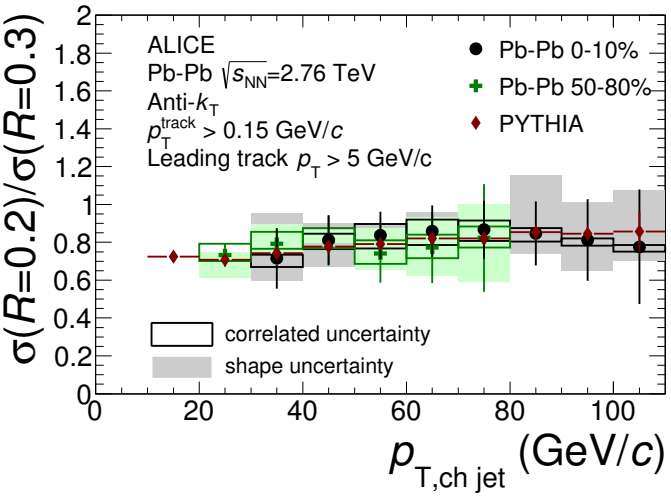

Fig. 9.7 Ratio of charged jet p_{T}-spectra with radius parameter $R = 0.2$ and 0.3 and a leading charged particle $p_{\mathrm{T}}^{\text{leading track}} > 5$ GeV$/c$ in Pb–Pb data and simulated PYTHIA events [19].

the effect of the nuclear PDFs on the jet production in the reported kinematic regime is almost negligible.

In Fig. 9.8 (left) the jet spectra for $-0.65 < \eta_{\mathrm{lab}} < -0.25$ and $0.25 < \eta_{\mathrm{lab}} < 0.65$ are compared to results from the symmetric selection $|\eta_{\mathrm{lab}}| < 0.5$ [26]. Here, the η_{lab} denotes the pseudorapidity of the jet axis. The first selection roughly corresponds to a small window around mid-rapidity for the nucleon-nucleon center-of-mass system, while the second is separated from it by about one unit in rapidity. No significant change of the jet spectra is observed for these two pseudorapidity regions. Thus, the jet measurement has no strong sensitivity to the rapidity shift.

The ratio of charged jet production cross sections for two different resolution parameters, $R = 0.2$ and $R = 0.4$, is shown in Fig. 9.9 [26]. It can be used to test the possible cold nuclear matter effects on the jet structure in p–Pb collisions. The ratio in p–Pb is compared to the ratio from PYTHIA6 (Perugia 2011 tune) and NLO pQCD (POWHEG+PYTHIA8 with nuclear PDFs) calculations at $\sqrt{s_{\mathrm{NN}}} = 5.02$ TeV and to ALICE results in pp collisions at $\sqrt{s}$ = 7 TeV [406]. All ratios show the expected increase with the jet p_{T} due to increasing collimation of jets for higher transverse momentum and agree within the uncertainties. No significant energy dependence or change with collision systems is observed. The p–Pb ratio is well described by the NLO pQCD as well as by the PYTHIA6 pp simulations at the same collision energy.

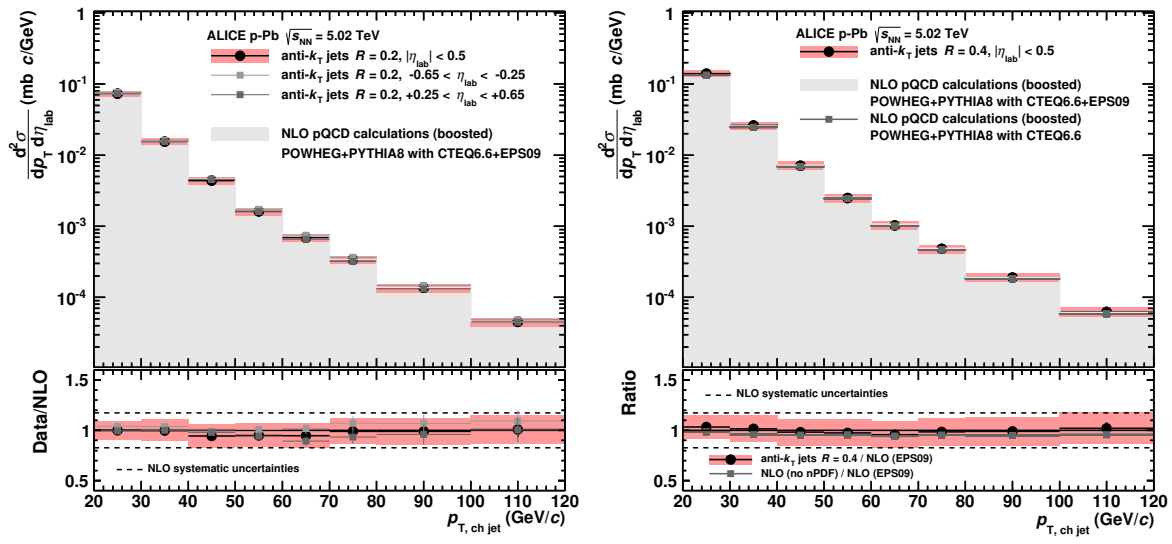

Fig. 9.8 The p_{T}-differential production cross section of charged jets measured with resolution parameters $R = 0.2$ (left) and $R = 0.4$ (right) in p–Pb collisions at $\sqrt{s_{\mathrm{NN}}} = 5.02$ TeV [26]. The spectra are compared to NLO pQCD calculations (POWEG+PYTHIA8) [425, 426] with nuclear PDFs (CTEQ6.6 + EPS09) [198, 379]. The boxes around data points denote p_{T}-dependent systematic uncertainties. The normalization uncertainty of 3.5% is not shown. The uncertainties on the pQCD calculation are only shown in the ratio plot as dashed lines (lower panels). The pQCD calculations take into account the rapidity shift of the nucleon-nucleon center-of-mass system in p–Pb with a boosted parton system.

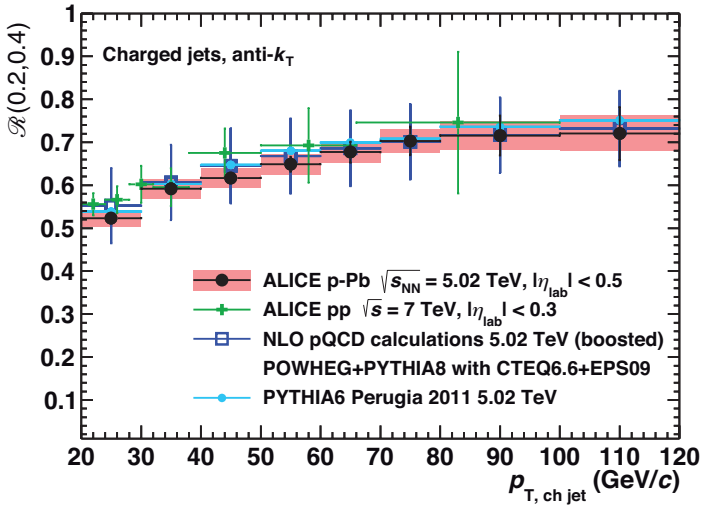

Fig. 9.9 Charged jet production cross section ratio for different resolution parameters. The data in p–Pb collisions at $\sqrt{s_{\mathrm{NN}}} = 5.02$ TeV [26] are compared to PYTHIA6 (Perugia-2011 tune, no uncertainties are shown) and POWHEG+PYTHIA8 (combined stat. and syst. uncertainties are shown) at the same energy, and to pp collisions at $\sqrt{s} = 7$ TeV (only stat. uncertainties are shown) [406].

Chapter 10
Measurement of Nuclear Modification Factors of Charged Particles

In order to quantify nuclear effects the nuclear modification factors were determined for Pb–Pb and p–Pb collisions at the LHC. The p–Pb measurements were needed to establish whether the initial state of colliding nuclei plays a role in the production of hard probes. The nuclear modification factors of charged particles [15–17, 21, 22, 28], which were obtained by author, are presented in this chapter. The comparison with other measurements at RHIC and at the LHC, and with model calculations, is also discussed.

10.1 R_{pPb} of Charged Particles

Figure 10.1 shows the nuclear modification factor R_{pPb} for charged particles at $|\eta_{\mathrm{cms}}| < 0.3$ (left) and at $-0.3 < \eta_{\mathrm{cms}} < 1.3$ (right) measured in NSD p–Pb collisions at $\sqrt{s_{\mathrm{NN}}} = 5.02$ TeV [16, 21, 28]. The first R_{pPb} measurement at the LHC was performed for charged particles with $0.5 < p_{\mathrm{T}} < 20$ GeV/c and $|\eta_{\mathrm{cms}}| < 0.3$, for data collected in 2012 [16]. The R_{pPb} measurement was later extended for particles with $0.15 < p_{\mathrm{T}} < 50$ GeV/c using higher statistics of p–Pb data collected in 2013 [21]. The pp reference spectrum used for the determination of R_{pPb} was constructed based on measurements at different collision energies, as described in Sec. 6.3.2. The resulting R_{pPb} are compared in Fig. 10.1 (left). The R_{pPb} measured in the broader pseudorapidity range $-0.3 < \eta_{\mathrm{cms}} < 1.3$ [21] is compared in Fig. 10.1 (right) with the R_{pPb} from the reanalysis of p–Pb data, determined with the measured pp reference at the same collision energy of $\sqrt{s} = 5.02$ TeV [28].

One can note that the R_{pPb} is consistent with unity for $p_{\mathrm{T}} \geq 2$ GeV/c. R_{pPb} shows a small maximum at $p_{\mathrm{T}} \approx 4$ GeV/c, in the p_{T} region where a strong Cronin effect is seen at lower energy p–A collisions [292, 427, 428]. At RHIC, in d–Au collisions at $\sqrt{s_{\mathrm{NN}}} = 200$ GeV, R_{dAu} reaches values of about 1.4 for charged hadrons with $3 < p_{\mathrm{T}} < 5$ GeV/c [282, 284, 290, 291]. The present measurement clearly indicates a small magnitude of the Cronin effect at the LHC energies. The data are consistent with no enhancement within systematic uncertainties. For the region of several tens of GeV, binary collision scaling was experimentally confirmed in Pb–Pb collisions at the LHC by the measurements of electroweak bosons, direct photons [429], Z^0

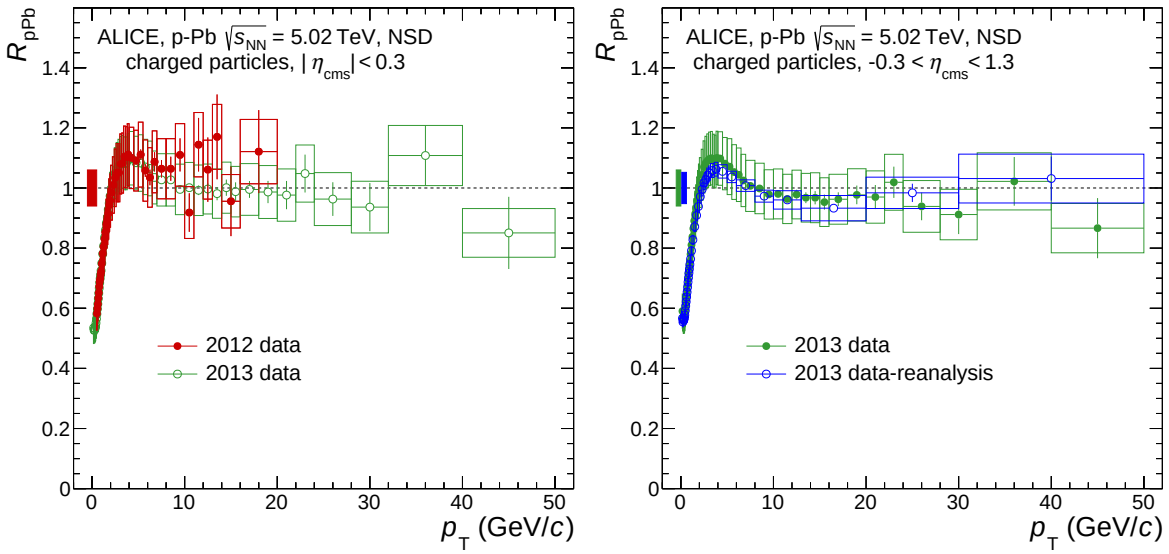

Fig. 10.1 Left: R_{pPb} as a function of p_{T} for charged particles measured in $|\eta_{\mathrm{cms}}| < 0.3$, in NSD p–Pb collisions at $\sqrt{s_{\mathrm{NN}}} = 5.02$ TeV collected in 2012 [16] and 2013 [21]. Right: R_{pPb} of charged particles measured in $-0.3 < \eta_{\mathrm{cms}} < 1.3$, in NSD p–Pb collisions at $\sqrt{s_{\mathrm{NN}}} = 5.02$ TeV collected in 2013 [21], in comparison with the results from the reanalysis of p–Pb data with the measured pp reference at $\sqrt{s} = 5.02$ TeV [28]. The p_{T}-dependent systematic uncertainties are shown as the boxes around data points. The normalization uncertainties including normalization of pp and p–Pb spectra and $\langle T_{\mathrm{AA}} \rangle$ determination are indicated by the boxes at unity.

[430], and $W^{\pm}$ [431], which are not affected by strong interactions with the QCD matter. The presented measurement in p–Pb collisions extends this important experimental verification down to the GeV scale and to hadronic observables.

The nuclear modification factors measured in p–Pb collisions are important to constrain models including cold nuclear matter effects (see Sec. 3.1.1) on particle production. Figure 10.2 shows comparison of R_{pPb} measured at central rapidity with different saturation (CGC) models [432, 433] (top panel), with pQCD models with cold nuclear matter effects [434, 435] (middle panel), and with HIJING 2.1 [436] (lower panel). The calculations of Tribedy and Venugopalan [432] are shown for two implementations with running coupling Balitsky-Kovchegov (rcBK) and impact parameter dependent dipole saturation (IP-Sat) models. The calculations within IP-Sat are consistent with the data, while those within rcBK slightly underpredict the measurement. The Monte Carlo implementation of the rcBK model by Albacete et al. [433] (rcBK-MC) is consistent with measurements within the large uncertainties of the model. The pQCD NLO calculations with the EPS09s nuclear parton distribution functions by Helenius et al. [434] (calculations are for π^0) describe the data well. The pQCD LO calculations with cold nuclear effects (gluon shadowing) by Kang et al. yield R_{pPb} below unity for $p_{\mathrm{T}} > 6$ GeV/c, which is not supported by the data. The prediction from the HIJING 2.1 model [436], with the present shadowing parameter $s_{\mathrm{g}} = 0.28$, underpredicts the

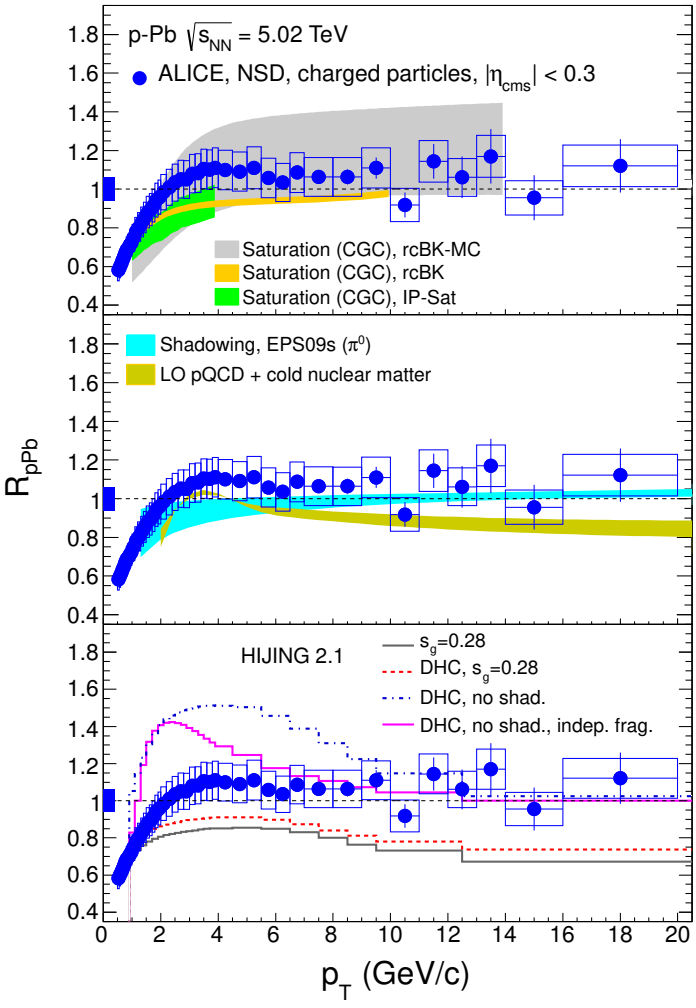

Fig. 10.2 R_{pPb} of charged particles measured at $|\eta_{\mathrm{cms}}| < 0.3$ in minimum-bias (NSD) p–Pb collisions at $\sqrt{s_{\mathrm{NN}}} = 5.02$ TeV [16]. The ALICE data are compared to model predictions including saturation (CGC) models [432, 433] (top panel), pQCD based models [434, 435] (middle panel), and HIJING 2.1 model [436] (lower panel). The boxes around data points denote p_{T}-dependent systematic uncertainties. The normalization error is shown as a filled box at unity.

data, however shows a proper trend. The HIJING implementation of decoherent hard collisions (DHCs) has a small influence on the results. When the independent fragmentation is included in the model it improves agreement with data at intermediate p_{T}. These comparisons demonstrate that the data are crucial for the theoretical understanding of cold nuclear matter as probed in p–Pb collisions at the LHC.

10.2 Q_{pPb} of Charged Particles

The various centrality estimators induce a bias on the nuclear modification factor in p–Pb collisions depending on the rapidity range they cover, as discussed in Ref. [22] (see also Sec. 2.5.2). In contrast to minimum-bias collisions, where the average number of binary nucleon-nucleon collisions can be obtained as $\langle N_{\mathrm{coll}} \rangle = \sigma_{\mathrm{pA}}/\sigma_{\mathrm{pp}}$, N_{coll} for a given centrality class cannot be used to calculate centrality-dependent R_{pPb}. Instead, for a given p–Pb collision centrality the Q_{pPb} is defined

$$Q_{\mathrm{pPb}} = \frac{\mathrm{d}N_{\mathrm{pPb}}/\mathrm{d}p_{\mathrm{T}}}{\langle N_{\mathrm{coll}}^{Glauber} \rangle \mathrm{d}N_{\mathrm{pp}}/\mathrm{d}p_{\mathrm{T}}} = \frac{\mathrm{d}N_{\mathrm{pPb}}/\mathrm{d}p_{\mathrm{T}}}{\langle T_{\mathrm{pPb}}^{Glauber} \rangle \mathrm{d}\sigma_{\mathrm{pp}}/p_{\mathrm{T}}}, \tag{10.1}$$

where $\langle N_{\mathrm{coll}}^{Glauber} \rangle$ and $\langle T_{\mathrm{pPb}}^{Glauber} \rangle$ are determined using a particular centrality estimator. In this notation, Q_{pPb} should be distinguished from R_{pPb} because the former is influenced by potential biases from the centrality estimator, which are not related to nuclear effects.

For determination of Q_{pPb} the p_{T} spectra measured in minimum-bias p–Pb collisions [21] (see Sec. 6.4) were used. The reference pp spectrum was constructed at low p_{T} by interpolating the data measured at $\sqrt{s} = 2.76$ and 7 TeV, and at high p_{T} by scaling the measurements at $\sqrt{s} = 7$ TeV using NLO pQCD calculations [18], as described in Sec. 6.3.2.

Figure 10.3 shows Q_{pPb} of charged particles measured as a function of p_{T} at mid-rapidity ($|\eta_{\mathrm{cms}}| < 0.3$) in NSD p–Pb collisions at $\sqrt{s_{\mathrm{NN}}} = 5.02$ TeV, for several centrality classes, which were determined using different centrality estimators (CL1, V0A, V0M and ZNA) [22]. These estimators used information from ALICE detectors located at different pseudorapidity ranges:

- CL1: the number of clusters in the outer layer of the SPD detector, $|\eta| < 1.4$;
- V0A: the amplitude in the V0 detector on the A side (the Pb-going side for the considered p–Pb event sample), $2.8 < \eta < 5.1$;
- V0M: the sum of amplitudes in the V0 detectors on the A and C sides (V0A+V0C), $2.8 < \eta < 5.1$ and $-3.7 < \eta < -1.7$;
- ZNA: the energy deposited in the neutron ZDC calorimeter on the A side, $\eta > 8.8$.

The uncertainties of the p-Pb and pp spectra were added in quadrature, separately, for the statistical and systematic uncertainties. The systematic uncertainties on the spectra are only shown for the V0A 0–5% centrality class. They are the same for the other centrality classes. The total systematic uncertainties on the normalization are given by the quadratic sum of the uncertainty on the normalization of the pp and p–Pb spectra. For simplicity, the $\langle T_{\mathrm{pPb}} \rangle$ uncertainty for the minimum-bias collisions is shown.

As expected, for CL1, V0M and V0A, Q_{pPb} strongly deviates from unity at high p_{T} for all centrality classes, with values well above unity for central collisions and below unity for peripheral collisions. However, the spread between centrality classes reduces with increasing rapidity gap between the range used for the centrality estimator and that used for the p_{T} measurement.

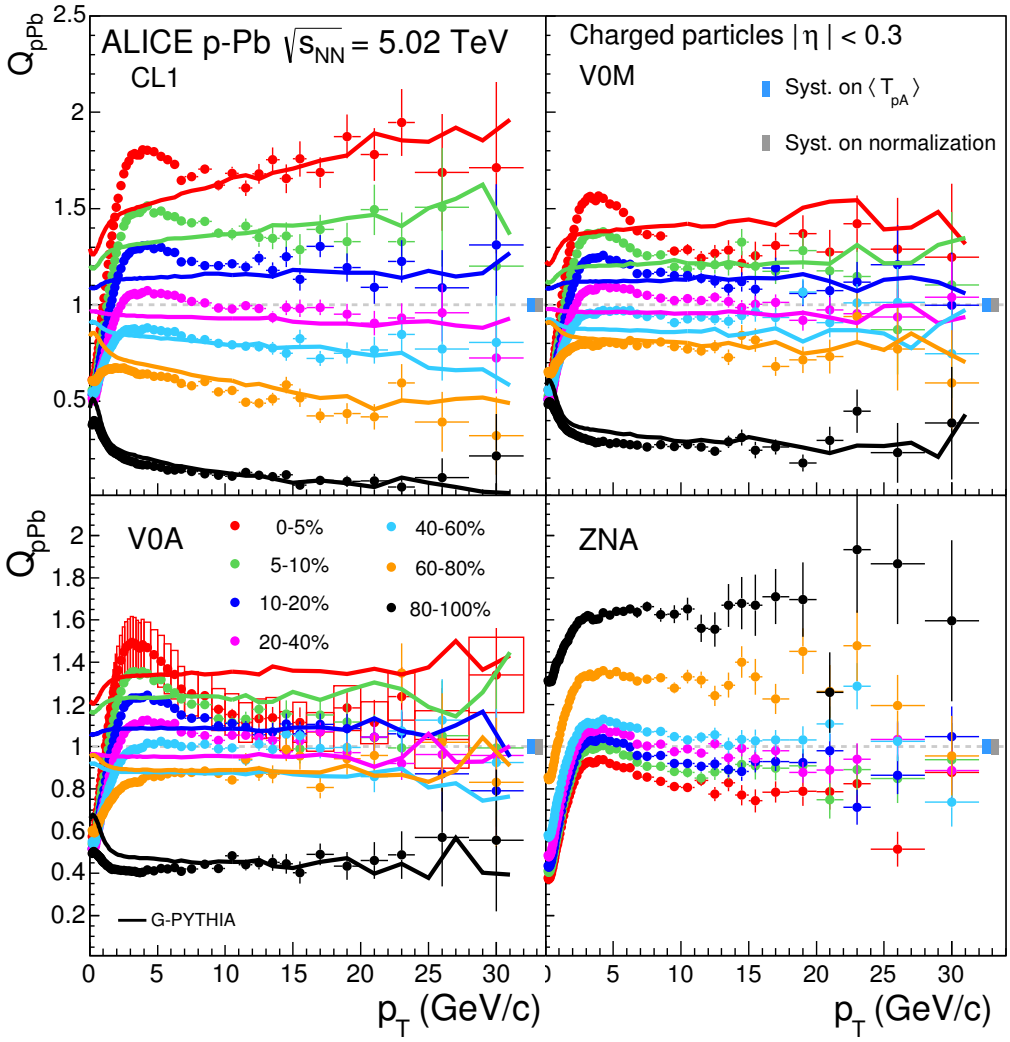

Fig. 10.3 Q_{pPb} as a function of p_{T} for charged particles measured at $|\eta| < 0.3$ in p–Pb collisions at $\sqrt{s_{\mathrm{NN}}}$ =5.02 TeV, for various centrality intervals determined with different centrality estimators [22]. The lines are from G-PYTHIA calculations [22]. The vertical error bars denote only statistical uncertainties. The p_{T}-dependent systematic uncertainties around data points are only shown for the V0A 0–5% central collisions and are the same for the other centrality classes. The normalization uncertainties including normalization of pp and p–Pb spectra and $\langle T_{\mathrm{pPb}} \rangle$ determination (only for the minimum-bias p–Pb) are indicated by the boxes at unity.

In order to study the centrality determination biases, the Q_{pPb} distributions are compared to the model calculations with G-PYTHIA model [22], which are shown with the solid lines in Fig. 10.3. In this model, the PYTHIA event generator was coupled to the Glauber model of p–Pb collisions, and for each p–Pb event PYTHIA generated N_{coll} independent pp collisions. The event centrality was obtained from the charged-particle multiplicity in the rapidity region covered by each estimator, in the same way as in data (see Sec. 2.5 for details). With this approach, the general trend at high p_{T} is reasonably well described for all centrality classes, particularly for CL1 estimator, which suggests that particle production at high p_{T} in p–Pb collisions can be approximated by an incoherent superposition of pp collisions. However, this agreement is not as good for V0A and V0M estimators, because this model is not capable to describe particle production at forward rapidities. One can also note that this model does not describe data at intermediate momenta ($p_{\mathrm{T}} \approx 3$ GeV$/c$), particularly for the central collisions, where the Cronin effect is reported [292]. The enhancement in the central collisions is about 15%, independently of selected centrality estimator. The particle production at intermediate p_{T} is expected to be dominated by the hard processes and should scale with N_{coll} in the absence of nuclear effects. From this, one can conclude that the observed enhancement is due to nuclear modification effects, as observed in other p–Pb measurements [20, 437, 438]. In contrast, at low p_{T} (below the Cronin maximum) the data are overestimated by the model, which is expected because the particle production at low p_{T} is dominated by soft processes and does not scale with N_{coll}.

Figure 10.3 (right-bottom panel) shows Q_{pPb} determined for the ZNA centrality classes. The Q_{pPb} distributions for different centrality classes are much more similar to each other as compared to other centrality estimators, as expected in the absence of multiplicity bias (dynamical bias due to large multiplicity fluctuations in p–Pb collisions [22]). The height of the Cronin maximum relative to the yield at high p_{T} is smaller for ZNA selected events than for V0A estimator, which might indicate that there is a remaining small bias for V0A event selection. For peripheral (60–80%, 80–100%) p–Pb events, the Q_{pPb} distributions are shifted with respect to those for other centralities. This is not due to the event selection but is due to the inaccurate estimate of $\langle N_{\mathrm{coll}} \rangle$ values for peripheral events, where a small uncertainty results in a large relative deviation in a Q_{pPb} determination [22].

As discussed in Sec. 2.5.2, the hybrid method uses centrality classes selected with ZNA and N_{coll} values determined with assumption on particle production. Figure 10.4 shows the resulting Q_{pPb} for $N_{\mathrm{coll}}^{\mathrm{Pb-side}}$ (left panel) and $N_{\mathrm{coll}}^{\mathrm{mult}}$ (right panel). The Q_{pPb} shown in Fig. 10.3 (right-bottom panel) and both panels of Fig. 10.4 have the same shapes by construction and differ only due to the N_{coll} scaling of the pp reference spectrum. The obtained Q_{pPb} are consistent with unity at high p_{T} for all centrality classes, which confirms the absence of initial-state effects for particle production, as observed for minimum-bias p–Pb collisions. The Cronin maximum, which has already been noted in minimum-bias collisions, is observed to be stronger in central collisions and nearly absent in peripheral collisions. However, this maximum is much smaller at $\sqrt{s_{\mathrm{NN}}} = 5.02$ TeV p–Pb collisions as compared to that observed at RHIC.

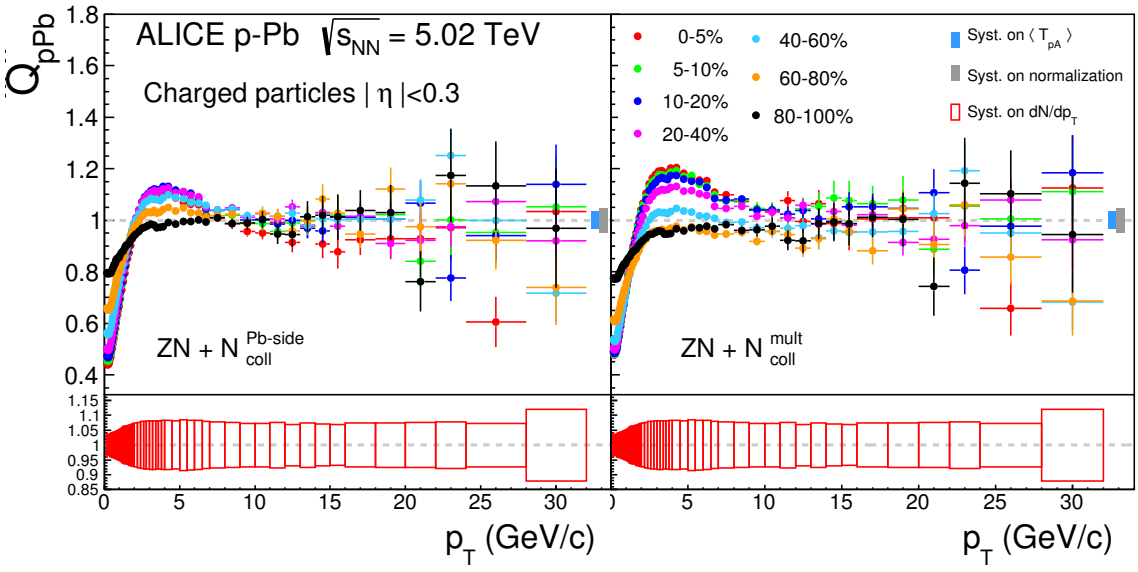

Fig. 10.4 Q_{pPb} as a function of p_{T} for charged primary particles measured in $|\eta| < 0.3$ in p–Pb collisions at $\sqrt{s_{\mathrm{NN}}}$ =5.02 TeV, for different centrality intervals determined with hybrid method [22]. The vertical error bars (upper panels) denote only statistical uncertainties. The p_{T}-dependent systematic uncertainties (from pp and p–Pb spectra added in quadrature) are shown in bottom panels. The normalization uncertainties including normalization of pp and p–Pb spectra, and $\langle T_{\mathrm{AA}} \rangle$ determination, are indicated by the boxes at unity.

10.3 R_{AA} of Charged Particles

The first measurement of nuclear modification factors of charged particles in Pb–Pb collisions at $\sqrt{s_{\mathrm{NN}}} = 2.76$ TeV has been reported by ALICE [15]. At that time, the pp measurements at the same $\sqrt{s}$ were not available and several approaches were applied to determine pp reference spectrum. The pp reference was obtained by interpolating the invariant yields of charged particles measured by ALICE in INEL pp collisions at $\sqrt{s} = 0.9$ and 7 TeV [14, 15]. The interpolation was performed in bins of p_{T}, based on assumption that the increase of the yield with $\sqrt{s}$ follows a power law. Above $p_{\mathrm{T}} = 2$ GeV/c, the measured spectra were parametrized by the modified Hagedorn function [377] to reduce bin-by-bin fluctuations. The interpolation procedure was verified using PHOJET and PYTHIA6 (D6T [439] and Perugia0 [371] tunes) spectra at $\sqrt{s} = 0.9$, 2.76 and 7 TeV. The generated and interpolated spectra agreed within uncertainties. Two alternative approaches were applied to construct pp reference spectrum for $p_{\mathrm{T}} > 6.5$ GeV/c. Replacing in interpolating procedure the p_{T} spectrum at $\sqrt{s} = 0.9$ TeV with the p_{T} spectrum measured in $\mathrm{p\bar{p}}$ collisions at $\sqrt{s} = 1.9$ TeV by CDF experiment [440] results in 5–15% lower than interpolated pp reference. A different procedure based on the NLO pQCD calculations [211] was applied to scale p_{T} spectrum from $\sqrt{s} = 0.9$ or 7 TeV to 2.76 TeV, as demonstrated by Eq. 6.8. Starting from the 7 TeV spectrum a good agree-

ment with the interpolated pp reference was found, while starting from 0.9 TeV results in 30–50% higher spectrum than the interpolated reference. The comparison of the interpolated pp reference spectrum with the references obtained in the following analysis [18] is shown in Fig. 6.6.

The resulting R_{AA} is shown in Fig. 10.5 (left) for central and peripheral collisions, corresponding to 0–5% and 70–80% of the hadronic Pb–Pb cross section, for particles in $|\eta| < 0.8$ and $0.3 < p_{\mathrm{T}} < 20$ GeV/c. The nuclear modification factor is below unity for both centrality intervals. At high p_{T}, where production from hard processes is expected to dominate, in peripheral collisions the R_{AA} is about 0.7 and shows no pronounced p_{T} dependence for $p_{\mathrm{T}} > 2$ GeV/c. In central collisions R_{AA} is below unity reaching a minimum of $R_{\mathrm{AA}} \approx 0.14$ at $p_{\mathrm{T}} = 6$–7 GeV/c. Above $p_{\mathrm{T}} = 7$ GeV/c, R_{AA} increases significantly to about 0.35 at the highest p_{T}. Below $p_{\mathrm{T}} = 6$ GeV/c, R_{AA} strongly depends on p_{T} with maximum at around 2 GeV/c, which is related to the radial flow developing in Pb–Pb collisions, as discussed in Sec. 5.2 and 7.2. The R_{AA} in central collisions determined using alternative pp references are plotted as histograms. For such scenarios, the overall R_{AA} is shifted depending on the pp reference, but without significant change in p_{T} dependence.

In Fig. 10.5 (right) the ALICE R_{AA} in central Pb–Pb collisions at the LHC [15] is compared to measurements of R_{AA} of charged hadrons in central Au–Au collisions by STAR [281] and PHENIX [283] experiments at RHIC. At low p_{T}, the measured R_{AA} is similar to the RHIC results. The position and shape of the maximum at intermediate p_{T} is also similar to that at RHIC. At high p_{T} (7–8 GeV/c), the nuclear modification factor is smaller than at RHIC, despite the much flatter p_{T} spectrum in pp and Pb–Pb collisions at the LHC, which points to an enhanced energy loss at LHC and therefore a denser medium.

The analysis of nuclear modification factors for Pb–Pb collisions at $\sqrt{s_{\mathrm{NN}}} = 2.76$ TeV has been later extended by ALICE by adding more Pb–Pb data samples and by including pp measurements at $\sqrt{s} = 2.76$ TeV [17]. The resulting R_{AA}, determined for nine centrality intervals and for $0.15 < p_{\mathrm{T}} < 50$ GeV/c, are shown in Fig 10.6. For the R_{AA} measurement, the reference pp spectrum was constructed based on the p_{T} spectra measured at $\sqrt{s} = 2.76$ TeV, as described in Sec. 6.3.1. In peripheral collisions (70–80%), only moderate suppression, $R_{\mathrm{AA}} \approx 0.7$, and a weak p_{T} dependence is observed. Towards more central collisions, a pronounced minimum at $p_{\mathrm{T}} = 6$–7 GeV/c develops, while for $p_{\mathrm{T}} > 7$ GeV/c there is a significant rise of the R_{AA} that becomes gradually less steep with increasing p_{T}. In the most central collisions (0–5%), the yield is most suppressed, with $R_{\mathrm{AA}} \approx 0.13$ at $p_{\mathrm{T}} = 6$–7 GeV/c. The R_{AA} reaches about 0.4 with no significant p_{T} dependence for $p_{\mathrm{T}} > 30$ GeV/c.

The maximum in R_{AA} at $p_{\mathrm{T}} \approx 2$ GeV/c results from collective expansion (radial flow), which change the shape of the p_{T} spectrum. As expected for collective effects, a strong centrality dependence is observed. The magnitude of radial flow depends on the particle mass, and thus also on the primary particle composition. It should be noted that at low p_{T} soft processes dominate particle production and binary collision scaling is not expected to hold, as soft processes rather scale with the average number of participating nucleons $\langle N_{\mathrm{part}} \rangle$ [175]. It is observed in the measurements of $\mathrm{d}N_{\mathrm{ch}}/\mathrm{d}\eta$ [302, 303], as shown in Fig. 5.1.

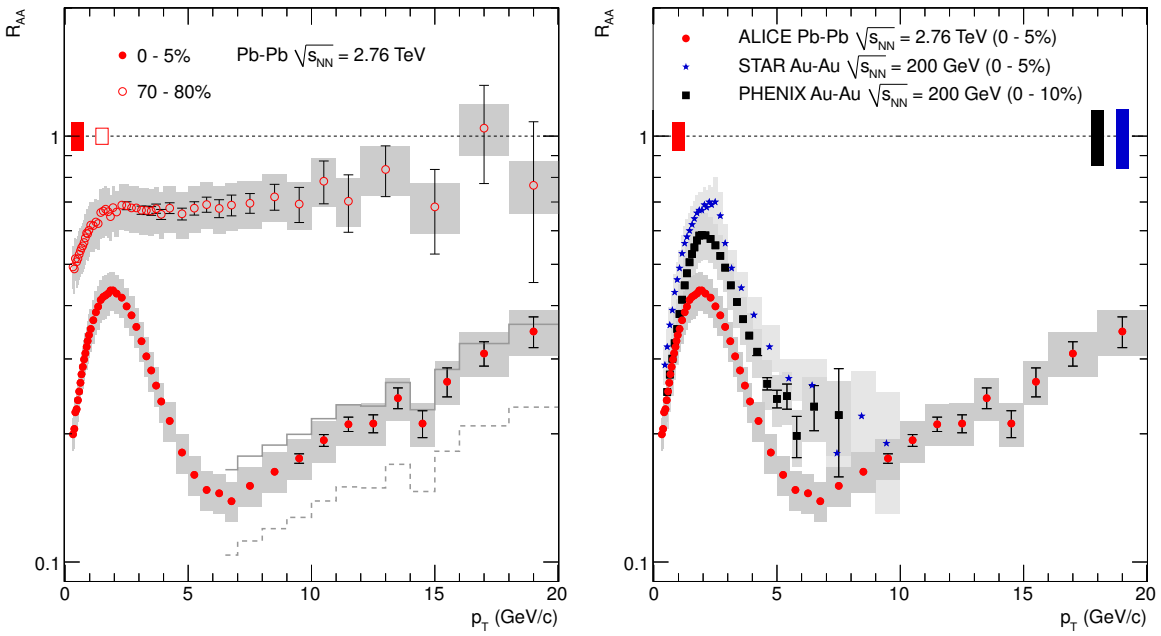

Fig. 10.5 Left: R_{AA} as a function of p_T for charged primary particles measured in $|\eta| < 0.8$ in central (0–5%) and peripheral (70–80%) Pb–Pb collisions at $\sqrt{s_{NN}}$ =2.76 TeV [15]. The boxes around data points denote the p_T dependent systematic uncertainties (from Pb–Pb and pp reference spectra added in quadrature). The histograms indicate, for central collisions only, the result for $R_{AA} > 6.5$ GeV/c using alternative pp references obtained by use of p$\bar{\text{p}}$ measurements at $\sqrt{s} = 1.9$ TeV [440] (solid histogram) and NLO pQCD scaling of the data at $\sqrt{s} = 900$ GeV [15] (dashed histogram). The total normalization uncertainties including normalization of pp spectra and $\langle T_{AA} \rangle$ determination are indicated by the boxes at unity. Right: Comparison of R_{AA} measured in central Pb–Pb collisions by ALICE to measurements by STAR [281] and PHENIX [283] experiments at RHIC. The statistical and systematic uncertainties of the PHENIX data are shown as error bars and boxes, respectively. The statistical and systematic errors of the STAR data are combined and shown as boxes. The total normalization uncertainty are shown as boxes at unity.

The dependence of R_{AA} on collision centrality, expressed by N_{part} and by the charged particle multiplicity density $dN_{ch}/d\eta$, are shown for different p_T intervals in Fig 10.7 [18]. The ALICE measurements are compared with results in Au–Au collisions at $\sqrt{s_{NN}} = 200$ GeV from PHENIX [283]. The strongest centrality dependence is observed for particles with $5 < p_T < 7$ GeV/c. At higher p_T, the centrality dependence is weaker. For the same p_T interval, the suppression observed at the LHC is larger than at RHIC by a factor of about 1.2, for all $\langle N_{part} \rangle$ (Fig. 10.7, top). The similar suppression is observed when RHIC and LHC results are compared as a function of $dN_{ch}/d\eta$ (Fig. 10.7, bottom). Larger values of suppression than at RHIC are observed in central collisions at the LHC, where the $dN_{ch}/d\eta$ exceeds that of the most central collisions at RHIC. It should be noted that the suppression at a given centrality interval results from the interplay between the parton spectrum, medium density,

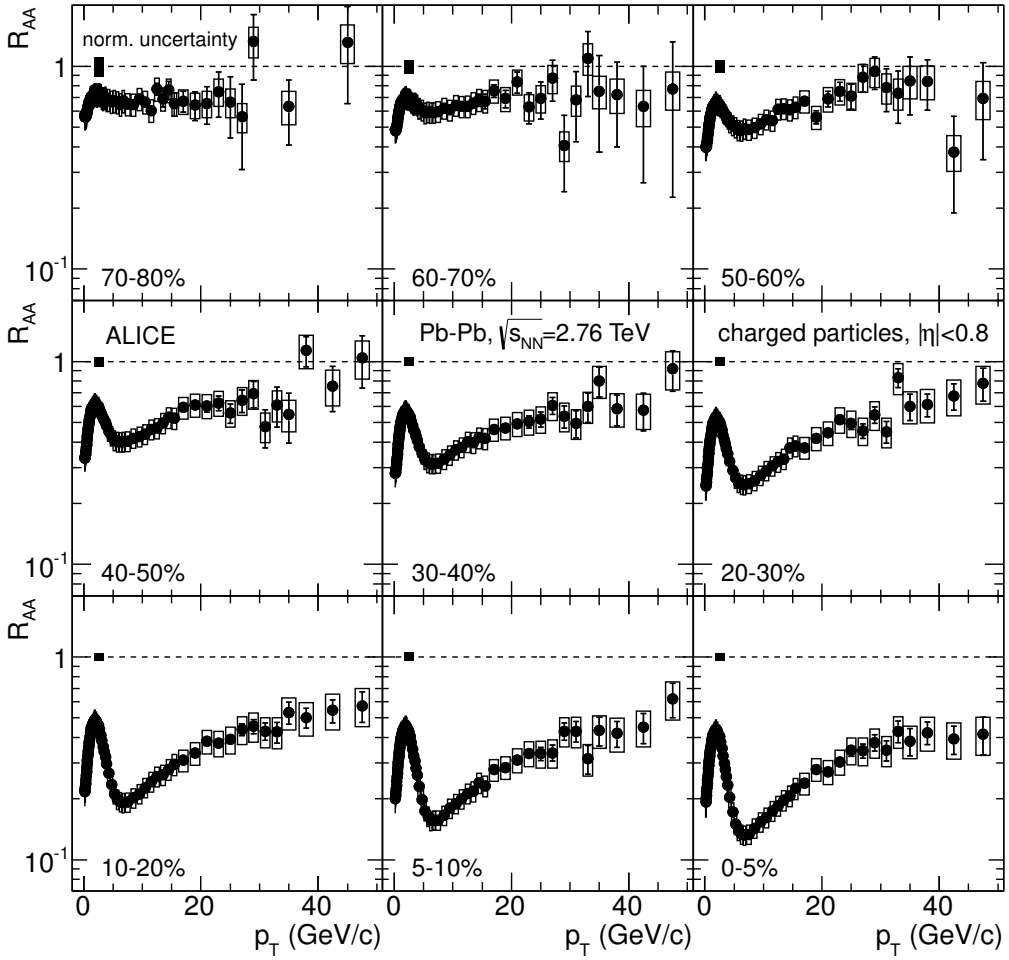

Fig. 10.6 R_{AA} as a function of p_{T} for charged particles measured at mid-rapidity in Pb–Pb collisions for nine centrality intervals [17]. Statistical and systematic uncertainties are plotted as vertical error bars and boxes around the points, respectively. The total normalization uncertainty including pp normalization and Pb–Pb centrality determination is indicated by the black boxes at unity.

and gluon-to-quark ratio, all of them exhibit a significant energy dependence. Therefore, the model studies are needed to evaluate their relative ratios.

Figure 10.8 shows R_{AA} measured by ALICE at $\sqrt{s_{\mathrm{NN}}} = 5.02$ TeV [28]. The R_{AA} are compared to R_{AA} at $\sqrt{s_{\mathrm{NN}}} = 2.76$ TeV from the reanalysis of ALICE data. In this analysis, the pp references for the two energies are fully based on the measured p_{T} spectra without applying interpolation or scaling procedures. The p_{T} spectra used for the R_{AA} determination are presented in Sec. 6.6. The nuclear modification factors have a strong centrality dependence, and are very similar in magnitude for the two collision energies. Given that the p_{T}

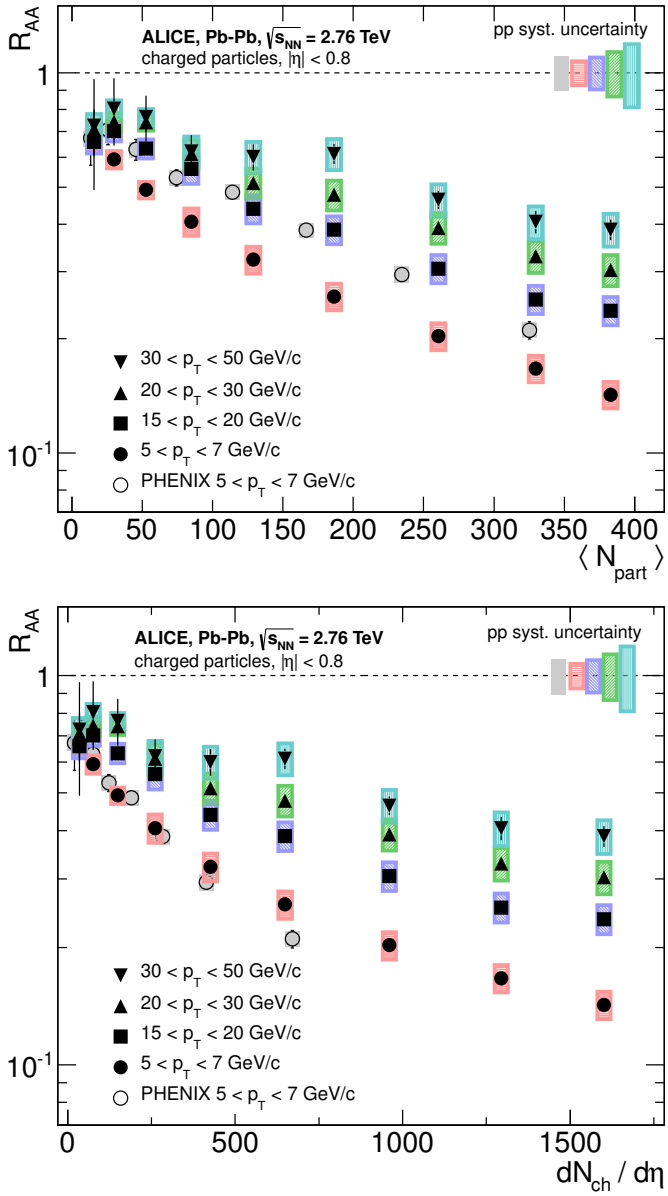

Fig. 10.7 R_{AA} of charged particles as a function of $\langle N_{part} \rangle$ (top) and $dN_{ch}/d\eta$ (bottom) measured in Pb–Pb collisions at $\sqrt{s_{NN}} = 2.76$ TeV for different p_T intervals [18]. For comparison, the PHENIX results for Au–Au collisions at $\sqrt{s_{NN}} = 200$ GeV for $p_T = 5$–7 GeV/c are shown [283]. The boxes around the data represent the p_T-dependent uncertainties on the Pb–Pb spectra. The boxes at $R_{AA} = 1$ represent the systematic uncertainties on the pp reference in different p_T-intervals. The systematic uncertainties on the overall normalization for ALICE and PHENIX are not shown.

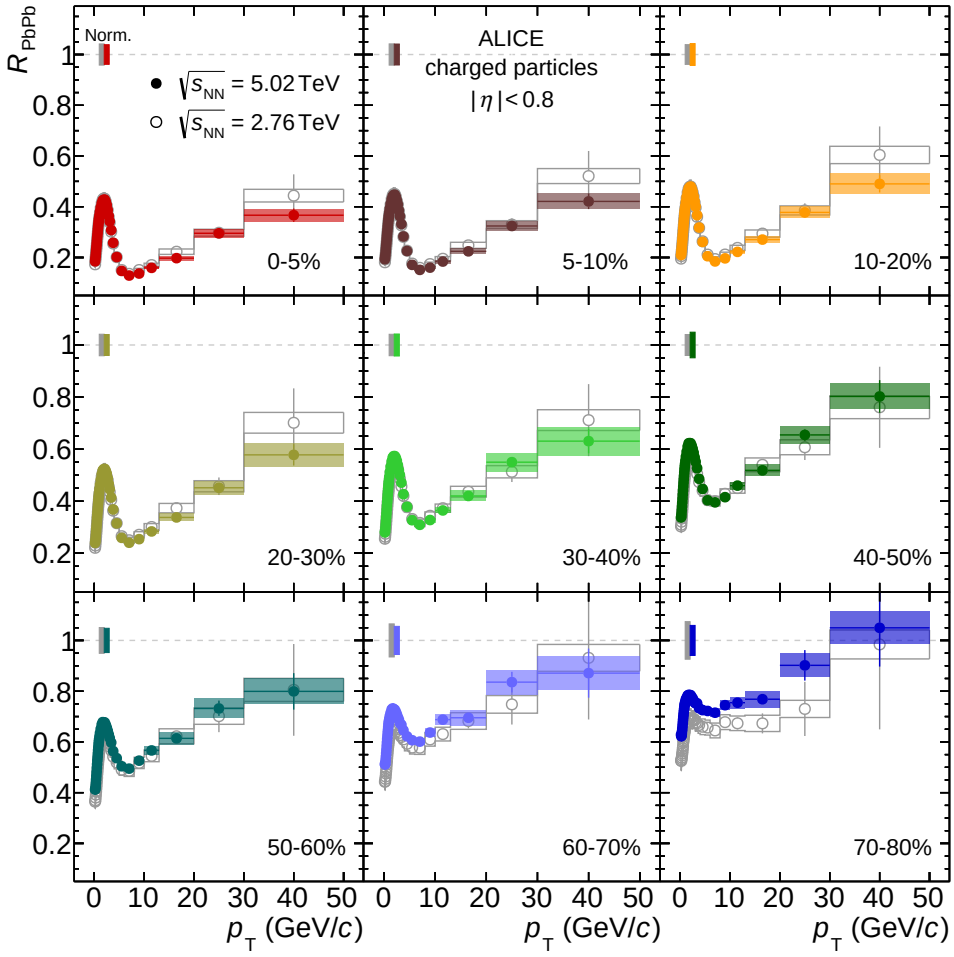

Fig. 10.8 R_{AA} as a function of p_T for charged particles measured in Pb–Pb collisions at $\sqrt{s_{NN}} = 2.76$ and 5.02 TeV for nine centrality intervals [28]. The R_{AA} at lower collision energy are from the reanalysis of previously published data [17]. Statistical and systematic uncertainties are plotted as vertical error bars and boxes around the points, respectively. The total normalization uncertainty (pp and Pb–Pb) is indicated by the boxes at unity.

spectrum is harder in pp collisions at the higher energy, as shown in Fig. 6.12, it indicates a larger parton loss in the hotter/denser and longer-lived QGP produced at $\sqrt{s_{NN}} = 5.02$ TeV. In 0–5% central collisions, the yield is most suppressed by a factor of about 8 ($R_{AA} \approx 0.13$) at $p_T = 6$–7 GeV/c. Above $p_T = 7$ GeV/c, there is a significant rise of the nuclear modification factor, which reaches a value of about 0.4 at the highest p_T. In 70–80% peripheral

collisions, the suppression is about 30% at intermediate p_{T} and decreases to approach unity at the highest p_{T}.

10.4 R_{pPb} vs. R_{AA} of Charged Particles at the LHC

Figure 10.9 (left) shows R_{pPb} in minimum-bias p–Pb collisions in comparison to R_{AA} in the 0–5% and 70–80% central Pb–Pb collisions at $\sqrt{s_{\mathrm{NN}}} = 5.02\ TeV$ [28]. The R_{pPb} exhibits maximum at $p_{\mathrm{T}} = 3$–5 GeV$/c$, which is for the larger p_{T} than maximum of R_{AA} seen at $p_{\mathrm{T}} = 1.5$–3 GeV$/c$, indicating that the origin of these maxima is different for the two collision systems. In p–Pb collisions, the maximum was identified with the Cronin effect, while in Pb–Pb collisions with the strong radial flow and particle production via regeneration mechanisms, which modify the particle spectra in this p_{T} range. The R_{pPb} is consistent with unity for $p_{\mathrm{T}} > 8$ GeV$/c$, which is also observed for the Q_{pPb} determined in centrality selected p–Pb collisions (Fig. 10.4). It indicates that the strong suppression observed in central Pb–Pb collisions is not related to the initial-state (or cold nuclear matter) effects.

There is also visible an onset of suppression in peripheral Pb–Pb collisions for p_{T} up to 20 GeV$/c$, which can be related to the biases introduces by centrality determination, as discussed in Ref. [441]. It can lead to the Pb–Pb event centrality selection for which the properties of the binary nucleon-nucleon scaling deviate from unbiased pp collisions. In this case, the R_{AA} can deviate from unity even in the absence of nuclear effects. There are two main origins of these biases. Firstly, it can be due to the different spacial distribution of nucleons in nuclei, in the plane transverse to the beam directions, with respect to the distributions of protons in colliding beams, leading to the bias on the nucleus-nucleus impact parameter. Secondly, centrality selection is based on measurements of bulk particle production (see Sec. 2.5 for details) and thus can bias the mean multiplicity of individual nucleus-nucleus collisions, and in case of correlation of soft and hard particle production the amount of hard processes in Pb–Pb collisions. It was estimated that the overall bias including both effects can reach up to 20% for the 70–80% peripheral collisions. Therefore, the calculations that attempt to address parton energy loss in peripheral collisions have to account for these effects.

The ALICE results for R_{AA} and R_{pPb} of charged particle measured at $\sqrt{s_{\mathrm{NN}}} = 5.02$ TeV [28] are compared in Fig. 10.9 (right) to measurements by CMS [442]. An agreement is observed for both R_{AA} and R_{pPb} within current uncertainties. One can note that the systematic uncertainties of ALICE measurements are much smaller than that shown by CMS. For the p_{T} values extending the ALICE range ($p_{\mathrm{T}} > 50$ GeV$/c$), the R_{pPb} measured by CMS is above unity, which might be related to the antishadowing effect (see Sec. 3.1.1 for details). The suppression of charged particle production in the most central Pb–Pb collisions continues up to the highest p_{T} measured by CMS and approaches unity in the vicinity of $p_{\mathrm{T}} = 200$ GeV$/c$.

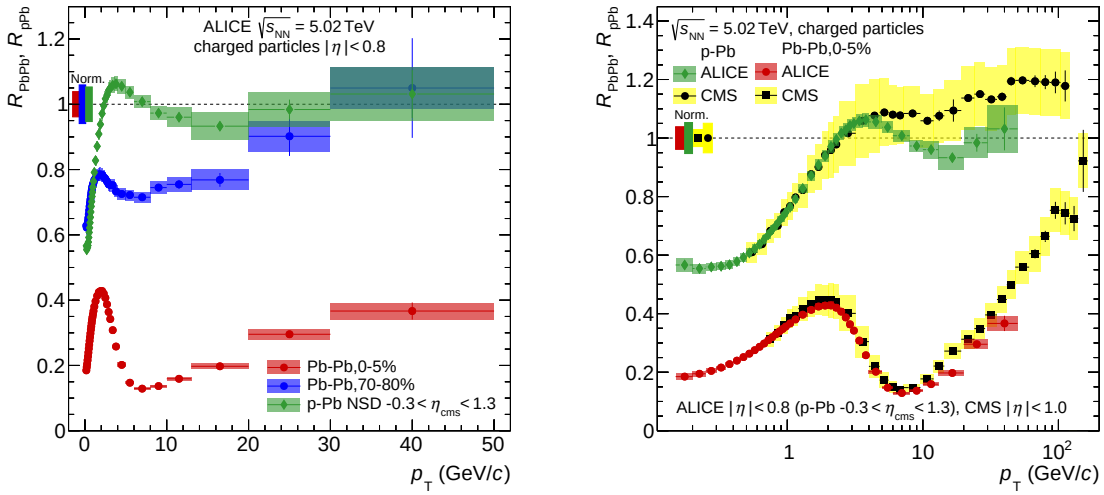

Fig. 10.9 Left: Nuclear modification factors measured by ALICE in central (0–5%) and peripheral (70–80%) Pb–Pb collisions and in p–Pb collisions at $\sqrt{s_{\mathrm{NN}}} = 5.02$ TeV [28]. Right: A comparison of the nuclear modification factors for central (0-5%) Pb–Pb and p–Pb collisions measured by ALICE [28] and CMS [442, 443]. In both figures, the p_{T}-dependent systematic uncertainties are shown as boxes around data points. The normalization uncertainties are shown as boxes around unity.

10.5 R_{AA} of Charged Particles vs. Models

10.5.1 Model Predictions at $\sqrt{s_{\mathrm{NN}}} = 2.76$ TeV

In Fig. 10.10, R_{AA} measured by ALICE in 0–5% central Pb–Pb collisions at $\sqrt{s_{\mathrm{NN}}} = 2.76$ TeV [17] is compared to the model predictions. All model calculations except WHDG [444] use a hydrodynamical description of the medium, but different extrapolation assumptions from RHIC to LHC. A variety of energy loss formalisms is used (see Sec. 3.2 for more details). The opacity expansion (WHDG), the multiple gluon soft gluon approximation (ASW) [255], and the Higher Twist (HT) [261, 262] models are based on analytical radiative energy loss formulations that include interference effects. The ASW and WHDG calculations show larger suppression than seen in the measurement, while one of the HT curves (Chen [261]) with lower medium density provides a good description. The other HT model (Majumder [262]) curve shows a stronger rise with p_{T} than measured. The elastic energy loss model by Renk (elastic [445]) overshoots data at low p_{T}. The YaJEM-D [446] model, which is based on medium-induced virtuality increases in a parton shower, shows too strong p_{T} dependence of R_{AA}.

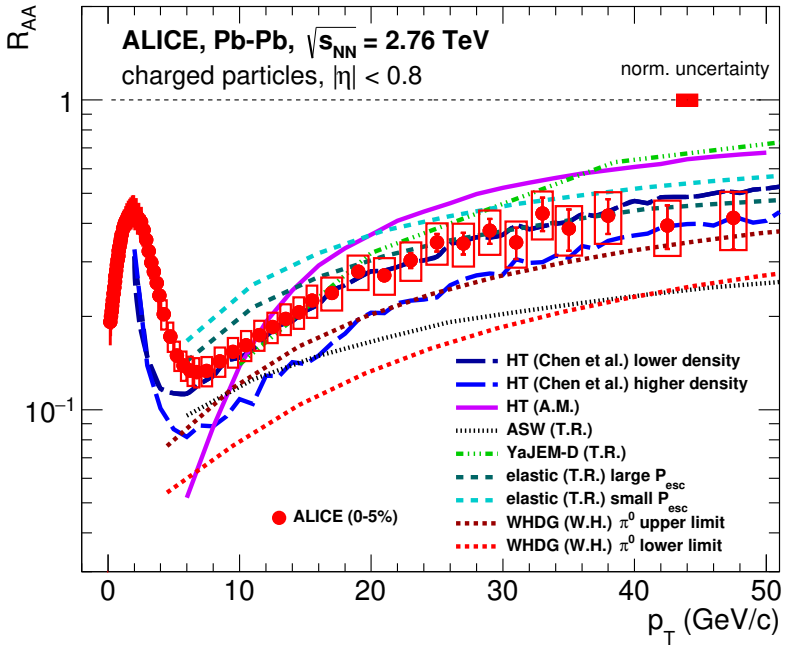

Fig. 10.10 R_{AA} of charged particles measured by ALICE in 0–5% central Pb–Pb collisions at $\sqrt{s_{NN}} = 2.76$ TeV [17] in comparison to model calculations [255, 261, 262, 444, 446, 447]. The boxes around the data points denote p_T-dependent systematic uncertainties. The systematic uncertainty on the normalization which is related to Pb–Pb centrality determination and pp spectra normalization are added in quadrature, and is shown as box at $R_{AA} = 1$.

10.5.2 Model Calculations at $\sqrt{s_{NN}} = 5.02$ TeV

Figure 10.11 shows R_{AA} measured by ALICE in 0–5% central Pb–Pb collisions at $\sqrt{s_{NN}} = 5.02$ TeV [28] in comparison to model calculations. The calculations by Vitev et al. are based on the SCET$_G$ model [448, 449], which uses an extended soft-collinear effective theory to describe inclusive particle production and suppression in the heavy-ion environment. This theoretical framework provides an analytic connection between generalized DGLAP evolution equations for the fragmentation functions in dense strongly-interacting matter and parton energy loss for hard processes. The calculations employ the pQCD-based hard cross section and QGP medium evolved parton-to-hadron fragmentation functions, combined with initial-state cold nuclear matter (CNM) effects, which include dynamical nuclear shadowing, the Cronin effect and initial-state parton energy loss (see [449] and references therein for details). The two upper and lower curves represent calculations for the nuclear modification factor with variations of the coupling strength $g = 1.9 \pm 0.1$.

Djordjevic et al. [450, 451] use a dynamical energy loss formalism based on pQCD calculations in a finite size dynamical QCD medium. While the initial p_T spectrum is the same as that used in the SCET$_G$ model, the dynamical description of the medium provides a consistent

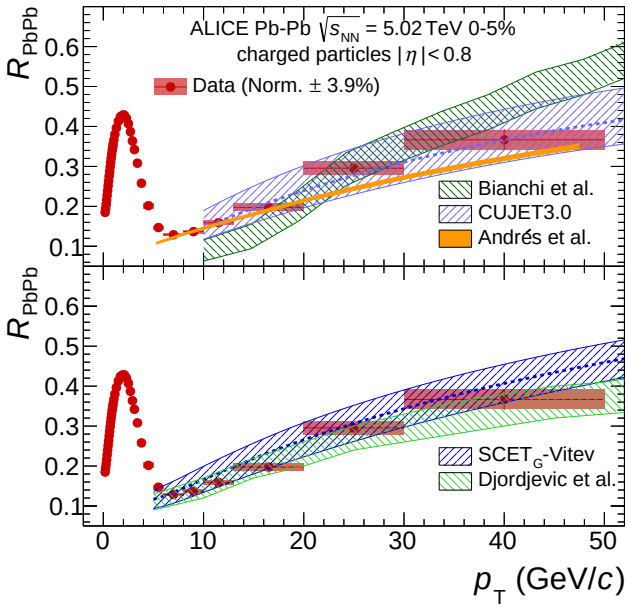

Fig. 10.11 R_{AA} of charged particles in the 0–5% central Pb–Pb collisions at $\sqrt{s_{NN}} = 5.02$ TeV [28] in comparison to model predictions [448–451] (lower panel) and [452–455] (upper panel). The red boxes around data points represent p_T dependent systematic uncertainties. The normalization uncertainty of the data (±3.9%) is not part of the uncertainties of the plotted data points.

treatment of both radiative and collisional energy loss, including a finite magnetic screening mass, which modifies the gluon self energy and therefore changes the energy loss, as well as a running coupling constant for the strongly-interacting medium. The two curves correspond to different electric-to-magnetic screening mass ratios in the range $0.4 < \mu_M/\mu_E < 0.6$.

The model of Bianchi et al. [452] uses the pQCD factorization scheme with a pQCD-based radiative energy loss in a hydrodynamically expanding medium. In this framework, high p_T hadrons arise from fragmentation of hard partons, which lose energy prior to hadronization via interactions with the medium. The amount of energy loss is regulated by the medium transport coefficient $\hat{q}$, which varies with the temperature-dependent entropy density of the medium as well as with the energy scale of jets propagating in the medium.

The CUJET 3.0 model [453, 454] is an extension of the perturbative-QCD-based CUJET 2.0 model, with the two complementary non-perturbative features of the QCD cross-over transition: the suppression of quark and gluon degrees of freedom and the emergence of chromo-magnetic monopoles. The calculations were performed varying the value of the QCD running coupling α_c from 0.95 to 1.33 for $Q < T_c$, and the ratio of electric to magnetic screening scales $c_m = g\mu_E/\mu_M$ ($c_m = 0, 0.3, 0.4$), where g is the QCD coupling constant. The value of α_C was

fixed for each c_{m} value by fitting a single reference datum, $R_{\mathrm{AA}}(p_{\mathrm{T}} = 12\ \mathrm{GeV}/c) \approx 0.3$, for charged hadrons in 20–30% central Pb–Pb collisions at the LHC.

The calculations by Andrés et al. [455] use the jet quenching formalism of quenching weights. This approach consists of fitting a K factor, defined as $K \equiv \hat{q}/2\varepsilon^{3/4}$, that quantifies departure of this parameter from the perturbative estimate, $\hat{q}_{\mathrm{ideal}} \sim 2\varepsilon^{3/4}$ [456], where the local energy density ε is taken from a hydrodynamical model of the medium. The K factor is the only free parameter in the fit of nuclear modification factors. Without including new data at $\sqrt{s_{\mathrm{NN}}} = 5.02$ TeV in the fit procedure, they predict a $\sim 15\%$ larger suppression at $\sqrt{s_{\mathrm{NN}}} = 5.02$ TeV as compared to $\sqrt{s_{\mathrm{NN}}} = 2.76$ TeV, assuming the same value of K as the one obtained from the fit to the data at the lower energy.

All models presented here describe the main features of the data. The models by Vitev et al., Djordjevic et al. and CUJET 3.0 give quantitatively good description of the data. The model by Bianchi et al. is consistent with data within 1.5σ while that by Andrés et al. underestimates the data at high p_{T}. However, one should note that this comparison is made between unbinned theory calculations and binned data in relatively large p_{T} bins, which might introduce additional uncertainty.

10.5.3 Determination of $\hat{q}$ in the QGP

The JET Collaboration has made attempt to determine the jet transport coefficient ($\hat{q}$) within five approaches to parton propagation and energy loss in dense matter produced in heavy-ion collisions at RHIC and at the LHC [221]. The calculations are constrained by R_{AA} measurements for single inclusive hadrons by PHENIX [457, 458], ALICE [17] (presented above) and CMS [383] experiments. The five different approaches to parton energy loss included: GLV-CUJET [257, 459], HT-M [262, 263], HT -BW [260, 261], MARTINI [460] and McGill-AMY [461]. A short characterization of the GLV, higher twist (HT-M, HT-BW) and AMY models can be found in Sec. 3.3.1.

The evolution of bulk medium used in the study for parton propagation was based on 2+1D [463] or 3+1D [464] viscous hydrodynamic models, which are also constrained by experimental data on bulk hadron spectra. The GLV-CUJET model uses a potential model for multiple scattering in the medium in which the controlling parameters for energy loss are the strong coupling constant, the Debye screening mass and the density of scattering centers. In the higher twist (HT-M, HT-BW) approaches the jet transport coefficient is the only parameter of parton energy loss and is extracted from the fit to the measured R_{AA}. The MARTINI and McGill-AMY models are based on hard-thermal-loop (HTL) resummed thermal field theory in which the only adjustable parameter is the strong coupling constant.

Within each model, $\hat{q}$ is a function of local temperature and jet energy which varies along jet propagation path. The calculation were performed for extreme conditions for the most central A–A collisions at an initial time $\tau_0 = 0.6$ fm/c, when hydrodynamic models are applied for the bulk evolution. The initial temperature was set to $T_0 =$ 346–373 MeV and 447–486 MeV for

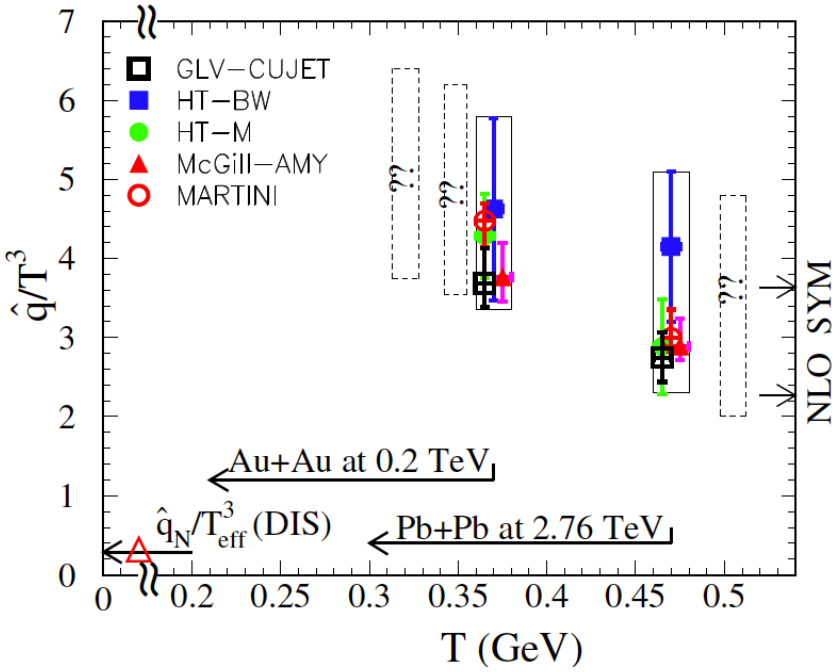

Fig. 10.12 Values of scaled jet transport parameter $\hat{q}/T^3$ from different jet quenching models, extracted for an initial light-quark jet with energy E = 10 GeV at the center of the most central A–A collisions and at an initial time $\tau_0 = 0.6$ fm/c [221], using R_{AA} measurements at RHIC [457, 458] and at the LHC [17, 383]. The calculations are shifted along T axis for better visibility. The vertical errors bars indicate uncertainties of the calculations. The dashed boxes indicate expected values at $\sqrt{s_{NN}} = 0.063$, 0.130 and 5.5 TeV, assuming the initial entropy is proportional to the charged particle multiplicity density ($dN_{ch}/d\eta$). The triangle denotes the value of $\hat{q}_N/T^3_{eff}$ in cold nuclear matter from DIS experiments [462]. The result from NLO calculations for the strongly coupled plasma (SYM) are indicated by the two arrows on the right axis.

Au–Au collisions at $\sqrt{s_{NN}}$ = 200 GeV at RHIC and Pb–Pb collisions at $\sqrt{s_{NN}} = 2.76$ TeV at the LHC, respectively. Values of scaled $\hat{q}$ extracted for light-flavor quark jet of energy 10 GeV are shown in Fig. 10.12, for the highest temperatures considered in the calculations.

Taking into account the variation of $\hat{q}$ values between different models as theoretical uncertainties, one can extract the range of values as constrained by the measured R_{AA} of single hadrons at RHIC and at the LHC, which results in

$$\frac{\hat{q}}{T^3} \approx \begin{cases} 4.6 \pm 1.2 & \text{RHIC}, \\ 3.7 \pm 1.4 & \text{LHC}, \end{cases} \tag{10.2}$$

at the highest temperatures reached in the most central A–A collisions. The corresponding absolute values of $\hat{q}$ amount to

$$\hat{q} \approx \begin{cases} 1.2 \pm 0.3 \text{ GeV}^2/\text{fm} & T = 370 \text{ MeV} \\ 1.9 \pm 0.7 \text{ GeV}^2/\text{fm} & T = 470 \text{ MeV}, \end{cases} \tag{10.3}$$

at an initial time $\tau_0 = 0.6$ fm/c, and temperature ranges considered in the calculations. The obtained values are close to the early estimates discussed in Ref. [231].

In Fig. 10.12, the value $\hat{q}_N/T_{\text{eff}}$ in cold nuclear matter extracted from jet quenching in DIS experiments [462], is shown for comparison. The value of $\hat{q}_N = 0.02$ GeV^2/fm and an effective temperature of an ideal quark gas with 3 quarks within each nucleon at the nucleon density in a large nucleus were used. The obtained value is an order of magnitude smaller than that in A–A collisions.

The results obtained with pQCD based calculations can be also compared to estimates from nonperturbative calculations using AdS/CFT correspondence (see Sec. 3.2.3 for more details). The jet quenching in $N = 4$ supersymetric Yang-Mills (SYM) plasma at the strong coupling limit can be calculated in leading order (LO) as [238]

$$\hat{q}^{\text{LO}}_{\text{SYM}} = \frac{\pi^{3/2}\Gamma(3/4)}{\Gamma(5/4)}\sqrt{\lambda}T^3_{\text{SYM}}, \tag{10.4}$$

where $\lambda = g^2_{\text{SYM}}N_c$ is the 't Hooft coupling, and N_c is the number of quark flavors. In order to compare $\hat{q}^{\text{LO}}_{\text{SYM}}$ to $\hat{q}$ obtained with pQCD based models, one should take into account different number of degrees of freedom for both theories. Since $\hat{q}$ is proportional to the local entropy density (gluon number density), it is possible to match the corresponding entropy density to obtain $3T^3_{\text{SYM}} \approx T^3$. The NLO calculations [465] yields values $\hat{q}^{\text{NLO}}_{\text{SYM}}/T^3 \approx 2.27$–$3.64$, which are in agreement with the $\hat{q}$ values, as indicated by the two arrows on the right axis of Fig. 10.12.

The jet quenching coefficient has been also estimated, based on non-perturbative calculations on a lattice [466–468]. The calculations were performed for two light quarks, at two different temperatures of 400 MeV and 2 GeV. It was found that the the non-perturbative soft contributions to $\hat{q}$ are large [468] and might play a dominant role in the parton energy loss in the QGP. The $\hat{q}$ obtained at lower temperature (accessible in A–A collisions at RHIC and LHC), including all perturbative contributions, is about 6 GeV^2/fm, with uncertainty of about 20%. It is larger as compared to results obtained with pQCD based models as well as with AdS/CFT calculations.

The improvements to theoretical calculations of the jet transport parameter with both perturbative and non-perturbative approaches are required to reduce modeling uncertainties in jet quenching studies within the wide energy and temperature range accessible at RHIC and at the LHC.

Chapter 11
Measurement of Nuclear Modification Factors of Identified Hadrons

The nuclear modification factors of charged pions, kaons and (anti)protons [23, 24, 27] and D-mesons [394] obtained by author in p–Pb and Pb–Pb collisions are discussed in this chapter. For completeness, the nuclear modification factors measured for D mesons in Pb–Pb collisions at $\sqrt{s_{\rm NN}}$ = 2.76 TeV [395, 396] and $\sqrt{s_{\rm NN}}$ = 5.02 TeV [28], in extended $p_{\rm T}$ range, are also presented. The comparison with other measurements at RHIC and at the LHC, and with model calculations is also discussed.

11.1 $R_{\rm pPb}$ and $R_{\rm AA}$ of $\pi^{\pm}$, $\rm K^{\pm}$ and p($\bar{\rm p}$)

Figure 11.1 shows the $R_{\rm pPb}$ of $\pi^{\pm}$, $\rm K^{\pm}$ and p($\bar{\rm p}$) measured at mid-rapidity ($-0.5 < y < 0$) in NSD p–Pb collisions at $\sqrt{s_{\rm NN}} = 5.02$ TeV [27]. The p–Pb and reference pp spectra used for the $R_{\rm pPb}$ determination are presented in Sec. 7.3 and Sec. 7.4, respectively. The $R_{\rm pPb}$ for identified hadrons are compared to that for inclusive charged particles ($\rm h^{\pm}$) [21] discussed in Sec. 10.1. At high $p_{\rm T}$ (> 10 GeV/c), all nuclear modification factors are consistent with unity within statistical and systematic uncertainties. At intermediate $p_{\rm T}$ (2–6 GeV/c), there is a Cronin enhancement seen for the (anit)protons, which is ~ 3 times larger than that for charged particles, while for charged pions and kaons the enhancement is below that of charged particles. The similar pattern was observed at RHIC, where the nuclear modification factor in minimum-bias d–Au collisions amounts to $R_{\rm dAu} = 1.24 \pm 0.13$ and 1.49 ± 0.17 in the range $2 < p_{\rm T} < 5$ GeV/c for cha rged pions and (anti)protons, respectively [469].

The analysis of identified particle spectra (see Sec. 7.3) show a strong multiplicity dependence of the proton-to-pion ratio for $p_{\rm T} < 10$ GeV/c, indicating that the modification of the (anti)proton spectral shape going from pp to p–Pb collisions could play a dominant role in the Cronin enhancement observed for inclusive charged particle $R_{\rm pPb}$ and $Q_{\rm pPb}$. However, the study of nuclear modification factor of identified hadrons as a function of p–Pb collision centrality are required to confirm such picture.

The nuclear modification factors of $\pi^{\pm}$, $\rm K^{\pm}$ and p($\bar{\rm p}$) measured at mid-rapidity as a collision centrality in Pb–Pb collisions at $\sqrt{s_{\rm NN}} = 2.76$ TeV are shown in Fig. 11.2 [24]. The resulting

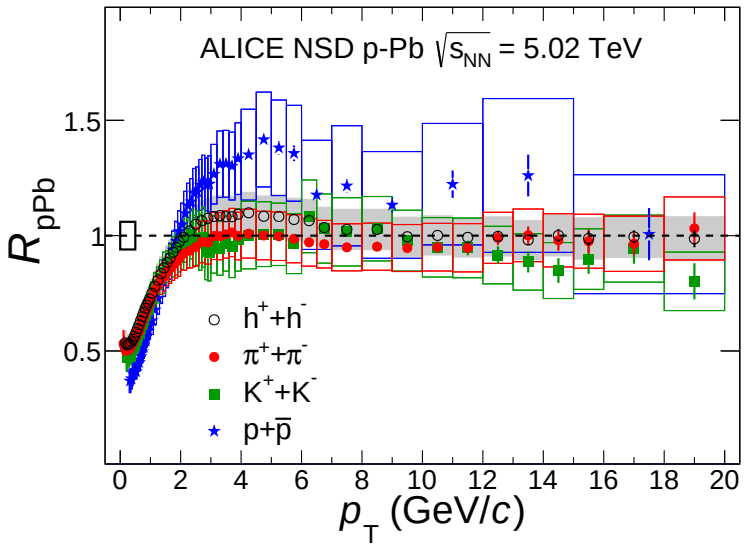

Fig. 11.1 R_{pPb} as a function of p_{T} for different particle species measured at mid-rapidity in NSD p–Pb collisions at $\sqrt{s_{\mathrm{NN}}} = 5.02$ TeV [27]. Statistical and systematic uncertainties are plotted as vertical error bars and boxes around the points, respectively. The total normalization uncertainty (pp and p–Pb) is indicated by the black box at unity.

R_{AA} are compared with the R_{AA} determined for inclusive charged particles ($\mathrm{h}^{\pm}$) [17]. The same suppression of $\pi^{\pm}$, $\mathrm{K}^{\pm}$ and p($\bar{\mathrm{p}}$) is observed for $p_{\mathrm{T}} > 10$ GeV/c. The suppression at high p_{T} is centrality dependent, and is similar to that for inclusive particles. This suggests that jet quenching does not affect significantly the particle composition (or fragmentation function) at high p_{T}. This observation is confirmed by the measurements of fragmentation functions for jets in pp and Pb–Pb collisions by CMS experiment [217, 470], which shows no modification of FFs in Pb–Pb as compared to FFs in pp, for jets with charged tracks with $p_{\mathrm{T}} > 3$ GeV/c. In contrast, ATLAS experiment has recently reported about a small modification (up to 20%) of FFs in Pb–Pb [215]. Therefore, further studies are required to resolve this issue.

The similarity of R_{AA} at high p_{T} implies that the particle ratios are also the same in pp and Pb–Pb collisions, as shown in Fig 7.6. Since the particle ratios are almost independent of p_{T} in this momentum range, the integrated particle ratios for $p_{\mathrm{T}} > 10$ GeV/c were used to elucidate the precision with which the suppression of charged pions, kaons and (anti)protons is similar. The resulting particle ratios were found to be the same within $\approx 10\%$ for kaons and pions, and within $\approx 20\%$ for protons and pions.

In Fig. 11.3, the R_{AA} for charged pions is compared to R_{AA} of neutral pions measured by PHENIX [458] at RHIC. The ALICE results are systematically below the PHENIX values for $p_{\mathrm{T}} < 10$ GeV/c and are consistent within systematic uncertainties at higher p_{T}. Based on a simple model of jet quenching [471], it was found that the energy loss is $\approx 40\%$ larger at the

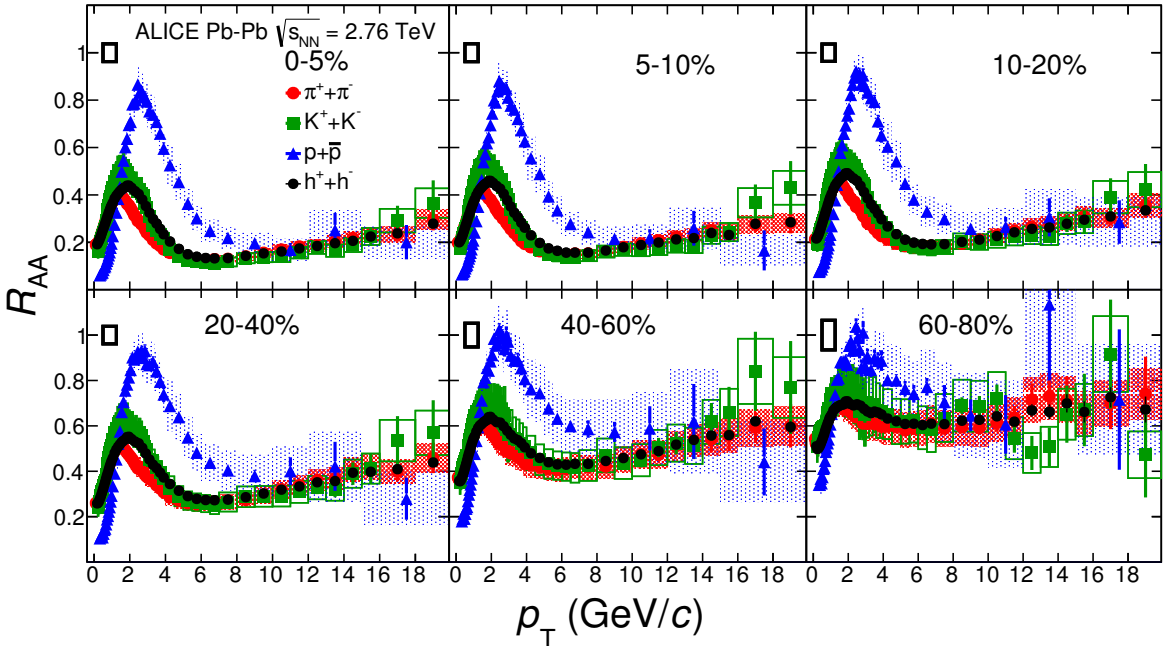

Fig. 11.2 R_{AA} as a function of p_{T} for different particle species measured at mid-rapidity ($-0.5 < y < 0$) in Pb–Pb collisions at $\sqrt{s_{\mathrm{NN}}} = 2.76$ TeV, for six centrality intervals [24]. Statistical and systematic uncertainties are plotted as vertical error bars and boxes around the points, respectively. The total normalization uncertainty (pp and Pb–Pb) is indicated by the black boxes at unity.

LHC than at the RHIC at $p_{\mathrm{T}} = 10$ GeV/c in all centrality classes; it scales as $\sqrt{\mathrm{d}N_{\mathrm{ch}}/\mathrm{d}\eta}$ for a fixed initial geometry.

At high p_{T}, it seems that the medium influence on a jet (hard core of the jet) as a whole rather than directly on its constituents, as discussed in Ref. [472]. Thus, a sizable fraction of the jets is unresolved by the medium, losing energy as a single parton without modifications of their intra-jet structure.

At intermediate p_{T} (2–6 GeV/c), the R_{AA} show maximum which magnitude depends on centrality and hadron species. In this region, more theoretical studies are needed to determine, whether models containing only hydrodynamics and jet quenching (e.g. [319]) can provide a good description or if additional processes such as recombination are needed. Since the initial geometry of the collision directly affects both the flow and the energy loss, the centrality dependence of R_{AA} is important for constraining both the low-p_{T} hydrodynamics (see Sec. 5.2) and the high-p_{T} jet quenching in the calculations.

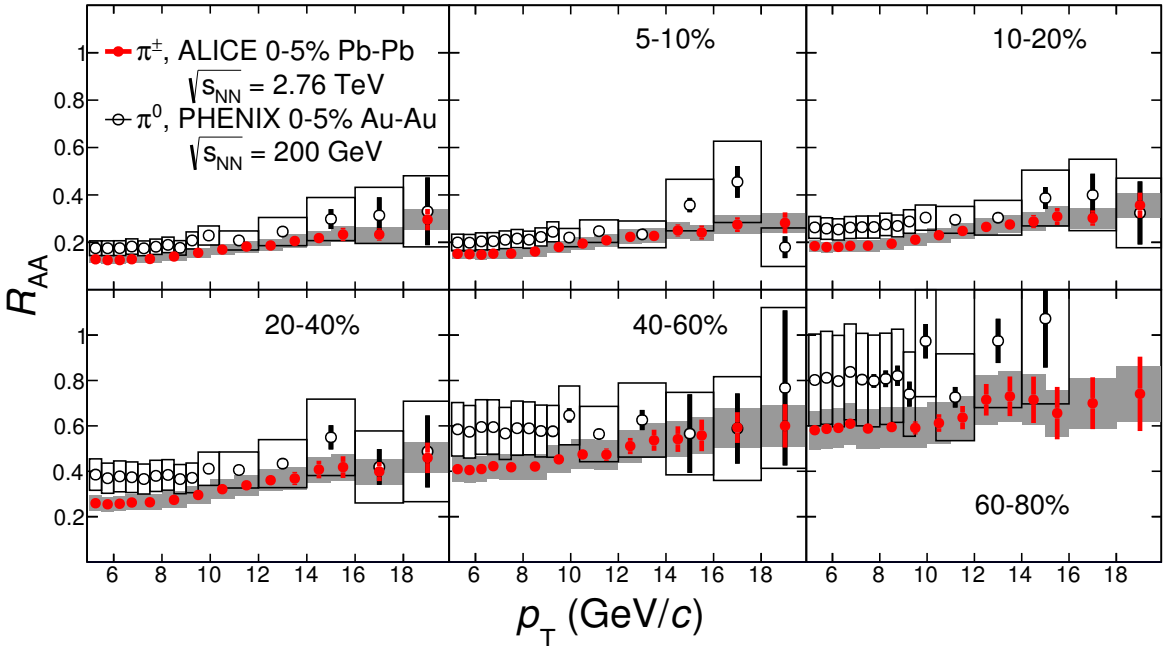

Fig. 11.3 R_{AA} as a function of p_{T} for charged pions measured at mid-rapidity ($-0.5 < y < 0$) in Pb–Pb collisions at $\sqrt{s_{\mathrm{NN}}} = 2.76$ TeV for six centrality intervals [24], compared with PHENIX results for neutral pions [458]. Statistical and systematic uncertainties are plotted as vertical error bars and boxes around the points, respectively.

11.2 R_{pPb} and Q_{pPb} of D^0 ($\bar{\mathrm{D}}^0$), $\mathrm{D}^{\pm}$, $\mathrm{D}^{*\pm}$ and $\mathrm{D}_{\mathrm{s}}^{\pm}$ Mesons

In this section, the measurement of nuclear modification factors R_{pPb} and Q_{pPb} of prompt D^0, D^+, D^{*+} and $\mathrm{D}_{\mathrm{s}}^+$ (and their antiparticles) in p–Pb collisions at $\sqrt{s_{\mathrm{NN}}} = 5.02$ TeV [392, 393] is presented. The reference pp spectra at $\sqrt{s} = 5.02$ TeV used for the determination of nuclear modification factors of D mesons, were obtained based on the pQCD scaling of the p_{T} spectra measured at $\sqrt{s} = 7$ TeV [391]. The scaling factor for each D-meson spectrum was determined as the ratio of the p_{T}-differential cross sections from the FONLL calculations at $\sqrt{s} = 5.02$ and 7 TeV (see Ref. [405] for more details).

The R_{pPb} of prompt D^0, D^+, D^{*+} and $\mathrm{D}_{\mathrm{s}}^+$ mesons measured at mid-rapidity in NSD p–Pb collisions are shown in Fig. 11.4 [392]. They are compatible with unity within the uncertainties in the measured p_{T} range. It shows that D-meson production in p–Pb collisions is consistent with the binary collision scaling of the production in pp collisions. Moreover, the R_{pPb} of $\mathrm{D}_{\mathrm{s}}^+$ is compatible with that of non-strange D mesons.

Figure 11.5 shows the average R_{pPb} of D^0, D^+, D^{*+} [392] in comparison to model predictions. The average was calculated using the relative statistical uncertainties as weights, while the systematic uncertainties on the average was calculated by propagating the uncertainties through the weighted average, where the contributions from tracking efficiency, B feed-down

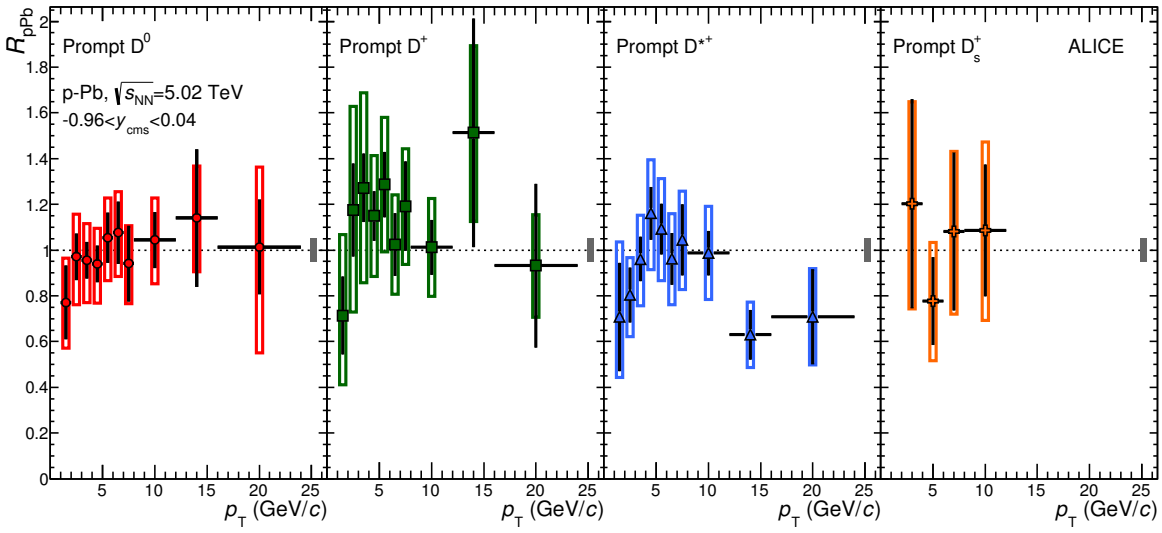

Fig. 11.4 $R_{\rm pPb}$ as a function of $p_{\rm T}$ for prompt $\rm D^0$, $\rm D^+$, $\rm D^{*+}$ and $\rm D_s^+$ mesons in p–Pb collisions at $\sqrt{s_{\rm NN}} = 5.02$ TeV [392]. Statistical (bars), systematic (empty boxes), and normalization (full box) uncertainties are shown.

correction, and scaling of the pp reference were taken as fully correlated among the three species. The model predictions include the NLO pQCD calculations (MNR [473]) of D meson production, with EPS09 [474] nuclear modification of CTEQ6M PDFs [204], the Color Glass Condensate (CGC) based model (Fujii-Watanabe [475]), and the model by Vitev et. al. [476] including cold-nuclear-matter energy loss, nuclear shadowing and $k_{\rm T}$ broadening. All models give reasonable good description of the data. The present uncertainties of the measurement do not allow yet to differentiate between models.

The average $\rm D^0$, $\rm D^+$, $\rm D^{*+}$ nuclear modification factors in different centrality classes obtained with the ZNA estimator, and applying the hybrid method to obtain $\langle T_{\rm pPb} \rangle$ for each centrality class (see Sec. 2.5.2 for details), are shown in Fig. 11.6 (left). The average $Q_{\rm pPb}$ are consistent with unity within the uncertainties for all centrality classes in the measured $p_{\rm T}$ interval. Thus, the D-meson $Q_{\rm pPb}$ results are consistent with binary collision scaling of the reference spectra in pp collisions, independent of the collision centrality.

The average D-meson $Q_{\rm pPb}$ as a function of centrality obtained with the three estimators CL1, V0A and ZNA (see Sec. 2.5.2 for details) in the $p_{\rm T}$ interval $8 < p_{\rm T} < 12$ GeV/c, are compared to $Q_{\rm pPb}$ of charged particles with $p_{\rm T} > 10$ GeV/c [22], which are presented in Sec. 10.2. In this transverse momentum region the production of charged hadrons is expected to scale with the number of binary nucleon-nucleon collisions. The $Q_{\rm pPb}$ determined for D mesons and charged hadrons at high $p_{\rm T}$ show a similar trends as a function of centrality and centrality estimator. As expected CL1 and V0A estimators introduce a strong bias on the $p_{\rm T}$ spectra and $Q_{\rm pPb}$ deviates from unity in central and peripheral collisions. The $Q_{\rm pPb}$ of

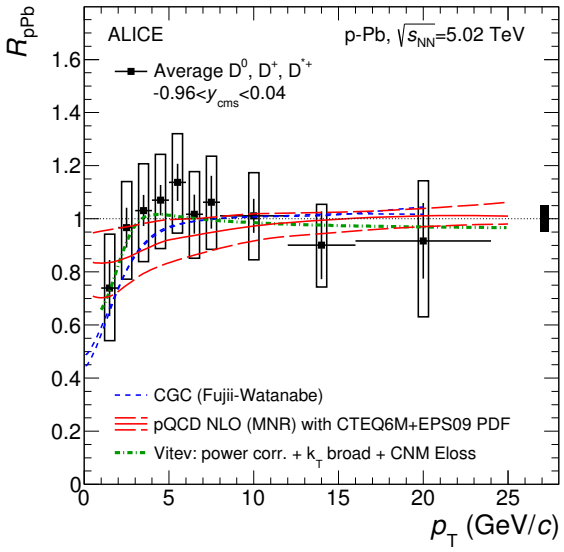

Fig. 11.5 Average R_{pPb} of prompt D^0, D^+, D^{*+} mesons as a function of p_{T} [392] compared to model calculations: pQCD NLO (MNR) [473], CGC (Fujii-Watanabe) [475] and Vitev et al. [476]. Statistical (bars), systematic (empty boxes), and normalization (full box) uncertainties are shown.

D mesons and charged particles are consistent with unity for all centrality classes determined based on hybrid method ($N_{\mathrm{coll}}^{\mathrm{mult}}$) with ZNA centrality estimator to determine $\langle T_{\mathrm{pPb}} \rangle$. This result allow for extending the studies of nuclear modification factors in p–Pb collisions as a function of centrality into the charm sector and down to low p_{T}.

11.3 R_{AA} of D^0 ($\bar{\mathrm{D}}^0$), $\mathrm{D}^{\pm}$ and $\mathrm{D}^{*\pm}$ Mesons

The nuclear modification factors for prompt D^0, D^+, D^{*+} mesons (and their antiparticles) measured at mid-rapidity in central (0–20%) and semi-peripheral (40–80%) Pb–Pb collisions at $\sqrt{s_{\mathrm{NN}}} = 2.76$ TeV [394], are shown in Fig. 11.7. This measurement was performed for the first time in heavy-ion collisions. The input Pb–Pb and pp reference spectrum are presented in Sec. 8.2. The results for the three D meson species are in agreement within uncertainties and they show a suppression, reaching a factor 3–4 ($R_{\mathrm{AA}} \approx$ 0.25–0.3) in central collisions for $p_{\mathrm{T}} > 5$ GeV/c. The suppression of D^0 decreases with smaller p_{T}. For semi-peripheral collisions, the suppression is weaker and R_{AA} amounts to 0.6–0.7.

The centrality dependence of the nuclear modification factor has been also studied in the two p_{T} intervals, $2 < p_{\mathrm{T}} < 5$ GeV/c, for D^0, and $6 < p_{\mathrm{T}} < 12$ GeV/c, for the three D mesons. The analysis was performed in five centrality classes from 0–10% to 60–80%, following the procedure described in Chap. 8. The resulting R_{AA} as a function of $\langle N_{\mathrm{part}} \rangle$ are shown in

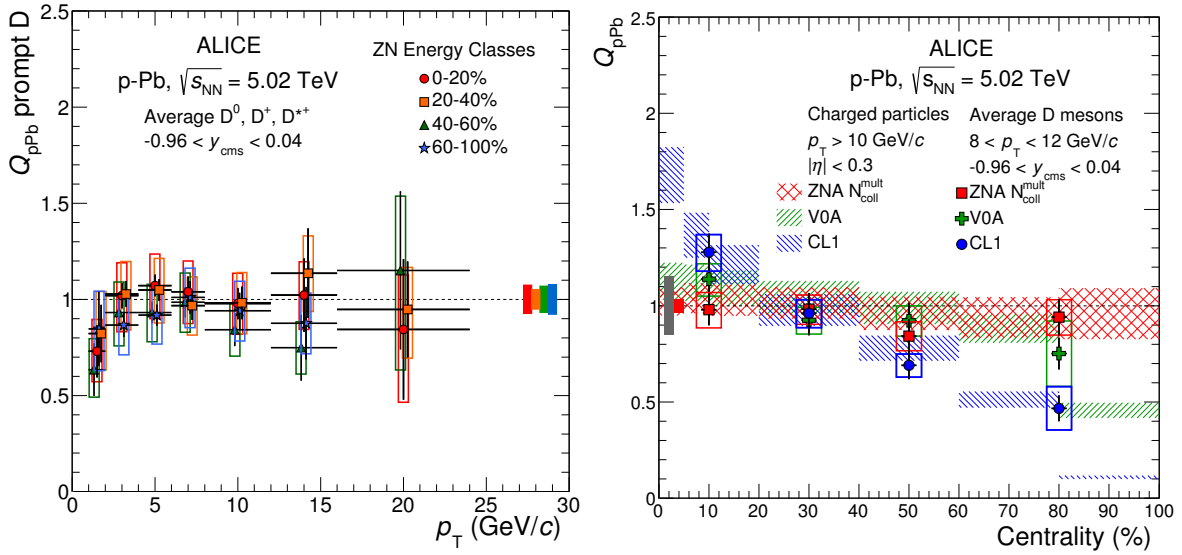

Fig. 11.6 Left: Average D^0, D^+, D^{*+} meson Q_{pPb} as a function of p_T in the 0–20%, 20–40%, 40–60% and 60–100% centrality classes selected with the ZNA estimator (hybrid method) [393]. The vertical error bars and the empty boxes represent the statistical and systematic uncertainties, respectively. The filled boxes at $Q_{pPb} = 1$ represent the normalization uncertainties. Symbols are displaced from the bin centre for clarity. Right: Average D-meson Q_{pPb} as a function of centrality with the CL, the V0A and the ZNA estimators [393]. The average D-meson Q_{pPb} for $8 < p_T < 12$ GeV/c is compared with the charged-particle Q_{pPb} calculated for $p_T > 10$ GeV/c [22]. The vertical error bars and the empty boxes represent the statistical and systematic uncertainties on the D-meson results.

Fig. 11.8 for D^0 meson (left) and D^0, D^+ and D^{*+} mesons (right). The contribution to the systematic uncertainty that is fully correlated between centrality classes (normalization and pp reference spectrum) and the remaining (uncorrelated) systematic uncertainties are displayed separately, by the filled and empty boxes, respectively. The suppression of D^0 at intermediate p_T increases with collision centrality from $R_{AA} \approx 0.6$ in peripheral (60–80%) to $R_{AA} \approx 0.3$ in central (0–10%) collisions. For $6 < p_T < 12$ GeV/c, the suppression increases with increasing collision centrality in similar way for all D mesons, reaching $R_{AA} \approx 0.2$ for the most central collisions.

The measurement of nuclear modification factors of D mesons in Pb–Pb collisions at $\sqrt{s_{NN}} = 2.76$ TeV has been extended by including high statistics Pb–Pb data collected by ALICE in 2011 [395, 396]. The pp reference for R_{AA} determination was obtained based on different methods, depending on the p_T range:

- in the range $2 < p_T < 16(24)$ GeV/c for D^0 (D^+ and D^{*+}), the spectrum at $\sqrt{s} = 7$ TeV [391] was scaled to $\sqrt{s} = 2.76$ TeV based on FONLL calculations [477];
- in the range $1 < p_T < 2$ GeV/c for D^0, an average of the aforementioned scaled p_T spectrum at $\sqrt{s} = 7$ TeV and of the measurement at $\sqrt{s} = 2.76$ TeV [390];

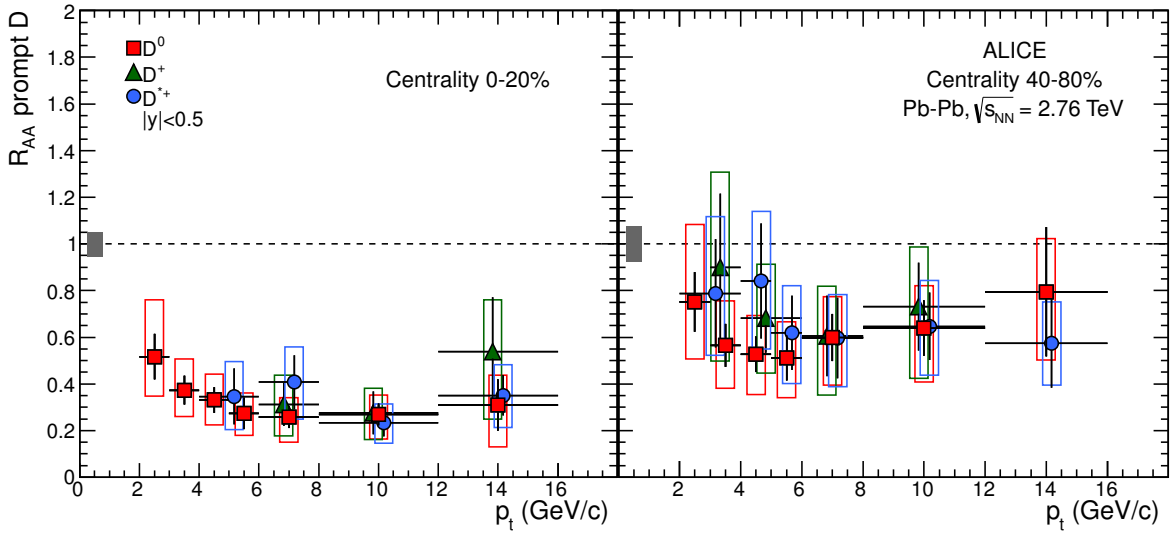

Fig. 11.7 R_{AA} for prompt D^0, D^+, D^{*+} in the 0–20% (left) and 40–80% (right) centrality classes [394]. Statistical (bars), systematic (empty boxes), and normalization (full box) uncertainties are shown. Horizontal error bars reflect bin widths, symbols were placed at the centre of the bin.

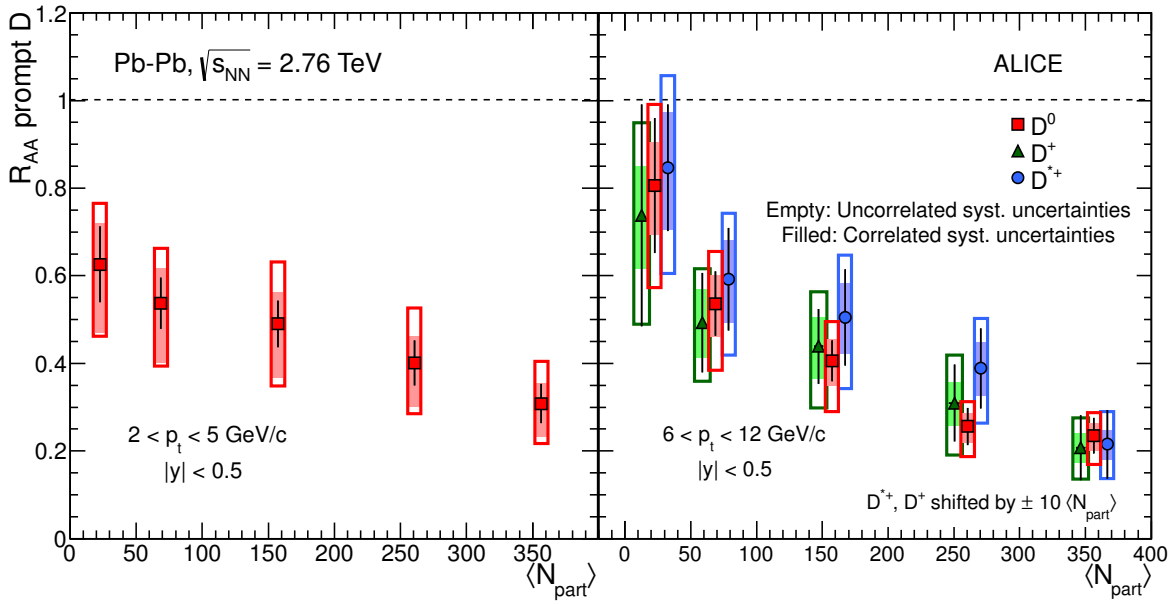

Fig. 11.8 Centrality dependence of R_{AA} for prompt D mesons [394]. Left: D^0 mesons with $2 < p_{\mathrm{T}} < 5$ GeV/c. Right: D^0, D^+, D^{*+} mesons with $6 < p_{\mathrm{T}} < 12$ GeV/c. D^+ and D^{*+} points are displaced horizontally for better visibility.

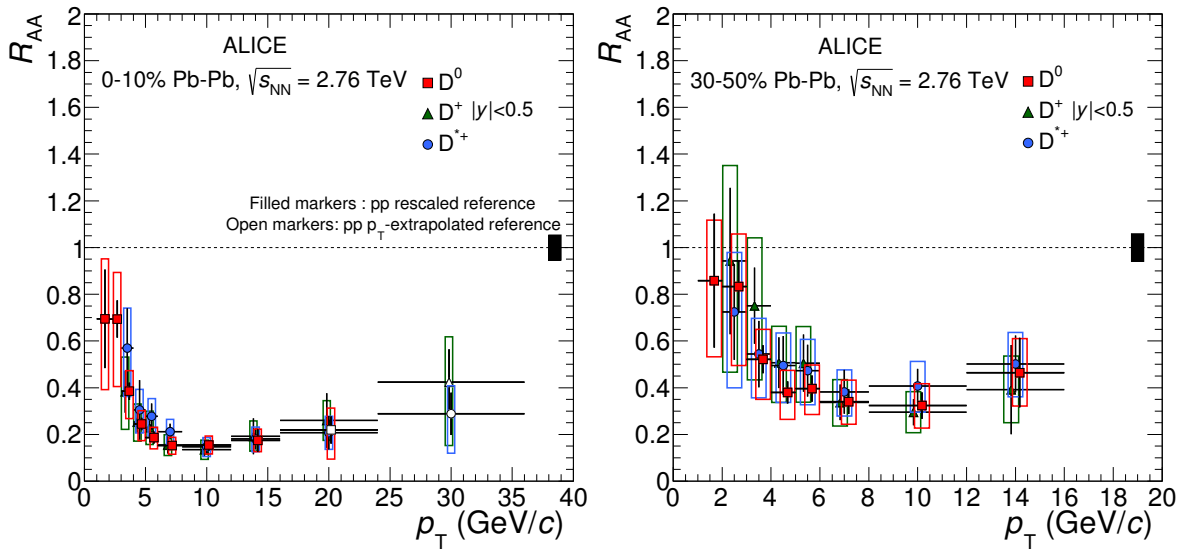

Fig. 11.9 R_{AA} for prompt D^0, D^+, D^{*+} in the 0–10% (left) and 30–50% (right) centrality classes [396]. Statistical (bars), systematic (empty boxes), and normalization (full box) uncertainties are shown. Horizontal error bars reflect bin widths, symbols were placed at the centre of the bin. D^+ and D^{*+} are shifted for better visibility.

- in the range $16(24) < p_T < 24(36)$ GeV/c for D^0 (D^+ and D^{*+}), where D meson spectra were not measured in pp collisions, the FONLL p_T spectrum at $\sqrt{s} = 2.76$ TeV [477] was used as a reference, after rescaling it to match central value of the data at lower p_T.

The resulting R_{AA} as a function of p_T is shown in Fig. 11.9 for the 0–10% (left) and 30–50% (right) central Pb–Pb collisions [396]. For the 0–10% central collisions, D meson spectra are most suppressed at around 10 GeV/c, by a factor of 5–6 with respect to the binary-scaled pp reference. The suppression decreases with decreasing p_T, and is about factor of 3 for $3 < p_T < 4$ GeV/c. For $p_T > 10$ GeV/c, the suppression seems to decrease with increasing p_T, but the large uncertainties does not allow to determine the trend. For 30–50% centrality class, the suppression is smaller than in the 0–10% centrality class, reaching about a factor of 3 at $p_T = 10$ GeV/c.

Figure 11.10 shows the R_{AA} as a function of centrality for D^0 (D^+ and D^{*+}) in the p_T intervals $5 < p_T < 8$ GeV/c (left) and $8 < p_T < 16$ GeV/c (right) [395]. The suppression increases with centrality and reaches a factor of 5–6 in the most central collisions for both p_T intervals.

ALICE has recently reported the measurement of prompt D^0, D^+, D^{*+} and D_s^+ mesons in Pb–Pb collisions at $\sqrt{s_{NN}} = 5.02$ TeV, in the centrality classes 0–10%, 30–50% and 60–80% [478]. The R_{AA} of D^0, D^+, D^{*+} mesons is shown in Fig. 11.11 (left panels), from central (top) to peripheral (bottom) collisions. The same suppression is observed for the three D-meson spectra in the measured p_T range. The obtained R_{AA} at $\sqrt{s_{NN}} = 5.02$ TeV is compatible with

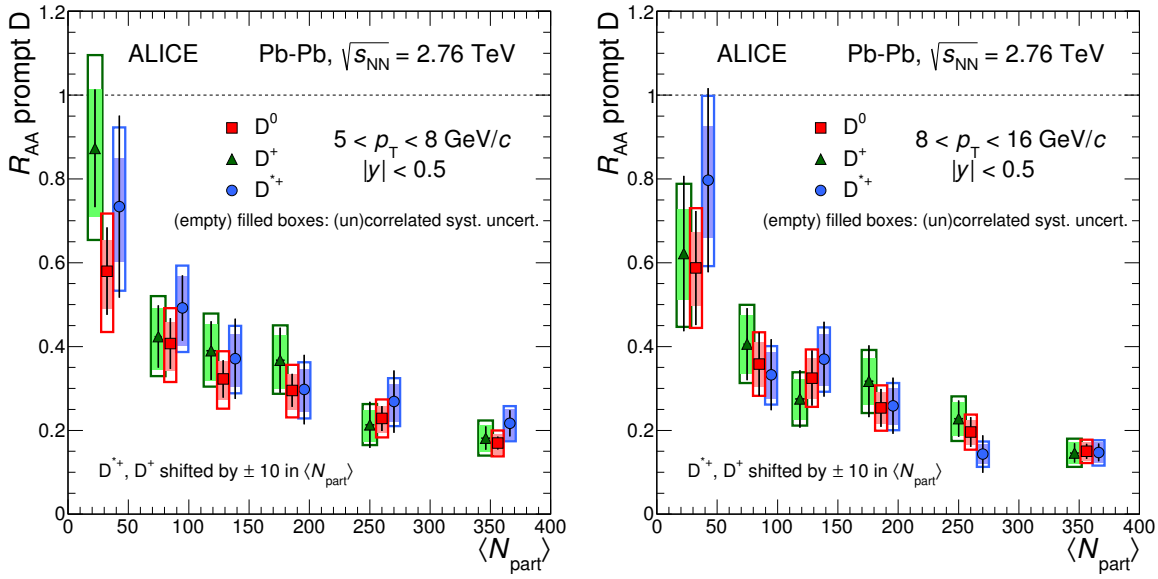

Fig. 11.10 Centrality dependence of R_{AA} for prompt D^0, D^+, D^{*+} mesons [395] in the p_T intervals $5 < p_T < 8$ GeV/c (left) and $8 < p_T < 16$ GeV/c (right). D^+ and D^{*+} points are displaced horizontally for better visibility.

that measured at lower collision energy of $\sqrt{s_{NN}} = 2.76$ TeV (Fig. 11.9), which can indicate that a parton energy loss is larger at higher $\sqrt{s_{NN}}$, as reported for the charged particles.

The average R_{AA} of D^0, D^+, D^{*+} mesons, shown in Fig. 11.11 (right pannels), was computed using the inverse of the squared relative statistical uncertainties as weights. The systematic uncertainties were propagated through the averaging procedure, discussed in detail in Ref. [478]. The average nuclear modification factors in the 0–10% and 30–50% centrality classes show the largest suppression in the range $6 < p_T < 7$ GeV/c, with $R_{AA} \approx 0.2$ and 0.4, respectively. The suppression is smaller with decreasing p_T for $p_T < 6$ GeV/c. For p_T larger than 7 GeV/c, the suppression weakly decreases with p_T to ≈ 0.4 and 0.5 for 0–10% and 30–50% central collisions, for the largest p_T. The average R_{AA} in the 60–80% centrality class shows a suppression by about 20–30%, without a pronounced p_T dependence. For comparison, the R_{AA} of prompt D_s^+ is shown for all centrality classes. The two measurements are compatible within one standard deviation of the combined uncertainties but there is a hint that the D_s^+ R_{AA} values are larger than that for D mesons without strangeness content. In the future, more precise measurements based on larger statistics data, which are planned at the LHC, should resolve this issue.

The suppression of D-meson production at high p_T with respect to binary nucleon-nucleon scaling, which is observed in Pb–Pb collisions at $\sqrt{s_{NN}} = 2.76$ and 5.02 TeV, is due to interactions of the charm quarks with the dense medium formed in the final-state of Pb–Pb collisions. This is confirmed by the nuclear modification factor measurements in NSD p–Pb collisions at

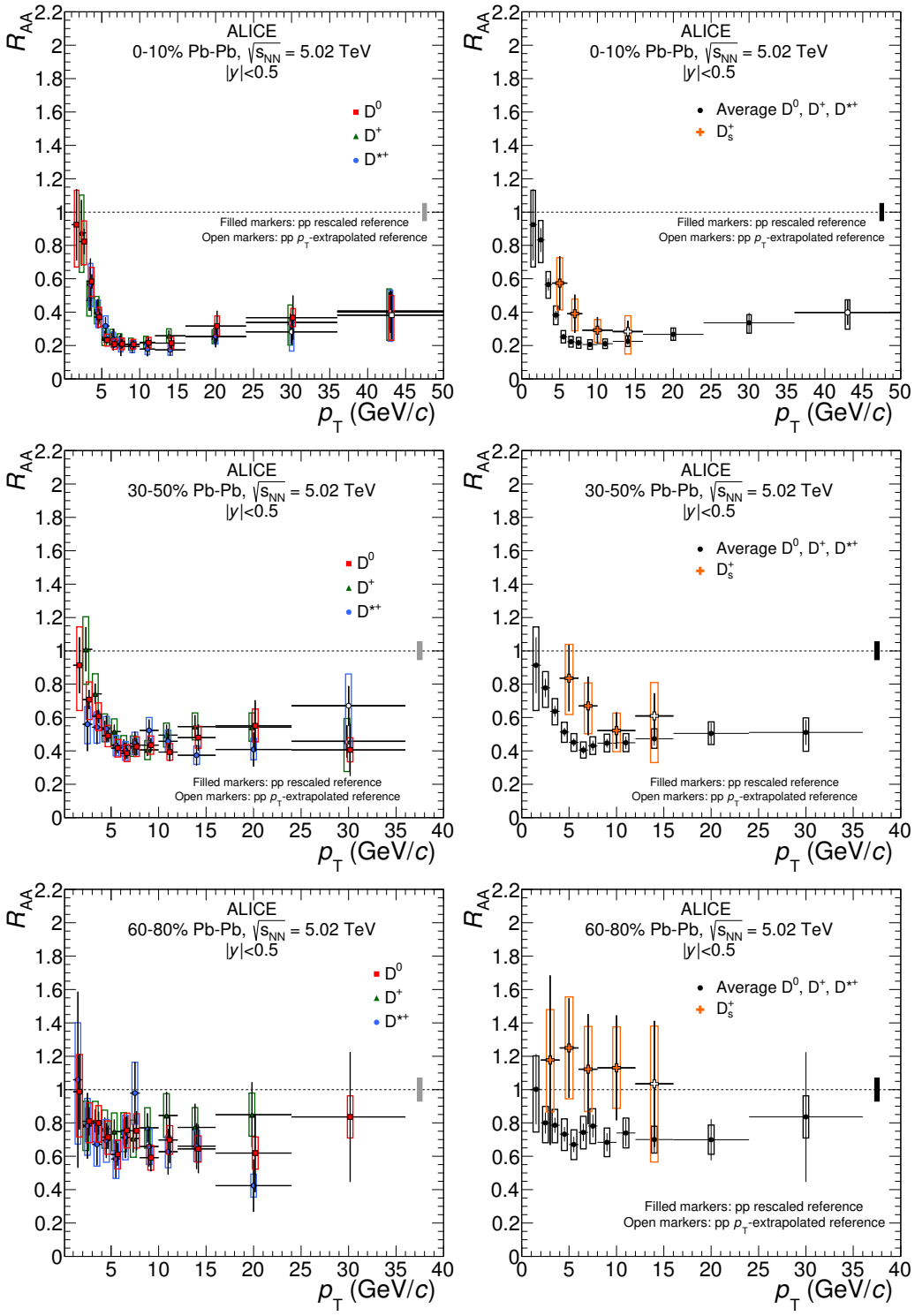

Fig. 11.11 R_{AA} of prompt D^0, D^+, D^{*+} mesons (left panels) and of prompt D_s^+ mesons compared with the average R_{AA} of the non-strange D mesons (right panels) for the 0–10%, 30–50% and 60–80% centrality classes [478]. Statistical (bars), systematic (empty boxes), and normalization (shaded box around unity) uncertainties are shown. Filled markers (pp rescaled reference), open markers (p_T-extraplolated reference).

$\sqrt{s_{\rm NN}} = 5.02$ TeV [392, 393], showing that D-meson $R_{\rm pPb}$ and $Q_{\rm pPb}$ are consistent with unity in the transverse momentum range $1 < p_{\rm T} < 24$ GeV/c (see Fig. 11.4 and Fig. 11.6).

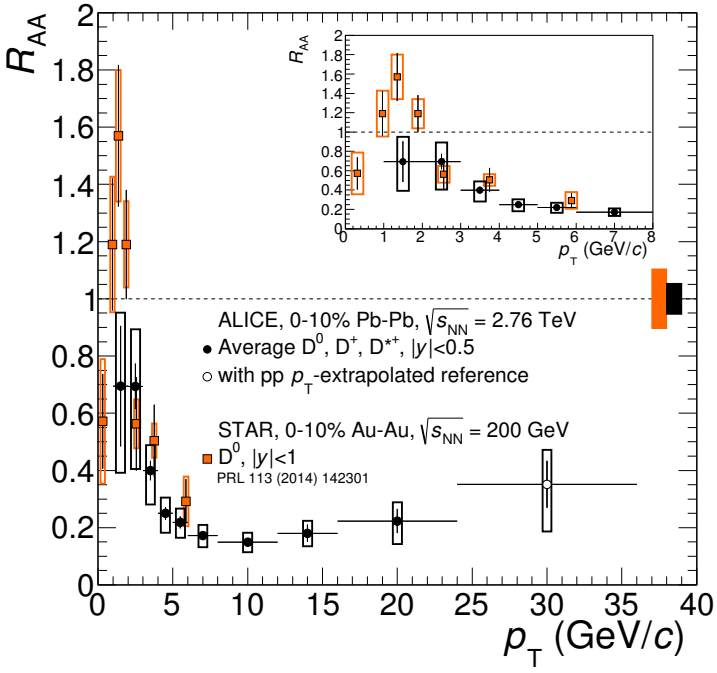

Fig. 11.12 Average D-meson $R_{\rm AA}$ as a function of $p_{\rm T}$ in the 0–10% central Pb–Pb collisions at $\sqrt{s_{\rm NN}} = 2.76$ TeV compared to $\rm D^0$ $R_{\rm AA}$ measured by STAR experiment in Au–Au collisions at $\sqrt{s_{\rm NN}} = 200$ GeV [479]. Inset shows the zoomed-in plot $p_{\rm T}$ range $0 < p_{\rm T} < 8$ GeV/c. Statistical (bars), systematic (empty boxes), and normalisation (shaded boxes at $R_{\rm AA} = 1$) uncertainties are shown. Horizontal bars represent bin widths. Symbols are placed at the centre of the bin.

The average D-meson $R_{\rm AA}$ measured in 0–10% central Pb–Pb collisions at $\sqrt{s_{\rm NN}} = 2.76$ TeV [396] is compared to the $\rm D^0$ $R_{\rm AA}$ measured by STAR experiment at RHIC in 0–10% central Au–Au collisions at $\sqrt{s_{\rm NN}} = 200$ GeV [479]. The D-meson $R_{\rm AA}$ measured at the two energies are compatible within uncertainties for $p_{\rm T} > 2$ GeV/c. At lower $p_{\rm T}$, the $R_{\rm AA}$ measured by STAR shows a maximum, which can be described by the models including parton energy loss, collective radial flow and the contribution of the recombination mechanism to charm-quark hadronization [300]. The $R_{\rm AA}$ measured by ALICE does not show a maximum, but precision of the measurement at this $p_{\rm T}$ region do not allow yet for a firm conclusion. A different pattern can be related to different initial-state effects related to modification of parton distribution functions [198] (see also Sec 3.1.1 for more details), which might lead to a stronger suppression of the heavy-flavor hadron production at low $p_{\rm T}$ with increasing $\sqrt{s_{\rm NN}}$, because of the smaller values of Bjorken-x probed. In addition, the Cronin effect is known to be more pronounced at lower $\sqrt{s_{\rm NN}}$. In the final state, the parton energy loss and collective ex-

pansion might affect the p_T distribution of charmed hadrons. The interactions of charm quarks with the medium constituents are expected to change momentum of low-p_T charm quarks and they can take part in collective radial flow of the medium. This effect could be enhanced by hadronisation via recombination (or regeneration), which is predicted in some models to contribute significantly to hadron formation at low and intermediate p_T (see Refs. [222, 480] for more details).

11.4 R_{AA} of D Mesons vs. Models

Figures 11.13 and 11.14 show D-meson R_{AA} in the 0–10% central collisions measured by ALICE at $\sqrt{s_{NN}}$ = 2.76 and 5.02 TeV [396, 478]. For a comprehensive model description and comparison see Refs. [222, 480].The interaction of heavy quarks with the medium constituents is computed considering radiative and collisional processes in the calculations indicated as Djordjevic [481], CUJET 3.0 [453, 454], WHDG [247, 444] and MC@sHQ+EPOS [482]. Only collisional energy loss is considered in TAMU elastic [483] and PHSD [484] models. For the Vitev model [476] two options with and without in-medium dissociation of heavy-flavor hadrons are considered. The SCET model [485] implements medium-induced gluon radiation via modified splitting functions with finite quark masses. The medium expansion is described using an underlying hydrodynamical model for most of the models except Djordjevic, WHDG and Vitev models, which do not include radial expansion.

The initial heavy-quark p_T distributions are based on NLO or FONLL perturbative QCD calculations in all model calculations. All models, with the exception of CUJET 3.0 include a nuclear modification of the parton distribution functions. The EPS09 NLO parameterization of the parton distribution functions is included in MC@sHQ+EPOS and TAMU elastic and PHSD models. The two latter models also include scattering of D mesons in the hadronic phase.

For the R_{AA} measured at $\sqrt{s_{NN}} = 2.76$ TeV, the pQCD-based models (Fig. 11.13, left) give relatively good description at high p_T (> 5 GeV/c). The Vitev model shows a better agreement at lower p_T when including the D-meson in-medium dissociation mechanism. The TAMU elastic and MC@sHQ+EPOS calculations of the nuclear medication factor, with and without including the EPS09 shadowing parameterization are shown in Fig, 11.13 (right). For $p_T > 7$ GeV/c, TAMU elastic model does not describe data, indicating that the radiative energy loss plays an important role at high p_T. For both models the inclusion of shadowing reduces the R_{AA} by up to 30–40% for $p_T < 5$ GeV/c, resulting in a better description of the data.

The pQCD-based calculations are in agreement with the R_{AA} measurements at $\sqrt{s_{NN}} =$ 5.02 TeV, as shown Fig. 11.14 (left). It indicates that the radiative energy loss is the dominant interaction mechanism in the p_T range used for comparison. In Fig. 11.14 (right) the non-strange and strange D-meson R_{AA} is compared with PHSD and TAMU transport models. An increase in D_s^+ R_{AA} seen for $p_T < 5$ GeV/c with respect to non-strange D mesons is described

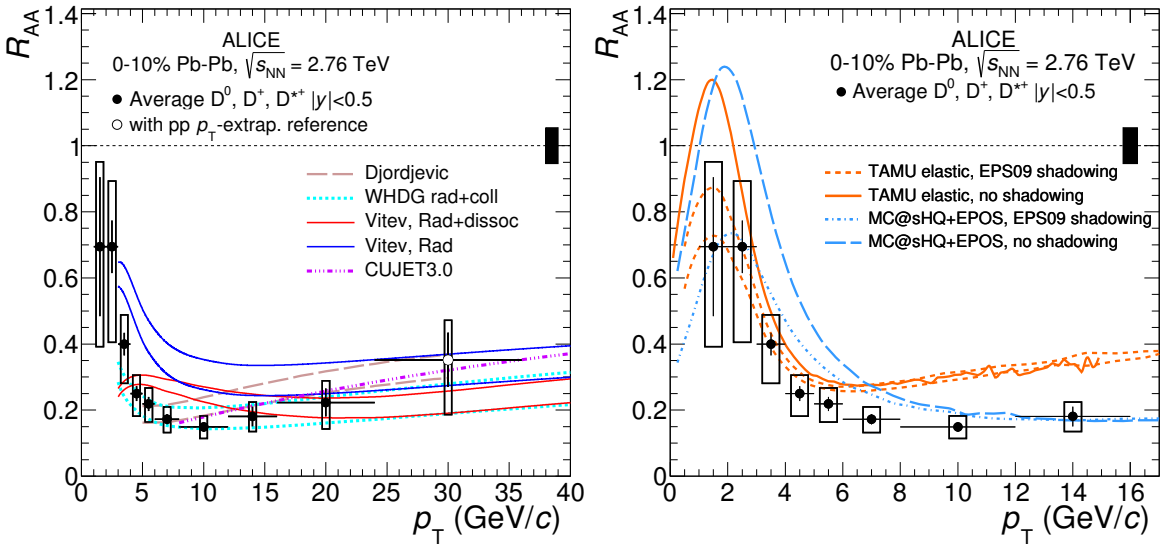

Fig. 11.13 Average R_{AA} of D^0, D^+ and D^{*+} mesons [396] compared with pQCD model calculations Djordjevic [481], CUJET3.0 [453, 454], WHDG [247, 444], Vitev [476] (left), and transport models TAMU elastic [483], MC@sHQ+EPOS [482] (right). Some of the model calculations are shown by two lines to represent their uncertainties or different componens.

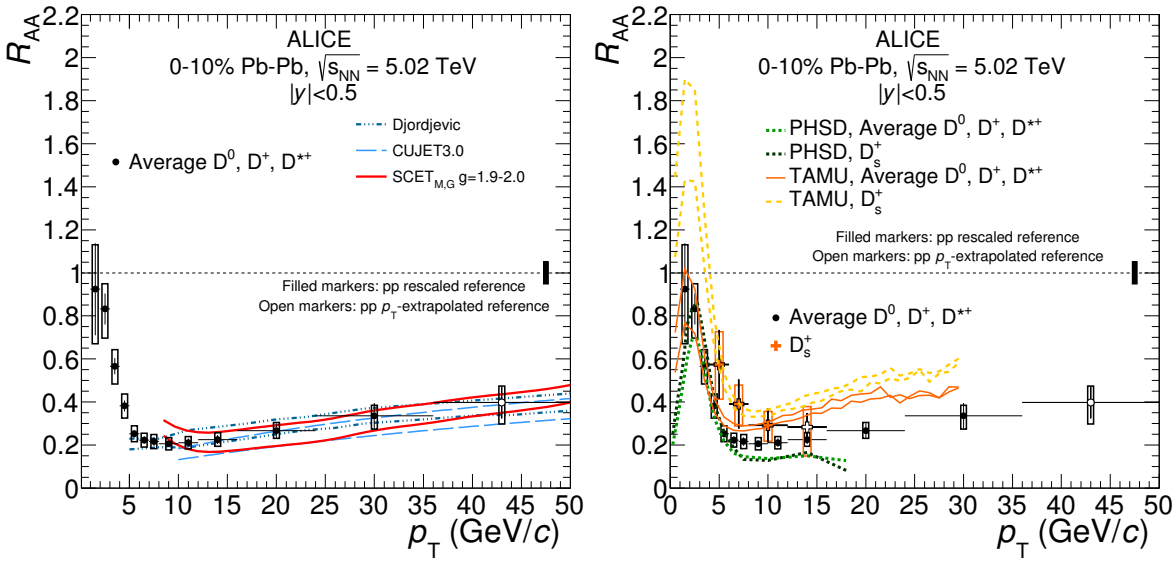

Fig. 11.14 Average R_{AA} of D^0, D^+ and D^{*+} mesons [478] compared with pQCD model calculations CUJET3.0 [454], Djordjevic [450] and SCET [485] (left), and transport models PHSD [484] and TAMU [483] (right). Some of the model calculations are shown by two lines to represent their uncertainties or different components.

by the TAMU model. This increase is induced by hadronization via quark recombination in the QGP and by different interaction cross sections for $\rm D_s^+$ and non-strange D mesons in the hadronic phase of the system evolution. The TAMU model predicts a sizable difference of about 30% up to about $p_{\rm T} = 8$ GeV/c, which is similar to that shown by the data. Both models fail to describe data at high $p_{\rm T}$, for $p_{\rm T} > 15$ GeV/c.

In order to judge about the quality of model calculations, the simultaneous comparison of $R_{\rm AA}$ and elliptic flow $\rm v_2$ measured at $\sqrt{s_{\rm NN}}$ = 2.76 and 5.02 TeV [363, 364] with the various models was performed in Refs. [222, 478, 480]. Presently, all of the considered models fail to describe simultaneously $R_{\rm AA}$ and $\rm v_2$ of D mesons. Therefore, the measurements provide significant constraints for the understanding of the interaction of charm quarks with the high-density QCD medium, especially at low and intermediate $p_{\rm T}$, where the $R_{\rm AA}$ is the result of a more complex interplay among several effects.

11.5 Comparison of $R_{\rm AA}$ for Light- and Heavy-flavor Hadrons

As discussed in Sec 3.2, the color-factor and quark-mass dependence of parton energy loss can be tested by comparing nuclear modification factors of light- and heavy-flavor hadrons. Figure 11.15 (left) shows the comparison of D-meson $R_{\rm AA}$ with charged-pion and charged-particle $R_{\rm AA}$ measured by ALICE in 0–10% central Pb–Pb collisions at $\sqrt{s_{\rm NN}} = 2.76$ TeV [17, 23, 396]. The comparison to $R_{\rm AA}$ of pions is performed in the range $1 < p_{\rm T} < 20$ GeV/c, while the $R_{\rm AA}$ of charged particles in the range $16 < p_{\rm T} < 40$ GeV/c. The charged-particle $R_{\rm AA}$ is shown in order to extend the comparison in $p_{\rm T}$, in which the D-meson $R_{\rm AA}$ was measured. This is justified because the light-flavor hadron suppression at high $p_{\rm T}$ is independent of particle species, as shown in Fig. 11.2. The $R_{\rm AA}$ of D mesons and light-favor hadrons are in agreement for $p_{\rm T} > 6$ GeV/c. At lower $p_{\rm T}$, the $R_{\rm AA}$ of D mesons tends to be higher than that of pions. It is estimated that $R_{\rm AA}^{\rm D} > R_{\rm AA}^{\pi}$ at low $p_{\rm T}$ with a significance of 1σ, taking into account current systematic uncertainties. However, a direct interpretation of this possible difference is not straightforward due to unknown $p_{\rm T}$ spectrum of light and charm quarks produced in hard interactions. In addition, the pion spectrum at low $p_{\rm T}$ has contribution from soft processes, which do not scale with the number of binary nucleon-nucleon collisions. Finally, the cold nuclear matter effects, radial flow and hadron production via recombination might affect $p_{\rm T}$ spectra of pions and D mesons in different way, introducing additional difficulty in quantitative $R_{\rm AA}$ comparison.

Figure 11.15 (right) shows comparison of D meson $R_{\rm AA}$ measured in 0–10% central Pb–Pb collisions with the $R_{\rm AA}$ of non-prompt $\rm J/\psi$ (arising from B meson decays) in 0–50% centrality class by ALICE [486] and in 0–20% centrality class by CMS [403]. A clear suppression of non-prompt $\rm J/\psi$ production is observed at intermediate and high $p_{\rm T}$, with $R_{\rm AA} \approx 0.4$. This suppression is weaker as compared to suppression of D meson production, which might indicate that there is indeed quark-mass dependence of in-medium energy loss. However, better precision data are required to draw a stronger conclusion. While comparing the $R_{\rm AA}$ of D

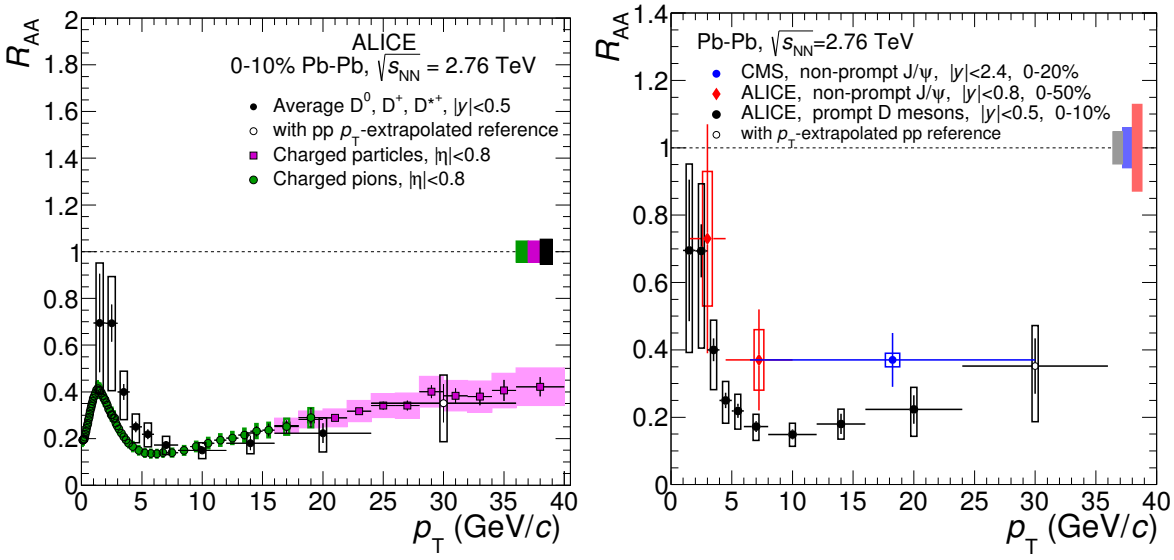

Fig. 11.15 Left: Average D-meson R_{AA} [396] compared to R_{AA} of charged pions [23] and charged particles [17]. Right: Non-prompt J/ψ R_{AA} from ALICE [486] at low p_T in the 0–50% centrality class and from CMS [403] at high p_T in the 0–20% centrality class, are compared to the prompt D-meson R_{AA} from ALICE [396]. The p_T-dependent systematic uncertainties are shown (both figures) as boxes around data points while the normalization uncertainties are depicted as boxes at $R_{AA} = 1$.

mesons and non-prompt J/ψ, one should note that the p_T of J/ψ is shifted to the lower momenta with respect to that of the parent B meson, due to the decay kinematics. The average p_T of the non-prompt J/ψ measured by CMS is about 10 GeV/c, which translates into an average B-meson p_T of 13 GeV/c, as estimated based on simulations of b-hadron decays [403].

Figure 11.16 shows the average R_{AA} of D^0, D^+ and D^{*+} mesons as a function of centrality, for the two p_T intervals, $5 < p_T < 8$ GeV/c (left) and in $8 < p_T < 16$ GeV/c (right) [395], compared with the R_{AA} of charged pions [23] in the same p_T intervals, and of non-prompt J/ψ mesons measured by CMS for $6.5 < p_T < 30$ GeV/c [403]. The p_T interval 8–16 GeV/c was chosen for comparison to have overlap with the p_T of B mesons decaying to J/ψ mesons with $6.5 < p_T < 30$ GeV/c. It was estimated based on FONLL simulations that about 70% of B mesons have momenta in the range 8–16 GeV/c, with median of about 11.3 GeV/c. For D mesons, the median is about 10 GeV/c in the considered p_T interval (see Ref. [395] for more details). The nuclear modification factors of charged pions and D mesons are compatible within uncertainties in all centrality classes for the two p_T intervals, as shown in Fig. 11.16 (left). The R_{AA} of D mesons in the p_T interval 8–16 GeV/c (Fig. 11.16, right) in the 0–10% and 10–20% central collisions is lower than that for non-prompt J/ψ mesons in 0–20% centrality interval, with significance of 3σ taking into account the statistical and systematic uncertainties.

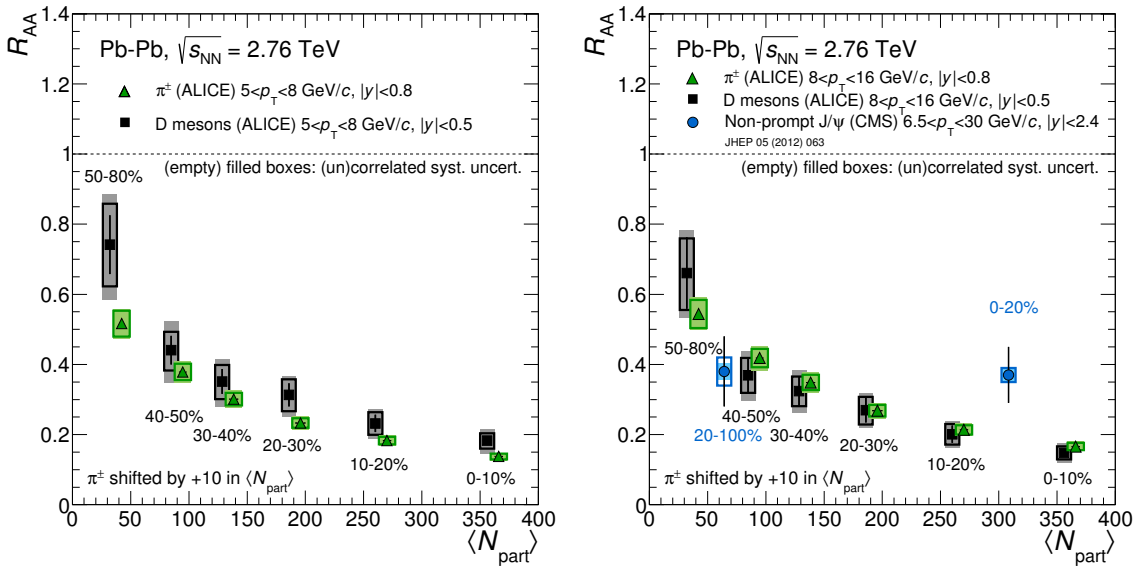

Fig. 11.16 Comparison of the average D meson R_{AA} [395] to the R_{AA} of charged pions [23] in $5 < p_T < 8$ GeV/c (left) and in $8 < p_T < 16$ GeV/c (right). The right figure also includes the R_{AA} of non-prompt J/ψ mesons in $6.5 < p_T < 30$ GeV/c measured by CMS [403]. The centrality-dependent systematic uncertainties are shown by boxes on the individual data points. The filled (empty) boxes represent the systematic uncertainties that are correlated (uncorrelated) among centrality intervals.

In Fig. 11.17, the R_{AA} for D mesons (average D^0, D^+ and D^{*+}) [395] and charged pions [23] in the interval $8 < p_T < 16$ GeV/c, and non-prompt J/ψ mesons in the interval $6.5 < p_T < 30$ GeV/c measured by CMS [403], are compared with the calculations by Djordjevic et al. [481]. This model implements energy loss for gluons, light and heavy quarks, including both radiative and collisional processes, as discussed in the previous section. The calculations closely describes the difference between D meson and charged pion R_{AA} over the entire centrality range, as shown in the left panel. In this calculations, the color-charge dependence of parton energy loss introduces a sizeable difference in the suppression of the gluon and c quark production. However, the combination of the different suppression and fragmentation patterns of gluons with respect to those of c quarks can lead to similar nuclear modification factors (see Ref. [487] for more details). As shown in the right panel, this calculation results in a larger suppression of D mesons with respect to non-prompt J/ψ, in qualitative agreement with the J/ψ data for the central collisions. In order to study the origin of this large difference in the calculation, the result for a test case with the energy loss of b quarks calculated using the c quark mass was considered [480]. Using this calculation, the non-prompt J/ψ R_{AA} was found to be close to that of D mesons, indicating that the largest difference between R_{AA} of D meson and non-prompt J/ψ originates from the quark mass dependence of the parton energy loss.

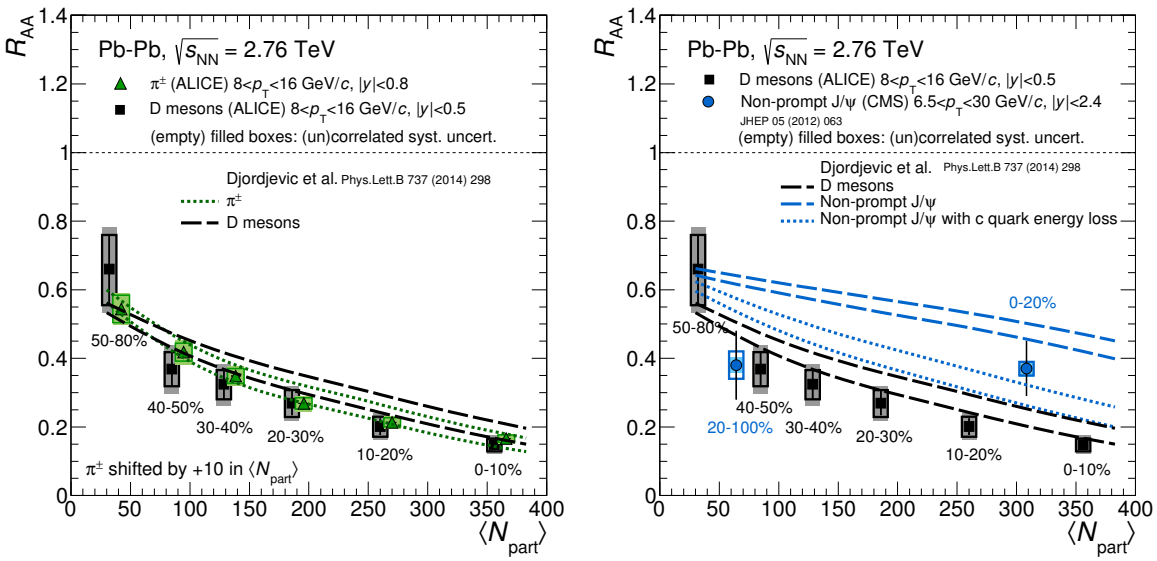

Fig. 11.17 Comparison of the R_{AA} measurements for D mesons [395], charged pions [23] by ALICE and non-prompt J/ψ mesons by CMS [403] with the calculations by Djordjevic et al. [481]. Lines of the same style enclose a band representing the theoretical uncertainty. Left: D mesons and charged pions in $8 < p_{\mathrm{T}} < 16$ GeV/c. Right: D mesons in $8 < p_{\mathrm{T}} < 16$ GeV/c and non-prompt J/ψ mesons in $6.5 < p_{\mathrm{T}} < 30$ GeV/c. For the latter, the model results for the case in which the b quark energy loss is calculated using the c quark mass are shown as well [480].

ALICE has recently measured D-meson nuclear modification factors in Pb–Pb collisions at $\sqrt{s_{\mathrm{NN}}} = 5.02$ TeV [28]. The comparison of the R_{AA} of prompt D mesons with that of charged particles measured in the same p_{T} intervals in Pb–Pb collisions at $\sqrt{s_{\mathrm{NN}}} = 5.02$ TeV, is shown in Fig 11.18 [28]. The measurements are shown for the 0–10% (left), 30-50% (middle) and 60–80% (right) centrality classes. The ratio of the nuclear modification factors is displayed in the bottom panels, for the three centrality classes. In central collisions, the R_{AA} of D mesons and charged particles differ by more than 2σ of the combined statistical and systematic uncertainties in all p_{T} bins for $3 < p_{\mathrm{T}} < 8$ GeV/c. In semi-central collisions, the difference is less than 2σ in the same p_{T} range. The measurements for D mesons and charged pions are compatible for $p_{\mathrm{T}} > 10$ GeV/c in central and semi-central collisions. In peripheral collisions, the measurements are compatible in the whole p_{T} range. A similar suppression of D^0 mesons in 0–10% collisions has been also reported by the CMS Collaboration [488].

The interpretation of the difference in $p_{\mathrm{T}} < 8$ GeV/c observed in central and semi-central collisions is problematic, because several effects can influence on the shape of the R_{AA}. The mentioned initial-state effects, different suppression and fragmentation patterns of gluons with respect to those of c quarks, soft production processes, radial flow and hadronization via recombination could affect D-meson and light-hadron yields differently at a given p_{T}. In order to resolve the issue of the color-charge and mass dependence of energy loss in the QGP more theoretical studies and more precise measurements of charm and beauty production are

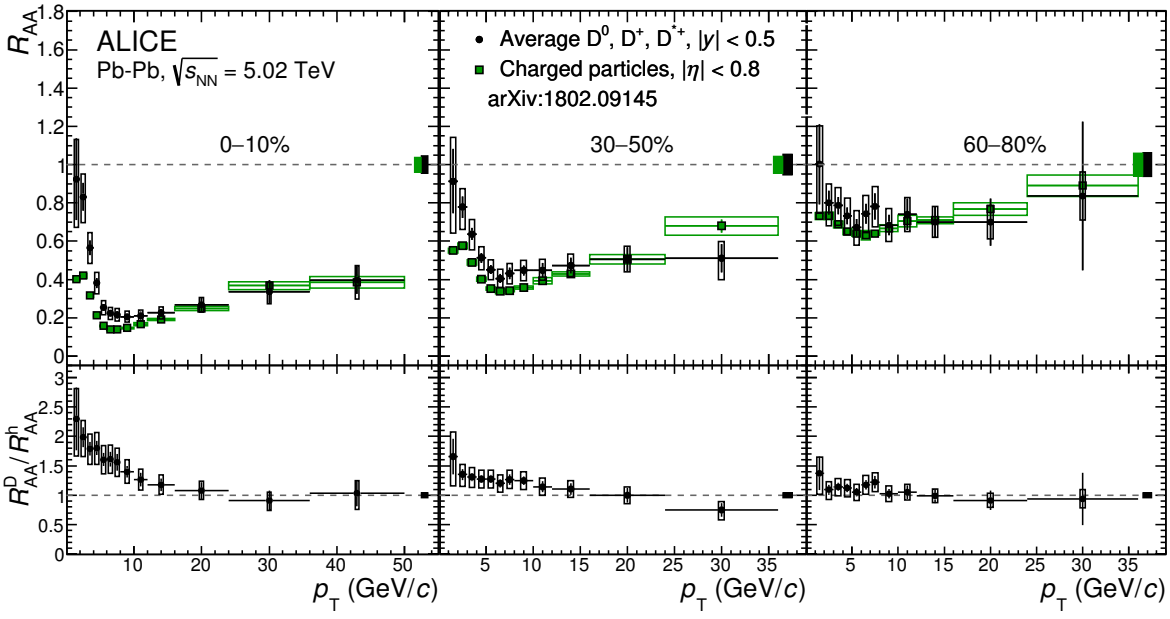

Fig. 11.18 Average R_{AA} of prompt D^0, D^+, D^{*+}) mesons in the 0–10% (left), 30–50% (middle) and 60–80% (right) centrality classes at $\sqrt{s_{\mathrm{NN}}} = 5.02$ TeV [478] compared to the R_{AA} of charged particles in the same centrality classes [28]. The ratios of the R_{AA} are shown in the bottom panels. Statistical (bars), systematic (empty boxes), and normalization (shaded boxes at unity) uncertainties are shown.

required. However, the presented measurements already provide significant constraints for model calculations of interactions of gluons and quarks with the high-density QCD medium.

Chapter 12
Measurement of Nuclear Modification Factors of Jets

The nuclear modification factors of charged jets [19, 26] in p–Pb and Pb–Pb collisions obtained by author are presented in this chapter. For comparison, the R_{AA} of full jets [248] is also shown. The comparison with measurements from other LHC experiments and model calculations is also discussed.

12.1 R_{pPb} of Charged Jets

Figure 12.1 shows the nuclear modification factor R_{pPb} of charged jets measured with $R = 0.2$ (left) and R = 0.4 (right) in p–Pb collisions at $\sqrt{s_{\mathrm{NN}}} = 5.02$ TeV [26]. The pp reference at $\sqrt{s} = 5.02$ TeV for R_{pPb} determination was based on the scaling of the charged jet spectrum measured by ALICE in pp collisions at $\sqrt{s} = 7$ TeV [406]. The scaling factors were determined based on the NLO pQCD calculations (POWEG + PYTHIA8) at the two energies, as discussed in Ref. [26]. The R_{pPb} is consistent with unity in the measured p_{T} range, indicating the absence of a large modification of the initial parton distributions or a strong final state effect on jet production. This is in agreement with results on the jet production in p–Pb collisions reported by ATLAS [489] and CMS [490] experiments. It was als estimated, based on the POWHEG+PYTHIA8 simulations [26], that the presented R_{pPb} for charged jets and charged particles [21] probes roughly the same parton p_{T}. Therefore, the results on high p_{T} charged particle production, which show R_{pPb} consistent with unity for p_{T} up to 50 GeV/c, are confirmed by the charged jet measurements. Since the jet measurements integrate the final state particles, they have a smaller sensitivity to the fragmentation pattern of partons than single particles. It also confirms that the hard part of fragmentation function is unaffected by the medium formed in p–Pb collisions.

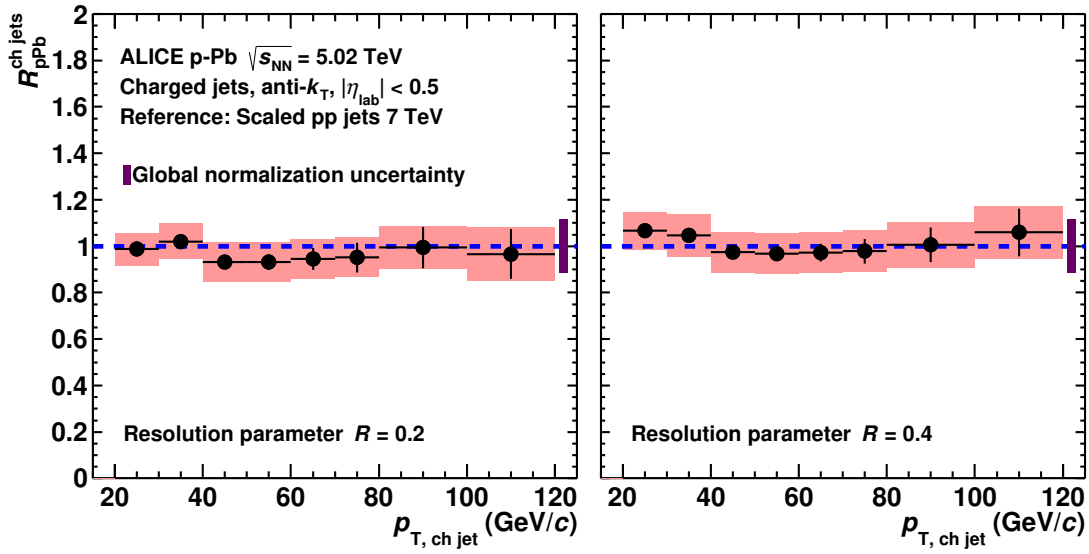

Fig. 12.1 Nuclear modification factors R_{pPb} of charged jets measured with the two different resolution parapeters $R = 0.2$ (left) and $R = 0.4$ (right) [26]. The combined global normalization uncertainty from $\langle T_{\mathrm{pPb}} \rangle$, the correction to NSD events, the measured pp cross section, and the reference scaling is depicted by the box around unity.

12.2 R_{CP} and R_{AA} of Charged and Full Jets

The jet suppression factor R_{CP} (defined in Sec. 3.4) is shown in Fig. 12.2 [19] for charged jets with $R = 0.2$ (left panels) and $R = 0.3$ (right panels) using peripheral centrality class (50–80%) as the reference. A strong jet suppression, $0.3 < R_{\mathrm{CP}} < 0.5$, is observed for 0–10% central collisions (top panels), while the suppression is reduced for more peripheral collisions to $R_{\mathrm{CP}} \approx 0.8$ for 30–50% central collisions (bottom panels). A weak decrease of suppression is observed at low jet p_{T} and it is almost constant above 50 GeV/c. The R_{CP} does not change significantly with the resolution parameter R for the range studied.

Figure 12.3 shows the R_{CP} as a function of collision centrality, expressed by the number of participating nucleons $\langle N_{\mathrm{part}} \rangle$, for jets with $60 < p_{\mathrm{T,ch\ jet}} < 70$ GeV/c and with resolution parameters $R = 0.2$ (left) and $R = 0.3$ (right) [19]. A decreasing trend of the R_{CP} as a function of $\langle N_{\mathrm{part}} \rangle$ is observed for unbiased (all) jets as well as for biased jets with a high p_{T} track selection. It indicates that the suppression is independent of the jet fragmentation pattern.

The first measurements of jets in heavy-ion collisions at the LHC showed a large energy imbalance for jet pairs [138, 491, 492], indicating that a significant fraction of recoil jet momentum is transported out of the jet cone due to interactions with the medium. The large suppression of charged jets with $R = 0.2$ and $R = 0.3$ also indicates that the momentum transport to large angles is an important effect. It can be further explore by comparing R_{CP} measured for single charged hadrons [17, 383] and jets [493] measured at the LHC, as shown in Fig-

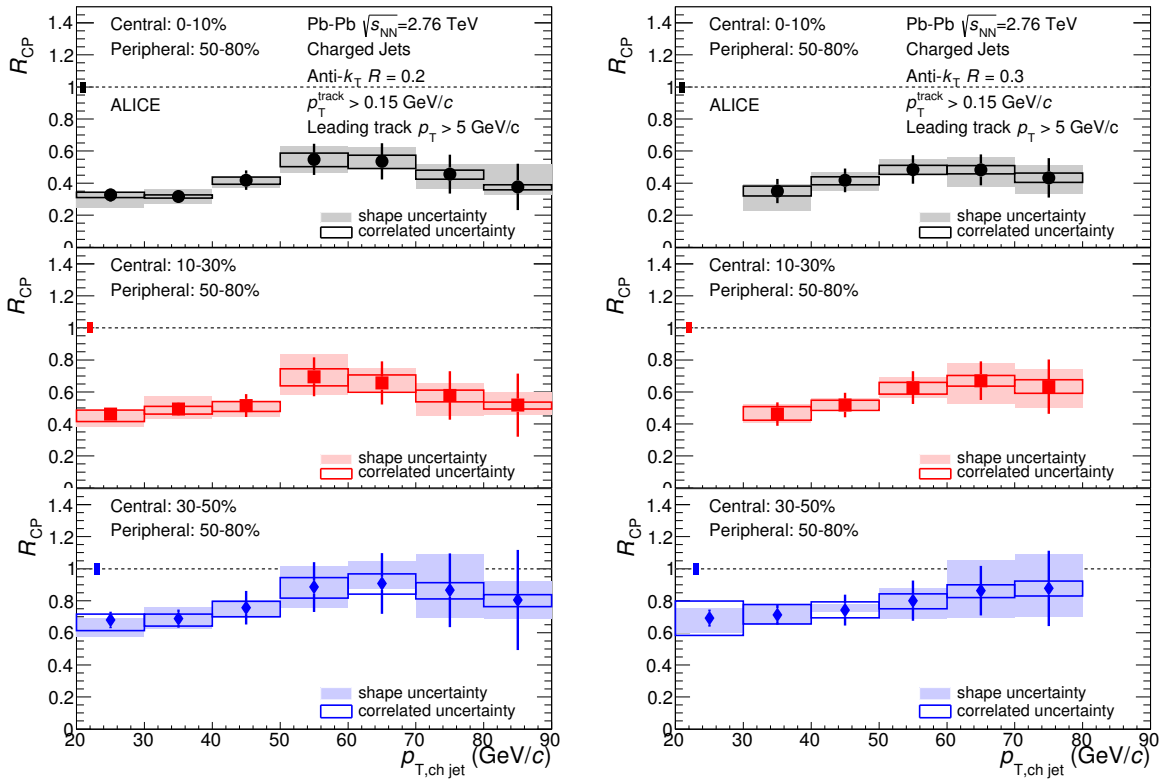

Fig. 12.2 Nuclear modification factor R_{CP} for charged jets with a leading charged particle with $p_T^{\text{leading track}} > 5$ GeV/c, with $R = 0.2$ (left panels) and $R = 0.3$ (right panels) and different centrality selections [19]. The correlated (shape) and uncorrelated uncertainties are depicted by filled and empty boxes around data points. The $\langle T_{AA} \rangle$ related uncertainties are indicated by boxes at unity.

ure 12.4 [19]. It can be seen that, the R_{CP} for jets is similar to that observed for single hadrons over a broad momentum range. It was verified based on PYTHIA simulations that the jets and the charged hadrons probe similar parton p_T. The estimated scaling factors for the measured p_T of charged jets and hadrons amount to approximately 1.4 and 2.9, respectively. The obtained results suggest that the jet momentum is redistributed to angles larger than $R = 0.3$ due to interaction with the medium.

ALICE has also measured R_{AA} of full jets reconstructed using the anti-k_T jet algorithm with a resolution parameter of $R = 0.2$ from charged and neutral particles [248], utilizing the ALICE tracking detectors and Electromagnetic Calorimeter (EMCal). Reconstructed jets were required to contain a leading charged particle with $p_T > 5$ GeV/c to suppress jets constructed from the combinatorial background in Pb–Pb collisions. The jet spectrum in pp collisions (pp reference) was measured in the same way as reported in Ref. [496], with additional requirement of leading track with $p_T > 5$ GeV/c. It was checked that the leading track selection applied to jet spectra both in pp and Pb–Pb collisions had a negligible effect on the R_{AA}. Figure 12.5 shows the resulting R_{AA} for jets reconstructed in 0–10% (left) and 10–30% (right)

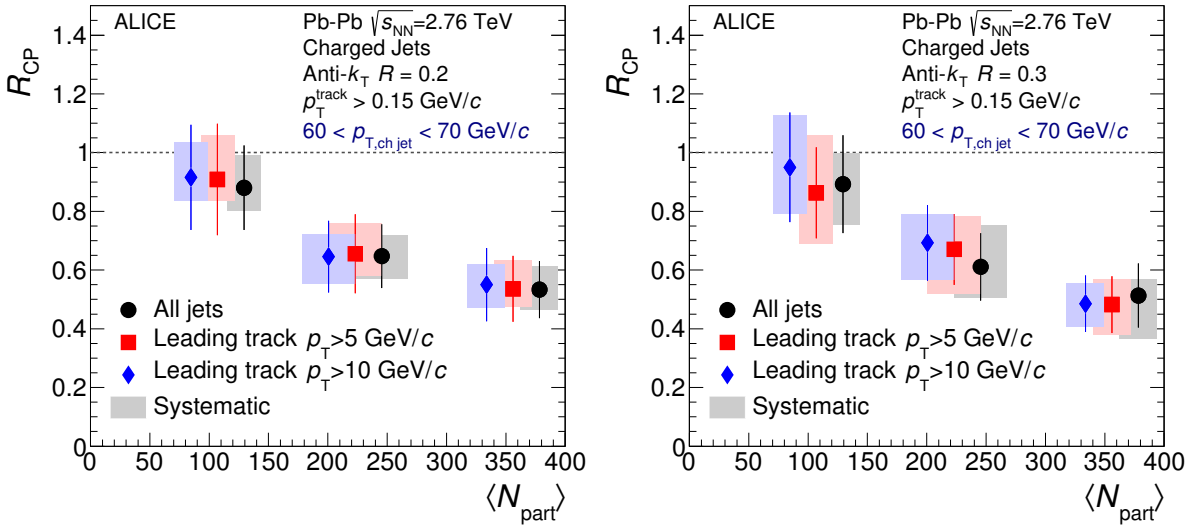

Fig. 12.3 R_{CP} for unbiased and leading track biased jets with $60 < p_{\mathrm{T,ch\ jet}} < 70$ GeV$/c$ as a function of the average number of participants in the collision [19], for jets with $R = 0.2$ (left) and $R = 0.3$ (right). For visibility the data points for all jets and for jets with $p_{\mathrm{T}}^{\text{leading track}} > 10$ GeV$/c$ are shifted to the left and right respectively.

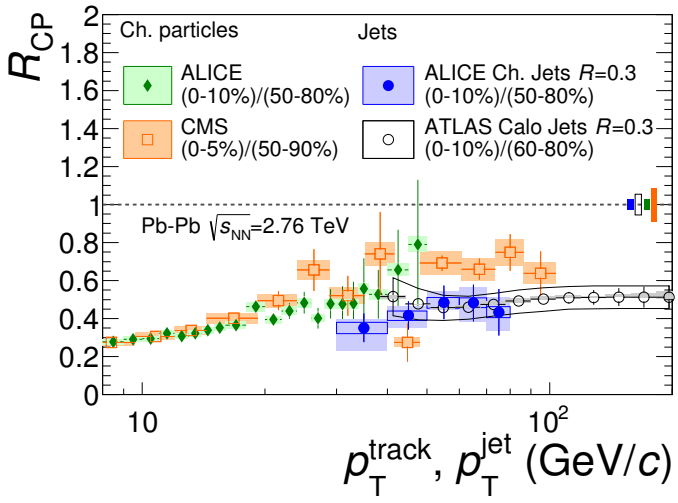

Fig. 12.4 Comparison to jet R_{CP} measured by ATLAS [493] and to charged particle suppression by ALICE [17] and CMS [383]. Note that the underlying parton p_{T} scale is different at the same measured p_{T} for charged particles, charged jets and full jets. Figure is taken from Ref. [19].

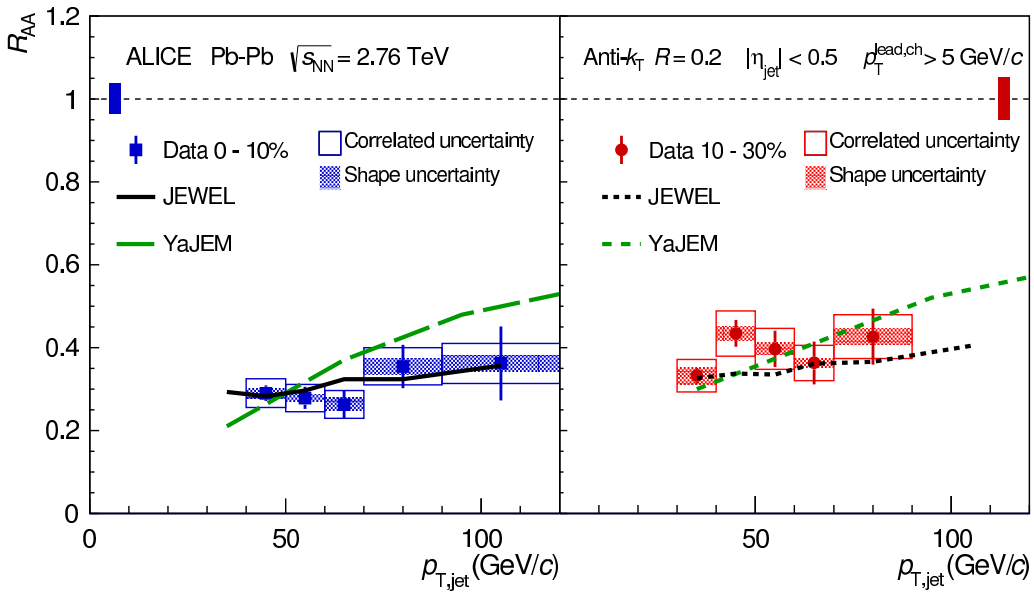

Fig. 12.5 R_{AA} for $R = 0.2$ jets with the leading track requirement of 5 GeV/c in 0–10% (left) and 10–30% (right) central Pb–Pb collisions [248] compared to calculations from YaJEM [494] and JEWEL [495]. The boxes at $R_{AA} = 1$ represent the systematic uncertainty on T_{AA}.

central Pb–Pb collisions at $\sqrt{s_{NN}} = 2.76$ TeV [248]. The R_{AA} shows that the jets in the measured p_T range are strongly suppressed. The average R_{AA} was found to have negligible p_T dependence, and amounts to around 0.3 and 0.4 for the 0–10% and 10–30% centrality classes, respectively. These results qualitatively agree with the suppression of charged jets [19]. The data are also compared to calculations from YaJEM [494] and JEWEL [495] models (see Sec. 3.3.2 for model description). Despite their different approaches, both calculations are found to reproduce the jet suppression. However, YaJEM exhibits a slightly steeper increase with jet p_T.

The R_{AA} of jets measured by ALICE [248] is compared with the R_{AA} reported by ATLAS for $R = 0.4$ [249] in Fig. 12.6. The results are consistent when ATLAS R_{AA} is scaled by the ratio of yields with different resolution parameters in different $p_{T,\,jet}$ intervals [493]. The CMS Collaboration has also recently reported the similar suppression of jets in Pb–Pb collisions at $\sqrt{s_{NN}} = 2.76$ TeV [250].

For comparison, the preliminary results on R_{AA} for charged jets measured by ALICE at $\sqrt{s_{NN}} = 5.02$ TeV are shown. Two alternative approaches to determine pp reference spectra at $\sqrt{s_{NN}} = 5.02$ TeV were applied. The first reference is based on pp data measured at the same collision energy, while the second is based on the scaling of the charged jet spectrum measured by ALICE in pp collisions at $\sqrt{s} = 7$ TeV [406] with factors from NLO pQCD calculations (POWHEG + PYTHIA8), as discussed in the previous section. The suppression

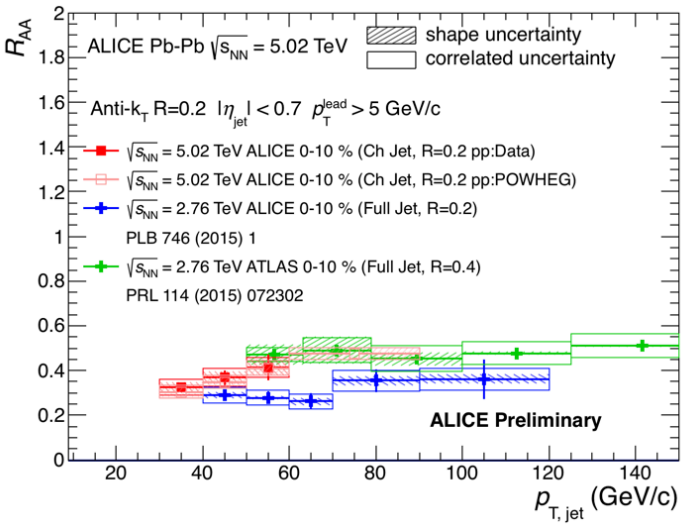

Fig. 12.6 Comparison of R_{AA} for jets measured by ALICE [248] and ATLAS [249] at $\sqrt{s_{NN}} = 2.76$ TeV and for charged jet measured by ALICE at $\sqrt{s_{NN}} = 5.02$ TeV (preliminary results). The R_{AA} of charged jets is determined using pp reference based on data and POWHEG simulations at the same collision energy. The normalization uncertainties ($\sim 4\%$) are not shown.

for charged and full jets measured by ALICE is similar at the two collision energies, and is consistent with results reported for the charged particles.

The production of jets associated to bottom quarks measured for the first time in Pb–Pb collisions at $\sqrt{s_{NN}} = 2.76$ TeV has been reported by CMS [497]. The jet spectra were measured for the 0–10%, 10–30%, 30–50% and 50-100% centrality classes, in the transverse momentum range $80 < p_T < 250$ GeV$/c$ and within pseudorapidity $|\eta| < 2$. The obtained nuclear modification factors show a strong suppression of b-jet yields with respect to binary scaled yields measured in pp collisions at the same energy. The yield is most suppressed in 0–10% central collisions with $R_{AA} \approx 0.4$ for jets with $80 < p_T < 110$ GeV$/c$. This value of R_{AA} is similar to results observed for inclusive jets. Although a sizable fraction of b-tagged jets come from gluon splitting, a large mass and/or color-factor dependence of parton energy loss can be excluded for this p_T range. A measurement of b-jet suppression at lower p_T would help to cross check a different suppression pattern observed for the non-prompt J$/\psi$ and prompt D mesons.

Chapter 13
Summary

This habilitation thesis summarizes the author's work on characterization of the hot and dense QCD matter produced in heavy-ion collisions at the LHC. The measurements have been performed with ALICE detector, designed to explore the physics of the strongly interacting matter at extreme density and temperature, where the formation of the quark-gluon plasma (QGP), the state of deconfined quarks and gluons, is expected. The existence of the QGP and its properties are key issues in QCD for the understanding of confinement and chiral symmetry restoration. This is also relevant for the early stage of the Universe as we go backward in the cosmic evolution, as well as in the understanding of the properties of the inner core of neutron stars, the densest cosmic objects.

The properties of the QCD matter have been explored with high p_{T} and/or high mass particles and jets (hard probes), which are well suited to study the hottest and densest phases of the reaction. The production of hard probes in high-energy hadron-hadron or nucleus-nucleus collisions can be computed from the underlying parton-parton hard processes using the QCD factorization theorem. The details of production and propagation of these probes can be used to explore the mechanism of parton energy loss and deconfinement in the medium. The parton energy loss, referred to as *jet quenching*, is quantified with the nuclear modification factors, which require the measurements of reference p_{T} spectra in pp (QCD vacuum) and p–Pb (cold nuclear matter) collisions. An ultimate goal is to determine the transport properties ($\hat{q}$) of the matter produced in the heavy-ion collisions at the LHC.

The heavy-ion measurements at RHIC, performed before the LHC era, have shown that the matter produced in these collisions exhibits the properties of the strongly interacting, nearly perfect liquid, which is often referred to as a strongly coupled quark-gluon plasma (sQGP). This state of matter is almost opaque to traversing partons, leading to a marked reduction of their energy and to the suppression of high-p_{T} hadron production.

The measurements of low-p_{T} particles in Pb–Pb collisions with ALICE at the LHC have shown that the density of matter in such collisions can reach ~ 14 GeV/fm^3, which is about factor of three higher than that at RHIC, and is much higher than the critical value from the lattice QCD calculations, $\varepsilon_{\mathrm{c}} = 0.18$–$0.5$ GeV/fm^3. Moreover, the fireballs formed in Pb–Pb collisions are larger and live longer (total lifetime ~ 10 fm/c) as compared to those at RHIC.

In addition, a strong collective expansion (flow) is observed at the LHC, with magnitude 10–30% larger than that at RHIC. Thus, the matter produced in Pb–Pb collisions at the LHC has the properties of a nearly perfect liquid.

A set of crucial measurements of p_{T} spectra in pp collisions at energies available at the LHC have been performed by ALICE. It was verified, that the shape of the spectra at high-p_{T} and the their relative $\sqrt{s}$ dependence are properly described by the NLO or FONLL pQCD calculations. It allows us to construct pp reference spectra for measurements of nuclear modification factors based on the pQCD scaling approach, in the case when the pp measurements at the p–Pb or Pb–Pb collision energy had not been available.

The nuclear modification factors R_{pPb} and Q_{pPb} measured in p–Pb collisions are important to verify whether the cold nuclear matter effects such as gluon saturation or Cronin effect influence on particle production at high p_{T}. The obtained results clearly indicate a small magnitude of these effects at the LHC. The nuclear modification factors determined in minimum-bias (R_{pPb}) and in centrality selected (Q_{pPb}) p–Pb collisions are consistent with unity for $p_{\mathrm{T}} \gtrsim 6$ GeV/c, for all studied light- and heavy-flavor hadrons and jets. For the region of several tens of GeV, binary collision scaling was experimentally confirmed in Pb–Pb collisions at the LHC by the measurements of electroweak bosons or direct photons, which are not affected by strong interactions with the QCD matter. The presented measurements in p–Pb collisions extends this important experimental verification down to the GeV scale and to hadronic observables. The nuclear modification factors measured in p–Pb collisions are important to constrain models including cold nuclear matter effects. In general, the saturation (Color Glass Condensate) models as well as pQCD-based calculations with cold nuclear matter effects, are consistent with the data. Unfortunately, the current precision of calculations and data do not allow to differentiate between models.

The measurements of nuclear modification factors R_{AA} of light- and heavy-flavor hadrons and jets in Pb–Pb collisions at the LHC have been performed to quantify the nuclear effects on the particle production in the hot and dense QCD matter. The results obtained for single hadrons show only moderate suppression ($R_{\mathrm{AA}} \approx 0.7$), and a weak p_{T} dependence in peripheral collisions. Towards more central collisions, a pronounced minimum at $p_{\mathrm{T}} = 6$–7 GeV/c develops, with the largest suppression ($R_{\mathrm{AA}} \approx 0.13$) seen in the central collisions. For $p_{\mathrm{T}} > 7$ GeV/c, there is a significant rise of the R_{AA} that becomes gradually less steep with increasing p_{T}, and R_{AA} reaches about 0.4 above $p_{\mathrm{T}} = 30$ GeV/c. The R_{CP} and R_{AA} values measured for jets confirm results obtained for single hadrons.

A similar suppression at high p_{T} ($\gtrsim 10$ GeV/c) is seen for the light-flavor hadrons (pions, kaons, protons) and prompt D mesons, which might indicate a weak quark mass dependence of the parton energy loss at the LHC. It is supported by the b-jet and g/q-jet measurements showing the same suppression. However, at the same time a weaker suppression of non-prompt J/ψ (from B meson decays) is observed as compared to other hadrons. In order to resolve this issue, precision measurements of heavy-flavor hadrons and jets in the extended p_{T} range are required.

The identified particle ratios (kaons-to-pions and protons-to-pions) determined at high p_{T} are collision energy and system independent. Taking into account that they also yield the same R_{AA}, one can conclude that the high-p_{T} fragmentation functions of light quarks and gluons are not affected by the medium. It is also confirmed by the measurements of fragmentation functions for jets in pp and Pb–Pb collisions at the LHC.

The interpretation of the different suppression pattern of light- and heavy-flavor hadrons at low momenta ($p_{\mathrm{T}} < 8$ GeV$/c$) observed in Pb–Pb collisions is problematic, because several effects can influence on the shape of the R_{AA}. The initial-state effects, different suppression and fragmentation patterns of gluons with respect to those of heavy quarks, soft production processes, radial flow and hadronization via recombination could affect D-meson and light-hadron yields differently at a given p_{T}. In order to resolve the issue of the color-charge and mass dependence of energy loss in the QGP more theoretical studies and precision measurements of charm and beauty production are required. However, the presented measurements already provide significant constraints for model calculations of interactions of gluons and quarks with the high-density QCD medium.

The similar suppression is observed when RHIC and LHC results are compared as a function of $\mathrm{d}N_{\mathrm{ch}}/\mathrm{d}\eta$. Larger values of suppression than at RHIC are observed in central collisions at the LHC, where the $\mathrm{d}N_{\mathrm{ch}}/\mathrm{d}\eta$ exceeds that of the most central collisions at RHIC. It should be noted that the suppression at a given centrality interval results from the interplay between the parton spectrum, medium density, and gluon-to-quark ratio, all of them exhibit a significant energy dependence. Therefore, the model studies are needed to evaluate their relative ratios.

The pQCD-based models including collisional and radiative parton energy loss describe the main features of the data at high p_{T}. The heavy-quark transport models with collisional and radiative energy loss, the nuclear PDFs, and scattering of D mesons in the hadronic phase, give reasonably good description of the prompt D-meson R_{AA}. However, all of the considered models fail to describe simultaneously R_{AA} and elliptic flow v_2 of light- and heavy-flavor hadrons, originating from the same underlying processes. Therefore, the measurements provide significant constraints for the understanding of the interaction of partons with the high-density QCD medium, especially at low and intermediate p_{T}, where the R_{AA} is the result of a more complex interplay among several effects. The improvements to theoretical calculations of the jet transport parameter with both perturbative and non-perturbative approaches are required to reduce modeling uncertainties in jet quenching studies within the wide energy and temperature range accessible at RHIC and at the LHC.

In summary, the results obtained by the author are important contribution in the study of the quark-gluon plasma, in the unique energy regime available at the LHC. A strong suppression of single particle and jet production at high-p_{T} is observed in Pb–Pb collisions as compared to the scaled production in p+p collisions. The measurements in p–Pb collisions show that modification of parton distribution function in nuclei (in the initial state) do not influence on the particle production at high p_{T}, in the measured kinematic range. Therefore, one can conclude that the state of matter produced in heavy-ion collisions at the LHC has properties

of the strongly coupled quark-gluon plasma (sQGP), which is almost opaque to traversing partons. The precision achieved in the measurements of single-particle and jet spectra already allow to verify parton energy loss models, and determination of transport properties of the plasma. The obtained results can be also used to constrain models of particle production at low p_{T}, where the radial flow and particle production mechanisms via recombination play an important role.

Acknowledgements

I would like to express my gratitude to all people who have helped me during my scientific career in the past years. My special thanks go to Prof. Dr. Peter Braun-Munzinger for giving me opportunity to participate in the ALICE experiment and for his continued support. Many thanks to Dr. Marian Ivanov, Dr. Michael Knichel, Prof. Dr. Anton Andronic, Dr. Julius Gronefeld, Dr. Alexander Kalweit, Prof. Dr. Harald Appelshäuser, Dr. Philipe Lüttig and Prof. Dr. Henner Büsching for the fruitful collaboration on the data analysis and detector work. I also want to thank to Prof. Dr. Silvia Masciocchi and Prof. Dr. Hab. Marek Kowalski for incredible support during my stay at GSI and now in Krakow.

List of figures

List of tables

References

[1] B. Predel, M. J. Poll, and M. Hoh. *Phase Diagram and Heterogenous Equilibria: A Practical Introduction*. Springer, Berlin, 2004.

[2] R. Hagedorn. Statistical thermodynamics of strong interactions at high-energies. *Nuovo Cim. Suppl.*, 3:147–186, 1965.

[3] H. Fritzsch, M. Gell-Mann, and H. Leutwyler. Advantages of the Color Octet Gluon Picture. *Phys. Lett.*, B47:365–368, 1973.

[4] C. Patrignani et al. (Particle Data Group). 2016 Review of Particle Physics. *Chin. Phys.*, C40:100001, 2016.

[5] H. D. Politzer. Reliable Perturbative Results for Strong Interactions? *Phys. Rev. Lett.*, 30:1346–1349, 1973.

[6] D. J. Gross and F. Wilczek. Ultraviolet Behavior of Non-Abelian Gauge Theories. *Phys. Rev. Lett.*, 30:1343–1346, 1973.

[7] N. Itoh. Hydrostatic Equilibrium of Hypothetical Quark Stars. *Prog. Theor. Phys.*, 44:291–292, 1970.

[8] A. Chodos, R. L. Jaffe, K. Johnson, Charles B. Thorn, and V. F. Weisskopf. A New Extended Model of Hadrons. *Phys. Rev.*, D9:3471–3495, 1974.

[9] N. Cabibbo and G. Parisi. Exponential Hadronic Spectrum and Quark Liberation. *Phys. Lett.*, 59B:67–69, 1975.

[10] J. C. Collins and M. J. Perry. Superdense Matter: Neutrons or Asymptotically Free Quarks? *Phys. Rev. Lett.*, 34:1353–1356, 1975.

[11] E. V. Shuryak. Quantum chromodynamics and the theory of superdense matter. *Phys. Rep.*, 61:71–158, 1980.

[12] K. .G. Wilson. Confinement of Quarks. *Phys. Rev.*, D10:2445–2459, 1974.

[13] M. Creutz. Gauge Fixing, the Transfer Matrix, and Confinement on a Lattice. *Phys. Rev.*, D15:1128–1136, 1977.

[14] K Aamodt et al. Transverse momentum spectra of charged particles in proton-proton collisions at $\sqrt{s} = 900$ GeV with ALICE at the LHC. *Phys. Lett.*, B693:53–68, 2010.

[15] K. Aamodt et al. Suppression of Charged Particle Production at Large Transverse Momentum in Central Pb-Pb Collisions at $\sqrt{s_{\rm NN}} = 2.76$ TeV. *Phys. Lett.*, B696:30–39, 2011.

[16] B. Abelev et al. Transverse momentum distribution and nuclear modification factor of charged particles in p-Pb collisions at $\sqrt{s_{\rm NN}} = 5.02$ TeV. *Phys. Rev. Lett.*, 110:082302, 2013.

[17] B. Abelev et al. Centrality dependence of charged particle production at large transverse momentum in Pb–Pb collisions at $\sqrt{s_{\rm NN}} = 2.76$ TeV. *Phys. Lett.*, B720:52–62, 2013.

[18] B. Abelev et al. Energy dependence of the transverse momentum distributions of charged particles in pp collisions measured by ALICE. *Eur. Phys. J.*, C73:2662, 2013.

[19] B. Abelev et al. Measurement of charged jet suppression in Pb–Pb collisions at $\sqrt{s_{\rm NN}} =$ 2.76 TeV. *JHEP*, 1403:013, 2014.

[20] B. B. Abelev et al. Multiplicity dependence of the average transverse momentum in pp, p-Pb, and Pb-Pb collisions at the LHC. *Phys. Lett.*, B727:371–380, 2013.

[21] B. Abelev et al. Transverse momentum dependence of inclusive primary charged-particle production in p-Pb collisions at $\sqrt{s_{\rm NN}} = 5.02$ TeV. *Eur. J. Phys.*, C74:3054, 2014.

[22] J. Adam et al. Centrality dependence of particle production in p-Pb collisions at $\sqrt{s_{\rm NN}}$= 5.02 TeV. *Phys. Rev.*, C91:064905, 2015.

[23] B. B. Abelev et al. Production of charged pions, kaons and protons at large transverse momenta in pp and Pb-Pb collisions at $\sqrt{s_{\rm NN}}$ =2.76 TeV. *Phys. Lett.*, B736:196–207, 2014.

[24] J. Adam et al. Centrality dependence of the nuclear modification factor of charged pions, kaons, and protons in Pb-Pb collisions at $\sqrt{s_{\rm NN}} = 2.76$ TeV. *Phys. Rev.*, C93:034913, 2016.

[25] J. Adam et al. Pseudorapidity and transverse-momentum distributions of charged particles in proton-proton collisions at $\sqrt{s} = 13$ TeV. *Phys. Lett.*, B753:319–329, 2016.

[26] J. Adam et al. Measurement of charged jet production cross sections and nuclear modification in p-Pb collisions at $\sqrt{s_{\rm NN}}$ = 5.02 TeV. *Phys. Lett.*, B749:68–81, 2015.

[27] J. Adam et al. Multiplicity dependence of charged pion, kaon, and (anti)proton production at large transverse momentum in p–Pb Collisions at $\sqrt{s_{\rm NN}}$ = 5.02 TeV. *Phys. Lett.*, B760:720–735, 2016.

[28] S. Acharya et al. Transverse momentum spectra and nuclear modification factors of charged particles in pp, p-Pb and Pb-Pb collisions at the LHC. *arXiv:1802.09145 [nucl-ex]*, 2018.

[29] M. Gell-Mann. Eightfold Way: A Theory of Strong Interaction Symmetry. *Caltech Synchrotron Laboratory Report No. CTSL-20, TID-12608 (unpublished)*, 1961.

[30] Y. Ne'eman. Derivation of Strong Interactions from a Gauge Invariance. *Nucl. Phys*, 26:222–229, 1961.

[31] V. E. Barnes et al. Observation of a Hyperon with Strangeness Minus Three. *Phys. Rev. Lett.*, 12:204, 1964.

[32] M. Gell-Mann. A Schematic Model of Baryons and Mesons. *Phys. Lett.*, 8:214–215, 1964.

[33] G. Zweig. An SU_3 Model for Strong Interaction Symmetry And its Breaking. *CERN Report CERN-TH-401*, 1964.

[34] G. Zweig. An SU_3 Model for Strong Interaction Symmetry And its Breaking II. *CERN Report CERN Report No.8419/TH.412*, 1964.

[35] B. J. Bjørken and S.L. Glashow. Elementary particle SU(4). *Phys. Lett*, 11:255–257, 1964.

[36] E. D. Bloom et. al. Observed Behavior of Highly Inelastic Electron-Proton Scattering. *Phys. Rev. Lett.*, 23:935–939, 1969.

[37] G. Miller et. al. Inelastic Electron-Proton Scattering at Large Momentum Transfers and the Inelastic Structure Functions of the Proton. *Phys. Rev. D*, 5:528, 1972.

[38] J. D. Bjorken. Asymptotic Sum Rules at Infinite Momentum. *Phys. Rev.*, 179:1547, 1969.

[39] R. P. Feynman. Very High-Energy Collisions of Hadrons. *Phys. Rev. Lett.*, 23:1415–1417, 1969.

[40] R. P. Feynman. The behavior of hadron collisions at extreme energies. *Conf. Proc.*, C690905:237–258, 1969.

[41] C. G. Callan and D. G. Gross. High-energy electroproduction and the constitution of the electric current. *Phys. Rev. Lett.*, 22:156–159, 1969.

[42] J. D. Bjorken and E. A. Paschos. Inelastic Electron-Proton and γ-Proton Scattering and the Structure of the Nucleon. *Phys. Rev.*, 185:1975, 1969.

[43] E. M. Riordan et al. Extraction of $R = \sigma_L/\sigma_T$ from Deep Inelastic e-p and e-d Cross Sections. *Phys. Rev. Lett.*, 33:561, 1974.

[44] E. M. Riordan et al. Tests of scaling of the proton electromagnetic structure functions. *Phys. Lett.*, B52:249–252, 1974.

[45] W. B. Atwood et al. Inelastic electron scattering from hydrogen at 50° and 60°. *Phys. Lett.*, B64:479–482, 1976.

[46] A. Bodek et al. Experimental Studies of the Neutron and Proton Electromagnetic Structure Functions. *Phys. Rev.*, D20:1471, 1979.

[47] I. Budagov et al. Measurement of structure factors in inelastic neutrino scattering. *Phys. Lett*, B30:364–368, 1969.

[48] H. Deden et al. Experimental Study of Structure Functions and Sum Rules in Charge Changing Interactions of Neutrinos and anti-neutrinos on Nucleons. *Nucl. Phys.*, B85:269–288, 1975.

[49] J. Kuti and V. F. Weisskopf. Inelastic Lepton-Nucleon Scattering and Lepton Pair Production in the Relativistic Quark-Parton Model. *Phys. Rev.*, 4:3418, 1971.

[50] M. S. Chanowitz and S. D. Drell. Speculations on the Breakdown of Scaling at 10^{-15} cm. *Phys. Rev. Lett.*, 30:807, 1973.

[51] O. W. Greenberg. Spin and unitary-spin independence in a paraquark model of baryons and mesons. *Phys. Rev. Lett.*, 13:598–602, 1964.

[52] B. Bartoli et al. Electron-Positron Interactions at High Energies. *Phys. Rev.*, D6:2374–2405, 1970.

[53] V. Silvestrini. Electron-positron interactions. In *Proceedings, 16th International Conference on High-Energy Physics, ICHEP, Batavia, Illinois, 6-13 Sep 1972*, volume C720906V4, pages 1–40, 1972.

[54] J. J. Aubert et al. Experimental Observation of a Heavy Particle J. *Phys. Rev. Lett.*, 33:1404–1406, 1974.

[55] J.-E. Augustin et al. Discovery of a Narrow Resonance in e^+e^- Annihilation. *Phys. Rev. Lett.*, 33:1406–1408, 1974.

[56] G. Hanson et al. Evidence for Jet Structure in Hadron Production by e^+e^- Annihilation. *Phys. Rev. Lett.*, 35:1609–1612, 1975.

[57] S. W. Herb et al. Observation of a Dimuon Resonance at 9.5 GeV in 400 GeV Proton-Nucleus Collisions. *Phys. Rev. Lett.*, 39:252, 1977.

[58] R. Brandelik et al. Evidence for Planar Events in e^+e^- Annihilation at High-Energies. *Phys. Lett.*, B86:243–249, 1979.

[59] D. P. Barber et al. Discovery of Three-Jet Events and a Test of Quantum Chromodynamics at PETRA. *Phys. Rev. Lett.*, 43:830–833, 1979.

[60] Ch. Berger et al. Evidence for Gluon Bremsstrahlung in e^+e^- Annihilations at High-Energies. *Phys. Lett.*, B86:418–425, 1979.

[61] F. Abe et al. Observation of Top Quark Production in $p\bar{p}$ Collisions with the Collider Detector at Fermilab. *Phys. Rev. Lett.*, 74:2628–2631, 1995.

[62] S. Abachi et al. Observation of the Top Quark. *Phys. Rev. Lett.*, 74:2632–2637, 1995.

[63] F. Englert and R. Brout. Broken Symmetry and the Mass of Gauge Vector Mesons. *Phys. Rev. Lett.*, 13:321–323, 1964.

[64] P. W. Higgs. Broken Symmetries and the Masses of Gauge Bosons. *Phys. Rev. Lett.*, 13:508–509, 1964.

[65] G. S. Guralnik, C. R. Hagen, and T. W. B. Kibble. Global Conservation Laws and Massless Particles. *Phys. Rev. Lett.*, 13:585–587, 1964.

[66] P. Abreu et al. Energy dependence of the differences between the quark and gluon jet fragmentation. *Z. Phys.*, C70:179–195, 1996.

[67] T. Affolder et al. Charged-Particle Multiplicity in jets in $p\bar{p}$ collision at $\sqrt{s} = 1.8$ TeV. *Phys. Rev. Lett.*, 87:211804, 2001.

[68] Y. Watanabe et al. Test of Scale Invariance in Ratios of Muon Scattering Cross Sections at 150 and 56 GeV. *Phys. Rev. Lett.*, 35:898–901, 1975.

[69] C. Chang et al. Observed Deviations from Scale Invariance in High-Energy Muon Scattering. *Phys. Rev. Lett.*, 35:901–904, 1975.

[70] H. L. Anderson et al. A Measurement of the Nucleon Structure Functions. *Phys. Rev.*, D20:2645–2691, 1979.

[71] J. G. H. de Groot et al. Inclusive Interactions of High-Energy Neutrinos and anti-neutrinos in Iron. *Z. Physik C*, C1:143–162, 1979.

[72] Y. Nambu. Axial Vector Current Conservation in Weak Interactions. *Phys. Rev. Lett.*, 4:380–382, 1960.

[73] Y. Nambu and G. Jona-Lasinio. Dynamical Model of Elementary Particles Based on an Analogy with Superconductivity I. *Phys. Rev.*, 122:345–358, 1960.

[74] Y. Nambu and G. Jona-Lasinio. Dynamical Model of Elementary Particles Based on an Analogy with Superconductivity II. *Phys. Rev.*, 124:377–380, 1961.

[75] J. Goldstone. Field Theories with Superconductor Solutions. *Nuovo Cim.*, 19:154–164, 1961.

[76] C. S Fischer. Infrared properties of QCD from Dyson-Schwinger equations. *J. Phys.*, G32:R253–R291, 2006.

[77] E. Laermann and O. Philipsen. Gauge fixing, the transfer matrix, and confinement on a lattice. *Annu. Rev. Nucl. Part. Sci.*, 53:163–198, 2003.

[78] Z. Fodor and S. D. Katza. Critical point of QCD at finite T and μ, lattice results for physical quark masses. *JHEP*, 04:050, 2004.

[79] Y. Aoki et al. The order of the quantum chromodynamics transition predicted by the standard model of particle physics. *Nature*, 443:675–678, 2006.

[80] S. Borsanyi et al. Is there still any T_c mystery in lattice QCD? Results with physical masses in the continuum limit III. *JHEP*, 09:073, 2010.

[81] S. Borsanyi et al. Full result for the QCD equation of state with 2+1 flavors. *Phys. Lett.*, B730:99, 2014.

[82] A. Bazavov et al. The chiral and deconfinement aspects of the QCD transition. *Phys. Rev.*, D85:054503, 2012.

[83] A. Bazavov et al. The equation of state in (2+1)-flavor QCD. *Phys. Rev.*, D90:094503, 2014.

[84] D. Boyanovsky et al. Phase transitions in the early and the present universe. *Ann. Rev. Nucl. Part. Sci.*, 56:441–500, 2006.

[85] Mégevand, A. and Ramrez, S. Bubble nucleation and growth in slow cosmological phase transitions. *Nucl. Phys.*, B928:38–71, 2018.

[86] M. Laine and M. Meyer. Standard Model thermodynamics across the electroweak crossover. *JCAP*, 07:035, 2015.

[87] S. Borsanyi et al. Lattice QCD for Cosmology. *Nature*, 539:69, 2016.

[88] Philippe de Forcrand. Simulating QCD at finite density. In *Proceedings, 27th International Symposium on Lattice field theory (Lattice 2009): Beijing, P.R. China, July 26-31, 2009*, volume LAT2009, page 010, 2009.

[89] C. R. Allton et al. The qcd thermal phase transition in the presence of a small chemical potential. *Phys. Rev.*, D66:074507, 2002.

[90] Sz. Borsanyi, G. Endrodi, Z. Fodor, S. D. Katz, S. Krieg, C. Ratti, and K. K. Szabo. QCD equation of state at nonzero chemical potential: continuum results with physical quark masses at order μ^2. *JHEP*, 08:053, 2012.

[91] Günther et al. The QCD equation of state at finite density from analytical continuation. In *Proceedings, 12th Conference on Quark Confinement and the Hadron Spectrum (Confinement XII): Thessaloniki, Greece*, volume 137, page 07008, 2017.

[92] A. Bazavov et al. QCD equation of state to $O(\mu_B^6)$ from lattice QCD. *Phys. Rev.*, D95:054504, 2017.

[93] B. C. Barrois. Superconducting Quark Matter. *Nucl. Phys.*, B129:390–396, 1977.

[94] Steven C. Frautschi. Asymptotic freedom and color superconductivity in dense quark matter. In *Workshop on Theoretical Physics: Hadronic Matter at Extreme Energy Density Erice, Italy, October 13-21, 1978*, page 18, 1978.

[95] D. Bailin and A. Love. Superfluid Quark Matter. *J. Phys.*, A12:L283, 1979.

[96] D. Bailin and A. Love. Superfluidity and Superconductivity in Relativistic Fermion Systems. *Phys. Rept.*, 107:325–385, 1984.

[97] M. G. Alford et al. QCD at Finite Baryon Density: Nucleon Droplets and Color Superconductivity. *Phys. Lett.*, B422:247–256, 1998.

[98] R. Rapp et al. Diquark Bose Condensates in High Density Matter and Instantons. *Phys. Rev. Lett.*, 81:53, 1998.

[99] M. G. Alford et al. Color-Flavor Locking and Chiral Symmetry Breaking in High Density QCD. *Nucl. Phys.*, B537:443–458, 1999.

[100] L. N. Cooper J. Bardeen and J. R. Schrieffer. Microscopic Theory of Superconductivity. *Phys. Rev.*, 106:162–164, 1957.

[101] K. Fukushima and C. Sasaki. The phase diagram of nuclear and quark matter at high baryon density. *Prog. Part. Nucl. Phys.*, 72:99–154, 2013.

[102] Kenji Fukushima and Toru Kojo. The Quarkyonic Star. *Astrophys. J.*, 817:180, 2016.

[103] A. Kurkela et al. Constaining Neutron Star Matter with Quantum Chromodynamics. *Astrophys. J.*, 789:127, 2014.

[104] E. Annala et al. Gravitational-wave constraints on the neutron-star-matter Equation of State. *Phys. Rev. Lett.*, 120:172703, 2018.

[105] P. B. Demorest et al. A two-solar-mass neutron star measured using Shapiro delay. *Nature*, 467:1081–1083, 2010.

[106] J. Antoniadis et al. A Massive Pulsar in a Compact Relativistic Binary. *Science*, 340:1233232, 2013.

[107] B. P. Abbott et al. GW170817: Observation of Gravitational Waves from a Binary Neutron Star Inspiral. *Phys. Rev. Lett.*, 119:161101, 2017.

[108] J. D. Bjorken. Highly Relativistic Nucleus-Nucleus Collisions: The Central Rapidity Region. *Phys. Rev.*, D27:140–151, 1983.

[109] J. Breitweg et al. ZEUS Results on the Measurement and Phenomenology of F_2 at Low x and Low Q^2. *Eur. Phys. J.*, 67:609–630, 1999.

[110] E. Iancu, A. Leonidov, and L. McLerran. Nonlinear gluon evolution in the color glass condensate. 1. *Nucl. Phys.*, A692:583–645, 2001.

[111] E. Ferreiro, E. Iancu, A. Leonidov, and L. McLerran. Nonlinear gluon evolution in the color glass condensate. 2. *Nucl. Phys.*, A703:489–538, 2002.

[112] S. Chatrchyan et al. Measurement of the pseudorapidity and centrality dependence of the transverse energy density in PbPb collisions at $\sqrt{s_{\mathrm{NN}}} = 2.76$ TeV. *Phys. Rev. Lett.*, 109:152303, 2012.

[113] J. Berges, J.-P. Blaizot, and F. Gelis. EMMI Rapid Reaction Task Force on 'Thermalization in Non-abelian Plasmas'. *J. Phys.*, G39:085115, 2012.

[114] L. McLerran T. Lappi. Some features of the glasma. *Nucl. Phys.*, A772:200–212, 2006.

[115] M. Gyulassy and L. McLerran. New forms of QCD matter discovered at RHIC. *Nucl. Phys.*, A750:30–63, 2005.

[116] B. Müller, J. Schukraft, and B. Wysłouch. First Results from Pb+Pb Collisions at the LHC. *Annu. Rev. Nucl. Part. Sci.*, 62:361–386, 2012.

[117] A. Andronic, P. Braun-Munzinger, and J. Stachel. Thermal hadron production in relativistic nuclear collisions: The hadron mass spectrum, the horn, and the QCD phase transition. *Phys. Lett.*, B673:142–145, 2009.

[118] S. Acharya et al. Production of ^{4}He and $^4\overline{\mathrm{He}}$ in Pb-Pb collisions at $\sqrt{s_{\mathrm{NN}}}$ = 2.76 TeV at the LHC. *Nucl. Phys.*, A971:1–20, 2018.

[119] E. Schnedermann, J. Sollfrank, and U. W. Heinz. Thermal phenomenology of hadrons from 200-A/GeV S+S collisions. *Phys. Rev.*, C48:2462–2475, 1993.

[120] B. Abelev et al. Centrality dependence of π, K, p production in Pb-Pb collisions at $\sqrt{s_{\mathrm{NN}}} = 2.76$ TeV. *Phys. Rev.*, C88:044910, 2013.

[121] U. Heinz and M. Jacob. Evidence for a new state of matter: An Assessment of the results from the CERN lead beam program. *arXiv:nucl-th/0002042 [nucl-th]*, 2000.

[122] A. Aduszkiewicz et al. Recent results from NA61/SHINE. *Nucl. Phys.*, A00:1–8, 2017.

[123] I. Arsene et al. Quark-gluon plasma and color glass condensate at RHIC? The perspective from the BRAHMS experiment. *Nucl. Phys.*, A757:1–27, 2005.

[124] B. B. Back et al. The PHOBOS perspectives on discoveries at RHIC. *Nucl. Phys.*, A757:28–101, 2005.

[125] J. Adams et al. Experimental and theoretical challenges in the search for the quark-gluon plasma: The STAR Collaboration's critical assessment of the evidence from RHIC collisions. *Nucl. Phys.*, A757:102–183, 2005.

[126] K. Adcox et al. Formation of the dense matter in the relativistic nucleus-nucleus collisions at rhic. experimental evaluation by the PHENIX Collaboration. *Nucl. Phys.*, A757:184–283, 2005.

[127] J. D. Bjorken. Energy loss of energetic partons in quark - gluon plasma: possible extinction of high p_{T} jets in hadron - hadron collisions. Technical Report FERMILAB-PUB-82-059-T, Fermilab, 1982.

[128] K. Adcox et al. Suppression of hadrons with large transverse momentum in central Au+Au collisions at $\sqrt{s_{\mathrm{NN}}} = 130$ GeV. *Phys. Rev. Lett.*, 88:022301, 2002.

[129] C. Adler et al. Centrality dependence of high p_{T} hadron suppression in Au+Au collisions at $\sqrt{s_{\mathrm{NN}}} = 130$ GeV. *Phys. Rev. Lett.*, 89:202301, 2002.

[130] C. Adler et al. Disappearance of back-to-back high p_{T} hadron correlations in central Au+Au collisions at $\sqrt{s_{\mathrm{NN}}}$ = 200 GeV. *Phys. Rev. Lett.*, 90:082302, 2003.

[131] X. Luo and N. Xu. Search for the qcd critical point with fluctuations of conserved quantities in relativistic heavy-ion collisions at rhic : An overview. *Nucl. Sci. Tech.*, 28:112, 2017.
[132] L. Evans and P. Bryant. LHC Machine. *JINST*, 3:S08001, 2008.
[133] K. Aamodt et al. The ALICE experiment at the CERN LHC. *JINST*, 3:S08002, 2008.
[134] G. Aad at al. The ATLAS Experiment at the CERN Large Hadron Collider. *JINST*, 3:S08003, 2008.
[135] R. Adolphi et al. The CMS experiment at the CERN LHC. *JINST*, 3:S08004, 2008.
[136] A. Augusto Alves, Jr. et al. The LHCb Detector at the LHC. *JINST*, 3:S08005, 2008.
[137] P. Lebrun. Interim Summary Report on the Analysis of the 19 September 2008 Incident at the LHC. Technical Report EDMS 973073, CERN, 2008.
[138] G. Aad at al. Observation of a Centrality-Dependent Dijet Asymmetry in Lead-Lead Collisions at $\sqrt{s_{\mathrm{NN}}} = 2.76$ TeV with the ATLAS Detector at the LHC. *Phys. Rev. Lett.*, 105:252303, 2010.
[139] N. Ahmad et al. ALICE Technical Proposal for A Large Ion Collider Experiment at the CERN LHC. Technical Report CERN-LHCC-95-71, LHCC-P-3, CERN, 1995.
[140] B Alessandro et al. ALICE: Physics Performance Report, Volume I. *J. Phys. G: Nucl. Part. Phys.*, 30:1517–1763, 2004.
[141] B Alessandro et al. ALICE: Physics Performance Report, Volume II. *J. Phys. G: Nucl. Part. Phys.*, 32:12952040, 2006.
[142] C. Lefèvre. The CERN accelerator complex. Technical Report CERN-DI-0812015, CERN, 2008.
[143] L Batev et al. Definition of the ALICE Coordinate System and Basic Rules for Sub-detector Components Numbering. Technical Report ALICE-INT-2003-038, CERN, 2003.
[144] B. B. Abelev et al. Performance of the ALICE experiment at the CERN LHC. *Int. J. Mod. Phys.*, A29:1430044, 2014.
[145] G. Dellacasa et al. ALICE Technical Design Report of the Inner Tracking System (ITS). Technical Report CERN-LHCC-99-012, CERN, 1999.
[146] G. Dellacasa et al. ALICE Technical Design Report of the Time Projection Chamber. Technical Report CERN-LHCC-2000-001, CERN, 2000.
[147] J. Alme et al. The ALICE TPC, a large 3-dimensional tracking device with fast readout for ultra-high multiplicity events. *Nucl. Instrum. Methods A*, 622:316–367, 2010.
[148] P. Cortese et al. ALICE Technical Design Report of the Transition Radiation Detector. Technical Report CERN-LHCC-2001-021, CERN, 1997.
[149] S. Acharya et al. The ALICE Transition Radiation Detector: Construction, operation, and performance. *Nucl. Instrum. Meth.*, A881:88, 2017.
[150] G. Dellacasa et al. ALICE Technical Design Report of the Time of Flight System (TOF). Technical Report CERN-LHCC-2000-012, CERN, 2000.
[151] P. Cortese et al. ALICE Addendum to the Technical Design Report of the Time of Flight System (TOF). Technical Report CERN-LHCC-2002-016, CERN, 2002.

[152] G. Dellacasa et al. ALICE Technical Design Report of the Photon Spectrometer (PHOS). Technical Report CERN-LHCC-99-004, CERN, 1999.

[153] D. V. Aleksandrov et al. A high resolution electromagnetic calorimeter based on lead-tungstate crystals. *Nucl. Instrum. Meth.*, A550:169–184, 2005.

[154] P. Cortese et al. ALICE Electromagnetic Calorimeter Technical Design Report. Technical Report CERN-LHCC-2008-014, CERN, 2008.

[155] U. Abeysekara et al. ALICE EMCal Physics Performance Report. *arXiv:1008.0413 [physics.ins-det]*, 2010.

[156] J. Allen et al. ALICE DCal: An Addendum to the EMCal Technical Design Report Di-Jet and Hadron-Jet correlation measurements in ALICE. Technical Report CERN-LHCC-2010-011, CERN, Jun 2010.

[157] M. Yu. Bogolyubsky et al. Charged Particle Veto Detector with Open Geometry for the PHOS Spectrometer. Technical Report CERN-ALICE-INT-2000-21, CERN, Geneva, 2000.

[158] S. Evdokimov et al. The ALICE CPV Detector. In *Proceedings, 3rd International Conference on Particle Physics and Astrophysics (ICPPA 2017): Moscow, Russia, October 2-5, 2017*, volume 3, pages 260–267, 2018.

[159] S. Beole et al. ALICE high-momentum particle identification: Technical Design Report. Technical Report CERN-LHCC-98-019, CERN, 1998.

[160] G. Dellacasa et al. ALICE technical design report of the dimuon forward spectrometer. Technical Report CERN-LHCC-99-22, CERN, 1999.

[161] G. Dellacasa et al. ALICE dimuon forward spectrometer : addendum to the Technical Design Report. Technical Report CERN-LHCC-2000-046, CERN, 2000.

[162] P. Cortese et al. ALICE Technical Design Report on Forward Detectors: FMD, T0 and V0. Technical Report CERN-LHCC-2004-025, CERN, 2004.

[163] E. Abbas et al. Performance of the ALICE VZERO system. *JINST*, 8:P10016, 2013.

[164] G. Dellacasa et al. ALICE technical design report of the zero degree calorimeter (ZDC). Technical Report CERN-LHCC-99-05, CERN, 1999.

[165] A. Villatoro Tello. AD, the ALICE diffractive detector. In *Proceedings, 9th International Workshop on Diffraction in High Energy Physics (Diffraction 2016): Santa Tecla di Acireale, Catania, Italy, September 2-8, 2016*, volume 1819, page 040020, 2017.

[166] G. Dellacasa et al. ALICE Technical Design Report of the Photon Multiplicity Detector (PMD). Technical Report CERN-LHCC-99-032, CERN, 1999.

[167] P. Cortese et al. ALICE Addendum to the Technical Design Report of the Photon Multiplicity Detector (PMD). Technical Report CERN-LHCC-2003-038, CERN, 2003.

[168] P. Billoir. Track fitting with multiple scattering: A new method. *Nucl. Instrum. Methods*, A225:352–366, 1984.

[169] M. Ivanov et al. Track reconstruction in high density environment. *Nucl. Instrum. Meth.*, A566:70–74, 2006.

[170] L. Aphecetche et al. Numerical Simulations and and Offline Reconstruction of the Muon Spectrometer of ALICE. Technical Report ALICE-INT-2009-044, CERN, 2009.

[171] E. Bruna et al. Vertex reconstruction for proton-proton collisions in ALICE. Technical Report ALICE-INT-2009-018, CERN, 2009.

[172] S. Bufalino. Performance of ALICE Silicon Tracking Detectors. In *Proceedings, 21st International Workshop on Vertex Detectors (Vertex 2012): Jeju, Korea, September 16-21, 2012*, volume Vertex2012, page 048, 2013.

[173] Ch. W. Fabjan et al. ALICE trigger data-acquisition high-level trigger and control system: Technical Design Report. Technical Report CERN-LHCC-2003-062, CERN, 2004.

[174] R. J. Glauber. *in Lectures in Theoretical Physics*. ed. W. E. Brittin, L. G. Dunham, Interscience, New York, 1959.

[175] A. Białas, M. Bleszyński, and W. Czyż. Multiplicity distribution in nucleus-nucleus collisions at high-energies. *Nucl. Phys.*, B111:461–476, 1976.

[176] A. Białas, M. Bleszyński, and W. Czyż. Relation Between the Glauber Model and Classical Probability Calculus. *Acta. Phys. Pol*, B8:389–392, 1977.

[177] M. Miller et al. Glauber Modeling in High-Energy Nuclear Collisions. *Ann. Rev. Nucl. Part. Sci.*, 57:205–243, 2007.

[178] B. Abelev et al. Centrality determination of Pb–Pb collisions at $\sqrt{s_{\rm NN}} = 2.76$ TeV with ALICE. *Phys. Rev.*, C88:044909, 2013.

[179] F. Sikler. Centrality control of hadron nucleus interactions by detection of slow nucleons. *arXiv:hep-ph/0304065 [hep-ph]*, 2003.

[180] R. Brun et al. *GEANT: Detector Description and Simulation Tool*. CERN Program Library. CERN, Geneva, 1993. Long Writeup W5013.

[181] B. Andersson et al. Parton Fragmentation and String Dynamics. *Phys. Rept.*, 97:31–145, 1983.

[182] T. Sjostrand et al. High-energy physics event generation with PYTHIA 6.1. *Comput. Phys. Commun.*, 135:238–259, 2001.

[183] T. Sjöstrand, S. Mrenna, and P. Z. Skands. PYTHIA 6.4 Physics and Manual. *JHEP*, 05:026, 2006.

[184] T. Sjöstrand, S. Mrenna, and P. Z. Skands. A Brief Introduction to PYTHIA 8.1. *Comput. Phys. Commun.*, 178:852–867, 2008.

[185] T. Sjöstrand et al. An Introduction to PYTHIA 8.2. *Comput. Phys. Commun.*, 191:159–177, 2015.

[186] R. Engel, J. Ranft, and S. Roesler. Hard diffraction in hadron hadron interactions and in photoproduction. *Phys. Rev.*, D52:1459–1468, 1995.

[187] A. Capella, U. Sukhatme, C-I Tan, and J. Tran Thanh Van. Dual parton model. *Phys. Rept.*, 236:225–329, 1994.

[188] S. Donnachie, H. G. Dosch, O. Nachtmann, and P. Landshoff. Pomeron physics and QCD. *Camb. Monogr. Part. Phys. Nucl. Phys. Cosmol.*, 19:1–347, 2002.

[189] T. Sjostrand. The Lund Monte Carlo for Jet Fragmentation and e^+e^- Physics: Jetset Version 6.2. *Comput. Phys. Commun.*, 39:347–407, 1986.

[190] T. Sjostrand and M. Bengtsson. The Lund Monte Carlo for Jet Fragmentation and e^+e^- Physics. Jetset Version 6.3: An Update. *Comput. Phys. Commun.*, 43:367, 1987.
[191] J. Ranft. The Dual parton model at cosmic ray energies. *Phys. Rev.*, D51:64–84, 1995.
[192] S. Roesler, R. Engel, and J. Ranft. The Monte Carlo event generator DPMJET-III. In *Advanced Monte Carlo for radiation physics, particle transport simulation and applications. Proceedings, Conference, MC2000, Lisbon, Portugal, October 23-26, 2000*, pages 1033–1038, 2000.
[193] P. Aurenche et al. Multiparticle production in a two component dual parton model. *Phys. Rev.*, D45:92–105, 1992.
[194] X.-N. Wang and M. Gyulassy. HIJING: A Monte Carlo model for multiple jet production in p–p, p–A and A–A collisions. *Phys. Rev.*, D44:3501–3516, 1991.
[195] Bo Andersson, G. Gustafson, and B. Nilsson-Almqvist. A Model for Low p_{T} Hadronic Reactions, with Generalizations to Hadron - Nucleus and Nucleus-Nucleus Collisions. *Nucl. Phys.*, B281:289–309, 1987.
[196] A. Accardi et al. Hard Probes In Heavy Ion Collisions at the LHC: Jet Physics. *arXiv:hep-ph/0310274*, 2003.
[197] John C. Collins, D. E. Soper, and G. F. Sterman. Factorization for Short Distance Hadron - Hadron Scattering. *Nucl. Phys.*, B261:104–142, 1985.
[198] K.J. Eskola, H. Paukkunen, and C.A. Salgado. EPS09 - A new generation of NLO and LO nuclear parton distribution functions. *JHEP*, 04:065, 2009.
[199] K.J. Eskola, P. Paakkinen, H. Paukkunen, and C.A. Salgado. EPPS16: Nuclear parton distributions with LHC data. *Eur. Phys.J.*, C77:163, 2016.
[200] A. Metz and V. Vossen. Parton Fragmentation Functions. *Prog. Part. Nucl. Phys.*, 91:136–202, 2016.
[201] David d'Enterria. Jet quenching. *Landolt-Bornstein*, 23:471–520, 2010.
[202] J. J. Aubert et al. The ratio of the nucleon structure functions F_2^N for iron and deuterium. *Phys. Lett.*, B123:275–278, 1983.
[203] J. Ashman et al. Measurement of the Ratios of Deep Inelastic Muon - Nucleus Cross-Sections on Various Nuclei Compared to Deuterium. *Phys. Lett.*, B202:603–610, 1988.
[204] D. Stump et al. Inclusive jet production, parton distributions, and the search for new physics. *JHEP*, 10:046, 2003.
[205] S. Chekanov et al. ZEUS next-to-leading-order QCD analysis of data on deep inelastic scattering. *Phys. Rev.*, D67:012007, 2003.
[206] M. Froissart. Asymptotic behavior and subtractions in the Mandelstam representation. *Phys. Rev.*, 123:1053–1057, 1961.
[207] D. de Florian, R. Sassot, M. Epele, R. J. Hernndez-Pinto, and M. Stratmann. Parton-to-Pion Fragmentation Reloaded. *Phys. Rev.*, D91:014035, 2015.
[208] D. de Florian, R. Sassot, and M. Stratmann. Global analysis of fragmentation functions for pions and kaons and their uncertainties. *Phys. Rev.*, D75:114010, 2007.
[209] D. P. Anderle, F. Ringer, and M. Stratmann. Fragmentation Functions at Next-to-Next-to-Leading Order Accuracy. *Phys. Rev.*, D92:114017, 2015.

[210] D. de Florian, R. Sassot, and M. Stratmann. Global analysis of fragmentation functions for protons and charged hadrons. *Phys. Rev.*, D76:074033, 2007.

[211] R. Sassot, P. Zurita, and M. Stratmann. Inclusive Hadron Production in the CERN-LHC Era. *Phys. Rev.*, D82:074011, 2010.

[212] B. Abelev et al. Neutral pion and η meson production in proton-proton collisions at $\sqrt{s} = 0.9$ TeV and $\sqrt{s} = 7$ TeV. *Phys. Lett.*, B717:162–172, 2012.

[213] G. Aad et al. Measurement of the jet fragmentation function and transverse profile in proton-proton collisions at a center-of-mass energy of 7 TeV with the ATLAS detector. *Eur. Phys. J.*, C71:1795, 2011.

[214] G. Aad et al. Measurement of inclusive jet charged-particle fragmentation functions in Pb+Pb collisions at $\sqrt{s_{\mathrm{NN}}} = 2.76$TeV with the ATLAS detector. *Phys. Lett.*, B739:320–342, 2014.

[215] M. Aaboud et al. Measurement of jet fragmentation in Pb+Pb and pp collisions at $\sqrt{s_{\mathrm{NN}}} = 2.76$ TeV with the ATLAS detector at the LHC. *Eur. Phys. J.*, C77:379, 2017.

[216] M. Aaboud et al. Measurement of jet fragmentation in 5.02 TeV proton-lead and proton-proton collisions with the ATLAS detector. *arXiv:1706.02859 [hep-ex]*, 2017.

[217] S. Chatrchyan et al. Measurement of jet fragmentation into charged particles in pp and PbPb collisions at $\sqrt{s_{\mathrm{NN}}} = 2.76$ TeV. *JHEP*, 10:087, 2012.

[218] S. Chatrchyan et al. Jet Fragmentation Function in pPb Collisions at $\sqrt{s_{\mathrm{NN}}}$ = 5.02 TeV and pp Collisions at $\sqrt{s}$ = 2.76 and 7 TeV. Technical Report CMS-PAS-HIN-15-004, CERN, Geneva, 2015.

[219] Vit Kučera et. al. Production of strange particles in charged jets in Pb–Pb and p–Pb collisions measured with ALICE. *Nucl. Part. Phys. Proc.*, 276-278:181–184, 2016.

[220] N. Armesto et al. Comparison of Jet Quenching Formalisms for a Quark-Gluon Plasma 'Brick'. *Phys. Rev.*, C86:064904, 2012.

[221] K. M. Burke et al. Extracting jet transport coefficient from jet quenching at RHIC and LHC. *arXiv:1312.5003 [nucl-th]*, 2013.

[222] F. Prino and R. Rapp. Open Heavy Flavor in QCD Matter and in Nuclear Collisions. *J. Phys.*, G43(9):093002, 2016.

[223] S. Peigné and A. V. Smilga. Energy losses in relativistic plasmas: QCD versus QED. *Phys.-Usp*, 52:659–685, 2009.

[224] T. Renk. Constraining the Physics of Jet Quenching. *Phys. Rev.*, C85:044903, 2012.

[225] M. H. Thoma and M. Gyulassy. Quark damping and energy loss in the high temperature QCD. *Nucl. Phys.*, B351:491–506, 1991.

[226] E. Braaten and M. H. Thoma. Energy loss of a heavy quark in the quark-gluon plasma. *Phys. Rev.*, D44:R2625–R2630, 1991.

[227] A. Peshier. QCD Collisional Energy Loss Reexamined. *Phys. Rev. Lett*, 97:212301, 2006.

[228] M. Gyulassy and M. Plümer. Jet quenching in dense matter. *Phys. Lett.*, B243:432–438, 1990.

[229] M. Gyulassy and X. N. Wang. Multiple collisions and induced gluon bremsstrahlung in QCD. *Nucl. Phys.*, B420:583–614, 1994.

[230] B. G. Zakharov. Radiative energy loss of high energy quarks in finite-size nuclear matter and quark-gluon plasma. *JETP Lett.*, 65:615–620, 1997.

[231] R. Baier, Y. L. Dokshitzer, A. H. Mueller, S. Peigne, and D. Schiff. Radiative energy loss and $p_\perp$ broadening of high-energy partons in nuclei. *Nucl. Phys.*, B484:265–282, 1997.

[232] R. Baier, D. Schiff, and B. G. Zakharov. Energy Loss In Perturbative QCD. *Annu. Rev. Nucl. Part. Sci.*, 50:3769, 2000.

[233] M. Gyulassy, P. Levai, and I. Vitev. Non-Abelian Energy Loss at Finite Opacity. *Phys. Rev. Lett.*, 85:5535–5538, 2000.

[234] B. G. Zakharov. Parton Energy Loss in an Expanding QuarkGluon Plasma: Radiative vs. Collisional. *JETP Lett.*, 86:444–450, 2007.

[235] Yu. L. Dokshitzer and D. E. Kharzeev. Heavy-quark colorimetry of QCD matter. *Phys. Lett.*, B519:199–206, 2001.

[236] Yu. L. Dokshitzer, V. A. Khoze, and S. I. Troian. On specific QCD properties of heavy quark fragmentation ('dead cone'). *J. Phys.*, G17:1602, 1991.

[237] H. Liu, K. Rajagopal, and U. Achim Wiedemann. Calculating the jet quenching parameter from AdS/CFT. *Phys. Rev. Lett.*, 97:182301, 2006.

[238] H. Liu, K. Rajagopal, and U. A. Wiedemann. Wilson loops in heavy ion collisions and their calculation in AdS/CFT. *JHEP*, 03:066, 2007.

[239] J. Casalderrey-Solana and D. Teaney. Heavy quark diffusion in strongly coupled N=4 Yang-Mills. *Phys. Rev.*, D74:085012, 2006.

[240] W. A. Horowitz and M. Gyulassy. Heavy quark jet tomography of Pb + Pb at LHC: AdS/CFT drag or pQCD energy loss? *Phys. Lett.*, B666:320–323, 2008.

[241] F. Dominguez, C. Marquet, A. H. Mueller, B. Wu, and B.-W. Xiao. Comparing energy loss and $p_\perp$ - broadening in perturbative QCD with strong coupling N = 4 SYM theory. *Nucl. Phys.*, A811:197–222, 2008.

[242] C. Marquet and T. Renk. Jet quenching in the strongly-interacting quark-gluon plasma. *Phys. Lett.*, B685:270–276, 2010.

[243] R. Morad and W. A. Horowitz. Strong-coupling Jet Energy Loss from AdS/CFT. *JHEP*, 11:017, 2014.

[244] W. A. Horowitz. Fluctuating heavy quark energy loss in a strongly coupled quark-gluon plasma. *Phys. Rev.*, D91:085019, 2015.

[245] J. M. Maldacena. The Large N limit of superconformal field theories and supergravity. *Int. J. Theor. Phys.*, 38:1113–1133, 1999.

[246] E. Witten. Anti-de Sitter space and holography. *Adv. Theor. Math. Phys.*, 2:253–291, 1998.

[247] S. Wicks, W. Horowitz, M. Djordjevic, and M. Gyulassy. Elastic, inelastic, and path length fluctuations in jet tomography. *Nucl. Phys.*, A784:426–442, 2007.

[248] J. Adam et al. Measurement of jet suppression in central Pb-Pb collisions at $\sqrt{s_{\rm NN}}$ = 2.76 TeV. *Phys. Lett.*, B746:1–14, 2015.

[249] G. Aad et al. Measurements of the Nuclear Modification Factor for Jets in Pb+Pb Collisions at $\sqrt{s_{\rm NN}} = 2.76$ TeV with the ATLAS Detector. *Phys. Rev. Lett.*, 114:072302, 2015.

[250] V. Khachatryan et al. Measurement of inclusive jet cross sections in pp and PbPb collisions at $\sqrt{s_{\rm NN}} = 2.76$ TeV. *Phys. Rev.*, C96(1):015202, 2017.

[251] R. Baier, Y. L. Dokshitzer, A. H. Mueller, S. Peigne, and D. Schiff. Radiative energy loss of high-energy quarks and gluons in a finite volume quark - gluon plasma. *Nucl. Phys.*, B483:291–320, 1997.

[252] B. G. Zakharov. Fully quantum treatment of the Landau-Pomeranchik-Migdal effect in QED and QCD. *JETP Lett.*, 63:952–957, 1996.

[253] U. A. Wiedemann. Gluon radiation off hard quarks in a nuclear environment: Opacity expansion. *Nucl. Phys.*, B588:303–344, 2000.

[254] C. A. Salgado and U. A. Wiedemann. Medium modification of jet shapes and jet multiplicities. *Phys. Rev. Lett.*, 93:042301, 2004.

[255] C. A. Salgado and U. A. Wiedemann. Calculating quenching weights. *Phys. Rev.*, D68:014008, 2003.

[256] N. Armesto, C. A. Salgado, and U. A. Wiedemann. Medium induced gluon radiation off massive quarks fills the dead cone. *Phys. Rev.*, D69:114003, 2004.

[257] M. Gyulassy, P. Levai, and I. Vitev. Reaction operator approach to nonAbelian energy loss. *Nucl. Phys.*, B594:371–419, 2001.

[258] M. Djordjevic and M. Gyulassy. Heavy quark radiative energy loss in QCD matter. *Nucl. Phys.*, A733:265–298, 2004.

[259] M. Djordjevic and U. W. Heinz. Radiative energy loss in a finite dynamical QCD medium. *Phys. Rev. Lett.*, 101:022302, 2008.

[260] X.-N. Wang and X.-f. Guo. Multiple parton scattering in nuclei: Parton energy loss. *Nucl. Phys.*, A696:788–832, 2001.

[261] X.-F. Chen, T. Hirano, E. Wang, X.-N. Wang, and H. Zhang. Suppression of high $p_{\rm T}$ hadrons in $Pb+Pb$ Collisions at LHC. *Phys. Rev.*, C84:034902, 2011.

[262] A. Majumder, R. J. Fries, and Berndt Muller. Photon bremsstrahlung and diffusive broadening of a hard jet. *Phys. Rev.*, C77:065209, 2008.

[263] A. Majumder and C. Shen. Suppression of the High $p_{\rm T}$ Charged Hadron R_{AA} at the LHC. *Phys. Rev. Lett.*, 109:202301, 2012.

[264] P. B. Arnold, G. D. Moore, and L. G. Yaffe. Transport coefficients in high temperature gauge theories. 1. Leading log results. *JHEP*, 11:001, 2000.

[265] P. B. Arnold, G. D. Moore, and L. G. Yaffe. Transport coefficients in high temperature gauge theories. 2. Beyond leading log. *JHEP*, 05:051, 2003.

[266] S. Jeon and G. D. Moore. Energy loss of leading partons in a thermal QCD medium. *Phys. Rev.*, C71:034901, 2005.

[267] S. Turbide, C. Gale, S. Jeon, and G. D. Moore. Energy loss of leading hadrons and direct photon production in evolving quark-gluon plasma. *Phys. Rev.*, C72:014906, 2005.

[268] M. Gyulassy, P. Levai, and I. Vitev. Jet tomography of Au+Au reactions including multigluon fluctuations. *Phys. Lett.*, B538:282–288, 2002.

[269] I. Vitev. Testing the mechanism of QGP-induced energy loss. *Phys. Lett.*, B639:38–45, 2006.

[270] J.-w. Qiu and G. F. Sterman. Power corrections in hadronic scattering. 1. Leading $1/Q^2$ corrections to the Drell-Yan cross-section. *Nucl. Phys.*, B353:105–136, 1991.

[271] J.-w. Qiu and G. F. Sterman. Power corrections to hadronic scattering. 2. Factorization. *Nucl. Phys.*, B353:137–164, 1991.

[272] A. B. Migdal. Bremsstrahlung and pair production in condensed media at high-energies. *Phys. Rev.*, 103:1811–1820, 1956.

[273] V. N. Gribov and L. N. Lipatov. Deep inelastic e p scattering in perturbation theory. *Sov. J. Nucl. Phys.*, 15:438–450, 1972.

[274] G. Altarelli and G. Parisi. Asymptotic Freedom In Parton Language. *Nucl. Phys.*, B126:298–318, 1977.

[275] Yu. L. Dokshitzer. Calculation of the Structure Functions for Deep Inelastic Scattering and e^+e^- Annihilation by Perturbation Theory in Quantum Chromodynamics. *Sov. Phys. JETP*, 46:641–653, 1977.

[276] T. Sjöstrand. High-energy physics event generation with PYTHIA 5.7 and JETSET 7.4. *Comput. Phys. Commun.*, 82:74–89, 1994.

[277] G. Corcella et al. HERWIG 6.5 Release Note. Technical Report CERN-TH-2002-270, CERN, Geneva, 2002.

[278] K. C. Zapp. JEWEL 2.0.0: directions for use. *Eur. Phys. J.*, C74:2762, 2014.

[279] T. Renk. A Comparison study of medium-modified QCD shower evolution scenarios. *Phys. Rev.*, C79:054906, 2009.

[280] B. B. Back et al. Charged hadron transverse momentum distributions in Au + Au collisions at $\sqrt{s_{\rm NN}}$ = 200 GeV. *Phys. Lett.*, B578:297–303, 2004.

[281] J. Adams et al. Transverse momentum and collision energy dependence of high $p_{\rm T}$ hadron suppression in Au+Au collisions at ultrarelativistic energies. *Phys. Rev. Lett.*, 91:172302, 2003.

[282] J. Adams et al. Evidence from d + Au measurements for final state suppression of high $p_{\rm T}$ hadrons in Au+Au collisions at RHIC. *Phys. Rev. Lett.*, 91:072304, 2003.

[283] S. S. Adler et al. High $p_{\rm T}$ charged hadron suppression in Au + Au collisions at $\sqrt{s_{\rm NN}}$ = 200 GeV. *Phys. Rev.*, C69:034910, 2004.

[284] I. Arsene et al. Transverse momentum spectra in Au+Au and d+Au collisions at $\sqrt{s_{\rm NN}}$ = 200 GeV and the pseudorapidity dependence of high $p_{\rm T}$ suppression. *Phys. Rev. Lett.*, 91:072305, 2003.

[285] S. S. Adler et al. Suppressed π^0 production at large transverse momentum in central Au+ Au collisions at $\sqrt{s_{\rm NN}}$ = 200 GeV. *Phys. Rev. Lett.*, 91:072301, 2003.

[286] S. S. Adler et al. A Detailed Study of High-p_T Neutral Pion Suppression and Azimuthal Anisotropy in Au+Au Collisions at $\sqrt{s_{NN}}$ = 200 GeV. *Phys. Rev.*, C76:034904, 2007.

[287] A. Adare et al. Suppression Pattern of Neutral Pions at High Transverse Momentum in Au+Au Collisions at $\sqrt{s_{NN}} = 200$ GeV and Constraints on Medium Transport Coefficients. *Phys. Rev. Lett.*, 101:232301, 2008.

[288] S. S. Adler et al. Common suppression pattern of eta and pi0 mesons at high transverse momentum in Au+Au collisions at $\sqrt{s_{NN}}$ = 200 GeV. *Phys. Rev. Lett.*, 96:202301, 2006.

[289] S. S. Adler et al. Centrality dependence of direct photon production in $\sqrt{s_{NN}}$ = 200 GeV Au + Au collisions. *Phys. Rev. Lett.*, 94:232301, 2005.

[290] S. S. Adler et al. Absence of suppression in particle production at large transverse momentum in $\sqrt{s_{NN}} = 200$ GeV d + Au collisions. *Phys. Rev. Lett.*, 91:072303, 2003.

[291] B. B. Back et al. Pseudorapidity dependence of charged hadron transverse momentum spectra in d+Au collisions at $\sqrt{s_{NN}} = 200$ GeV. *Phys. Rev. C*, 70:061901, 2004.

[292] J. W. Cronin et al. Production of hadrons with large transverse momentum at 200, 300, and 400 GeV. *Phys. Rev.*, D11:3105–3123, 1975.

[293] I. Vitev and M. Gyulassy. High p_T tomography of d + Au and Au+Au at SPS, RHIC, and LHC. *Phys. Rev. Lett.*, 89:252301, 2002.

[294] S. S. Adler et al. High transverse momentum η meson production in $p+p$, d+Au and Au+Au collisions at $\sqrt{s_{NN}}$ = 200 GeV. *Phys. Rev.*, C75:024909, 2007.

[295] A. Adare et al. Identified charged hadron production in $p+p$ collisions at $\sqrt{s} = 200$ and 62.4 GeV. *Phys. Rev.*, C83:064903, 2011.

[296] S. S. Adler et al. Identified charged particle spectra and yields in Au+Au collisions at $\sqrt{s_{NN}}$ = 200 GeV. *Phys. Rev.*, C69:034909, 2004.

[297] A. Adare et al. Heavy Quark Production in $p+p$ and Energy Loss and Flow of Heavy Quarks in Au+Au Collisions at $\sqrt{s_{NN}} = 200$ GeV. *Phys. Rev.*, C84:044905, 2011.

[298] S. S. Adler et al. Nuclear modification of electron spectra and implications for heavy quark energy loss in Au+Au collisions at $\sqrt{s_{NN}}$ = 200 GeV. *Phys. Rev. Lett.*, 96:032301, 2006.

[299] A. Adare et al. Energy Loss and Flow of Heavy Quarks in Au+Au Collisions at $\sqrt{s_{NN}}$ = 200 GeV. *Phys. Rev. Lett.*, 98:172301, 2007.

[300] B. I. Abelev et al. Transverse momentum and centrality dependence of high-p_T non-photonic electron suppression in Au+Au collisions at $\sqrt{s_{NN}} = 200$ GeV. *Phys. Rev. Lett.*, 98:192301, 2007. [Erratum: Phys. Rev. Lett.106:159902, 2011].

[301] K Aamodt et al. Charged-particle multiplicity density at mid-rapidity in central Pb-Pb collisions at $\sqrt{s_{NN}} = 2.76$ TeV. *Phys. Rev. Lett.*, 105:252301, 2010.

[302] K. Aamodt et al. Centrality dependence of the charged-particle multiplicity density at mid-rapidity in Pb-Pb collisions at $\sqrt{s_{NN}} = 2.76$ TeV. *Phys. Rev. Lett.*, 106:032301, 2011.

[303] J. Adam et al. Centrality dependence of the charged-particle multiplicity density at midrapidity in Pb-Pb collisions at $\sqrt{s_{\rm NN}}$ = 5.02 TeV. *Phys. Rev. Lett.*, 116:222302, 2016.

[304] A. Breakstone et al. Charged Multiplicity Distribution in p p Interactions at ISR Energies. *Phys. Rev.*, D30:528, 1984.

[305] R. Nouicer et al. Pseudorapidity distributions of charged particles in d + Au and p + p collisions at $\sqrt{s_{\rm NN}}$ = 200 GeV. *J. Phys.*, G30:S1133–S1138, 2004.

[306] V. Khachatryan et al. Pseudorapidity distribution of charged hadrons in proton-proton collisions at $\sqrt{s}$ = 13 TeV. *Phys. Lett.*, B751:143–163, 2015.

[307] Jaroslav Adam et al. Charged-particle multiplicities in proton-proton collisions at $\sqrt{s}$ = 0.9 to 8 TeV. *Eur. Phys. J.*, C77:33, 2017.

[308] G. J. Alner et al. Scaling of Pseudorapidity Distributions at c.m. Energies Up to 0.9 TeV. *Z. Phys.*, C33:1–6, 1986.

[309] B. Abelev et al. Pseudorapidity density of charged particles in p + Pb collisions at $\sqrt{s_{\rm NN}} = 5.02$ TeV. *Phys. Rev. Lett.*, 110:032301, 2013.

[310] G. Aad et al. Measurement of the centrality dependence of the charged particle pseudorapidity distribution in lead-lead collisions at $\sqrt{s_{\rm NN}} = 2.76$ TeV with the ATLAS detector. *Phys. Lett.*, B710:363–382, 2012.

[311] S. Chatrchyan et al. Dependence on pseudorapidity and centrality of charged hadron production in PbPb collisions at a nucleon-nucleon centre-of-mass energy of 2.76 TeV. *JHEP*, 08:141, 2011.

[312] M. C. Abreu et al. Scaling of charged particle multiplicity in Pb+Pb collisions at SPS energies. *Phys. Lett.*, B530:43–55, 2002.

[313] I. G. Bearden et al. Charged particle densities from Au+Au collisions at $\sqrt{s_{\rm NN}}$ = 130 GeV. *Phys. Lett.*, B523:227–233, 2001.

[314] I. G. Bearden et al. Pseudorapidity distributions of charged particles from Au+Au collisions at the maximum RHIC energy. *Phys. Rev. Lett.*, 88:202301, 2002.

[315] K. Adcox et al. Centrality dependence of charged particle multiplicity in Au–Au collisions at $\sqrt{s_{\rm NN}}$ = 130 GeV. *Phys. Rev. Lett.*, 86:3500–3505, 2001.

[316] B. I. Abelev et al. Systematic Measurements of Identified Particle Spectra in pp, d+Au and Au+Au Collisions from STAR. *Phys. Rev.*, C79:034909, 2009.

[317] B. Alver et al. Phobos results on charged particle multiplicity and pseudorapidity distributions in Au+Au, Cu+Cu, d+Au, and p+p collisions at ultra-relativistic energies. *Phys. Rev.*, C83:024913, 2011.

[318] S. S. Adler et al. Systematic studies of the centrality and $\sqrt{s_{\rm NN}}$ dependence of the $dE_T/d\eta$ and $dN_{ch}/d\eta$ in heavy ion collisions at mid-rapidity. *Phys. Rev.*, C71:034908, 2005. [Erratum: Phys. Rev. C71:049901, 2005].

[319] K. Werner, Iu. Karpenko, M. Bleicher, T. Pierog, and S. Porteboeuf-Houssais. Jets, Bulk Matter, and their Interaction in Heavy Ion Collisions at Several TeV. *Phys. Rev.*, C85:064907, 2012.

[320] A. Andronic, P. Braun-Munzinger, and J. Stachel. Hadron production in central nucleus-nucleus collisions at chemical freeze-out. *Nucl. Phys.*, A772:167–199, 2006.

[321] J. Cleymans, I. Kraus, H. Oeschler, K. Redlich, and S. Wheaton. Statistical model predictions for particle ratios at $\sqrt{s_{\rm NN}}$ = 5.5-TeV. *Phys. Rev.*, C74:034903, 2006.

[322] Petrán, M. and Letessier, J. and Petráček, V. and Rafelski, J. Hadron production and quark-gluon plasma hadronization in Pb-Pb collisions at $\sqrt{s_{\rm NN}} = 2.76$ TeV. *Phys. Rev.*, C88:034907, 2013.

[323] P. Bozek and I. Wyskiel-Piekarska. Particle spectra in Pb-Pb collisions at $\sqrt{s_{\rm NN}}$ = 2.76 TeV. *Phys. Rev.*, C85:064915, 2012.

[324] Iu. A. Karpenko, Yu. M. Sinyukov, and K. Werner. Uniform description of bulk observables in the hydrokinetic model of $A+A$ collisions at the BNL Relativistic Heavy Ion Collider and the CERN Large Hadron Collider. *Phys. Rev.*, C87:024914, 2013.

[325] C. Shen, U. Heinz, P. Huovinen, and H. Song. Radial and elliptic flow in Pb+Pb collisions at the Large Hadron Collider from viscous hydrodynamic. *Phys. Rev.*, C84:044903, 2011.

[326] M. A. Lisa, S. Pratt, R. Soltz, and U. Wiedemann. Femtoscopy in relativistic heavy ion collisions. *Ann. Rev. Nucl. Part. Sci.*, 55:357–402, 2005.

[327] K. Aamodt et al. Two-pion Bose-Einstein correlations in central Pb-Pb collisions at $\sqrt{s_{NN}} = 2.76$ TeV. *Phys. Lett.*, B696:328–337, 2011.

[328] M. A. Lisa et al. Bombarding energy dependence of π^- interferometry at the Brookhaven AGS. *Phys. Rev. Lett.*, 84:2798–2802, 2000.

[329] C. Alt et al. Bose-Einstein correlations of π^- π^- pairs in central Pb+Pb collisions at A-20, A-30, A-40, A-80, and A-158 GeV. *Phys. Rev.*, C77:064908, 2008.

[330] S. V. Afanasiev et al. Energy dependence of pion and kaon production in central Pb + Pb collisions. *Phys. Rev.*, C66:054902, 2002.

[331] D. Adamova et al. Beam energy and centrality dependence of two pion Bose-Einstein correlations at SPS energies. *Nucl. Phys.*, A714:124–144, 2003.

[332] B. I. Abelev et al. Pion Interferometry in Au+Au and Cu+Cu Collisions at RHIC. *Phys. Rev.*, C80:024905, 2009.

[333] B. B. Back et al. Transverse momentum and rapidity dependence of HBT correlations in Au + Au collisions at $\sqrt{s_{\rm NN}}$ = 62.4 GeV and 200 GeV. *Phys. Rev.*, C73:031901, 2006.

[334] B. B. Back et al. Charged-particle pseudorapidity distributions in Au+Au collisions at $\sqrt{s_{\rm NN}}$ = 62.4 GeV. *Phys. Rev.*, C74:021901, 2006.

[335] J. Adams et al. Pion interferometry in Au+Au collisions at $\sqrt{s_{\rm NN}}$ = 200 GeV. *Phys. Rev.*, C71:044906, 2005.

[336] P. Bozek. Spectra, flow and HBT in Pb-Pb collisions at the LHC. *J. Phys.*, G38:124043, 2011.

[337] J.-Y. Ollitrault. Anisotropy as a signature of transverse collective flow. *Phys. Rev.*, D46:229–245, 1992.

[338] S. Voloshin and Y. Zhang. Flow study in relativistic nuclear collisions by Fourier expansion of Azimuthal particle distributions. *Z. Phys.*, C70:665–672, 1996.

[339] A. M. Poskanzer and S. A. Voloshin. Methods for analyzing anisotropic flow in relativistic nuclear collisions. *Phys. Rev.*, C58:1671–1678, 1998.

[340] B. Abelev et al. Directed Flow of Charged Particles at Midrapidity Relative to the Spectator Plane in Pb-Pb Collisions at $\sqrt{s_{\rm NN}}$=2.76 TeV. *Phys. Rev. Lett.*, 111:232302, 2013.

[341] B. Alver and G. Roland. Collision geometry fluctuations and triangular flow in heavy-ion collisions. *Phys. Rev.*, C81:054905, 2010. [Erratum: Phys. Rev. C82:039903, 2010].

[342] K. Aamodt et al. Higher Harmonic Anisotropic Flow Measurements of Charged Particles in Pb-Pb Collisions at $\sqrt{s_{\rm NN}} = 2.76$ TeV. *Phys. Rev. Lett.*, 107:032301, 2011.

[343] G. Aad et al. Measurement of the azimuthal anisotropy for charged particle production in $\sqrt{s_{\rm NN}} = 2.76$ TeV lead-lead collisions with the ATLAS detector. *Phys. Rev.*, C86:014907, 2012.

[344] C. Gale, S. Jeon, B. Schenke, P. Tribedy, and R. Venugopalan. Event-by-event anisotropic flow in heavy-ion collisions from combined Yang-Mills and viscous fluid dynamics. *Phys. Rev. Lett.*, 110:012302, 2013.

[345] J. Adam et al. Anisotropic flow of charged particles in Pb-Pb collisions at $\sqrt{s_{\rm NN}} = 5.02$ TeV. *Phys. Rev. Lett.*, 116:132302, 2016.

[346] P. Kovtun, D. T. Son, and A. O. Starinets. Viscosity in strongly interacting quantum field theories from black hole physics. *Phys. Rev. Lett.*, 94:111601, 2005.

[347] P. Romatschke and U. Romatschke. Viscosity Information from Relativistic Nuclear Collisions: How Perfect is the Fluid Observed at RHIC? *Phys. Rev. Lett.*, 99:172301, 2007.

[348] M. Luzum and P. Romatschke. Conformal Relativistic Viscous Hydrodynamics: Applications to RHIC results at $\sqrt{s_{\rm NN}}$ = 200 GeV. *Phys. Rev.*, C78:034915, 2008. [Erratum: Phys. Rev. C79:039903, 2009].

[349] H. Song and U. W. Heinz. Extracting the QGP viscosity from RHIC data - A Status report from viscous hydrodynamics. *J. Phys.*, G36:064033, 2009.

[350] H. Song, S. A. Bass, U. Heinz, T. Hirano, and C. Shen. Hadron spectra and elliptic flow for 200 A GeV Au+Au collisions from viscous hydrodynamics coupled to a Boltzmann cascade. *Phys. Rev.*, C83:054910, 2011. [Erratum: Phys. Rev. C86:059903, 2012].

[351] J. Adam et al. Higher harmonic flow coefficients of identified hadrons in Pb-Pb collisions at $\sqrt{s_{\rm NN}}$ = 2.76 TeV. *JHEP*, 09:164, 2016.

[352] C. Shen, Z. Qiu, H. Song, J. Bernhard, S. Bass, and U. Heinz. The iEBE-VISHNU code package for relativistic heavy-ion collisions. *Comput. Phys. Commun.*, 199:61–85, 2016.

[353] K Aamodt et al. Elliptic flow of charged particles in Pb-Pb collisions at $\sqrt{s_{\rm NN}}$ = 2.76 TeV. *Phys. Rev. Lett.*, 105:252302, 2010.

[354] G. Aad et al. Measurement of the distributions of event-by-event flow harmonics in lead-lead collisions at $\sqrt{s_{\rm NN}}$ = 2.76 TeV with the ATLAS detector at the LHC. *JHEP*, 11:183, 2013.

[355] S. Chatrchyan et al. Measurement of the elliptic anisotropy of charged particles produced in PbPb collisions at $\sqrt{s}_{NN}$=2.76 TeV. *Phys. Rev.*, C87:014902, 2013.

[356] B. Schenke, P. Tribedy, and R. Venugopalan. Fluctuating Glasma initial conditions and flow in heavy ion collisions. *Phys. Rev. Lett.*, 108:252301, 2012.

[357] B. B. Abelev et al. Elliptic flow of identified hadrons in Pb-Pb collisions at $\sqrt{s_{\rm NN}} = 2.76$ TeV. *JHEP*, 06:190, 2015.

[358] S. A. Bass et al. Microscopic models for ultrarelativistic heavy ion collisions. *Prog. Part. Nucl. Phys.*, 41:255–369, 1998. [Prog. Part. Nucl. Phys.41,225(1998)].

[359] Z-W. Lin, C. M. Ko, B.-A. Li, B. Zhang, and S. Pal. A Multi-phase transport model for relativistic heavy ion collisions. *Phys. Rev.*, C72:064901, 2005.

[360] B. Abelev et al. Anisotropic flow of charged hadrons, pions and (anti-)protons measured at high transverse momentum in Pb-Pb collisions at $\sqrt{s_{\rm NN}}$=2.76 TeV. *Phys. Lett.*, B719:18–28, 2013.

[361] W. A. Horowitz and M. Gyulassy. Quenching and Tomography from RHIC to LHC. *J. Phys.*, G38:124114, 2011.

[362] S. Chatrchyan et al. Azimuthal Anisotropy of Charged Particles at High Transverse Momenta in Pb-Pb Collisions at $\sqrt{s_{\rm NN}} = 2.76$ TeV. *Phys. Rev. Lett*, 109:022301, 2012.

[363] B. Abelev et al. D meson elliptic flow in non-central Pb-Pb collisions at $\sqrt{s_{\rm NN}}$ = 2.76TeV. *Phys. Rev. Lett.*, 111:102301, 2013.

[364] S. Acharya et al. *D*-meson azimuthal anisotropy in midcentral Pb-Pb collisions at $\sqrt{\mathbf{s}_{\rm NN}} = \mathbf{5.02}$ TeV. *Phys. Rev. Lett.*, 120:102301, 2018.

[365] E. Abbas et al. J/Psi Elliptic Flow in Pb-Pb Collisions at $\sqrt{s_{\rm NN}}$ = 2.76 TeV. *Phys. Rev. Lett.*, 111:162301, 2013.

[366] S. Acharya et al. J/ψ elliptic flow in Pb-Pb collisions at $\sqrt{s_{\rm NN}} = 5.02$ TeV. *Phys. Rev. Lett.*, 119:242301, 2017.

[367] S Acharya et al. The ALICE definition of primary particles. Technical Report ALICE-PUBLIC-2017-005, CERN, 2017.

[368] M. L. Knichel. *Transverse momentum distributions of primary charged particles in pp, p–Pb and Pb–Pb collisions measured with ALICE at the LHC*. PhD thesis, Technical University Darmstadt, Darmstadt, 2014.

[369] B. Abelev et al. Measurement of inelastic, single- and double-diffraction cross sections in proton-proton collisions at the LHC with ALICE. *Eur. Phys. J.*, C73:2456, 2013.

[370] J Adam et al. ALICE luminosity determination for pp collisions at $\sqrt{s} = 5$ TeV. Technical Report ALICE-PUBLIC-2016-005, CERN, 2016.

[371] P. Z. Skands. The Perugia Tunes. In *Proceedings, 1st International Workshop on Multiple Partonic Interactions at the LHC (MPI08): Perugia, Italy, October 27-31, 2008*, pages 284–297, 2009.

[372] P. Skands, S. Carrazza, J. Rojo. Tuning PYTHIA 8.1: the Monash 2013 tune. *Eur. Phys. J. C*, 74:3024, 2014.
[373] B. Alver et al. The PHOBOS Glauber Monte Carlo. *arXiv:0805.4411 [nucl-ex]*, 2008.
[374] O. Djuvsland and J. Nystrand. Single and Double Photonuclear Excitations in Pb+Pb Collisions at $\sqrt{s_{\rm NN}}$ = 2.76 TeV at the CERN Large Hadron Collider. *Phys. Rev.*, C83:041901, 2011.
[375] B. Abelev et al. Multiplicity Dependence of Pion, Kaon, Proton and Lambda Production in p–Pb Collisions at $\sqrt{s_{\rm NN}}$ = 5.02 TeV. *Phys. Lett.*, B728:25–38, 2014.
[376] A. A. Bylinkin and A. A. Rostovtsev. Systematic studies of hadron production spectra in collider experiments. In *Proceedings, 40th International Symposium on Multiparticle Dynamics (ISMD 2010): Antwerp, Belgium, September 21-25, 2010*, pages 103–108, 2010.
[377] R. Hagedorn. Multiplicities, $p_{\rm T}$ distributions and the expected hadron $\rightarrow$ quark-gluon phase transition. *Riv. Nuovo Cim.*, 6:1–50, 1983.
[378] M. Stratmann R. Sassot, P. Zurita. Inclusive hadron production in the CERN-LHC era. *Phys. Rev. D*, 82:074011, 2010.
[379] P. M. Nadolsky et al. Implications of CTEQ global analysis for collider observables. *Phys. Rev.*, D78:013004, 2008.
[380] D. de Florian, R. Sassot, and M. Stratmann. Global analysis of fragmentation functions for pions and kaons and their uncertainties. *Phys. Rev.*, D75:114010, 2007.
[381] D. de Florian, R. Sassot, and M. Stratmann. Global analysis of fragmentation functions for protons and charged hadrons. *Phys. Rev.*, D76:074033, 2007.
[382] S. Chatrchyan et al. Charged particle transverse momentum spectra in pp collisions at $\sqrt{s_{\rm NN}} = 0.9$, and 7 TeV. *JHEP*, 1108:086, 2011.
[383] S. Chatrchyan et al. Study of high-$p_{\rm T}$ charged particle suppression in PbPb compared to pp collisions at $\sqrt{s_{\rm NN}} = 2.76$ TeV. *Eur. Phys. J.*, C72:1945, 2012.
[384] E. Abbas et al. Centrality dependence of the pseudorapidity density distribution for charged particles in Pb-Pb collisions at $\sqrt{s_{\rm NN}}$ = 2.76 TeV. *Phys. Lett.*, B726:610–622, 2013.
[385] C. Loizides, J. Kamin, and D. d'Enterria. Improved Monte Carlo Glauber predictions at present and future nuclear colliders. *Phys. Rev.*, C97:054910, 2018.
[386] K. Aamodt et al. Production of pions, kaons and protons in pp collisions at $\sqrt{s} = 900$ GeV with ALICE at the LHC. *Eur. Phys. J.*, C71:1655, 2011.
[387] A. Adare et al. Spectra and ratios of identified particles in Au+Au and d+Au collisions at $\sqrt{s_{\rm NN}} = 200$ GeV. *Phys. Rev.*, C88:024906, 2013.
[388] B. I. Abelev et al. Identified baryon and meson distributions at large transverse momenta from Au+Au collisions at $\sqrt{s_{\rm NN}}$ = 200 GeV. *Phys. Rev. Lett.*, 97:152301, 2006.
[389] J. Adam et al. Measurement of pion, kaon and proton production in proton-proton collisions at $\sqrt{s} = 7$ TeV. *Eur. Phys. J.*, C75:226, 2015.
[390] B. Abelev et al. Measurement of charm production at central rapidity in proton-proton collisions at $\sqrt{s} = 2.76$ TeV. *JHEP*, 07:191, 2012.

[391] B. Abelev et al. Measurement of charm production at central rapidity in proton-proton collisions at $\sqrt{s} = 7$ TeV. *JHEP*, 01:128, 2012.
[392] B. B. Abelev et al. Measurement of prompt *D*-meson production in $p-Pb$ collisions at $\sqrt{s_{\rm NN}}$ = 5.02 TeV. *Phys. Rev. Lett.*, 113:232301, 2014.
[393] J. Adam et al. Measurement of D-meson production versus multiplicity in p-Pb collisions at $\sqrt{s_{\rm NN}} = 5.02$ TeV. *JHEP*, 08:078, 2016.
[394] B. Abelev et al. Suppression of high transverse momentum D mesons in central Pb-Pb collisions at $\sqrt{s_{\rm NN}} = 2.76$ TeV. *JHEP*, 09:112, 2012.
[395] J. Adam et al. Centrality dependence of high-p_T D meson suppression in Pb-Pb collisions at $\sqrt{s_{\rm NN}} = 2.76$ TeV. *JHEP*, 11:205, 2015. [Addendum: JHEP06,032(2017)].
[396] J. Adam et al. Transverse momentum dependence of D-meson production in Pb-Pb collisions at $\sqrt{s_{\rm NN}} = 2.76$ TeV. *JHEP*, 03:081, 2016.
[397] K.A. Olive et al. (Particle Data Group). Review of particle physics. *Chin. Phys. C*, 38:090001, 2014.
[398] D. Aosta et al. Measurement of prompt charm meson production cross sections in $p\bar{p}$ collisions at $\sqrt{s} = 1.96$ TeV. *Phys. Rev. Lett.*, 91:241804, 2003.
[399] M. Cacciari, M. Greco, and P. Nason. The $p_{\rm T}$ spectrum in heavy flavor hadroproduction. *JHEP*, 05:007, 1998.
[400] M. Cacciari, S. Frixione, and P. Nason. The $p_{\rm T}$ spectrum in heavy flavor photoproduction. *JHEP*, 03:006, 2001.
[401] D. Lange. The EvtGen particle decay simulation package. *Nucl. Instum. Meth.*, A462:152–155, 2001.
[402] N. Armesto, A. Dainese, C. A. Salgado, and U. A. Wiedemann. Testing the color charge and mass dependence of parton energy loss with heavy-to-light ratios at RHIC and CERN LHC. *Phys. Rev.*, D71:054027, 2005.
[403] S. Chatrchyan et al. Suppression of non-prompt J/ψ, prompt J/ψ, and Y(1S) in PbPb collisions at $\sqrt{s_{\rm NN}} = 2.76$ TeV. *JHEP*, 05:063, 2012.
[404] K. Nakamura et al. Review of particle physics. *J. Phys.*, G37:075021, 2010.
[405] R. Averbeck, N. Bastid, Z. Conesa del Valle, P. Crochet, A. Dainese, and X. Zhang. Reference Heavy Flavour Cross Sections in pp Collisions at $\sqrt{s}$ = 2.76 TeV, using a pQCD-Driven $\sqrt{s}$-Scaling of ALICE Measurements at $\sqrt{s}$ = 7 TeV. *arXiv:1107.3243 [hep-ph]*, 2011.
[406] B. B. Abelev et al. Charged jet cross sections and properties in proton-proton collisions at $\sqrt{s} = 7$ TeV. *Phys. Rev.*, D91:112012, 2015.
[407] S. Catani et al. Longitudinally invariant k_t clustering algorithms for hadron hadron collisions. *Nucl.Phys.*, B406:187–224, 1993.
[408] G. P. Salam M. Cacciari and G. Soyez. The anti-kt jet clustering algorithm. *JHEP*, 0804:063, 2008.
[409] G. P. Salam. Towards jetography. *Eur. Phys. J.*, C67:637–686, 2010.
[410] M. Cacciari and G. P. Salam. Pileup subtraction using jet areas. *Phys. Lett. B*, 659:119–126, 2008.

[411] B. Abelev et al. (ALICE Collaboration). Measurement of event background fluctuations for charged particle jet reconstruction in Pb-Pb collisions at $\sqrt{s_{\rm NN}} = 2.76$ TeV. *JHEP*, 03:053, 2012.

[412] M. Cacciari, G. P. Salam, and G. Soyez. FastJet User Manual. *Eur. Phys. J.*, C72:1896, 2012.

[413] M. Cacciari and G. P. Salam. The catchment area of jets. *JHEP*, 04:005, 2008.

[414] M. Cacciari, J. Rojo, G. P. Salam, and G. Soyez. Jet Reconstruction in Heavy Ion Collisions. *Eur. Phys. J.*, C71:1539, 2011.

[415] B. Abelev et al. Underlying Event measurements in pp collisions at $\sqrt{s} = 0.9$ and 7 TeV with the ALICE experiment at the LHC. *JHEP*, 07:116, 2012.

[416] P. Z. Skands. Tuning Monte Carlo Generators: The Perugia Tunes. *Phys. Rev. D*, 82:074018, 2010.

[417] M. Vajzer. Charged jet spectra in proton-proton collisions with the ALICE experiment at the LHC. In *Proceedings, 2013 European Physical Society Conference on High Energy Physics (EPS-HEP 2013): Stockholm, Sweden, July 18-24, 2013*, volume EPS-HEP2013, page 464, 2013.

[418] G. D'Agostini. A Multidimensional unfolding method based on Bayes' theorem. *Nucl. Instrum. Meth.*, A362:487–498, 1995.

[419] V. Blobel. An Unfolding method for high-energy physics experiments. In *Advanced Statistical Techniques in Particle Physics. Proceedings, Conference, Durham, UK, March 18-22, 2002*, pages 258–267, 2002.

[420] M. Schmelling. The Method of reduced cross entropy: A General approach to unfold probability distributions. *Nucl. Instrum. Meth.*, A340:400–412, 1994.

[421] T. Adye. Unfolding algorithms and tests using RooUnfold. In *Proceedings, PHYSTAT 2011 Workshop on Statistical Issues Related to Discovery Claims in Search Experiments and Unfolding, CERN,Geneva, Switzerland 17-20 January 2011*, pages 313–318, Geneva, 2011. CERN, CERN.

[422] G. D'Agostini. Bayesian inference in processing experimental data: Principles and basic applications. *Rept. Prog. Phys.*, 66:1383–1420, 2003.

[423] S. Chatrchyan et al. Modification of jet shapes in PbPb collisions at $\sqrt{s_{\rm NN}} = 2.76$ TeV. *Phys. Lett.*, B730:243–263, 2014.

[424] B. B. Abelev et al. Measurement of visible cross sections in proton-lead collisions at $\sqrt{s_{\rm NN}}$ = 5.02 TeV in van der Meer scans with the ALICE detector. *JINST*, 9:P11003, 2014.

[425] P. Nason. A New method for combining NLO QCD with shower Monte Carlo algorithms. *JHEP*, 11:040, 2004.

[426] S. Frixione, P. Nason, and G. Ridolfi. A Positive-weight next-to-leading-order Monte Carlo for heavy flavour hadroproduction. *JHEP*, 09:126, 2007.

[427] B.Z. Kopeliovich, J. Nemchik, A. Schafer, and A.V. Tarasov. Cronin effect in hadron production off nuclei. *Phys. Rev. Lett.*, 88:232303, 2002.

[428] A. Accardi. Cronin effect in proton nucleus collisions: A Survey of theoretical models. *arXiv:hep-ph/0212148 [hep-ph]*, 2002.

[429] S. Chatrchyan et al. Measurement of isolated photon production in pp and PbPb collisions at $\sqrt{s_{\mathrm{NN}}} = 2.76$ TeV. *Phys. Lett.*, B710:256–277, 2012.

[430] S. Chatrchyan et al. Study of Z boson production in PbPb collisions at $\sqrt{s_{\mathrm{NN}}}$ = 2.76 TeV. *Phys. Rev. Lett.*, 106:212301, 2011.

[431] S. Chatrchyan et al. Study of W boson production in PbPb and pp collisions at $\sqrt{s_{\mathrm{NN}}} =$ 2.76 TeV. *Phys. Lett. B*, 715:66–87, 2012.

[432] R. Tribedy, P.and Venugopalan. QCD saturation at the LHC: comparisons of models to p+p and A+A data and predictions for p+Pb collisions. *Phys. Lett.*, B710:125–133, 2012.

[433] J. L. Albacete, A. Dumitru, H. Fujii, and Y. Nara. CGC predictions for p+Pb collisions at the LHC. *Nucl. Phys.*, A897:1–27, 2013.

[434] I. Helenius, K. J. Eskola, H. Honkanen, and C. A. Salgado. Impact-parameter dependent nuclear parton distribution functions: EPS09s and EKS98s and their applications in nuclear hard processes. *JHEP*, 1207:073, 2012.

[435] Z.-B. Kang, I. Vitev, and H. Xing. Nuclear modification of high transverse momentum particle production in p+A collisions at RHIC and LHC. *Phys. Lett.*, B718:482–487, 2012.

[436] R. Xu, W.-T. Deng, and X.-N. Wang. Nuclear modification of high-p_{T} hadron spectra in p+A collisions at LHC. *Phys. Rev.*, C86:051901, 2012.

[437] B. Abelev et al. Long-range angular correlations on the near and away side in p–Pb collisions at $\sqrt{s_{\mathrm{NN}}} = 5.02$ TeV. *Phys. Lett.*, B719:29–41, 2013.

[438] B. B. Abelev et al. Long-range angular correlations of pi, K and p in p–Pb collisions at $\sqrt{s_{\mathrm{NN}}} = 5.02$ TeV. *Phys. Lett. B*, 726:164–177, 2013.

[439] M. G. Albrow et al. Tevatron-for-LHC Report of the QCD Working Group. *arXiv:hep-ph/0610012 [hep-ph]*, 2006.

[440] T. Aaltonen et al. Measurement of Particle Production and Inclusive Differential Cross Sections in $p\bar{p}$ Collisions at $\sqrt{s} = 1.96$ TeV. *Phys. Rev.*, D79:112005, 2009. [Erratum: Phys. Rev. D82:119903, 2010].

[441] C. Loizides and A. Morsch. Absence of jet quenching in peripheral nucleus-nucleus collisions. *Phys. Lett.*, B773:408–411, 2017.

[442] V. Khachatryan et al. Nuclear Effects on the Transverse Momentum Spectra of Charged Particles in pPb Collisions at $\sqrt{s_{\mathrm{NN}}} = 5.02$ TeV. *Eur. Phys. J.*, C75:237, 2015.

[443] V. Khachatryan et al. Charged-particle nuclear modification factors in PbPb and pPb collisions at $\sqrt{s_{\mathrm{NN}}} = 5.02$ TeV. *JHEP*, 04:039, 2017.

[444] W. A. Horowitz and M. Gyulassy. The Surprising Transparency of the sQGP at LHC. *Nucl. Phys.*, A872:265–285, 2011.

[445] T. Renk, H. Holopainen, J. Auvinen, and Kari J. Eskola. Energy Loss in a Fluctuating Hydrodynamical Background. *Phys. Rev.*, C85:044915, 2012.

[446] T. Renk. Pathlength dependence of energy loss within in-medium showers. *Phys. Rev.*, C83:024908, 2011.
[447] T. Renk. The Phenomenology of Elastic Energy Loss. *Phys. Rev.*, C76:064905, 2007.
[448] Z.-B. Kang, R. Lashof-Regas, G. Ovanesyan, P. Saad, and I. Vitev. Jet quenching phenomenology from soft-collinear effective theory with Glauber gluons. *Phys. Rev. Lett.*, 114:092002, 2015.
[449] Y.-T. Chien, A. Emerman, Z.-B. Kang, G. Ovanesyan, and I. Vitev. Jet quenching from QCD evolution. *Phys. Rev.*, D93:074030, 2016.
[450] M. Djordjevic and M. Djordjevic. Predictions of heavy-flavor suppression at 5.1 TeV Pb+Pb collisions at the CERN Large Hadron Collider. *Phys. Rev.*, C92:024918, 2016.
[451] M. Djordjevic, B. Blagojevic, and L. Zivkovic. Mass tomography at different momentum ranges in quark-gluon plasma. *Phys. Rev.*, C94:044908, 2016.
[452] E. Bianchi, J. Elledge, A. Kumar, A. Majumder, G.-Y. Qin, and C. Shen. The x and Q^2 dependence of $\hat{q}$, quasi-particles and the JET puzzle. *arXiv:1702.00481 [nucl-th]*, 2017.
[453] J. Xu, J. Liao, and M. Gyulassy. Consistency of Perfect Fluidity and Jet Quenching in semi-Quark-Gluon Monopole Plasmas. *Chin. Phys. Lett.*, 32:092501, 2015.
[454] J. Xu, J. Liao, and M. Gyulassy. Bridging soft-hard transport properties of quark-gluon plasmas with CUJET3.0. *JHEP*, 02:169, 2016.
[455] C. Andrés, N. Armesto, M. Luzum, C. A. Salgado, and P. Zurita. Energy versus centrality dependence of the jet quenching parameter $\hat{q}$ at RHIC and LHC: a new puzzle? *Eur. Phys. J.*, C76:475, 2016.
[456] R. Baier. Jet quenching. *Nucl. Phys.*, A715:209–218, 2003.
[457] A. Adare et al. Suppression pattern of neutral pions at high transverse momentum in Au + Au collisions at $\sqrt{s_{\rm NN}}$ = 200 GeV and constraints on medium transport coefficients. *Phys. Rev. Lett.*, 101:232301, 2008.
[458] A. Adare et al. Neutral pion production with respect to centrality and reaction plane in Au+Au collisions at $\sqrt{s_{\rm NN}}$=200 GeV. *Phys. Rev.*, C87:034911, 2013.
[459] A. Buzzatti and M. Gyulassy. Jet Flavor Tomography of Quark Gluon Plasmas at RHIC and LHC. *Phys. Rev. Lett.*, 108:022301, 2012.
[460] B. Schenke, C. Gale, and S. Jeon. MARTINI: An Event generator for relativistic heavy-ion collisions. *Phys. Rev.*, C80:054913, 2009.
[461] G.-Y. Qin, J. Ruppert, C. Gale, S. Jeon, G. D. Moore, and M. G. Mustafa. Radiative and collisional jet energy loss in the quark-gluon plasma at RHIC. *Phys. Rev. Lett.*, 100:072301, 2008.
[462] W.-t. Deng and X.-N. Wang. Multiple Parton Scattering in Nuclei: Modified DGLAP Evolution for Fragmentation Functions. *Phys. Rev.*, C81:024902, 2010.
[463] Z. Qiu and U. Heinz. Hydrodynamic event-plane correlations in Pb+Pb collisions at $\sqrt{s} = 2.76$ATeV. *Phys. Lett.*, B717:261–265, 2012.
[464] B. Schenke, S. Jeon, and C. Gale. Elliptic and triangular flow in event-by-event (3+1)D viscous hydrodynamics. *Phys. Rev. Lett.*, 106:042301, 2011.

[465] Z.-q. Zhang, D.-f Hou, and H.-c. Ren. The finite 't Hooft coupling correction on jet quenching parameter in a $\mathcal{N} = 4$ Super Yang-Mills Plasma. *JHEP*, 01:032, 2013.

[466] A. Majumder. Calculating the jet quenching parameter $\hat{q}$ in lattice gauge theory. *Phys. Rev.*, C87:034905, 2013.

[467] S. Caron-Huot. O(g) plasma effects in jet quenching. *Phys. Rev.*, D79:065039, 2009.

[468] M. Panero, K. Rummukainen, and A. Schäfer. Lattice Study of the Jet Quenching Parameter. *Phys. Rev. Lett.*, 112:162001, 2014.

[469] J. Adams et al. Identified hadron spectra at large transverse momentum in p+p and d+Au collisions at $\sqrt{s_{\rm NN}}$ = 200 GeV. *Phys. Lett.*, B637:161–169, 2006.

[470] S. Chatrchyan et al. Measurement of jet fragmentation in PbPb and pp collisions at $\sqrt{s_{\rm NN}} = 2.76$ TeV. *Phys. Rev.*, C90:024908, 2014.

[471] P. Christiansen, K. Tywoniuk, and V. Vislavicius. Universal scaling dependence of QCD energy loss from data driven studies. *Phys. Rev.*, C89(3):034912, 2014.

[472] J. Casalderrey-Solana, Y. Mehtar-Tani, C. A. Salgado, and K. Tywoniuk. New picture of jet quenching dictated by color coherence. *Phys. Lett.*, B725:357–360, 2013.

[473] M. L. Mangano, P. Nason, and G. Ridolfi. Heavy quark correlations in hadron collisions at next-to-leading order. *Nucl. Phys.*, B373:295–345, 1992.

[474] K. J. Eskola, H. Paukkunen, and C. A. Salgado. EPS09: A New Generation of NLO and LO Nuclear Parton Distribution Functions. *JHEP*, 04:065, 2009.

[475] H. Fujii and K. Watanabe. Heavy quark pair production in high energy pA collisions: Open heavy flavors. *Nucl. Phys.*, A920:78–93, 2013.

[476] R. Sharma, I. Vitev, and B.-W. Zhang. Light-cone wave function approach to open heavy flavor dynamics in QCD matter. *Phys. Rev.*, C80:054902, 2009.

[477] M. Cacciari et al. Theoretical predictions for charm and bottom production at the LHC. *JHEP*, 10:137, 2012.

[478] S. Acharya et al. Measurement of D^0, D^+, D^{*+} and $\mathrm{D}_{\rm s}^+$ production in Pb-Pb collisions at $\sqrt{\mathbf{s}_{\rm NN}} = 5.02$ TeV. *arXiv:1804.09083 [nucl-ex]*, 2018.

[479] L. Adamczyk et al. Observation of D^0 Meson Nuclear Modifications in Au+Au Collisions at $\sqrt{s_{\rm NN}} = 200$ GeV. *Phys. Rev. Lett.*, 113(14):142301, 2014.

[480] A. Andronic et al. Heavy-flavour and quarkonium production in the LHC era: from proton-proton to heavy-ion collisions. *Eur. Phys. J.*, C76:107, 2016.

[481] M. Djordjevic, M. Djordjevic, and B. Blagojevic. RHIC and LHC jet suppression in non-central collisions. *Phys. Lett.*, B737:298–302, 2014.

[482] M. Nahrgang, J. Aichelin, P. B. Gossiaux, and K. Werner. Influence of hadronic bound states above T_c on heavy-quark observables in Pb + Pb collisions at at the CERN Large Hadron Collider. *Phys. Rev.*, C89:014905, 2014.

[483] M. He, R. J. Fries, and R. Rapp. Heavy Flavor at the Large Hadron Collider in a Strong Coupling Approach. *Phys. Lett.*, B735:445–450, 2014.

[484] T. Song, H. Berrehrah, D. Cabrera, W. Cassing, and E. Bratkovskaya. Charm production in Pb + Pb collisions at energies available at the CERN Large Hadron Collider. *Phys. Rev.*, C93:034906, 2016.

[485] Z.-B. Kang, F. Ringer, and I. Vitev. Effective field theory approach to open heavy flavor production in heavy-ion collisions. *JHEP*, 03:146, 2017.

[486] J. Adam et al. Inclusive, prompt and non-prompt J/ψ production at mid-rapidity in Pb-Pb collisions at $\sqrt{s_{\rm NN}}$ = 2.76 TeV. *JHEP*, 07:051, 2015.

[487] M. Djordjevic. Heavy flavor puzzle at LHC: a serendipitous interplay of jet suppression and fragmentation. *Phys. Rev. Lett.*, 112(4):042302, 2014.

[488] A. M. Sirunyan et al. Nuclear modification factor of D^0 mesons in PbPb collisions at $\sqrt{s_{\rm NN}} = 5.02$ TeV. *Phys. Lett.*, B782:474–496, 2018.

[489] G. Aad et al. Centrality and rapidity dependence of inclusive jet production in $\sqrt{s_{\rm NN}} =$ 5.02 TeV proton-lead collisions with the ATLAS detector. *Phys. Lett.*, B748:392–413, 2015.

[490] S. Chatrchyan et al. Studies of dijet transverse momentum balance and pseudorapidity distributions in pPb collisions at $\sqrt{s_{\rm NN}} = 5.02$ TeV. *Eur. Phys. J.*, C74:2951, 2014.

[491] S. Chatrchyan et al. Jet momentum dependence of jet quenching in PbPb collisions at $\sqrt{s_{\rm NN}} = 2.76$ TeV. *Phys. Lett.*, B712:176–197, 2012.

[492] S. Chatrchyan et al. Observation and studies of jet quenching in PbPb collisions at nucleon-nucleon center-of-mass energy = 2.76 TeV. *Phys. Rev.*, C84:024906, 2011.

[493] G. Aad et al. Jet size dependence of single jet suppression in lead-lead collisions at $\sqrt{s_{\rm NN}} = 2.76$ TeV with the ATLAS detector at the LHC. *Phys. Lett. B*, 719:220–241, 2013.

[494] T. Renk. Physics probed by the $p_{\rm T}$ dependence of the nuclear suppression factor. *Phys. Rev.*, C88:014905, 2013.

[495] K. C. Zapp, F. Krauss, and U. A. Wiedemann. A perturbative framework for jet quenching. *JHEP*, 03:080, 2013.

[496] B. Abelev et al. Measurement of the inclusive differential jet cross section in pp collisions at $\sqrt{s} = 2.76$ TeV. *Phys. Lett.*, B722:262–272, 2013.

[497] S. Chatrchyan et al. Evidence of b-Jet Quenching in PbPb Collisions at $\sqrt{s_{\rm NN}} = 2.76$ TeV. *Phys. Rev. Lett.*, 113:132301, 2014. [Erratum: Phys. Rev. Lett.115:029903, 2015].